OXYGEN AND RADIOGENIC ISOTOPE CONSTRAINTS ON THE GENERATION OF COEXISTING SILICA-UNDERSATURATED AND OVERSATURATED FELSIC MAGMAS OF THE DITRĂU ALKALINE MASSIF (ROMANIA)

Ágnes Ódri

Supervisors: Prof Chris Harris and Dr Petrus Le Roux

Dissertation is presented for the degree of Doctor of Philosophy in the Department of Geological Sciences, University of Cape Town, South Africa

June 2018

Declaration

I, Ágnes Ódri, hereby declare that the work on which this thesis is based is my original work (except where acknowledgements indicate otherwise) and that neither the whole work nor any part of it has been, is being, or is to be submitted for another degree in this or any other university. I authorise the University to reproduce for the purpose of research either the whole or any portion of the contents in any manner whatsoever.

Signed by candidate

29 June 2018

ACKNOWLEDGEMENTS

I am grateful to my supervisors Professor Chris Harris and Dr Petrus Le Roux for guiding me through this journey.

I would like to thank Fayrooza Rawoot, Phil Janney, Christel Tinguely and Sherissa Roopnarain for the technical assistance.

I would like to express my gratitude to the staff and students of Department of Geological Sciences, especially Dr Emese Bordy whose counsel I could always rely on, both personally and academically.

I would like to thank the Ministry of Human Resources (Government of Hungary) for the National Scholarship of Young Talents grant that supported my isotope analyses.

And finally, I am grateful to the Department of Mineralogy, Geochemistry and Petrology (University of Szeged, Hungary) for providing samples for the project.

ABSTRACT

The Ditrău Alkaline Massif (DAM) is a Mesozoic igneous complex (~200-230 Ma) was generated in a continental rift environment. This study has investigated the relationship between the silica-undersaturated and oversaturated Ditrău rocks based on oxygen, Sr, Nd and Pb isotope data. Different models have been proposed previously to explain the coexisting silica-undersaturated and oversaturated rocks in general: (1) both silica-undersaturated and oversaturated magmas evolve from the same mantle-derived, undersaturated melt, with the oversaturated rocks being produced by crustal assimilation (Foland et al., 1993); (2) both are derived from the same mantle source, but do not evolve from the same parental melt (Giret and Lameyre, 1985); (3) the sources are heterogeneous on a scale that allows undersaturated and oversaturated melts to be produced (Harris, 1995). The previous petrogenetic model of the DAM emphasises the importance of fractional crystallisation of a silica-undersaturated, mantle-derived magma (e.g. Morogan et al., 2000). The Ditrău rocks show variable initial $^{87}Sr/^{86}Sr$ ratios up to 0.72372, whereas εNd_i values are from +5.5 to +0.8. High-temperature equilibrium O-isotope fractionations between minerals are generally preserved, but there was some sub-solidus O-isotope re-equilibration during slow cooling. Quartz, zircon and amphibole were used as a proxy for the magma $\delta^{18}O$ values. The estimated magma $\delta^{18}O$ values for Ditrău rocks are from 5.7 to 11.7‰. Isotope data are consistent with the involvement of both mantle and crustal sources in the formation of the DAM. The Nd and O isotope values of quartz monzonite can be explained by the subequal contribution of mantle-derived camptonite and the lower crustal partial melts generated by the intrusion of hot, mantle magmas. Both O and Nd isotope values show the dominantly mantle origin of hornblendites, diorites and nepheline syenites. The Nd and O isotope variations imply the involvement of 20-65% upper crustal melts into the re-injected camptonite magma to generate the Ditrău syenites, quartz syenites and granites. The isotope results of the DAM require the combination of the previously proposed models to explain its evolution and the relationship of the silica-undersaturated and oversaturated rocks.

TABLE OF CONTENTS

Chapter 1: Introduction

1.1 Introduction

Since it was first mentioned in the geological literature (Lilienbach, 1833), many studies have described the petrology and geochemistry of the Ditrău Alkaline Massif [DAM] (e.g. Koch,1879; Ianovici, 1938; Codarcea et al., 1957; Anastasiu and Constantinescu, 1979, 1980; Pál-Molnár, 1992, 1998, 2000; Pál-Molnár and Árva-Sós, 1995; Dallmeyer et al., 1997; Kräutner and Bindea, 1998; Jakab, 1982, 1998; Morogan et al., 2000; Batki et al., 2014; Pál-Molnár et al., 2015b). However, it owes its position of importance mostly to the work of the Swiss geologist Albert Streckeisen (1931, 1938, 1952, 1954, 1960; Streckeisen and Hunziker, 1974).

The Ditrău Alkaline Massif is a Mesozoic alkaline igneous complex which was generated in an extensional, rift related environment in an intraplate setting. It is located in the Eastern part of the Carpathian Mountains in Romania. The diameter of its presumed surface extent in a NW-SE and NE-SW direction is 19 and 14 km, and the total area of underlain by the DAM is approximately 225 km^2.

A wide variety of igneous rocks have been described in the massif, ranging from ultramafic to intermediate rocks (Tarniţa Complex: peridotites, gabbros, diorites), felsic silica-saturated and oversaturated syenites, quartz syenites and granites, as well as undersaturated alkaline rocks (nepheline syenites) (Pál-Molnár, 2000). However, there is no agreement on the petrological evolution of the DAM after 200 years of investigation, due to the wide range of rock types, their complicated field relationships combined with poor outcrop exposures, and the absence of isotope data. As a consequence, there are several unanswered questions or potentially misconstrued interpretations about the formation of the DAM. In particular, the relationship between the silica-undersaturated and versaturated felsic rocks have not been fully explained. For this reason, the focus is on the felsic rocks in this study and their isotopic implications, as well as their origin and possible relationships with the other rocks of the DAM.

1.2 Aim and objectives of the dissertation

The project is the first research which utilized oxygen isotope analyses of minerals from the Ditrău Alkaline Massif. Complementing these data with whole rock radiogenic isotope, major and trace element measurements, or petrographic observations the study aims to make significant advances in understanding of the evolution of the felsic rocks, focusing on

granites, in the Ditrău massif. To achieve this, the primary objectives of this research are given as follows:

1. Determine the variations in the oxygen isotope composition of minerals within the felsic rocks from the Ditrău Alkaline Massif.
2. Estimate the degree and influence of hydrothermal alterations.
3. Estimate the oxygen isotope composition of the parental melt of the felsic rocks and constrain their origin.
4. Evaluate the relative contributions of the mantle- and crustal-derived melts in the evolution of these rocks by the identification of open-system processes such as assimilation or magma mixing.
5. Identify the possible petrogenetic relationship between the felsic rocks and determine their relations to the Ditrău ultramafic and mafic rocks.
6. Assess the petrogenesis of the Ditrău felsic rocks.
7. Integrate the findings on the felsic rocks into the petrogenetic history of the whole DAM.

1.3 Application of isotopes in igneous petrogenetic studies

Application of stable (e.g. O, N, S, H) and radiogenic isotopes (e.g. the ^{87}Rb-^{87}Sr, ^{147}Sm-^{143}Nd and ^{235}U-^{207}Pb, ^{238}U-^{206}Pb, ^{232}Th-^{208}Pb isotope systems) in igneous petrology provides significant insights into magma sources and processes.

Even though the recognition about the possible utilization of isotopes in geology was more than 100 years ago (Rutherford and Soddy, 1903), isotope geochemistry is still a constantly developing branch of igneous petrology, mainly due to the large number of isotope systems that are presented in geological agents in a wide variety and the continuously refined analytical techniques. Whereas the geochronology uses only the long lived radioactive decay aspect of the radiogenic isotopes, isotope geochemical studies are also based on the fact that the isotope ratios of heavier elements (atomic mass > 40) are constant during chemical fractionation as their mass differences are too small to allow them to be separated. As a consequence of this any magma that forms will initially have the same isotope composition as its source during the partial melting and will remain unchanged in the course of the closed system fractional crystallisation. Since, however the radiogenic isotope composition of rocks depends on the age and the ratios of parent and daughter elements, cogenetic rocks can have different present-day isotope ratios but their initial ratios will be the same as their common source. Thus, radiogenic isotopes are very important means to assess the origin of rocks. Fig.

1 represents how the distinct parent-daughter ratios of the mantle and crust have an influence on the present-day ratios in function of time, illustrated on the example of the Rb-Sr isotope system. Nd and Pb isotopes are not presented here as they do not show anything like the same change in ratio with time. As the measured radiogenic isotope compositions are expressed with the content of the daughter and the stable, non-radiogenic isotope that abundance is constant, $^{87}Sr/^{86}Sr$ values represent the different isotope ratios of the mantle and continental crust in Fig. 1.

As a consequence of the distinct incompatibility of Sr and Rb, the latter will be concentrated in the crust, inducing different present-day radiogenic isotope ratio. Another impact of the higher crustal ratios is the evolved nature of these rocks meaning the older components of the crust that extracted from the mantle at earlier times are characterised by higher present day $^{87}Sr/^{86}Sr$ values. On account of the different radiogenic isotope composition of the crust and the mantle, radiogenic isotopes can be used to identify processes operating in igneous systems like crustal contamination or mixing between magmas from distinct source regions.

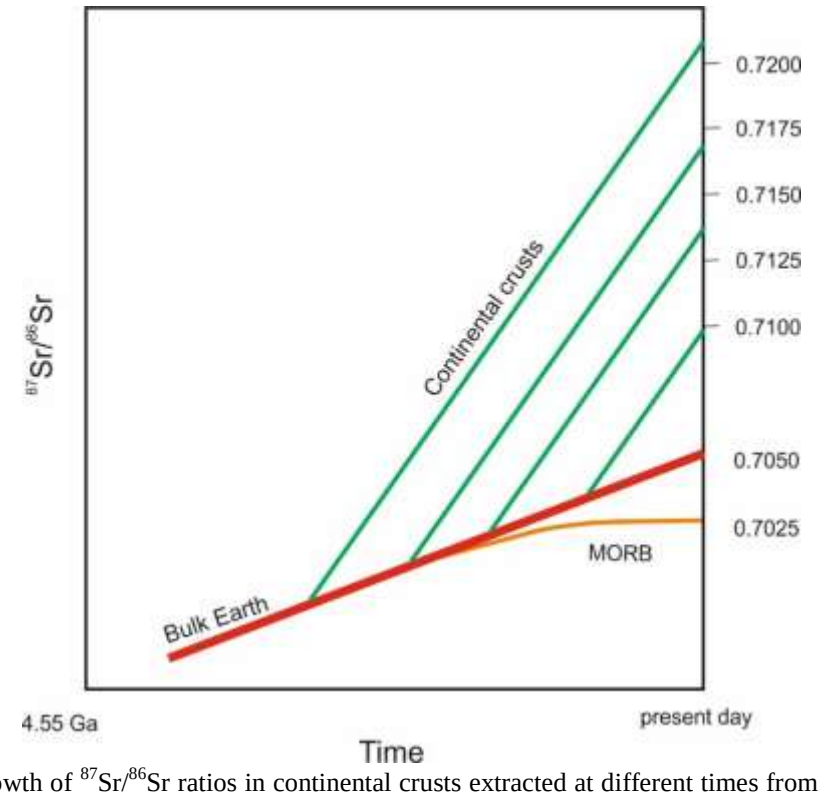

Figure 1. The growth of $^{87}Sr/^{86}Sr$ ratios in continental crusts extracted at different times from the mantle or the isotopic evolution of their depleted mantle source (Allégre, 2008)

The Sm-Nd isotope system works very similarly to Rb-Sr isotope system. However, during partial melting and fractional crystallisation Nd preferentially concentrated in the melt compared to Sm. Thus, the newly formed crustal material has lower $^{147}Sm/^{144}Nd$ ratio than the

mantle, because of which the subsequent increase of $^{143}Nd/^{144}Nd$ ratio of the crust is much slower than that of the mantle. As for the U-Th-Pb isotope system, U and Th are both enriched in melts relative to Pb. Due to this, the crust has elevated U/Pb and Th/Pb ratios than the mantle. At the same time, because U and Th are preferentially concentrated in the upper crust, the Pb isotope ratios of the lower and upper crust are different.

The first application of stable isotopes in geology related to geothermometry. It started with the recognition by Urey (1947) that unlike the radiogenic isotopes the mass fractionation of stable isotopes through physical processes is possible. He suggested that high $^{18}O/^{16}O$ ratios in limestones compared to sea water is temperature-controlled, therefore it could provide significant geological information like the temperature of ancient ocean waters. The methodology was quickly adopted from geothermometry and developed for high temperature systems and igneous processes as well.

Oxygen has three stable isotopes ^{16}O (99.76%), ^{17}O (0.04%) and ^{18}O (0.2%). Oxygen isotope variations are reported in delta notation (Equation 1.) that is traditionally used in stable isotope geochemistry and expressed in parts per thousand (‰):

$$\delta^{18}O = \left[\frac{(^{18}O/^{16}O)_{\text{sample}} - (^{18}O/^{16}O)_{\text{SMOW}}}{(^{18}O/^{16}O)_{\text{SMOW}}}\right] \text{x } 1000$$

Equation 1.

where the standard is Vienna Mean Standard Ocean Water (VSMOW) with $^{18}O/^{16}O$ ratio of $2.0052 \text{ x } 10^{-3}$ (Baertschi, 1976).

Whereas in the case of radiogenic isotopes the variation of the examined isotope system over time due to the radioactive decay is fundamental, interpretation of oxygen isotope data considers the distinct partition of heavy (^{18}O) and light (^{16}O) isotopes into different phases in function of temperature. Thus, because of the solid-liquid mass fractionation, partial melting and fractional crystallisation should cause O-isotope variations in the melt relative to its source, however at magmatic temperature it is insignificant (Faure, 1986). During fractional crystallisation from basaltic to rhyolitic compositions the increase of oxygen isotope values is typically less than 1‰ (Fig. 2; e.g. Sheppard and Harris, 1985). For this reason, similarly to radiogenic isotopes, oxygen isotopes are also intensively used in petrogenetic investigations to detect the origin of the rocks.

Behaviour of O-isotopes at low temperature (<350°C) differs from that of at magmatic temperature as the heavier isotope prefers being in the solid phase under this conditions that

affects the oxygen isotope content of crustal rocks, or also essential for the interpretation of low temperature alteration processes (e.g. Hoefs, 1987). Due to this large fractionation at surface temperatures, chemical or biochemical sedimentary rocks are characterised by significant ^{18}O-enrichment as most of them are precipitated at low temperature.

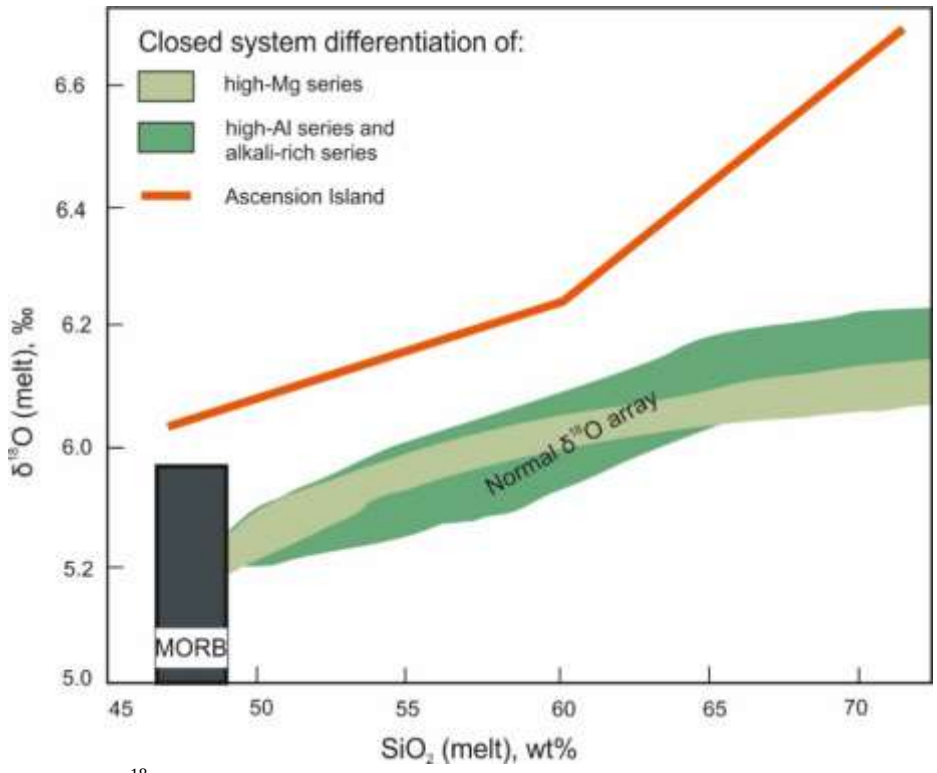

Figure 2. Variation of $\delta^{18}O$ during the closed system differentiation of the two most common island arc series (after Bindeman et al., 2008) and Ascension Island (after Sheppard and Harris, 1985)

In addition, low temperature fluid-rock interactions (e.g. the reaction between the surface and the penetrating sea water) also markedly increase the $^{18}O/^{16}O$ ratio of the rocks, while the fluid is depleted with respect to ^{18}O (Kyser, 1987). Interactions with meteoric water, which are depleted in ^{18}O, are mainly responsible for the negative oxygen isotope values (Bindeman, 2008). The $\delta^{18}O$ values of mantle-derived magmas have a narrow range (from 5 to 5.6‰; Fig. 3) compared to crustal rocks which are ^{18}O-enriched ($\delta^{18}O$ generally >6‰; James, 1981). Different waters are also characterised by distinct oxygen isotope compositions (Fig. 3). Oxygen isotope composition of meteoric water also strongly depends on geographic factors like altitude, latitude or distance inland from the coast due to their influence on the temperature (Dansgaard, 1964; Clark and Fritz, 1999). Accordingly, rainwater becomes depleted in ^{18}O at higher latitudes, towards the inland areas, and at higher elevations.

Considering that the oxygen is the most abundant element in the rocks and fluids and the varying isotope composition of the different potential reservoirs, oxygen isotopes are a powerful means to ascertain the role of the mantle and the crust in magma genesis. They also allow sub-solidus exchange between rocks and different fluids to be recognised. Modifying the oxygen isotope compositions of the rocks by interaction with fluids disturb the closed-system oxygen isotope equilibrium between the rock forming minerals. The degree of the internal equilibrium can be estimated on the basis of the per mil differences between the coexisting phases. As the distribution of oxygen isotopes between the minerals is a function of chemical bonds vibration frequencies (e.g. Zheng et al., 1993a, b; Hoefs, 2005), coexisting phases can be characterised by different $\delta^{18}O$ values. The heavy isotope of oxygen is preferentially partitioned into the mineral with the most covalent (i.e. strongest) bond.

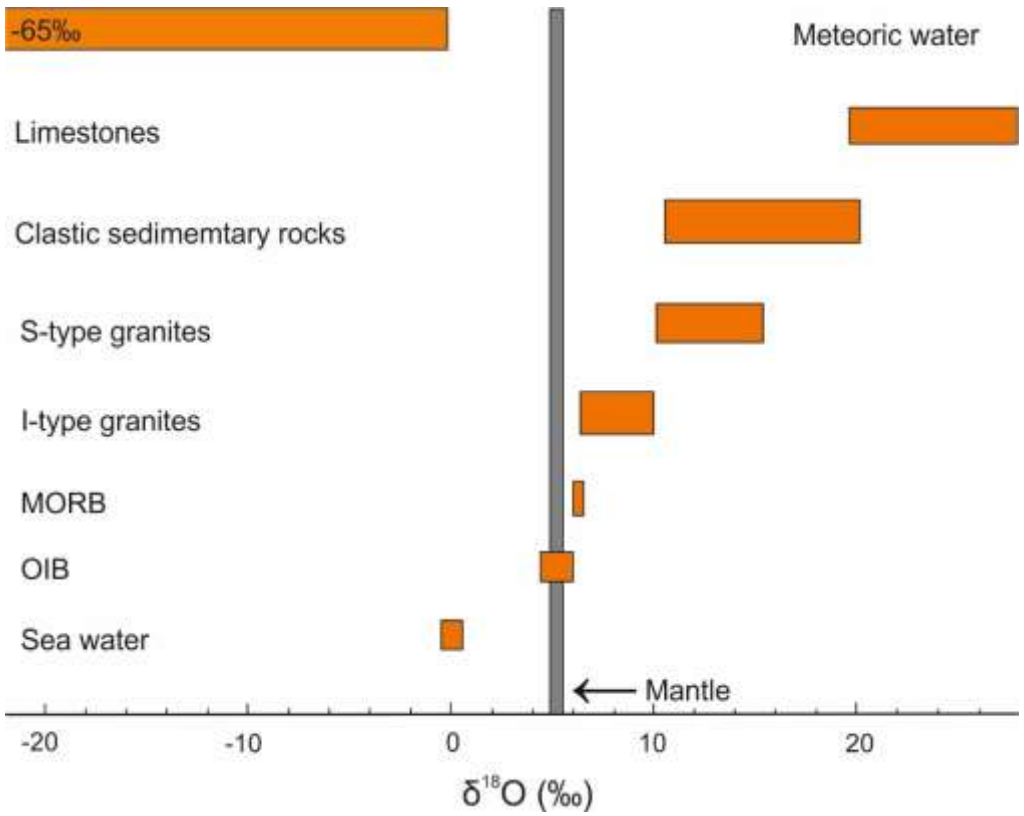

Figure 3. Oxygen isotope variations in magmas and rocks (modified after Bindeman, 2008)

Bindeman (2008) calculated the O-isotope contents of minerals from a hypothetic, polymineralic granite at 850°C with the $\delta^{18}O_{WR} = 7.8‰$ and he found that those were showing continuous decrease in $\delta^{18}O$ values: quartz (8.2‰) > albite/K-feldspar (7.5‰) > anorthite (6.6‰) > zircon (6.4‰) ≥ pyroxene (6.3‰) ≈ amphibole ≥ biotite ≥ garnet ≈ olivine (6.1‰) > sphene (5.4‰) ≥ ilmenite (4.9‰) > apatite ≥ magnetite (3.5‰). The fractionation factor for

oxygen isotopes between the major igneous minerals can be expressed according to the Equation 2:

$$1000\ln\alpha_{\mathrm{mineralA-mineralB}} = \frac{\delta^{18}O_{\mathrm{mineralA}}}{\delta^{18}O_{\mathrm{mineralB}}}$$

Equation 2.

As mentioned above isotope fractionation is a strong function of the temperature. It is small at high magmatic conditions and more significant at lower temperatures. Thus, the general relationship between the fractionation factor and the temperature can be defined by the Equation 3., where A is an experimentally determined equilibrium constant and T is given in K.

$$1000\ln\alpha = \frac{10^6 A}{T^2}$$

Equation 3.

The difference between the oxygen isotope compositions of the coexisting minerals can be expressed as per mil difference ($\Delta^{18}O = \delta^{18}O_{mineralA}-\delta^{18}O_{mineralB}$). In that case if the $\delta^{18}O$ values of the measured phases are relatively similar (δ values are less than 10‰), the fractionation factor (α) is related to the per mil difference by the relationship: $1000\ln\alpha_{mineralA- mineralB} \sim \Delta^{18}O_{mineralA-mineralB}$ (Sharp, 2006), thus the fractionation factor can be replaced by the difference of the measured oxygen isotope contents of the examined minerals:

$$\Delta^{18}{}_{\mathrm{mineralA-mineralB}} = \frac{10^6 A}{T^2}$$

Equation 4.

Knowing the ideal $\Delta^{18}O$ values of the mineral pairs at the given temperature, assessment of O-isotope equilibrium is possible by comparing it to per mil differences calculated from the measured $\delta^{18}O$ values of minerals. At the same time, the estimation of the temperature by using the calculated per mil differences between mineral pairs can be easily determined as well, especially in the case of pairs with significant A factor (Fig 4.).

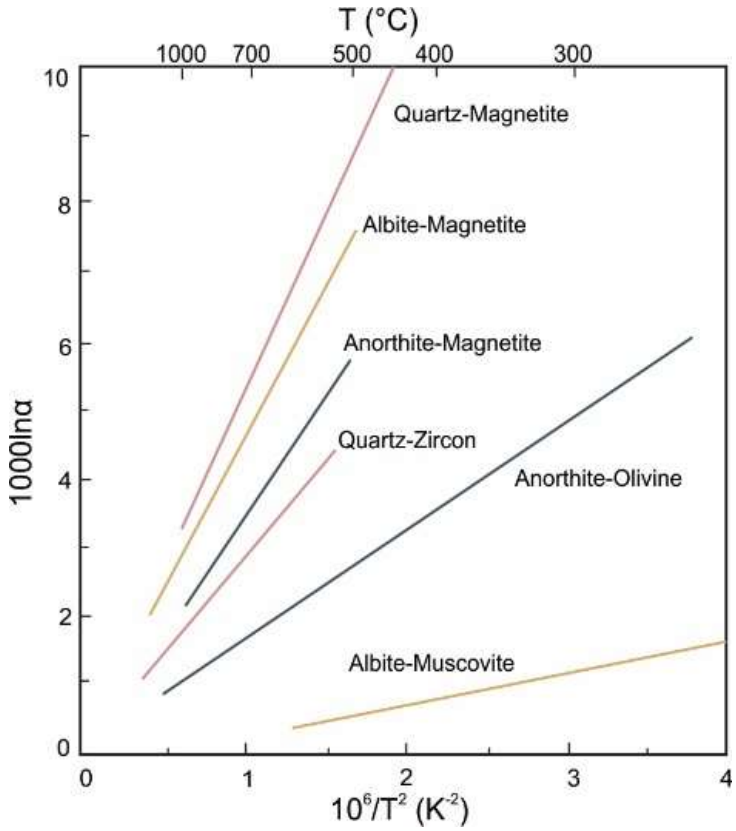

Figure 4. Oxygen isotope fractionation between coexisting minerals in function of temperature (Figure is modified after Bindeman, 2008)

1.4 Coexistence of silica-undersaturated and oversaturated rocks

Alkaline igneous complexes commonly occur in intraplate settings providing information on extensional magmatic processes (e.g. Wilson et al., 1995). This type of magmatism produces several different magmatic series out of which the coexistence of silica-undersaturated and oversaturated suites in the same igneous complex has been a long-standing issue. Whereas the silica-undersaturated rocks are believed to derive from mantle source (e.g. Kramm and Kogarko, 1994; Dunworth and Bell, 2001), the origin of silica-oversaturated rocks is explained mainly by the interaction of mantle-derived undersaturated melts with upper and/or lower crust (Davies and Mcdonald, 1987; Heaman and Machado, 1992; Mingram et al., 2000; Schmitt et al., 2000; Marks et al., 2003). The reason why these associations are highly debated is the presence of the low pressure thermal divide, represented by the alkali feldspar join (Ab-Or join), in the Petrogeny`s Residua System (Bowen, 1937), which separates the silica-undersaturated compositions from the oversaturated ones (Fig. 5).

The existence of this thermal barrier means that those melts which are evolved enough to crystallise alkali feldspar, fall on or the either side of the thermal divide,

depending on their silica saturation and will fractionate either towards the rhyolite minimum to produce silica-oversaturated liquids, or towards the phonolite minimum and generate the undersaturated liquids (Fig. 5B) (Hamilton and MacKenzie, 1965). Because the melt cannot cross the thermal divide by fractional crystallisation in a closed system, different models have been proposed to explain the coexistence of silica-oversaturated and undersaturated magmas:

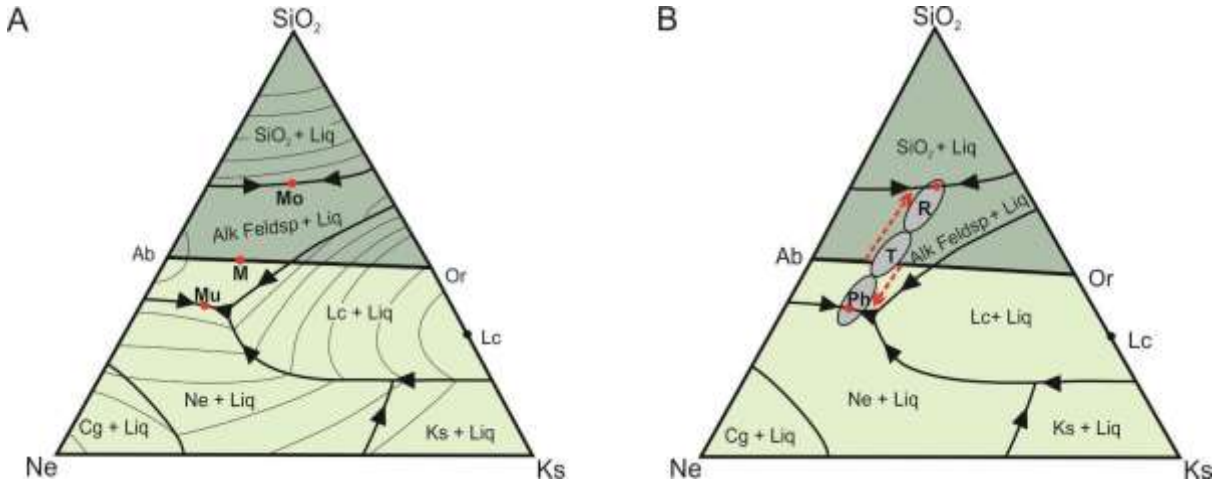

Figure 5. (A) Phase relations in the ternary system of nepheline-kalsilite-silica at 1 atm pressure (modified after Schairer, 1950) (B) Possible fractionation paths of a liquid with trachytic compositions. Mu - silica-undersaturated thermal minimum, Mo - silica-oversaturated thermal minimum, M - lowest point of the Ab-Or thermal barrier. Red dashed lines-direction of fractional crystallisation; R - rhyolitic magma, T - trachytic magma, Ph - phonolitic magma

1.4.1 Derivation from a common parental melt

Silica-undersaturated and oversaturated rocks can be derived from the same silica-undersaturated parental magma. In this case, the mechanisms that causes silica saturation leading to saturated and oversaturated rocks is the assimilation of siliceous continental crust and subsequent fractional crystallisation (Fitton, 1987). Foland et al. (1993) investigated coexisted quartz and nepheline syenites from the Marangudzi (southeast Zimbabwe) and Mt. Brome (southern Quebec, Canada) complexes. Both rock types are related to the same parental magma and according to Foland et al. (1993) their differencies are the consequences of

a.) AFC processes

As the radiogenic isotope data of the oversaturated rocks showed significant crustal input, Foland et al. (1993) supposed that the crustal contamination is the main process which can drive the undersaturated magma to cross the thermal divide (Ab-Or join) and evolve to the rhyolite minimum. Assuming that the required heat for the assimilation is provided

by the latent heat of the fractional crystallisation, they calculated liquid composition paths for AFC from undersaturated magmas with different compositions in the Petrogeny`s Residua System (Fig. 6), demonstrating that the formation of oversaturated rocks requires crustal input.

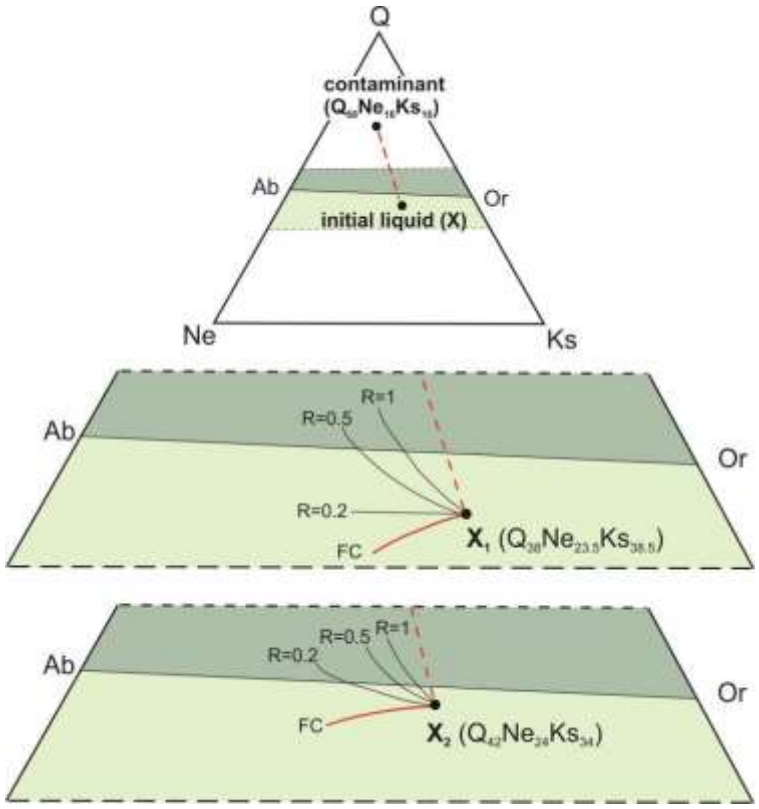

Figure 6. Calculated liquid AFC and FC trends in the Petrogeny`s Residua System for two different parental magma compositions (X_1, X_2) on the basis of Foland et al. (1993). The R values show the ratios of assimilation to fractionation

b.) magmatic differentiation

Unlike the silica-oversaturated rocks, the closed system fractionation of the same silica-undersaturated melt can produce only silica-undersaturated rocks suggested by the calculated fractionation paths from Foland et al. (1993) in Fig. 6.

Also, if the starting point of the initial magma is less undersaturated, smaller degree of assimilation is required for the magma to cross the thermal divide and produce oversaturated rocks.

Another way to produce silica-saturated and oversaturated rocks from a primarily undersaturated melt is the fractional crystallisation of amphibole (Giret et al., 1980; Downes, 1984). The chemical composition of this mineral could play an important role in the chemical evolution of the parental magma. According to Bonin and Giret (1984) Ca-rich amphiboles

(e.g. kearsutite, hastingsite or pargasite) are always silica-undersaturated compared to their host rock and coexisting phases. Therefore, the early fractionation of these amphiboles can increase the silica-saturation of the residual melt and promote the formation of silica-oversaturated rocks from undersaturated magmas.

1.4.2 Derivation from different parental melts

a.) by polybaric melting of a common mantle source

Both continental and oceanic within-plate magmatism can produce the two main types of basaltic magmas: the silica-saturated tholeiitic and the undersaturated alkaline (Kumar et al., 2007). It is now generally accepted that low-degree partial melting of mantle peridotite at higher pressure produces silica-undersaturated alkali basalts, basanites or nephelinites, whereas at lower pressure (< 5-7 kbar) and increasing melt fraction oversaturated magmas can form (Boyd et al., 1964; Kushiro, 1968; Holm et al., 2006). The eutectic point of the initial liquid can be shifted towards the more undersaturated compositions (Fig. 7A) with increasing pressure in the forsterite-nepheline-quartz system. Volatiles have a strong influence on the magma composition. If H_2O is added to the volatile-absent system at 2 GPa, it will drive the eutectic point to the oversaturated field, whereas the melting of the mantle in the presence of CO_2 favours the formation of alkaline, silica-undersaturated magmas (Kushiro, 1968; Eggler, 1974; Dasgupta et al., 2007; Fig. 7B).This implies that the tholeiitic basalts have essentially hydrous character and magmas from deeper levels of the mantle are anhydrous. Based on the above one of the main factor that significantly affects the magma composition in intraplate settings is the depth of the melting.

To explain the coexistence of the over- and undersaturated rocks in this tectonic environment, the dynamics of the lithosphere have to be considered. During the first stage of the rift development the lithosphere is still thick, consequently the pressure of mantle melting is high, which favours the generation of silica-undersaturated magmas. During the widening phase, the depth of the melting is decreasing because of the thinning of the lithosphere and saturated magmas are produced (Giret and Lameyre, 1985). Good evidence for the derivation of primary oversaturated mantle-derived magmas at shallow depths is the presence of silica-oversaturated series and granitic rocks in the oceanic environment where the continental crust is not available e.g. at Ascension Island in the south Atlantic (Weis, 1983), plagiogranite intrusions emplaced in the Oman ophiolite (Amri et al., 1996) or in the Sarikaraman ophiolite (Anatolia, Turkey; Floyd et al., 1998).

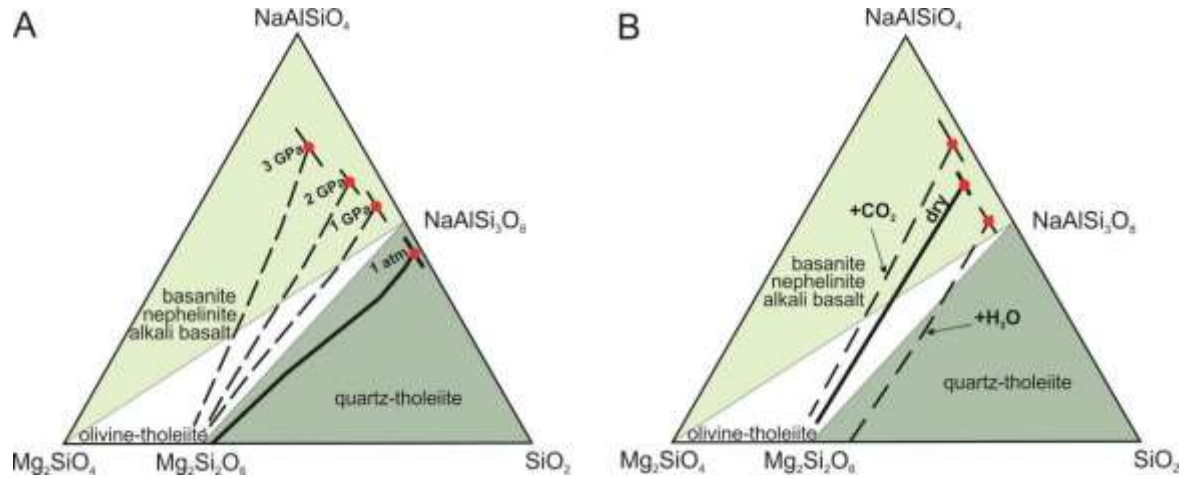

Figure 7. (A) Changing the minimum point of the initial liquid in function of the pressure and (B) the volatiles in the forsterite-nepheline-quartz system. Dashed and solid lines - forsterite-enstatite solid solution liquidus boundaries

b.) by melting of heterogeneous sources

On the basis of the above the presence of silica-oversaturated alkaline rocks beneath the continents requires crustal contamination, whereas they appear to be the products of fractional crystallisation in the oceanic tectonic settings. It is clear that the conditions of their formation are different, however, both of them are the members of magmatic series that display a continuous range from basaltic to felsic rocks. In most of these cases the genetic relationship between the end-members are obvious, however there is a type of magmatic suite which is an appropriate example to demonstrate the different origin of these rocks. As there is a hiatus between the basaltic and felsic rocks in these series, their name is bimodal magmatic suites. The processes that cause bimodal magmatic events are still highly debated, however recent numerical modelling suggests the generation of felsic magmas by crustal anatexis during the emplacement of basaltic magmas (Annen et al., 2006). These underplated mafic magmas provide the heat and the H_2O for the partial melting of the surrounding crust (Fig. 8). In the course of the early stage of the bimodal suites the generation of felsic magmas is dominant then decreases with time as the crust becomes progressively refractory. Finally, the return to mafic magmatism can produce the bimodal suites (Meade et al., 2014).

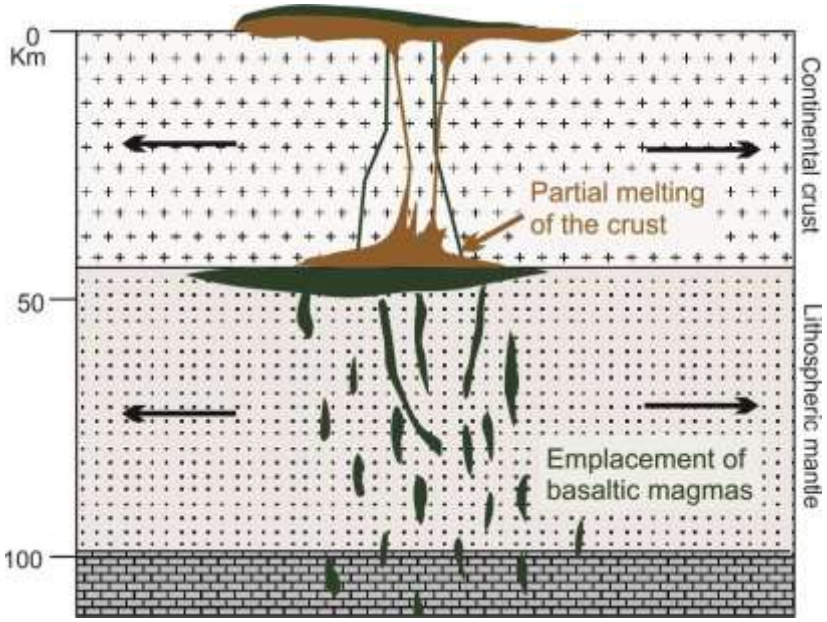

Figure 8. Schematic cross section of the bimodal magmatism induced by the underplated mafic magmas

Harris (1995) proved that the oversaturated rocks generated by crustal anatexis do not necessarily relate to the bimodal magmatic suites. His oxygen isotope investigation of the Damaraland complexes (northwest Namibia) revealed that some of the silica-oversaturated and undersaturated complexes show different $\delta^{18}O$ values that suggest different origins. Harris (1995) accepted and applied Foland`s model (see above) in order to explain the formation of undersaturated and certain oversaturated complexes, however as the $\delta^{18}O$ values of two of them (Spitzkoppe, Erongo) were too high or the initial εNd values were too low (Trumbull et al., 2004) to be the result of crustal contamination, thus he extended Foland's theory. In agreement with the presence of silica-oversaturated rocks requires crustal contamination of their undersaturated parental magma, he also stated that the generation of some of the high $\delta^{18}O$, low εNd_i granitic complexes can be explained by them being partial melts of the continental crust.

Chapter 2: Review of intraplate granites

2.1 Definition and origin of granitic rocks

A distinction is not always made between the terms granitoid and granite, although these are not equivalent. According to the IUGS descriptive classification (QAPF classification), granitoid is used to describe wide range of felsic, plutonic rocks which mainly contain feldspar and quartz whereas granite contains alkali feldspar, plagioclase feldspar and quartz in roughly the same amount (Streckeisen, 1973; Le Maître, 1989). Streckeisen (1973) specified precise definitions of these felsic rocks on the basis of their modal mineralogical compositions. According to this granite has 20-60% modal quartz content and the plagioclase is 10-65% of total feldspar. With less than 10% plagioclase feldspar we can talk about alkali-feldspar granite, while above 65% the rocks are granodiorite (65-90%) and tonalite (> 90%).

As granitic rocks constitute around 86% of the upper continental crust (Wedepohl, 1991), granitoids are one of the best studied rocks. And exactly this abundance on the continental crust was one of the main reasons why the most petrologists envisaged granites as the melting product of the continental crust in the earlier times and did not ascribe much role to the mantle-derived melts in the granite petrogenesis (Chappell and White, 1974). It was generally thought that the chemical composition of these rocks is inconsistent with a mantle source and granites in oceanic areas (like plagiogranite) were generally not considered important (Leake et al., 1980). However, White (1979) demonstrated that there are granites whose formation requires high temperatures and the intrusion of mantle-derived mafic magmas are the only process which can provide this sufficient heat to produce such granites. This idea was very important step for researchers to reinterpret the contribution of mantle- derived melts for the generation of granitic rocks. Presently, granites are viewed as either as the end-product of the fractional crystallisation (±assimilation) of mantle-derived magmas (Musselwhite et al., 1989; Grove et al., 2003; Frost and Frost, 2011) or the products of re- melting of pre-existing crustal rocks (Tepper et al., 1993; Petford and Atherton, 1996; Chappell and White, 2001).

2.2 The SIMA classification and the A-type nomenclature

In spite of the fact that granites are the most abundant rocks in the continental crust (77%), (Taylor and McLennan, 1985), it is hard to find a not solely descriptive, genetic

granite classification scheme referring to the origin and petrogenesis of granitoids, which is accepted by everybody. Since granites are genetically very complex rocks, which means that they can be produced by variety of processes from partial melting of distinct sources, petrologists have tried to classify the various granite types many different ways e.g. mineralogically (Ishihara, 1977; Pupin, 1980; Lameyre and Bowden, 1982), chemically (La Roche et al., 1980; Pearce et al., 1984; Maniar and Piccoli, 1989), tectonically (Pitcher, 1983, 1987) or on the basis of their enclave content (Didier and Lameyre, 1969). Currently, the most often used genetic classification in the literature is the so-called `alphabet soup` or SIMA classification, initiated by Chappell and White in 1974. They examined granites in the Lachlan Fold Belt (southeastern Australia) and identified two granite types on the basis of their presumed source: S-type and I-type granites referring to their (meta)sedimentary and (meta)igneous derivation.

This classification was further expanded by Loiselle and Wones (1979) who recognised a granite type which occurs in rift zones and originate from alkaline and relatively anhydrous magmas. According to their definition it crystallises under low H_2O and oxygen fugacity conditions from the differentiation of alkali basalt parental magma (with or without crustal contamination) in anorogenic settings. Moreover, they are enriched in HFSE and LILE and have low trace element concentrations like Ba, Sr and Eu. Loiselle and Wones named them A-type granites supposedly referring to the anorogenic, alkaline and anhydrous natures. In the same year, White (1979) also identified a granite type which has alkaline, anhydrous nature and occurs in non-orogenic settings like Loiselle and Wones`s A-type granites, however White considered its source as the granulitic residue which remains in the lower crust after a previous melting event. He named this new type of granites R-type - after their residual source - in his oral presentation at the GSA Annual Meeting, but subsequently the term R-type has not been generally accepted and Collins et al. (1982) was the first study which used the A-type term for these granites in connection with Gabo and Mumbulla Suites (southeastern Australia) and developed further this model. At the same time White (1979) introduced another granite type, formed by hydration and the subsequent melting of the heterogeneous mantle wedge above the subducting slab in the convergence zones, or they also can be derived from the melting of the subducting oceanic crust. As it has direct or indirect mantle derivation, he used the letter M to express this. The short summary of the above-mentioned granite types is listed in Table 1.

The alphabetic method became very popular although it is not uniform. While the letters I, S and M refer to the composition of the source material, the letter A implies the

tectonic setting and the nature of the magma. A drawback of this genetic classification is that it suggests single source, which would be easy to identify on the basis of the geochemical features of the rocks or major and accessory mineral assemblages, however, granite intrusions are mostly formed by interaction (e.g. assimilation, mixing) of mantle-derived and crustal materials and they are not solely from one source (Miller et al. 1990, Kemp et al., 2005b).

Table 1. Summary of the features of different granite types (Chappell and White, 1974; White and Chappell, 1983; Loiselle and Wones, 1979; White, 1979; Collins et al., 1982; Clarke, 1992; Eby, 1992).

	I-type granitoids	S-type granitoids	A-type granitoids	M-type granitoids
tectonic settings	continental arc settings	continental collision zones	anorogenic, post orogenic settings; intraplate rift zones	island arc settings, ocean intraplate
Source	partial melting of metaigneous lower crust in the subduction zones crystallised from the underplated mantle-derived mafic melts	partial melting of metasedimentary rocks during the crustal thickening	partial melting of lower crustal granulite; differentiation of mantle-derived magmas (+assimilation)	indirect mantle origin-partial melting of subducated oceanic crust; direct mantle origin - fractional crystallisation of basalt
ASI	metaluminous	peraluminous	peraluminous, metaluminous, peralkaline	metaluminous
associated minerals	hornblende, biotite, magnetite	muskovite (with biotite) and other Al-rich phases, ilmenite	Fe-rich biotite, alkali pyroxene, amphibole, magnetite	hornblende, biotite, magnetite
isotopes	$^{87}Sr/^{86}Sr_i<0.705$ $\delta^{18}O=6.6\text{-}9.9‰$	$^{87}Sr/^{86}Sr_i<0.707$ $\delta^{18}O=9.5\text{-}11.4‰$	$^{87}Sr/^{86}Sr_i=0.703\text{-}0.720$ $\delta^{18}O=6.6\text{-}9.9‰$	$^{87}Sr/^{86}Sr_i<0.705$ $\delta^{18}O<9‰$

Besides the SIMA classification the purely geochemical classification of Frost et al. (2001) is widely used as well. Their classification scheme is based on three geochemical parameters (Fe-number, modified alkali-lime index and aluminium saturation index) that are not influenced by the mode of the generation and the tectonic setting of the granites. Whereas Fe-number (Fe*= FeO / (FeO + MgO)) distinguishes ferroan and magnesian granitoids, on the basis of the modified alkali-lime index (MALI = $Na_2O + K_2O - CaO$) those can be further classified into alkalic, alkali-calcic, calc-alkalic and calcic groups. Peraluminous, metaluminous and peralkaline character of the granitoids is reflected by the aluminium

saturation index (ASI = Al / (Ca - 1.67P + Na + K)). Fe* provides information about the differentiation history of the granitic magma by expressing the degree of iron enrichment in the rocks. As the abundance and composition of feldspars of the granitoids affects the value of MALI, it reflects the source of their magma. ASI is influenced by mainly the mica content of the rocks and oher alumina phases, ASI indicates the condition of melting and the source characteristics of the magma. Based on the above-mentioned chemical inidicators, rocks can be divide into 16 compositional groups, which conveys information about the source compositions and different petrologic processes. According to Frost and Lindsey (1991) alkaline basalts from extensional environments can undergo FeO-enrichment or reduction through differentiation compared to MgO, whereas the relatively oxidised arc basaltic magmas cannot. This leads to the conclusion that iron-enriched rocks crystallised form reduced basaltic magmas in contrast with the rocks with minimal iron-enrichment that relate to oxidised arc magmas (Frost and Frost, 1997). As magmatic suites with A-type characteristics mainlybelong to the iron-enriched suites, Frost et al. (2001) suggested the term ferroan granites to designate the granites with the A-type characteristics.

2.3 Summary of A-type granites

2.3.1 Nature and characteristics of A-type granites

The term A-type has been applied to a wide variety of granite composition with different origin, but their certain geochemical characteristics are uniform enough to belong to the same group and be separated from other granites types. Whalen et al. (1987) reported detailed description about their geochemical and mineralogical features. According to theirdefinition they are high Na_2O+K_2O, FeO^t/MgO, HFSE (Zr, Nb, Ta), REE (except Eu) content rocks with elevated halogen element concentrations (F, Cl). Moreover, they are low in CaO, Al_2O_3 and those trace elements which are compatible in mafic minerals (Co, Sc, Ni, Cr) and feldspars (Eu, Ba, Sr). Whalen et al. (1987) was the first study that combined the high Ga and low Al of A-type granites in order to discriminate them from other granite types (Ga/Al > 2.6). According to the definition they have strong alkali affinities and in terms of Alumina Saturation Index A-type granites are mainly peralkaline or metaluminous, however they may have peraluminous compositions as well (Collins et al., 1982; Whalen et al., 1987; Eby, 1990; Frost et al., 2001).

Their major element chemical composition is reflected in their mineralogy. Namely, by the Fe-rich mafic minerals that are generally interstitial grains as they crystallise late

during the magmatic solidification. An exception to this rule is the Ca-amphiboles which can crystallise in the early stage of the magmatic evolution (Collins et al., 1982). Alkali-rich minerals like riebeckite, arfvedsonite or aegirine occur in peralkaline granites, whereas in the metaluminous A-type granites Ca-amphibole is the common mafic mineral next to the biotite. Feldspars are mostly presented with albite-orthoclase composition. Micrographic intergrowths of quartz and alkali feldspar common as an indication of the crystallisation at shallow crust (Eby, 1990).

Granitoid rocks in terms of tectonic settings are separated into orogenic granites, which form during collisional events (I and S-type granites) and anorogenic granites which occur in extensional environment. According to the definition of A-type granite they belong to this last group as they emplace into rift zones within the stable continental environment, although there are reports about granites from the ocean islands (e.g. Ascension and Kerguelen granites) and post-orogenic environments (e.g. Lachlan Fold Belt granites) in the literature that show A-type characteristics (Giret, 1990; Sylvester, 1989). Eby (1992) also distinguished the post-orogenic granites from those ones that occur in the rift-related settings. As mentioned above, he distinguished two different types of A-type granites with different sources and these two groups are characterised by distinct tectonic settings. According to him granites that belong to the mantle-derived group occur in continental rift systems or intraplate environments, whereas post-orogenic granites are presented in the wide variety of tectonic environment.

On the basis of the above, A-type granites can be emplaced into a broad range of tectonic settings. The only general feature is the non-orogen intrusion e.g. anorogenic environment, as the igneous activity never takes place in the main stage of the compressive geodynamic settings.

2.3.2 Petrogenetic models of A-type granites

Several models have been proposed to explain the generation of A-type granites. As the geochemical range of this granite type is quite broad on account of the variety of their sources (Pearce et al., 1984; Poitrasson et al., 1995), several theories have been proposed for the formation of A-type granites. The challenge of these models is to give an adequate explanation for their relatively anhydrous, high temperature, high FeO^t and halogen and HFSE contents. Among the many speculations there are similarities that were used to create 3 petrogenetic models: (1) A-type granitoids are highly fractionated products of mantle-derived parental mafic magmas (Loiselle and Wones, 1979; Eby, 1990, 1992; Turner et al.,

1992; Frost and Frost, 1997). (2) The second model suggests a significant role of crustal material, includes partial melting of granulite-facies lower crust, which had undergone a previous partial melting event of the orogenic I-type granite (Collins et al., 1982; Clemens, 1986; Whalen et al., 1987). (3) The generation of A-type granites by low degree partial melting of tonalite and granodiorite was suggested by Anderson (1983) and several authors accepted and developed it further (Creaser et al., 1991; Skjerlie and Johnson, 1993; Patino Douce, 1997).

1. Differentiation of mantle-derived magmas

As mentioned above, A-type granites are characterised by high Fe/Mg ratios and crystallise from a relatively dry melt under low oxygen fugacity conditions. Osborne (1959) determined that the early precipitation of magnetite increases the Fe/Mg ratio in the residue. As this can take place only under low fO_2 conditions, Frost and Lindsley (1992) suggested tholeiitic basalts as the parental magma for A-type granites since they can ensure the required low H_2O and oxygen fugacity to provide the reduced condition for the Fe/Mg ratio elevation. The derivatives of these tholeiitic basaltic magmas also can serve an appropriate source for the reduced granites with high Fe/Mg content (Frost and Frost, 1997): basaltic magmas can stall beneath the lower crust and produce REEs and Zr enriched ferrodioritic rocks with high Fe/Mg by differentiation which becomes the part of the newly formed mafic lower continental crust (Fig. 9A). On account of further mafic intrusions and rising asthenosphere during continued rifting, this underplated mafic lower crust can be partially re-melted and produce hot, anhydrous granitic melt with increased Fe/Mg ratio (Fig. 9B). Minor granite also can be produced by the fractionation of the mafic magmas. Frost and Frost (1997) do not exclude the possibility of crustal contamination either. According to them if the felsic crustal interaction is enhanced, it can have a significant influence on the granite composition.

Loiselle and Wones (1979) proposed that A-type granites are the fractionation products of alkali basaltic magmas (± crustal assimilation). Bailey (1978) discussed in his study that the alkali/peralkaline character can be developed by metasomatism before melting or early stage of the crystallisation, whereas Taylor et al. (1980) stated that alkali- and halogen-rich solutions also can cause alkali metasomatism during the late emplacement or after it. On the other hand, alkalinity can be a consequence of fractional crystallisation as well (Currie, 1986), however, this is still highly debated.

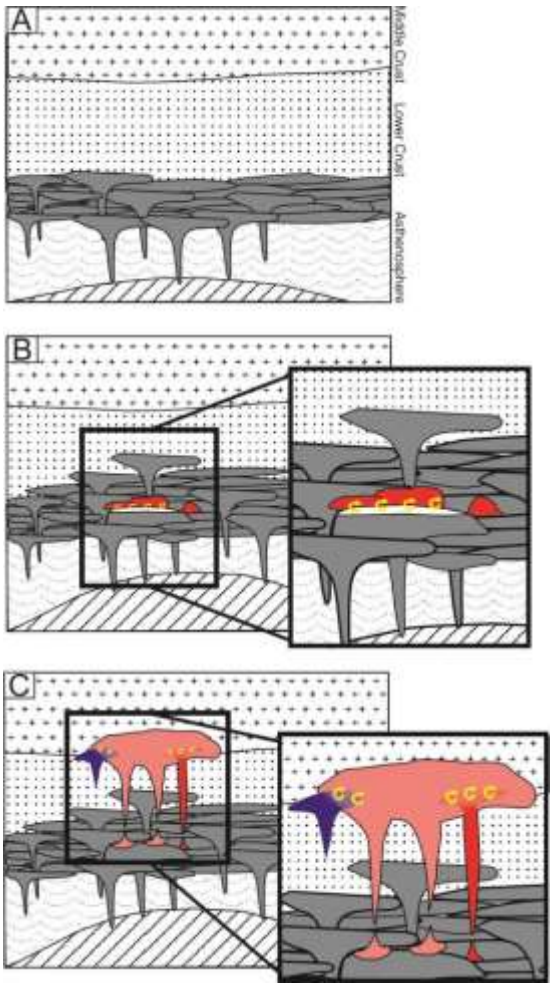

Figure 9. Schematic model for the formation of granites derived from tholeiitic basalts. (A) Tholeiitic magmas are intruded into the base of the lower crust during the beginning of rifting. (B) Low temperature differentiates of these magmas are partially re-melted and generate granitic melt (red colour). These magmas can combine with granite formed by fractionation of tholeiitic basalts (white colour) to produce granitic magma bodies. (C) These bodies are coalesced and form diapir (pink colour) that moves toward the middle crust and may interact with crustal melts (blue colour). The schematic representation is after Frost and Frost (1997)

The mantle derivation model can account for many A-type granites characteristics, e.g. high magmatic temperature as the consequence of the association with mafic magmas; Fe-enrichment because of the reduced parental magma, or the elevated halogen content, (and elevated HFSE content) as resulting from the anhydrous nature of the magma (Kilinc and Burnham, 1972). However, number of authors refute this model since, in most cases, intermediate rocks do not occur in the anorogenic complexes (Anderson, 1983). A-type granites are frequently in association with mafic rocks and there is a SiO_2 gap in the most suites (Clemens, 1986). In spite of the fact that Whalen et al. (1987) identified fractional crystallisation within some A-type suites utilizing the variation in the differentiation indicators such as Rb/Sr and Rb/Ba, he emphasised that the closed-system fractional crystallisation alone is not capable to produce the unique chemical nature of A-type granites.

2. Partial melting of granulite-facies lower crust

A residual source model was firstly suggested by Barker et al. (1975) and further developed by Collins et al. (1982). According to this model, the source of A-type granites is

the lower crustal felsic granulite that had undergone previous partial melting event that generated I-type granitic melt with relatively low temperature (< 850°). Melting of this residual felsic granulite is capable of produce granites with most of the A-type signatures, as it can explain the H_2O-poor nature of A-magmas, the enhanced halogen contents and the high abundances of highly charged elements. According to Collins et al. (1982) this fluid-absent melting of the lower crustal intermediate igneous rocks by the breakdown of hydrous minerals can leave granulite-facies residue with the residual mineral composition:

$$Bt + Hbl + Pl + Qtz = Qtz + Pl + Kfs + Opx \pm Cpx \pm Hbl, Bt + melt$$

As a consequence of this granite extraction, subsequent melting of these residual minerals (+ residual accessory phases) takes place only at higher temperature, which is consistent with the hot nature of A-type magmas. Breakdown of hornblende occurs at ~900°C (Clemens, 1986) and this fluid-absent reaction can provide the required volatile component for the melting of residual phases. Due to the breakdown of halogen-rich hornblende (± biotite), chlorine and fluorine will be concentrated into the melt. In addition to the high temperature, it also allows elevated concentrations of HFS elements. This is because F^- and Cl^- can depolymerise the melt framework by breaking the Si-O bridges of aluminosilicates (Collins, 1982; Clemens et al., 1986), this provides sites with various sizes and coordination for the highly charged elements to form high order coordination structures that ultimately contributes to the increased content of these elements in the rock in the course of the fractional crystallisation. The model also explains the elevated Ga/Al ratio of A-granites. As the GaF_6^{3-} complex is sT in the melt at high temperature and the Al prefers to be accommodated by the plagioclase in the residual phase, this affects the Ga/Al ratios of the crystallizing rock. In the case of peralkaline melts, Na and K ions together with the fluorine decrease the Zr concentration as a stable alkaline-fluorine complex in the melt, which prevents the precipitation of zircon. In peraluminous magmas, by contrast, alkalies are accommodated in feldspars and there is no excess of alkalies in the residual melt, which supports the early crystallisation of zircon and degreases the Zr in the melt.

On the basis of the above, the residual source model matches most if not all of the unique features of A-type suites, however not every petrologist accepts it without reservation. Creaser et al (1991) pointed out the weaknesses of this model. They do not consider the felsic granulitic lower crust as the source of A-type suites because it cannot provide the required, characteristic major element contents of the A-type criteria e.g. Ca-depletion, high alkalies and Fe/Mg ratios. According to their arguments the residual mineral

assemblage, demonstrated by Collins et al. (1982), represents a chemistry defined by higher Ca, Al (in plagioclase), Mg (in mafic minerals) and lower Si and K compared to the original protolith. Creaser et al (1991) also questioned the alkali feldspar and biotite as the part of the residual mineral assemblage after the extraction of I-type granite. In agreement with Collins et al. (1982) that the source of A-type magmas contains quartz, alkali and plagioclase feldspars among others, they completely refused the conception that the required mineral assemblage for the generation of A-type granite is resulted by a prior melt extraction. As a consequence of this, they proposed an alternative model for the source of A-type granites which is described below.

3. Low-degree melting of quartzofeldspathic rocks

Creaser et al. (1991) kept the crust as the main source, however, they suggested igneous, calc-alkaline rocks (tonalite, granodiorite) instead of meta-igneous ones as the source material of A-type granites. They did not exclude the possibility of some granulite facies metamorphic rock involvement in the formation of A-type granites, but it is not significant. According to them partial melts from tonalitic to granodioritic composition also can produce the A-type characteristics e.g. anhydrous nature, major element and enhanced halogen element criteria. Since the water content of OH-bearing phases is low in the source, only minor amount of water can be released into the melt via the high temperature breakdown of these minerals during the fluid-absent partial melting. Similarly to the previous model, the flourine content of amphibole and biotite or the modally minor apatite/titanite will be partitioned into the melt with the volatiles, which increases the halogen concentration of it and result the enrichment of highly charged elements. Creaser et al. (1991) also backed up their hypothesis with experimental results showing that 15-40% of an A-type granite melt can be produced from tonalite and granidiorite (10-15% mafic minerals) at 900-950 °C and 6-8 kbar.

Experiments performed by Patino Douce (1997) on tonalite (13% biotite, 13% amphibole) and granodiorite (7% biotite, 6% amphibole) at 950 °C and 4-8 kbar, support the quartzofeldspathic source theory. These experiments demonstrated that water-absent, incongruent melting of these rocks at 4 kbar generates 20-40% metaluminous melt with Ca-plagioclase, orthopyroxene and some clinopyroxene, while in the case of 8 kbar < 15% or 30% peraluminous melt was produced with clinopyroxene and some orthopyroxene. The differences between the mineral assemblages induce the distinct aluminium contents. As the main mineral phase at 4 kbar is plagioclase, it holds back the Al from the melt, hence the

residual melt will be metaluminous with reduced Al content, whereas at 8 kbar, clinopyroxene is the dominant phase, thus the melt will be Al-rich and peraluminous. This results in the characteristic Ga/Al ratio as well, that is higher in the case of metaluminous melt. The crystallisation of plagioclase also will decrease the Ca content of the melt on the lower pressure. This model also can serve as an appropriate explanation for the high Fe/Mg ratio of A-type granites. As mentioned above, the crystallisation of orthopyroxene takes place mainly at low pressure. This can remove the Mg from the melt, accounting for the increase of Fe/Mg ratio of the residual melt. As the result of the above we can say that melt with A-type affinities can be formed only by the low-pressure dehydration melting of tonalite or granodiorite in the shallow crust which also explains their occurrence in non-orogenic tectonic settings. In spite of this, Bonin (2007) argued that the melt that originates from these source rocks is too calcic and have too high K/Na ratio to fit the A-type nature.

The continental crust plays a very important role in the theory of Trumbull et al (2004) as well in connection with the Damaraland complexes (Namibia). All of the five complexes in the area are characterised by A-type nature, however compositionally they are very different, which in part reflects various magma sources. Based on their isotope compositions, granites from the Brandberg Complex have dominantly mantle origin, Gross Spitzkoppe and Erongo have dominantly sedimentary sources, whereas the Paresis and the Cape Cross complexes are the result of varying degrees of mixing. As all complexes show crustal involvement in their petrogenesis or have a crustal origin, Trumbull et al. (2004) concluded that the unifying key that transmits the A-type signatures to granites from different sources is the crust. In detail, crust with high melting temperature and anhydrous feature that has already experienced previous orogenic event. This suggests that the origin of the source rock has no significant role in the formation of A-type granite magma.

Based on the above many of the models for the petrogenesis of A-type granites can be refutable and supportable at the same time. Whereas recently the crustal and hybrid origins are the most popular theories (e.g. Misra et al., 2017; Murphy et al., 2018) those cannot give us proper explanations for the occurrence of A-type granites within oceanic environment or for the absence of the leucosome parts of migmatitic terranes with A-type signatures (Bonin, 2007).

Chapter 3: Geological overview

3.1 The geological setting of the Ditrău Alkaline Massif

The Ditrău Alkaline Massif (DAM) is located in the East Carpathian Mountains (Romania). The eastern part of Carpathians is divided into two different parts: the Outer Eastern Carpathians and the Inner Eastern Carpathians. The Ditrău massif occurs within the Inner Eastern Carpathian crystalline belt (Fig. 10). This segment of the mountain consists of Alpine nappe system, which formed on the South European continental margin during the compressional phase of Tethys Ocean in Cretaceous and obtained its final form during the Miocene collisional phase of the African and European tectonic plates (Săndulescu, 1981).

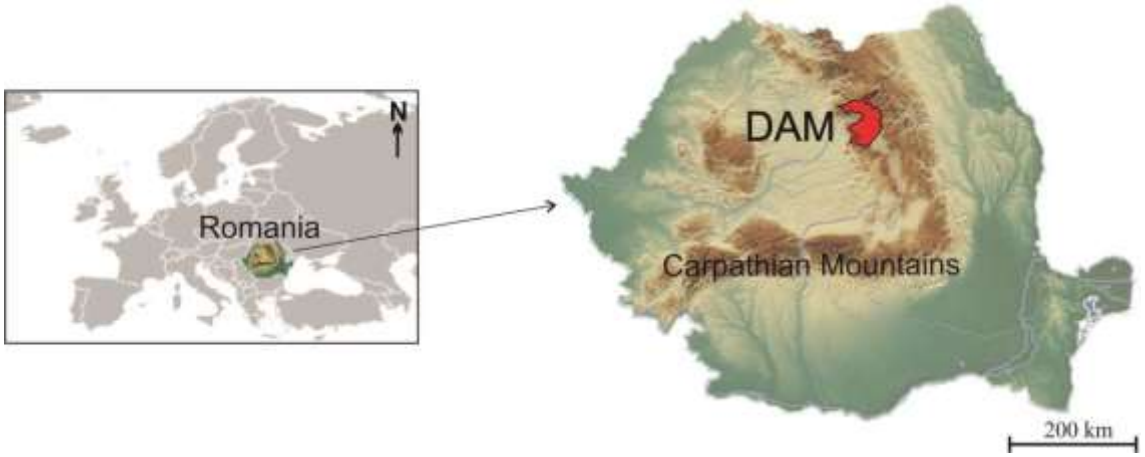

Figure 10. Location of the Ditrău Alkaline Massif in the Carpathian Mountains

The structural units of the Eastern Carpathians based on Kräutner and Bindea (1995) are shown in Fig. 11:

Inner Eastern Carpathian (Cretaceous) units

1. Transylvanides - one of the branches of the Tethys Ocean which started to open in Triassic and close in the Cretaceous. This fragment represents obducted Tethyan oceanic crust that lies on the Middle Dacides nappes
2. Middle/Median Dacides (Bucovinian nappes) - sequence of Variscan nappes from the South European continental margin, which made of Precambrian/Paleozoic crystalline unites and Mesozoic sediments. Later in the Middle-Cretaceous, as a part of the Alpine orogeny, these Variscan nappes were sheared and stacked to create the Bucovinian nappes system, which is separated into Bucovinian, Subbucovinian and Infrabucovinian Alpine nappes.

3. Inner Dacides - located the South part of Transylvanides and consist of continental crust nappes which made of pre-Campbrian/Paleozoic metamorphic rocks.
4. Outer Dacides – fragments of Civcin-Severin intracontinental rift system with basic and ultrabasic eruptive rocks and related flysch deposits.

Outer Eastern Carpathians (Miocene) units

5. Moldavides - was stacked in the Miocene and it is made up Cretaceous flysch sequences with Miocene molasses which are derived from an intracontinental trough.

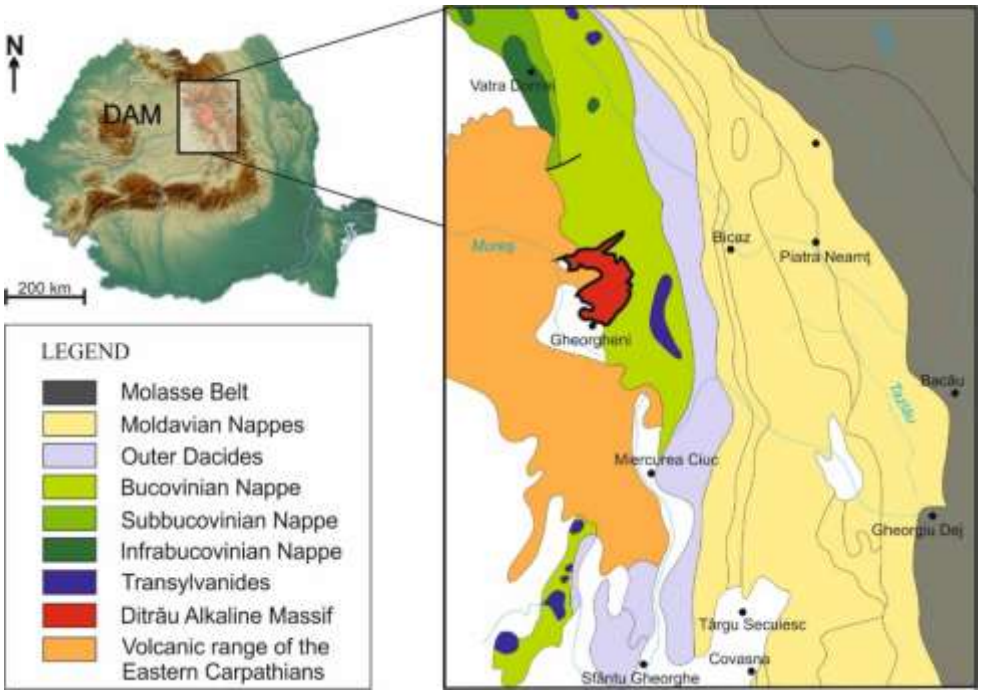

Figure 11. Structural units of Eatern Capathians (modified after Săndulescu, 1984)

The geological history of Eastern Carpathians is determined by the evolution of the Tethys Ocean. The structural units listed above at first were closely related to the pristine European margin of the Tethys but later detached (Fig. 12). The engine of structural evolution was the uneven drifting of the European and African plates. The geological evolution of the area, starting in the Permian and continuing up till now, has always been an integral part of the tectonic events of the Alpine orogeny. Obviously, these units also contain the signs and rocks of previous orogenic cycles (Variscan, Caledonian), which gives them a very complex geological structure. These Variscan nappes that are the main constituents of the metamorphic basement of the Eastern Carpathians (Kräutner and Bindea, 1998) were eroded in the Permian. During the Alpine orogeny, which started in the Lower-Triassic, this area was affected by the tectonic movements. Variscan rocks evolved as a carbonate platform

during the extensional phase of the Tethys on the South European continental margin (Fig. 12). This part of the Variscan basement with its Mesozoic sediments (called the Getic-Bucovinian microplate) detached from the continental margin in the Lias-Dogger along the Civcin- Severin rift system and got sheared and stacked as a consequence of the Cretaceous compressional phase creating the Middle Dacides/Bucovinian nappe system. The DAM formed during the Tethyan extension and was associated with a rifted passive continental margin (Fig. 12; Săndulescu, 1984). The emplacement started in the Late-Triassic on the western part of the continental margin by the uplift of mantle-derived magma (Dallmeyer et al., 1997) and the end of the process correlates with the Jurassic extension that produced the detachment of Getic-Bucovinian terrane from the passive European margin.

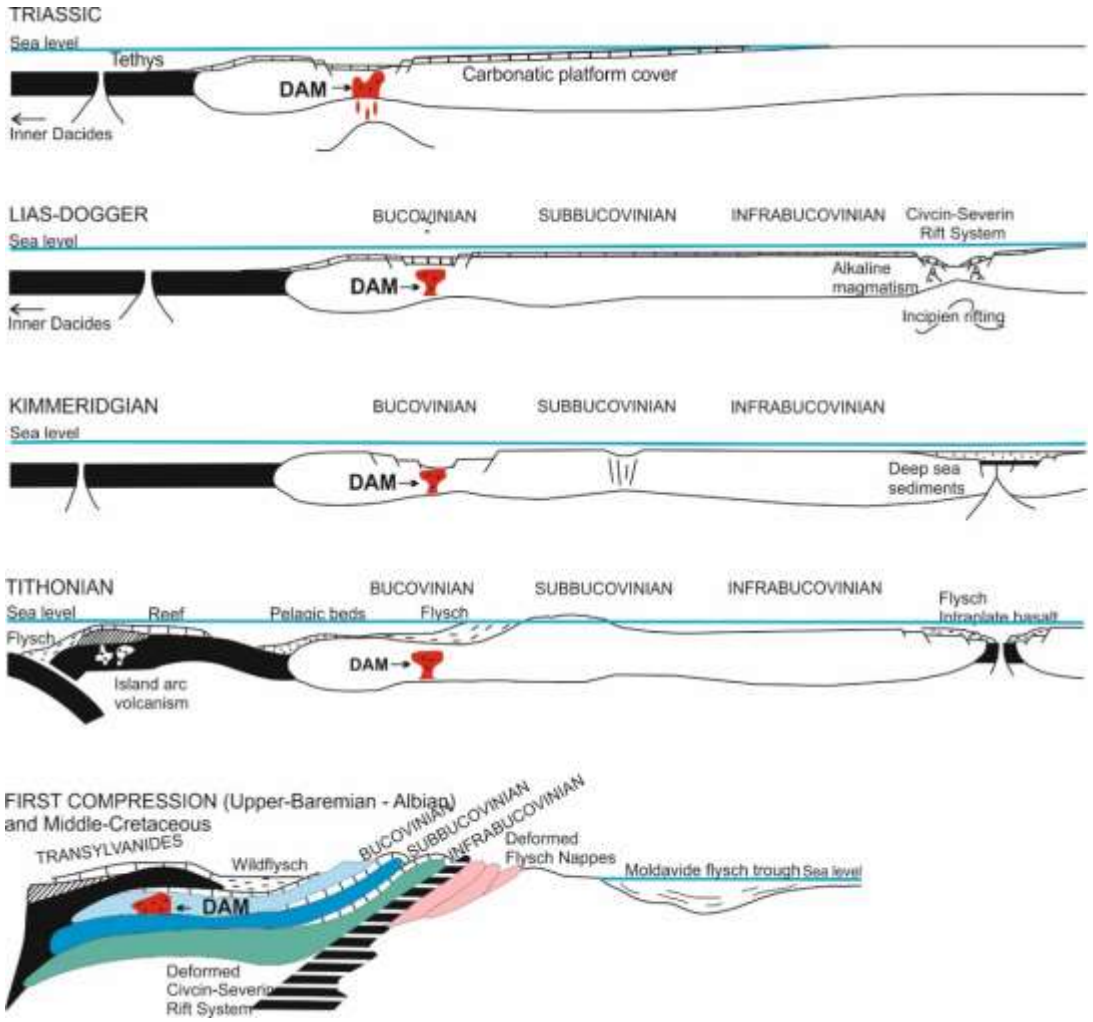

Figure 12. Reconstruction of the Alpine evolution of the DAM and its settings after Kräutner and Bindea (1995)

Later on, as a consequence of the crustal shorting, the following nappes were formed from the metamorphic pre-Alpine basement and its Mesozoic sediments (Săndulescu, 1984): Infrabucovinian, Subbucovinian and Bucovinian. Concerning these Alpine nappes, the latter one is the dominant in the basement of inner part of the Eastern Carpathians and the DAM is

also related to the Bucovinian Nappe (Figs. 11, 12). These Cretaceous nappe movements uprooted the massif from the original place of its intrusion and thus the DAM in the Bucovinian Nappe overlays on the Subbucovinian Nappe today by a tectonic unconformity (Fig. 12).

3.1.1 Structure of the Bucovinian nappe system

As mentioned above, the Bucovinian Nappe system consists of Variscan metamorphic basement and Mesozoic sedimentary rocks. The metamorphic rocks are represented by different lithologic and tectonic units, which can be detected mainly in the Bucovinian and Subbucovinian nappes. These tectonic units are the followings from bottom to top: Rarău Nappe, Putna Nappe, Pietrosu Bistriţei Nappe and Rodna Nappe (Balintoni et al., 1983). The different contacts are characterised by mylonites along the shear zones. These individual nappes are uniform in a petrological sense and built up of a single lithogroups (Vodă and Balintoni, 1994):

- *Rarău Nappe*: Bretila lithogroup, Hăşmaş granitoids – appears in the Variscan Rarău Nappe in the Bucovinian, Subbucovinian and Infrabucovinian Nappes. Its petrology is characterised by gneisses, mica-schists, quartzites, metarhyolites and rarely by carbonate intercalations and metagranitoids.
- *Putna Nappe*: Tulgheş lithogroup – builds up the Putna Nappe in the Bucovinian and Subbucovinian Nappes. Petrologically the Tulgheş lithogroup is characterised by acidic metavolcanic rocks. The rocks of the Tulgheş lithogroup are typical island arc volcanic rocks, which suffered low grade metamorphism.
- *Pietrosu Bistriţei Nappe*: Negrişoara lithogroup-Pietrosu Bistriţei Nappe appears in the Bucovinian and Subbucovinian Nappes. The Negrişoara lithogroup is composed of metadacites known as the Pietrosu porphyroid gneisses.
- *Rodna Nappe*: Rebra lithogroup - builds up the Variscan Rodna Nappe in the basement of the Bucovinian and Subbucovinian Nappes. The Rebra lithogroup is dominated by mica-schists and carbonate rocks, though paragneisses, amphibolites, white and black quartzites and black graphite-schists also occur.

The DAM is related to the Bucovinian Nappe in a structural sense and in contact with all its Pre-Alpine lithogroups (Fig. 13). According to Balintoni et al. (2009) the most extended contact is between the DAM and the Tulgheş lithogroup (abbreviation Tg in Fig. 13) of the Putna Nappe therefore this lithogroup will be discussed in more detail below.

3.1.2 Lithology of Tulgheş lithogroup in the Putna Nappe

The Tulgheş lithogroup (Tg) is a Cambrian-Ordovician island arc complex that metamorphosed under greenshist facies conditions (Moldoveanu, 2012) during an Early-Caledonian event. However, the Variscan orogeny and Alpine tectogenesis overprinted the Caledonian mineral parageneses and textures. The Tulgheş lithogroup consists of several rock types but the white or black quartzite and quartz-feldspar rocks are the dominant. It is made up by four formations (Tulgheş1- Tulgheş4) that are separated from each other with tectonical contacts (Kräutner and Bindea, 1995). The upper part of these formations (Tg1 and Tg2) is only exposed in the central part of Eastern Carpathians. These formations are presented in three discrete tectonic unites which are the followings: Săndomonic, Baratu-Mare and Balan nappes (Fig. 13).

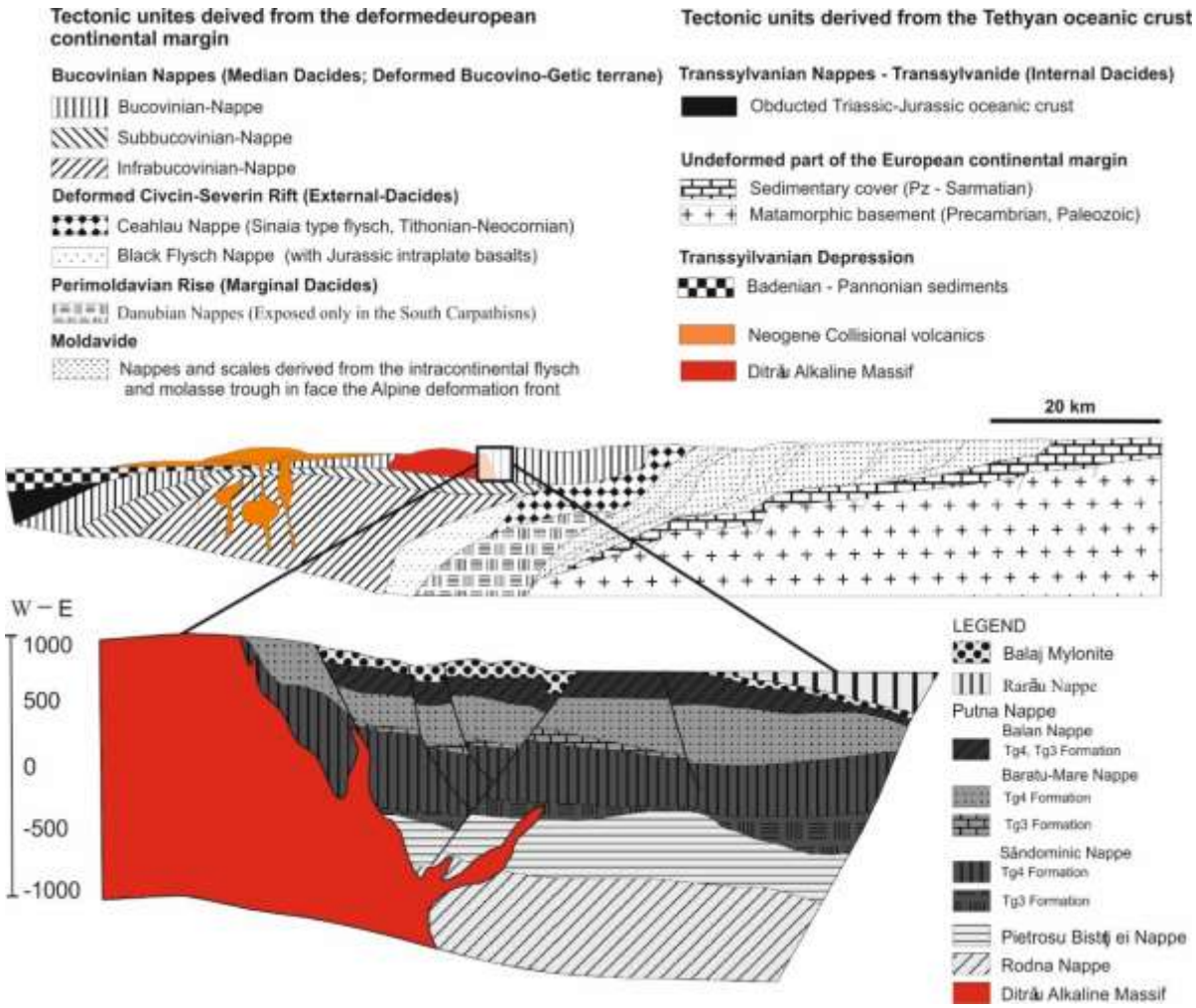

Figure 13. The contact between the Ditrău Alkaline Massif and the pre-Alpine nappes of the Bucovinian Nappe at the eastern part of the DAM (modified after Kräutner and Bindea, 1995)

These nappes are made of approximately the same lithology:

- Tg1 Formation: early siliciclastic platform which was followed by the
- Tg2 Formation: as an initial basinal stage
- Tg3 Formation: consists of mainly metavolcanic rocks with alkali-feldspar rhyolitic composition and metadetrital rocks, sericite-chlorite, albite-porphyroblast and quartz- sericite schists, or quartzite.
- Tg4 Formation: builds up mainly phillitic rocks with quartzites, metadetrital rocks, albite- porphyroblast schist as well as basaltic lava flow and intrusive gabbroic rock intercalations.

The largest part of the DAM is surrounded by this formation of the Săndomonic Nappe at the current erosion level and besides this nappe contains the greatest amount of metabasites, greenschists and black quartzite (Kräutner and Bindea, 1995) out of all the nappes (Fig. 14).

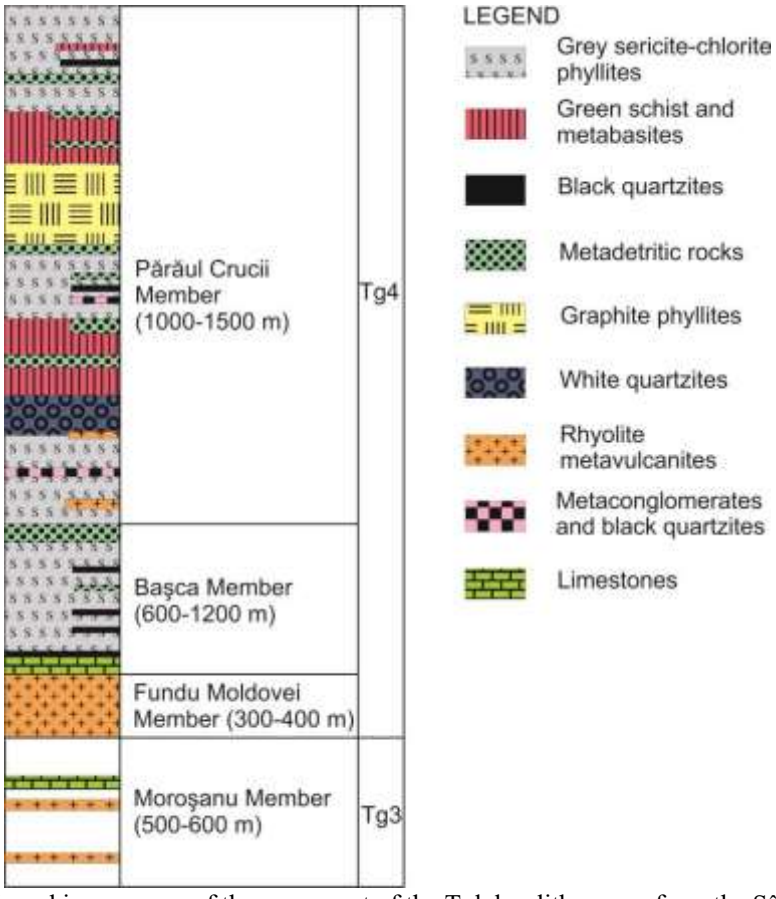

Figure 14. Lithostatigraphic sequence of the upper part of the Tulgheş lithogroup from the Sândominic Nappe (modified after Kräutner and Bindea, 1995)

3.2 Field relationships and geochronology of the Ditrău Alkaline Massif

The DAM is petrographically very diverse. It consists of hornblendites, diorites, monzodiorites, monzonites, quartz monzonites, syenites, quartz syenite, nepheline syenites and granites.

The granites crop out in the north-east parts whereas the north-west of the massif consists of ultrabasic cumulates enclosed in the gabbroic and dioritic rocks as lenticular and blocked shaped bodies (Fig. 15). Since there is a continuous gradual transition in the regard of minerals from the hornblendites toward the diorites in this small discrete mafic body, Pál-Molnár (2000) separated these rock from the rest part of the massif and named it Tarniţa Complex. Another continuous gradation can be observed in a larger scale between the Tarniţa Complex and monzonites, quartz monzonites, syenites, quartz syenites and granites from the north-west towards the north-east part of the DAM. This horizontal position of the supposed magmatic sequence is interpreted to be originated as a vertically crystallised magmatic succession that was broken away from its source and tectonically tilted by the nappe movements during the Alpine orogeny (Pál-Molnár et al., 2015b).

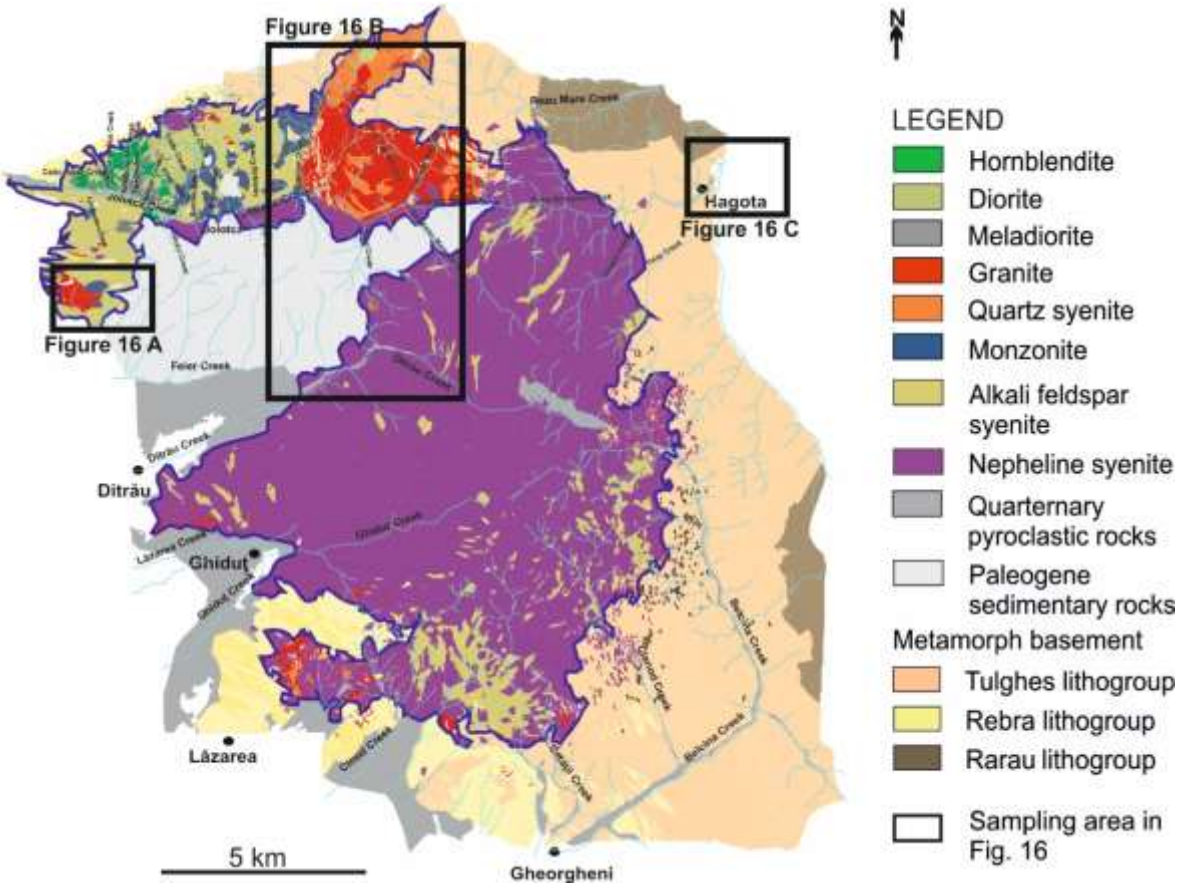

Figure 15. Schematic geological map of the Ditrău Alkaline Massif (after Pál-Molnár et al., 2015b)

The largest granite body outcrop is in the north-eastern part of the massif. Kräutner and Bindea (1995) reported metamorphic country rock xenoliths, which are included in syenitic and granitic rocks from this area. The central and eastern parts of the DAM are dominated by syenites and nepheline syenites. The entire massif is intercepted by young tinguaite, lamprophyre and syenite dykes, which are related to different magmatic phases and cut most of the rocks in the massif. As the syenite dykes are the only ones that crosscut all of the rocks, they represent the last magmatic stage in the history of the massif. The DAM is partly covered by Neogene-Quaternary andesitic pyroclastics and lava flows of the Călimani - Gurghiu - Harghita volcanic chain and by Pliocene-Pleistocene sediments and lignite-bearing lacustrine deposits of the Gheorgeni and Jolotca Basins (Codarcea et al., 1957).

As direct contact of the massif with sedimentary rocks is not observed, radiometric dating is the only method that provides an opportunity to determine the age of different rocks. The first K-Ar ages were recorded by Bagdasarian (1972) who collected 11 samples from the area. He pointed out a Jurassic age from whole-rock analyses of hornblendites (196±6 - 161±6Ma) and nepheline syenites (152±1 Ma). The syenites and granites proved to be younger with their Lower Cretaceous age (142±7 and 121±2 Ma).

Streckeisen and Hunziker (1974) obtained an age of 151±9 Ma age from the biotite of nepheline syenite by the K/Ar method and dated tinguaites at 161±7 Ma from the whole rock. Dallmeyer et al. (1997) determined Ar/Ar isotope-correlation ages on two gabbros and diorite samples and interpreted the resulting 231±0.1 and 227.1±0.1 Ma as the age of the pluton emplacement.

Pál-Molnár and Árva-Soós (1995) obtained K/Ar radiometric ages on 24 samples from the DAM, which they later supplemented with 9 more measurements. Their results are presented in Table 1. As argon easily escapes from potassium feldspar, in particular, because it is susceptible to exsolution, feldspars generally show the ages of a post-magmatic processes or subsequent geological events. Consequently, determination of crystallisation ages of rocks is primarily available by study of amphiboles and biotite although they also explained the unusual wide range of K/Ar age of diorites, reported by amphiboles, with the remobilization of Ar. Taking this into consideration, Pál-Molnár and Árva-Soós determined the following order of intrusion for the Ditrău rocks: The earliest intrusions were hornblendite followed by nepheline syenite, granite, diorite and syenite.

Table 2. Absolute ages of rocks from the Ditrău Alkaline Massif

Rock type	Mineral	K-Ar age (Ma)
Hornblendite	amphibole	237.4 ± 9.1 - 216.0 ± 8.8
Gabbro	amphibole	234.7 ± 10.8
	biotite(φ>0,315	162.4 ± 6.1
	mm)	168.3 ± 7.2
	biotite(φ<0,315	161.3 ± 9.8
Diorite	amphibole	218.7 ± 8.3 - 176.6 ± 6.7
	feldspar	138.2 ± 5.8 - 137.4 ± 5.5
Syenite	biotite	107.6 ± 4.1- 102.6 ± 4.0
	K-feldspar	113.5 ± 4,3 - 112.7 ± 6.9
Nepheline syenite	amphibole	216.0 ± 8.1
	biotite	182.4 ± 6.9
	K-feldspar	140.7 ± 5.3
	nepheline +	232.7 ± 8.8
Granite	amphibole	196.3 ± 7.4
	biotite	217.6 ± 8.3 – 198.3 ± 7.5
	feldspar	146.0 ± 5.6 – 135.9 ± 5.1

According to Kräutner and Bindea (1998) the emplacement of these rocks lasted for about 90 Ma. The intrusion of hornblendites-diorites was dated in Carnian (231-227 Ma) followed by the formation of syenites and granites in the Norian (216-212 Ma). During the Callovian-Oxfordian (160-154 Ma) nepheline syenites were produced accompanied by a long cooling period between 155-135 Ma (Berriasian-Valanginian). During this stage the rocks were affected by sub-solidus alterations at deep crustal levels.

3.3 Previous studies on the Ditrău granites and nepheline syenites

The first study that tried to explain the formation of felsic rocks, focusing on the granite, at Ditrău was Koch Antal`s synthesis of the Ditrău Alkaline Massif in 1879. According to him the granites evolved via assimilation of schists by magma with phonolothic composition.

Based on Albert Streckeisen`s examinations (1938) a mafic magma differentiated by fractional crystallisation, resulting in magmas with trachytic and later phonolitic compositions. These ascending felsic melts assimilated the quartz-rich country rock schists

in the upper part of the magmatic chamber producing quartz-bearing rocks as well as all the transitions between these rocks and the nepheline syenites.

Later Streckeisen (1960) came up with a new theory which supposed that the basis of the DAM was a parental magma with trachytic composition and the silica-oversaturated rocks were fractionated from this melt. The origin of the trachyte parental magma was not explained in this study. Streckeisen said that it cannot be a primary magma and that it formed at 'great depth' by 'special processes', however the exact nature of these processes was not discussed by him.

In 1974 Streckeisen and Hunziker extended this previous work and they stated that breaking through the pre-existed parts of the DAM (like the dioritic complex) this trachytic magma assimilated the adjacent metamorphic rocks at the edge of the massif, as a result of which silica-oversaturated rocks could develop.

Gyula Jakab (1981) suggested trachytic and phonolitic magma intrusions in the area. According to him these magmas originate from the same source at the base of the crust, and the granites are the products of the first trachytic intrusion together with the syenites, monzonites and quartz syenites. He presumed that granites could appear at the marginal parts of the complex as this magma assimilated the country rock schists.

Later, Gyula Jakab (1982) considered the trachytic intrusion only as the product of crustal melting, whilst the nepheline syenites and mafic-ultramafic rocks have mantle origin.

Whereas these early studies uniformly assumed felsic parental magmas in the generation of silica-oversaturated rocks of the DAM, the later articles agree that mantle-derived magmas played the main role in the genesis of Ditrău granites:

It was suggested by Pál-Molnár (2000) that the hornblendites, nepheline syenites and granites are co-genetic rocks. According to him hornblendites are alkaline- subalkaline rocks with an upper mantle origin formed in an intraplate tectonic environment and they show both slightly silica-saturated and -undersaturated character. He stated that during the evolution of this alkaline mantle-derived melt, it split up at the stage of trachytic composition, that gave rise to the formation of two different magmatic branches from the same parental magma. The separation into silica-oversaturated and undersaturated rocks probably relates to the assimilation of crustal rocks (note: the crustal assimilation has never been investigated by Pál-Molnár). The end-members of these magmatic branches are the nepheline syenites and granites in the DAM. According to Pál-Molnár (2000) the silica-undersaturated end-member is the product of fractional crystallisation of the mantle-derived melt, whereas the formation

of granites is probably the result of both fractional crystallisation and crustal assimilation.

In the same year Morogan et al. (2000) suggested that the DAM was generated from primitive basanitic magmas produced by low degrees of melting of an asthenospheric (OIB-like) source. The evolution of silica-oversaturated, evolved magmas was attributed to crustal assimilation combined with fractional crystallisation of primitive basanitic magma at the early stage in the development of the complex. This is supported by their whole-rock O-isotope data and their positive correlation with the SiO_2. After the generation of silica-rich rocks the crustal assimilation may have been insignificant that allowed the formation of the silica-undersaturated nepheline syenites.

The latest study of Ditrău granites by Pál-Molnár et al. (2015a) suggested that the A-type granite magmas were formed by fractional crystallisation of a mantle-derived parental mafic magma, in agreement with his earlier theory (Pál-Molnár, 2000; Pál-Molnár et al., 2015a). Pál-Molnár (2000) and Pál-Molnár et al. (2015a) did not exclude the possibility of a crustal contamination, however, it has not yet been investigated in detail.

The first studies of the nepheline syenites from Ditrău massif were mainly petrographic descriptions (Zirkel, 1866; Szádeczky, 1899; Mauritz, 1909, 1912; Mauritz et al., 1923, 1925).

The first attempt to explain the formation of Ditrău nepheline syenite was made by Streckeisen (1938). According to him the contamination of calc-alkaline mafic melt by the local limestones resulted the generation of alkaline basaltic magma. The fractional crystallisation of the alkaline basaltic melt produced the nepheline syenites. The differentiation started with the crystallisation of olivine, pyroxene and amphibole and the ongoing fractionation eventually resulted the generation of nepheline syenites through the formation of alkaline syenites.

Later, Földvári (1946) suggested that the nepheline syenites formed from a rhyolitic initial melt, which assimilated the local limestones. He also considered the local marbles as the products of the contact metamorhism induced by the intrusion of rhyolitic magma.

Streckeisen (1954) examined the relationships of the rocks in the DAM and concluded that there is a continuous transition between the nepheline syenites and alkaline syenites. He also revealed that the tinguaites and nepheline syenites chemically relate to each other and determined that the nepheline syenites are the youngest rocks in the massif based on the field relationships of the rocks.

Streckeisen (1960) rejected the theory of the assimilation of local limestones into the calc-alkaline mafic melt as the formation of the large quantity of Ditrău nepheline syenite by fractionation would require unrealistically large amount of alkaline basaltic magma. In his new theory Streckeisen supposed the existance of alkaline trachytic parental melt that probably assimilated the local limestones and probably evaporites and produced the nepheline syenites via fractionation. He did not specify the origin of the parent melt.

In 1974 Streckeisen and Hunziker proposed three different magma intrusions in the history of the DAM. The first intrusion produced the gabbros and diorites, granites and syenites were formed from a trachytic melt and eventually nepheline syenites were crystallised from a phonolitic magma. The intrusion of phonolitic magma is also responsible for the hybridization of Ditrău diorites.

The generation of trachytic and phonolitic magmas at the boundary of upper mantle and lower crust were suggested by Jakab (1981). According to him nepheline syenites and tinguaites were crystallised during the second intrusion from the phonolitic melt. This melt broke through the rocks formed in course of the first stage (hornblendites, diorites, monzonites, syenites, quartz syenites and granites) during its ascent towards the surface in the central part of the massif.

The formation of nepheline syenites according to the newest studies of the DAM (Morogan et al., 2000; Pál-Molnár, 2000) has been already described above together with the generation of Ditrău granites.

Based on the above it is evident that there is still no consensus in connection with the petrogenesis of felsic rocks from the DAM. In summar, whereas there is an agreement on the mantle source of nepheline syenites, two main hypotheses have emerged concerning the origin of the granites: (1) silica-oversaturated rocks have resulted from the differentiation of mantle-derived melts combined with crustal contamination or (2) those have been formed by fractional crystallisation from silica-saturated trachytic melts probably generated in the crust.

Chapter 4: Sampling and methods

4.1 Field work and the samples

The aim of the fieldwork was to collect, as far as possible, samples from all types of felsic igneous rocks and from all types of country rocks. However, the poor outcrop exposures made sample collection difficult. Much of the area of the complex is covered by a dense forest therefore outcrops were accessible for sampling only in the valleys of streams. A total of 31 samples were collected, mainly from the largest mass of granitoid rocks in the north-eastern part of Ditrău massif (Fig. 16). Out of these samples 25 were felsic rocks (2 syenites, 7 quartz syenites, 5 quartz monzonites, 4 granites and 7 nepheline syenites). During the sampling, 1 diorite, 1 hornblendite and 4 country rocks were collected too for the proper interpretation of chemical trends, to understand the compositional range in isotope composition, and to aid in the final petrogenetic model.

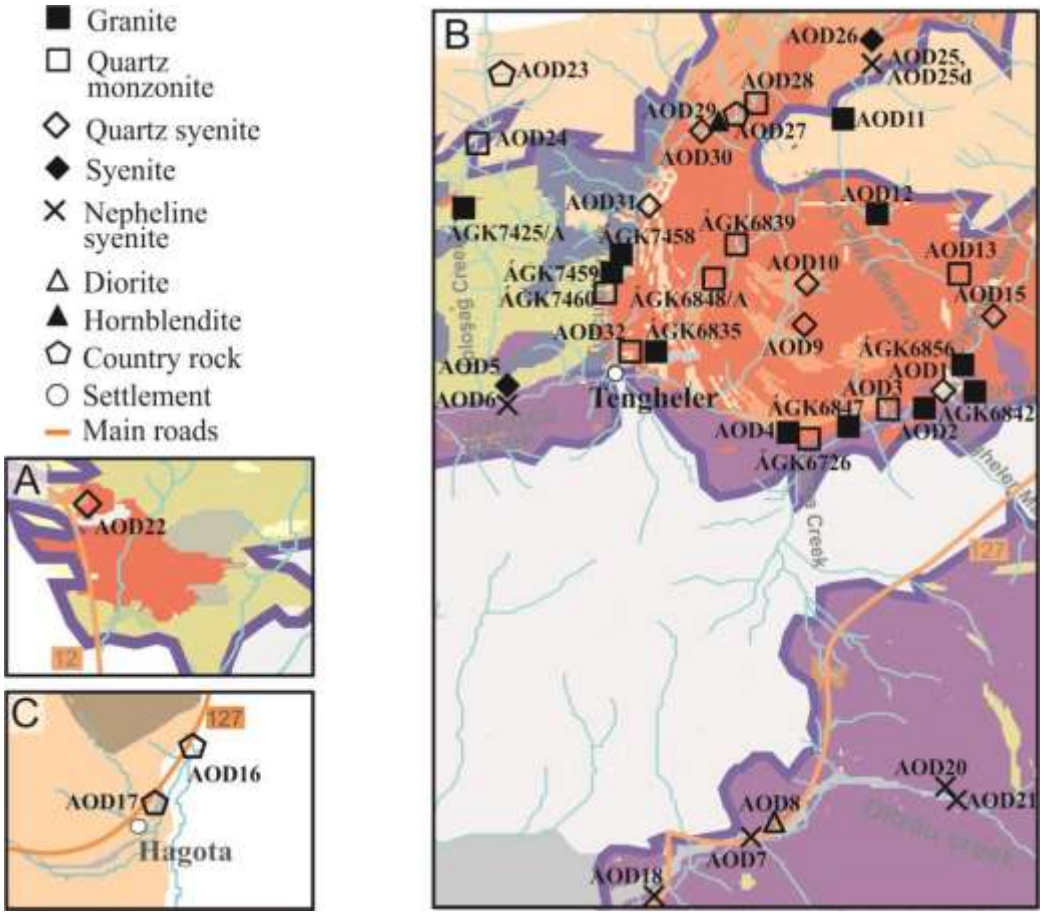

Figure 16. Sample locations in the northern part of the Ditrău Alkaline Massif (A, B, C are from Fig. 15)

An additional 18 quartz monzonite, syenite, nepheline syenite, diorite and hornblendite samples that we got from the Department of Mineralogy, Geochemistry and Petrology of the University of Szeged (Hungary) in cooperation with them are used in the course of this project as well. Their sampling locations are unknown except for 7 granit and 4 quartz monzonite samples, which are shown in Fig. 16B as well. The code of the Hungarian samples is marked by ÁGK, whereas the samples collected by us have the code AOD. As the GPS coordinates of the Hungarian samples are unknown, those are not shown on the Google Earth map (Fig. 17). As thin sections are not available from the Hungarian samples, those are used only in Chapters 6 and 7.

Figure 17. Sample locations in the northern part of the Ditrău Alkaline Massif on Google Earth map.

Nepheline syenites are the most abundant rocks in the Ditrău Alkaline Massif. They make up the 65% of the whole complex (Streckeisen, 1954). As can be seen in Fig. 15, nepheline syenites predominate in the central and eastern parts of the DAM, but they also occur in the north as tinguaite dykes that are the hypabyssal equivalent of phonolite. Towards the margins of the central nepheline syenite outcrop, they are associated with small amount of syenites, quartz syenites and granites. The largest area of syenites occurs in the north-northwestern part of the Ditrău massif between the Tarniţa Complex and granites, or in much smaller amount in the southern part together with nepheline syenites. Quartz syenites and quartz monzonites are the most abundant in the north part of the DAM. They appear

intermingled with the Ditrău granites. Granitic rocks dominantly crop out in the northern part of the massif, in lesser amount they can be found in the southern part associated with syenite, nepheline syenite and quartz syenite. The outcrops are distinct (Fig. 18). Their size varies from ca. 1 m to 15 m and they show differences in the degree of weathering. Nepheline syenites outcrops are less weathered than those of the other felsic rocks (Fig. 18C and F).

Figure 18. Photographs of the exposures of felsic rocks in the Ditrău Alkaline Massif. (A) Syenite outcrop in the N-E part of the DAM; (B) Intruded nepheline syenite into the diorite in the central part; (C) Quartz syenite and (D) granite outcrops in the eastern part of the DAM; (E) loose country rock in the north part of the massif; (F) broken and fresh nepheline syenite from the cetral part of the DAM.

Table 3. GPS coordinates of the collected samples from the Ditrău Alkaline Massif

Sample	Rock type	Longitude	Latitude
AOD 02	granite	25°35'03.7"	46°52'01.7"
AOD 04	granite	25°34'08.8"	46°51'46.1"
AOD 11	granite	25°34'22.7"	46°53'10.6"
AOD 12	granite	25°34'47.6"	46°52'44.8"
AOD 03	quartz monzonite	25°34'51.9"	46°51'58.7"
AOD 13	quartz monzonite	25°35'10.1"	46°52'30.9"
AOD 24	quartz monzonite	25°32'10.4"	46°53'09.9"
AOD 28	quartz monzonite	25°33'51.6"	46°53'28.6"
AOD 32	quartz monzonite	25°33'00.6"	46°52'12.7"
AOD 01	quartz syenite	25°35'03.6"	46°52'04.7"
AOD 09	quartz syenite	25°34'24.2"	46°52'21.8"
AOD 10	quartz syenite	25°34'20.7"	46°52'28.0"
AOD 15	quartz syenite	25°35'16.8"	46°52'22.6"
AOD 22	quartz syenite	25°28'49.6"	46°50'27.1"
AOD 30	quartz syenite	25°33'34.7"	46°53'19.7"
AOD 31	quartz syenite	25°33'06.9"	46°52'55.1"
AOD 05	syenite	25°32'28.1"	46°52'00.5"
AOD 26	syenite	25°32'28.1"	46°53'47.4"
AOD 06	nepheline syenite	25°32'28.1"	46°52'00.5"
AOD 07	nepheline syenite	25°33'58.9"	46°49'55.6"
AOD 20	nepheline syenite	25°35'18.1"	46°50'00.1"
AOD 21	nepheline syenite	25°35'18.1"	46°50'00.1"
AOD 25	nepheline syenite	25°34'25.2"	46°53'47.4"
AOD 25d	nepheline syenite	25°34'25.2"	46°53'47.4"
AOD 18	nepheline syenite	25°33'21.3"	46°49'43.6"
AOD 08	diorite	25°33'58.9"	46°49'55.6"
AOD 29	hornblendite	25°33'45.0"	46°53'22.6"
AOD 16	country rock	25°43'28.4"	46°53'50.6"
AOD 17	country rock	25°41'08.8"	46°52'42.8"
AOD 23	country rock	25°32'09.2"	46°53'39.4"
AOD 27	country rock	25°33'51.5"	46°53'25.7"

4.2 Whole rock geochemistry

A total of 25 whole-rock major element compositions of the Szeged samples were determined by HR-ICP mass spectrometer (Finnigan MAT Element), or the trace

elements/REEs were analysed by ICP atomic emission spectrometry using a Varian Vista AX spectrometer at the Department of Geological Sciences, University of Stockholm (Sweden). ICP-emission spectrometry and ICP mass spectrometry were also used to determine the bulk-rock compositions of certain samples at the Acme Analythical Laboratory, Vancouver (Canada).

A total of 31 samples of nepheline syenite, syenites, quartz syenites, quartz monzonites and granites collected as part of this project were analysed for bulk-rock major element compositions by X-ray fluorescence spectrometry (XRF) using a Panalytical Axios wavelength dispersive XRF spectrometer with a rhodium end-window X-ray tube at the University of Cape Town. Major elements were analysed using fusion disks where a LiT-LiM (in the proportion 57:43) flux and a LiBr releasing agent were used. Calibration standards used were a combination of natural standards from the USGS and SARMS (South African producers of Metallurgical and Geological Certified Reference Materials). Matrix corrections made use of the Fundamental Parameter method as described in Willis and Duncan (2008) or Rousseau et al. (1996).

Volatiles and loss of ignition (LOI) were calculated using a mass balance. Approximately 2g of whole rock powder was weighed and dried for overnight at 110°C and then left to cool down before being reweighed with the mass difference being recorded as the volatile content (Equation 5). After this samples were reheated to 800°C for 4 hours to determine loss on ignition (LOI) and ensure all Fe was oxidised to Fe^{3+}.

$$\text{LOI (wf\%)} = \frac{\text{Mass of wet powder} - \text{Mass of ignited powder}}{\text{Mass of wet powder}}$$

Equation 5.

Whole rock trace element data were obtained for the samples, along with BHVO-2 and JG-2 certified reference materials (CRM), via solution inductively coupled mass spectrometry (ICP-MS) on a Thermo-Fisher X-Series II Quadrupole ICP-MS. 50mg of each powdered sample was dissolved in a 4:1 concentrated HF-HNO_3 acid mixture in sealed teflon beakers. After digestion on a hotplate at ±140ºC for 48 hours and evaporation to dryness, 2 ml of concentrated HNO_3 was added to the samples in two stages. The final dried product was then taken up in 5% HNO_3 solution containing 10 ppb Re, Rh, In and Bi as internal standards. Standardisation was against artificial multi-element standard solutions. Errors throughout the concentration range were better than 3%. Accuracy and procedural blank levels were similar to values reported by le Roex et al. (2001).

4.3 Isotope measurements

4.3.1 Oxygen isotopes

The early investigations of oxygen isotopes in petrogenetic studies were based on whole rock data, however over the past 20 years the development of oxygen isotope technology has made the single crystal analyses possible (Elsenheimer and Valley, 1992). The study of altered minerals rather than whole rocks provides a better indication of the original magma $\delta^{18}O$ value as the secondary alteration affects can be eliminated by measuring of unaltered single crystals. It is true that minerals have different oxygen isotope content from their magmas, but the difference can be estimated from mineral - melt fractionation factors (see below).

Usage of $\delta^{18}O$ value of minerals to reveal the genesis of their host magma requires oxygen isotope data from resistant minerals, especially in the case of slow plutonic cooling, as they can resist to secondary isotope exchanges, therefore alteration processes are more restricted in the case of these minerals (Valley, 2001). Resistant phases to alteration are quartz and zircon in silicic rocks, thus O-isotope measurements were taken on quartz from every silica-oversaturated rocks and zircons from every examined rock types. Besides the highly resistant minerals, O-isotope composition of titanite and monazite were measured from samples where these minerals were available, feldspars were analysed from mostly all samples, or amphibole and pyroxene were measured from the less altered rocks. In addition, whole rock O-isotope measurements were made on wall-rock samples. Oxygen isotope data for the samples analysed are presented in Table 7.

Samples were crushed prior to the handpicking of minerals. Quartz grains were prepared for the measurements from 24 samples, feldspars from 32 and zircon from 9 samples. All O-isotope data presented in the thesis were produced in the Stable Isotope Laboratory at University of Cape Town. If it was required, quartz grains were cleaned in 10% HF to remove contaminations of residual minerals. Separated feldspars were analysed by conventional silicate line following methods described by Harris and Ashwal (2002), whereas quartz and zircon grains were analysed by laser fluorination following methods described by Harris and Vogeli (2010). For the conventional method 10 mg of feldspar powder was loaded into Ni tubes and degassed at 200°C then reacted with ClF_3 at 550°C to release the O_2 from the crystal lattices. The free O_2 was then passed over a hot platinized carbon rod to produce CO_2 gas. The CO_2 was then collected in break seal tubes. The in-house standard MQ was run in duplicate with each batch of 8 samples to convert the raw data to

SMOW scale. MQ has a $\delta^{18}O$ value of 10.10‰ calibrated against NBS-28, assuming a value of 9.64‰ for quartz standard NBS-28 (Coplen et al., 1983). The long-term variability of MQ suggests a 2σ error of 0.16 ‰.

Laser fluorination was used to analyse quartz, zircon, amphibole, biotite and titanite grains. Approximately 2 mg samples, varied from one to several grains, were loaded onto a highly polished Ni sample holder and reacted in the presence of 10 kPa BrF_5.The excess BrF_5 and the resultant Br were removed cryogenically, while the remaining gas passed through a KCl trap. Finally, the purified O_2 by a double-U trap with liquid nitrogen was collected on grains of a 5 Å molecular sieve in glass sample vessels. The O_2 reference gas had previously calibrated by converting an aliquot of O_2 to CO_2 using the carbon convector on the conventional extraction line. After that the measured ratios were used to calculate the raw δ values for each sample relative to SMOW scale. The Monastery garnet (MON GT) internal standard was used during the laser analysis, which are from the Monastery kimberlite pipe (Harris et al., 2000). The MON GT was calibrated against UWG-2 garnet standard from Valley et al. (1995) and has a $\delta^{18}O$ = 5.38‰ (Harris and Vogeli, 2010), which assumes $\delta^{18}O$ = 5.80‰ for the UWG-2. Thus, all raw data were normalised to 5.38‰, the $\delta^{18}O$ value of the MON GT. All O-isotope ratios were measured off-line using the gas source Finnegan Mat Delta XP mass spectrometer in the Archaeology Department at the University of Cape Town. Samples were analysed using the dual inlet mode and all data were reported in the standard δ- notation relative to SMOW, where $\delta^{18}O = (R_{sample}/R_{standard}-1)*1000$ and R is the measured ratio of $^{18}O/^{16}O$. The long-term average difference in $\delta^{18}O$ values of 2 internal MONT GT standards run with each batch of 10 samples was 0.11‰ (n = 216), corresponding to a 2σ value of 0.15‰

4.3.2 Radiogenic isotopes

Isotope ratios of Sr and Nd in the selected 29 samples were determined at the Department of Geological Sciences, University of Cape Town. For the dissolution of the 50 mg whole-rock powders, the samples were digested in sealed Savilex beakers with 4:1 concentrated HF and HNO_3 acid mixture for 48 hours. The solution was then quantitatively split into two fractions in order to determine elemental concentrations and the isotope ratios. Concentration data were attained by inductively coupled plasma mass spectrometry (ICP-MS) using a Thermo Fisher Xseries2 system according to the methods described by le Roex et al. (2003). After the conventional ion-exchange separation of Sr, Nd and Pb (based on Pin

et al., 1994; Míková J., Denková P., 2007), the Sr and Nd isotope compositions were measured with a Nu Instruments NuPlasma HR mass spectrometer equipped with a DSN-100 desolvating nebuliser. The measured $^{87}Sr/^{86}Sr$ and $^{143}Nd/^{144}Nd$ values were further normalised. Sr isotope data were referenced to the $^{87}Sr/^{86}Sr$ value of 0.710255 for the bracketing analyses of NIST SRM987. All Sr isotope data were corrected for Rb interference using a measured signal for ^{85}Rb and the natural $^{85}Rb/^{87}Rb$ ratio and instrumental mass fractionation using the exponential low and an $^{88}Sr/^{86}Sr$ value of 0.1194.

The Nd was analysed using the Nu Instruments DSN-100 desolvation nebulizer. The $^{143}Nd/^{144}Nd$ isotope data were normalised to a value of 0.512115 for bracketing analyses of JNdi-1 Nd-isotope standard (Tanaka et al., 2000). All Nd data were corrected for Sm and Ce interference as well as instrumental mass fractionation using the exponential law and a $^{146}Nd/^{144}Nd$ value of 0.7219. The $^{143}Nd/^{144}Nd$ ratio measured for BHVO-2 was 0.512990 ±14 that is within the range of Weis et al. (2006) of 0.512984 ±11 and long-term UCT average of 0.512987 ±17 (2σ; n = 86). During this work, the $^{87}Sr/^{86}Sr$ ratio obtained for BHVO-2 was 0.703464 ± 12, within error of the value obtained by Weis et al. (2006) of 0.703479 ±20, and the long-term UCT average of 0.703489 ±44 (2σ; n = 74).

The Pb isotope ratios of selected 16 samples were analysed as ±50 ppb 2% HNO_3 solutions using a Nu Instruments NuPlasma HR multi-collector inductively coupled plasma mass spectrometer (MC-ICP-MS) and DSN-100 desolvating nebuliser. NIST SRM997 Tl standard was added to all samples and standards to give a ±10:1 Pb: Tl ratio. NIST SRM981 was used as the reference standard with normalising values of 36.7219, 15.4963 and 16.9405 for $^{208}Pb/^{204}Pb$, $^{207}Pb/^{204}Pb$ and $^{206}Pb/^{204}Pb$, respectively, after Galer and Abouchami (1998). All Pb isotope data were corrected for:

1. Hg interference by subtraction of on-peak, gas-blank background measurements
2. Instrumental mass fractionation using the exponential law and a $^{205}Tl/^{203}Tl$ value of 2.3889 (Galer and Abouchami, 1998).

Within-run precision on individual ratio measurements is given by the (2σ mean) errors in the last significant digits. The BHVO-2 standard analysed in duplicate along with the samples gave average values of $^{208}Pb/^{204}Pb$, $^{207}Pb/^{204}Pb$, $^{206}Pb/^{204}Pb$ of 38.2502, 15.5315, and 18.6694, compared to published values of 38.237, 15.533, and 18.647 of Weis et al. (2006).

Chapter 5: Petrography

5.1 Nepheline syenites

The Ditrău nepheline syenites are coarse- to medium-grained, holocrystalline and phanerocrystalline rocks with grey-white colour (Fig. 19A). The coarse-grained ones are inequigranular (Fig. 19B), whereas the medium-grained samples are closely equigranular (Fig. 19C). The main constituents are nepheline, microcline, plagioclase feldspar, biotite, ± pyroxene. The amount of the mafic minerals in the nepheline syenites is smaller (3-6 modal%) compared to other felsic rocks. Titanite, zircon, magnetite, ilmenite, apatite and rarely calcite are presented as the accessory phases.

Nepheline and microcline have large grain size (5-8 mm) in the coarse-grained nepheline syenite (Fig. 19B). Nephelines occur as hexagonal or square-shaped euhedral phases (Fig. 19B). Smaller subhedral crystals can be observed as well (2-3 mm) in the groundmass. Nepheline generally shows alteration to cancrinite, liebenerite and sodalite, which are presented as reaction rims, crack fillings or pseudomorphs (Fig. 19D). Nepheline with smaller grain size in the coarse-grained type show less alteration. Plagioclase feldspars are subordinate and appear as subhedral grains. They often have serizitised cores. Large, tabular microclines and perthites rarely contain accessory minerals as inclusions (Fig. 19B). They are often altered to sericite. In one sample these huge crystals are surrounded and cut by wriggling lines of fine-grained alkali feldspars and cancrinite (0.5-1 mm) that could be produced by re-crystallisation (Fig. 19E). These small alkali feldspars occur as columnar, fresh grains. Biotite is the only mafic mineral presented in the coarse-grained nepheline syenite. It appears with light yellowish brown-dark greenish brown pleochroism and forms clusters together with titanite (Fig. 19F).

The medium-grained nepheline syenites are fresher compared to the coarse-grained ones. Nephelines are subhedral, anhedral with minor cancrinite and liebenerite replacements (Fig. 19B). Alkali feldspars are fresh grains. Plagioclase has tabular, euhedral shape, whereas microclines are mainly anhedral groundmass crystals (Fig. 19C).

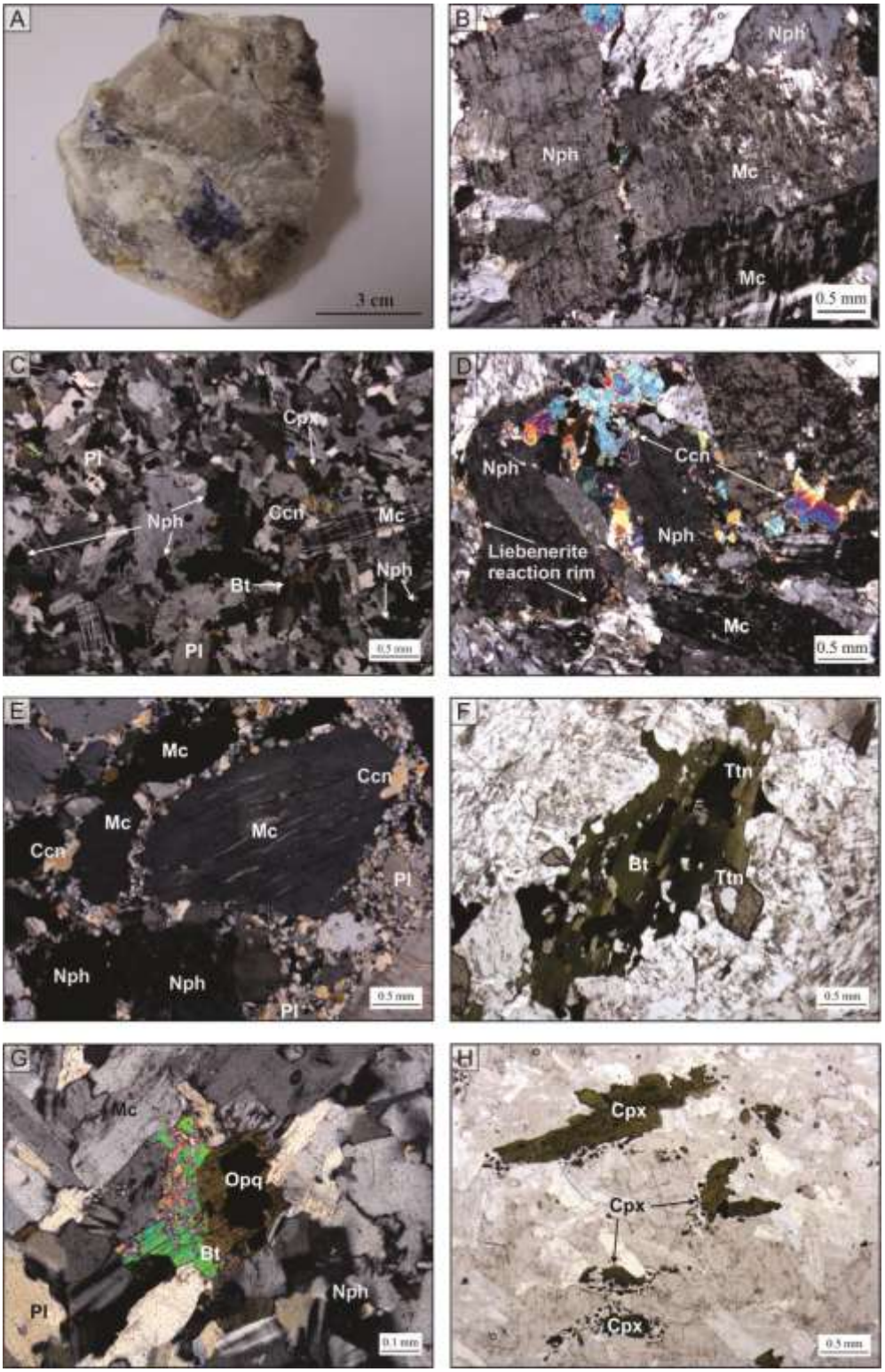

Figure 19. Photomicrographs of nepheline syenites from the Ditrău Alkaline Massif. (A) Handspecimen of the coarse-grained nepheline syenite with sodalite. (B) Crossed-polarised light (XPL) photomicrograph of a large perthite with exsolved patches of microcline in the coarse-grained nepheline syenite. (C) XPL view of typical texture of the finer-grained samples. (D) Alteration of nepheline to liebenerite and cancrinite in the coarse-grained rocks (XPL). (E) Re-crystallised texture in the coarse-grained nepheline syenite (XPL). (F) Plane- polarised light (PPL) photomicrograph of a biotite cluster in the coarse-grained samples. (G) Semi-bleached biotite with opaque mineral in the fresh part after baueritization and (H) PPL view of clinopyroxenes in the finer-grained nepheline syenites. Mineral abbreviations are after Whitney and Evans (2010): Nph - nepheline, Mc - microcline, Pl - plagioclase, Bt - biotite, Cpx - clinopyroxene, Opq - opaque, Ttn - titanite and Ccn - cancrinite.

Biotite has pleochroism from yellowish brown to dark greenish brown. It often occurs together with titanite and contains accessory mineral inclusions. Baueritization generally can be observed after the biotite probably as the result of post-magmatic processes, but fresh grains are also presented (Fig. 19G). Subhedral alkali clinopyroxenes (aegirin) occur only in few samples (Fig. 19H) in association with magnetite enclosing zircon and apatite. They have pleochroism from yellowish light green to brownish deep green.

5.2 Syenites

Syenites are medium-grained (1-3 mm), holocrystalline, phanerocrystalline, inequigranular rocks with light pinkish colour (Fig. 20A). They consist mainly of microcline and microcline-perthite, orthoclase and subordinately plagioclase feldspars. Mafic minerals are biotite and hornblende and the accessory minerals are titanite, zircon, magnetite, ilmenite, apatite, ±allanite, ±monazite.

The large K-feldspars are euhedral and fresh compared to the orthoclase which show high degree alterations to sericite and muscovite. Plagioclase feldspars are fresh grains. Smaller groundmass plagioclase feldspars show myrmecitic exsolution texture around the large microcline grains. They also occur as inclusions in these K-feldspars similarly to mafic minerals.

Biotite occurs as subhedral and anhedral crystal. The anhedral grains are affected by baueritization, therefore mostly only the fresh biotite rags can be observed or the completely faded crystals. The unaffected parts have pleochrosim from yellowish brown to dark greenish brown. Biotites are commonly intergrown with amphibole (hornblende), which are euhedral crystals showing pleochroism from yellowish green to blue (Fig. 20B).

Accessories are mostly enclosed by the mafic minerals. Zircons also occur as interstitial grains (Fig. 20C) as well as the huge titanites (1-1.5 mm). Sample AOD26 does not contain any titanite. Allanite is presented as euhedral grains in the groundmass (Fig. 20D).

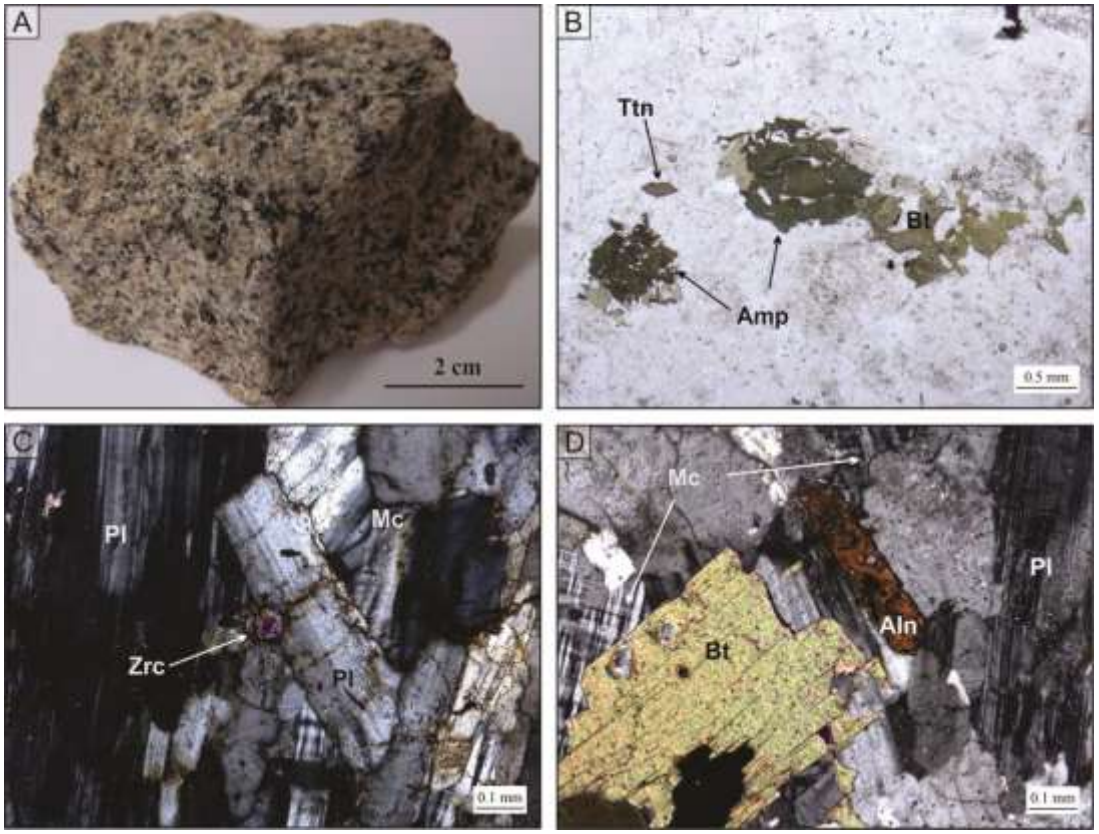

Figure 20. Photomicrographs of syenites from the Ditrău Alkaline Massif. (A) Hand specimen of the syenite with light pinkish colour. (B) PPL photomicrograph of amphiboles intergrown with biotites. (C) XPL view of a huge interstitial zircon crystal. (D) Euhedral allanite in the groundmass of syenite (XPL). Mineral abbreviations are after Whitney and Evans (2010): Mc - microcline, Pl - plagioclase, Bt - biotite, Amp - amphibole, Aln - allanite, Ttn - titanite and Zrc - zircon.

5.3 Quartz syenites and quartz monzonites

As quartz syenites and quartz monzonites have the same mineral compositions (quartz, plagioclase, K-feldspar, biotite, amphibole and accessories) and petrographic features they are described together in this section.

The rocks are medium- to fine-grained, holocrystalline, phanerocrystalline, inequigranular with pinkish colour (Figs. 21A and B). The main constituents are K- feldspars, plagioclase feldspars (quartz syenite 25-32 modal%; quartz monzonite 36-51 modal%), quartz (quartz syenite 6-10 modal%; quartz monzonite 8-17 modal%), hornblende and subordinate biotite. Apatite, zircon, titanite, magnetite, ilmenite and ±allanite, ±monazite are accessory minerals.

The large microclines and microcline-perthites are tabular grains that appear unaltered. Orthoclase crystals occur as rounded, anhedral grains in the groundmass having little alteration to sericite and muscovite. Plagioclase feldspars have columnar, euhedral

shape. Their cores are commonly replaced by sericite, rarely muscovite flakes or epidote (Fig. 21C). Plagioclase crystals with smaller sizes also can be found. Those are subhedral and occur mainly in the groundmass. They occur often around the big microclines or enclosed by them, showing myrmekitic texture at the margins (Fig. 21D). Quartz grains are mainly anhedral and show embayments as the consequence of the penetration of microcline (Fig. 21E). They also have undulose extinction.

Amphibole is presented as euhedral crystal, showing pleochroism from light brown to dark greenish-brown. They are mostly fresh, but in certain samples partly or completely replaced by secondary mineral assemblages with fine-grained titanite, epidote, opaque, ±clay minerals (Fig. 21F). Subhedral biotites appear with light brown-dark brown pleochroism, showing alteration to chlorite, hematite or clay minerals along the margins or along the cleavage planes. They are generally intergrown with the amphiboles (Fig. 21G) and occasionally they are enclosed in the large K-feldspars as well.

Titanite and allanite can be found as the part of these mafic aggregates as well as discrete interstitial grains (Fig. 21H). Titanite occurs with much smaller grain size in these rocks compared to syenites, moreover it is much less abundant in quartz monzonites and occurs only together with mafic aggregates. Accessory minerals with small sizes, like apatite, monazite and zircons, are mostly enclosed by these mafic minerals.

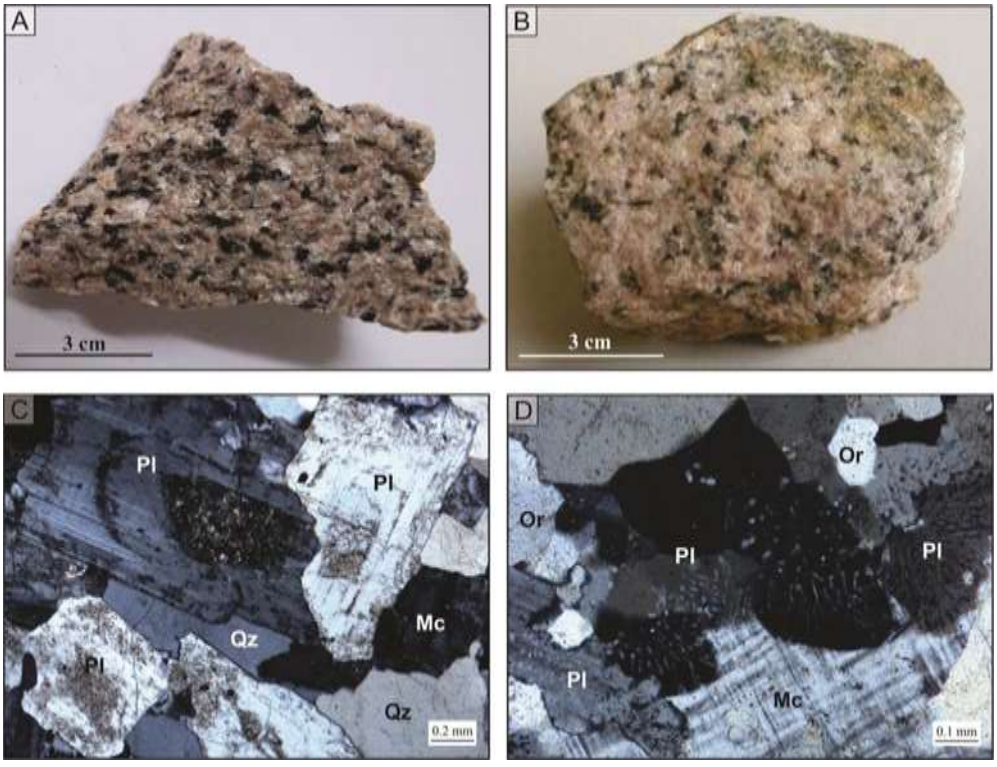

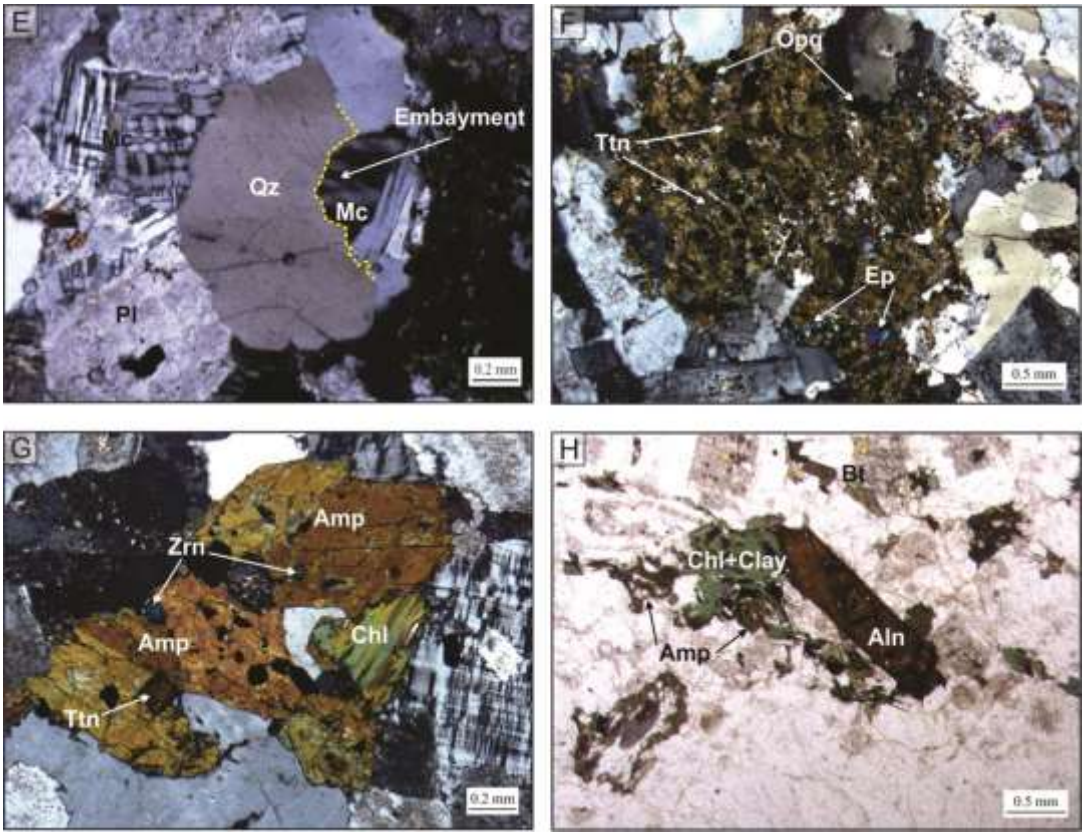

Figure 21. Photomicrographs of quartz syenites and quartz monzonites from the Ditrău Alkaline Massif. (A) and. (B) Hand specimen of quartz monzonite with light pinkish colour. (C) XPL view of the altered cores of plagioclase feldspars in quartz syenite. (D) Myrmekitic intergrowth of quartz and plagioclase in quartz monzonite (XPL). (E) XPL view of the formation of microcline on the expense of quartz in quartz monzonite. (F) XPL photomicrograph of a secondary mineral assemblage after amphibole in quartz syenite. (G) Fresh amphibole is intergrown with altered biotite in quartz monzonite (XPL). (H) PPL view of allanite in the groundmass of quartz monzonite. Mineral abbreviations are after Whitney and Evans (2010): Mc - microcline, Pl - plagioclase, Or - orthoclase, Qz - quartz, Bt - biotite, Amp - amphibole, Aln - allanite, Ttn – titanite, Zrc - zircon, Opq - opaque, Chl - chlorite and Ep - epidote.

5.4 Granites

The pink granites are holocrystalline, phanerocrystalline and inequigranular (Fig. 22A), consisting of quartz (25-37% modal%), microcline, microcline-perthite, orthoclase, biotite. Accessory phases are apatite, zircon, ilmenite, magnetite, ± allanite. Granites have very similar petrographic features to the quartz syenites and quartz monzonites.

K-feldspars are fresher compared to the euhedral plagioclase feldspars, which frequently have sericitised cores. Plagioclase is presented in the groundmass as well in smaller grain size. The smaller plagioclase crystals are often incorporated in the big, tabular microclines (Fig. 22B) showing myrmekites (Fig. 22C). Quartz grains are anhedral and because of the growth of K-feldspar it often shows embayments (Fig. 22D). They also have undulose extinction.

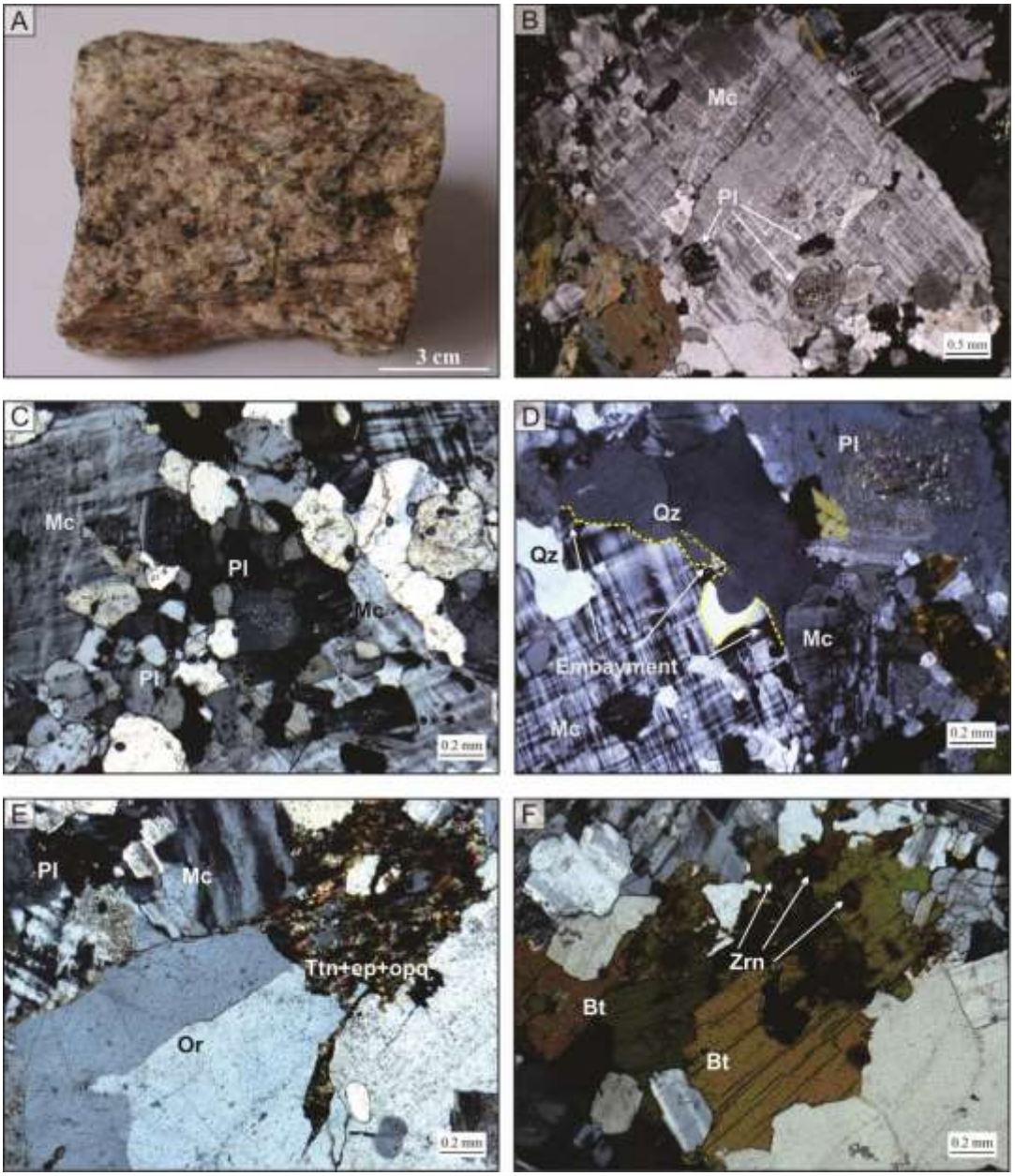

Figure 22. Photomicrographs of granites from the Ditrău Alkaline Massif. (A) Hand specimen of granite with light pinkish colour. (B) XPL view of the enclosed plagioclase feldspars by huge microcline. (C) Quartz-plagioclase feldspar intergrowth in contact with microcline (XPL). (D) Resorption of quartz due to the growth of microcline (E) XPL photomicrograph of secondary mineral assemblage after amphibole (F) Zircon inclusions in biotite grains (XPL). Mineral abbreviations are after Whitney and Evans (2010): Mc - microcline, Pl - plagioclase, Or - orthoclase, Qz - quartz, Bt - biotite, Ttn - titanite, Zrc - zircon, Opq - opaque and Ep - epidote.

Biotite appears as discrete subhedral to anhedral grains, inclusions in large K-feldspars as well as grain aggregates with light yellowish brown-dark greenish brown pleochroism. It is often altered to chlorite, ±clay and hematite or in certain samples they are faded because of the baueritization. Secondary chlorite after the biotite commonly contains rutile needles formed by the redistribution of Ti released from the biotite lattice during

alteration. Chlorite, titanite, epidote, opaque, ± clay minerals occur as alteration products after ferromagnesian minerals in certain samples (Fig. 22E). The remnants of the former minerals are not observable but based on the secondary minerals and considering the same alteration products of the quartz syenites and quartz monzonites, most likely those were originally amphiboles.

Monazite and zircon are enclosed in the biotite grains (Fig. 22F). As in the quartz syenites and quartz monzonites, allanite can be observed as discrete euhedral grains occasionally intergrowing with mafic minerals.

Chapter 6: Whole-rock chemistry results

In the following sections, the whole-rock major and trace element data are presented for each of the studied rocks from the Ditrău Alkaline Massif. By plotting major and trace elements against the LOI%, the possible secondary element mobility will be assessed. Major and trace element data also will be used for the general classification of the studied rocks e.g. rock type, volcanic series or Al-saturation. Moreover, variation of major and trace element contents of the rocks will also be used to identify the major differentiation processes dominated during the formation of the studied rocks.

CIPW normative compositions were calculated using the excel spreadsheet program by Kurt Hollocher (www.geologynet.com/programs/cipwnormexcel.xls; Union College, Schenectady, New York). The total iron was analysed in its oxidised state and recorded as Fe_2O_3 in this study. Thus, FeO and Fe_2O_3 were recalculated using the standard molecular ratios of Fe_2O_3/FeO = 0.2-0.5 depending on the rock types as it was recommended by Middlemost (1989) and Equation 6:

$$Fe_2O_3 = 0.3 \times FeO$$

$$FeO^t = Fe_2O_3^{(calc)} + (1.1113 \times FeO^{(calc)})$$

$$FeO^{(calc)} = FeO^t/1.4113$$

$$Fe_2O_3^{(calc)} = 0.3 \times FeO^{(calc)}$$

Equation 6.

Normalised concentrations of Europium on REE diagrams can be manifested as significant enrichments or depletions relative to its adjacent elements. The presence and the size of these anomalies can be important indicators of the fractionation of plagioclase feldspar. The Eu anomaly can be numerically expressed according to the Equation 7. The chondrite composition of Sun and McDonough (1995) were used during the normalization as the reference rock. The Eu anomaly was calculated using the following relationship:

$$Eu/Eu^* = \frac{Eu_N}{\sqrt{(Sm_N) \times (Gd_N)}}$$

Equation 7.

6.1 Alteration and element mobility

The alteration identified above in Chapter 5 indicates that post-magmatic element mobility may have influenced some aspects of geochemistry of the rocks. This might particularly affect O isotopes, but also might be important for Sr isotopes. As most of the secondary minerals (chlorite, sericite, liebenerite, epidote, clay) contain structural CO_2 or H_2O, loss of ignition (LOI%) can be a tool to assess the remobilization of the elements. In spite of the petrographic evidence for alterations the LOI of the bulk rocks are small in the case of most of the samples (LOI = 0.26-3.24% with average 0.90%; Fig. 23).

The highest value is shown by the nepheline syenite sample AOD 18, whereas most of the rocks (73% of the samples) have LOI below 1.00%, which is consistent with very limited post-crystallisation changes in composition. The lack of any correlation between the major and trace elements and the LOI might be the result of multiple different alteration events with effects on the bulk-rock compositions.

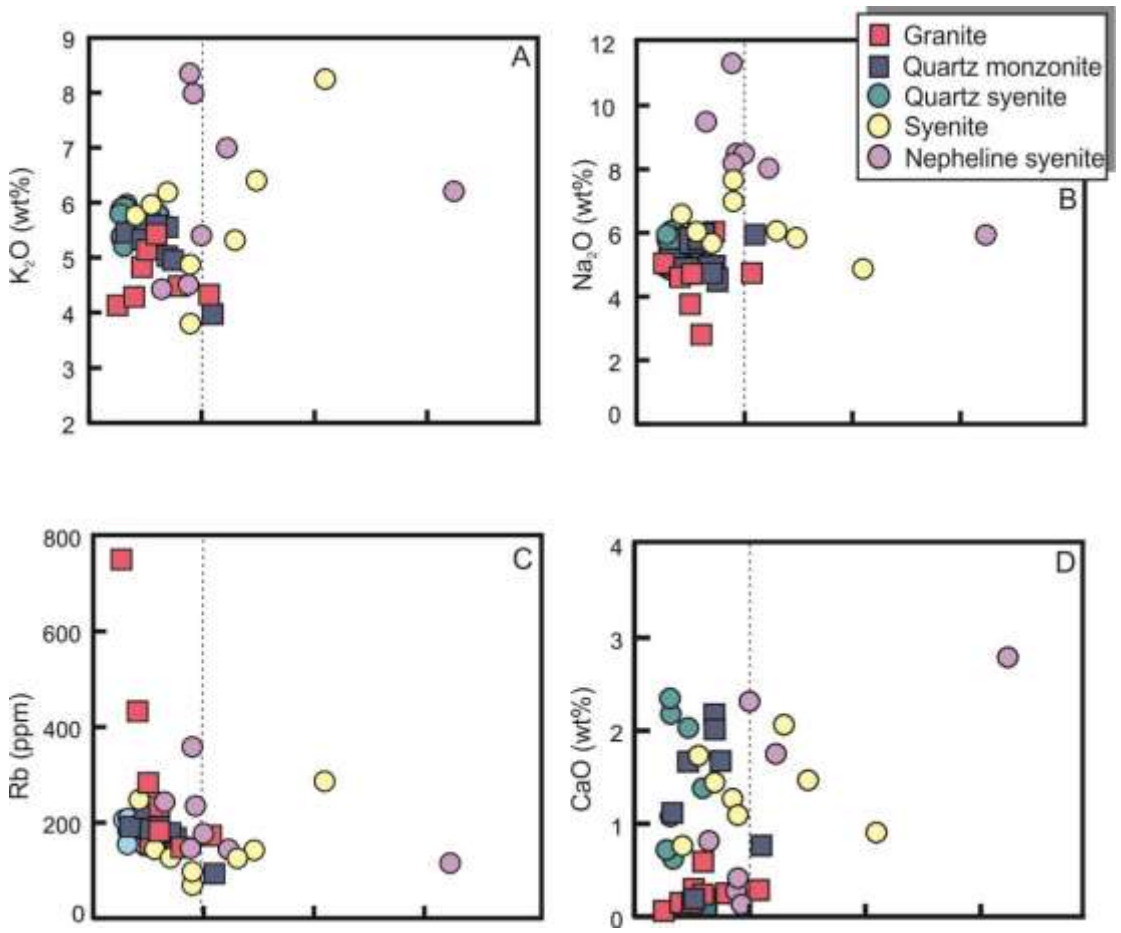

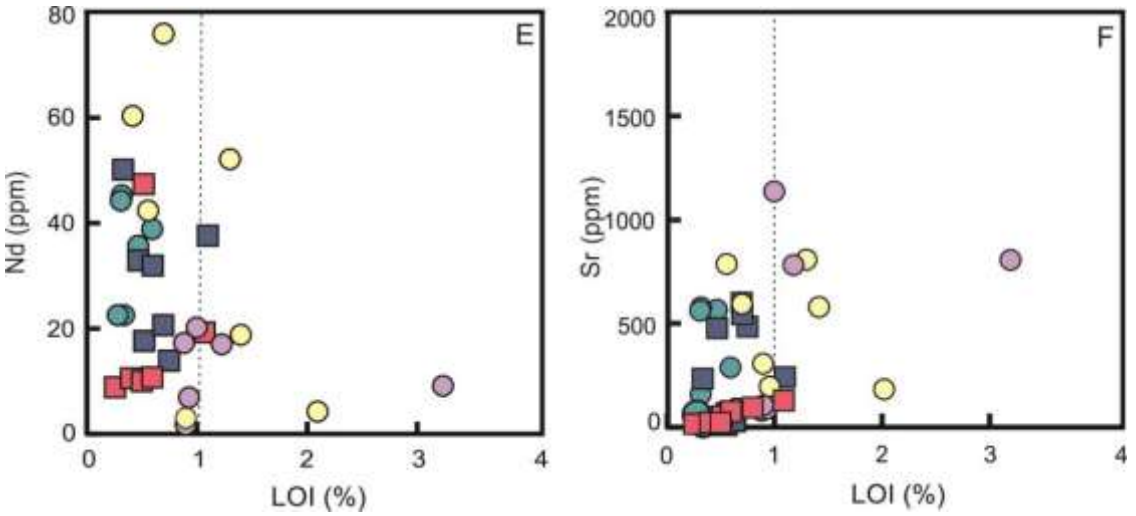

Figure 23. Plot of the selected major and trace elements versus loss of ignition (LOI%) of the felsic rocks from the Ditrău Alkaline Massif.

6.2 Classification

Analyses of 56 samples for bulk rock major element analyses for the examined rocks are presented in Table 4. On the basis of the major element compositions the rocks are hornblendites, diorites, nepheline syenites, syenites, quartz syenites, quartz monzonites and granites (Fig. 24). The data form a continuous array on the TAS diagram from the alkaline ultramafic-mafic rocks towards the trachytic composition including both the silica-undersaturated, alkaline and the silica-oversaturated, subalkaline systems.

The Aluminum Saturation Index (ASI) was calculated for all samples (Table 4) using the suggested method of Frost and Frost, (2008):

$$\text{Aluminum Saturation Index} = \text{molar } (Al / (Ca - 1.67 * P) + Na + K$$

The ASI vs. SiO_2 diagram shows that most of the rocks are metaluminous and there is an increase of ASI with the increasing SiO_2 from mafic to the felsic rocks (Fig. 25). Roughly half of the nepheline syenites, quartz monzonites, some of the syenites and mainly all the granites show slightly peraluminous character with ASI = below 1.2.

Most of the samples have corundum in their norm reflecting higher Al_2O_3 contents and therefore appear weakly peraluminous (Table 4). With a very few exceptions all the quartz-monzonite and granite contain normative corundum (*c* = 0.31-1.63 wt%). The lowest amount is presented by two quartz syenites with *c* = 0.03 and 0.05 wt%. Silica-undersaturated

and saturated syenites have the widest range of normative corundum from 0.07 to 1.42 wt% in nepheline syenites and from 0.18 to 3.80 wt% in syenites.

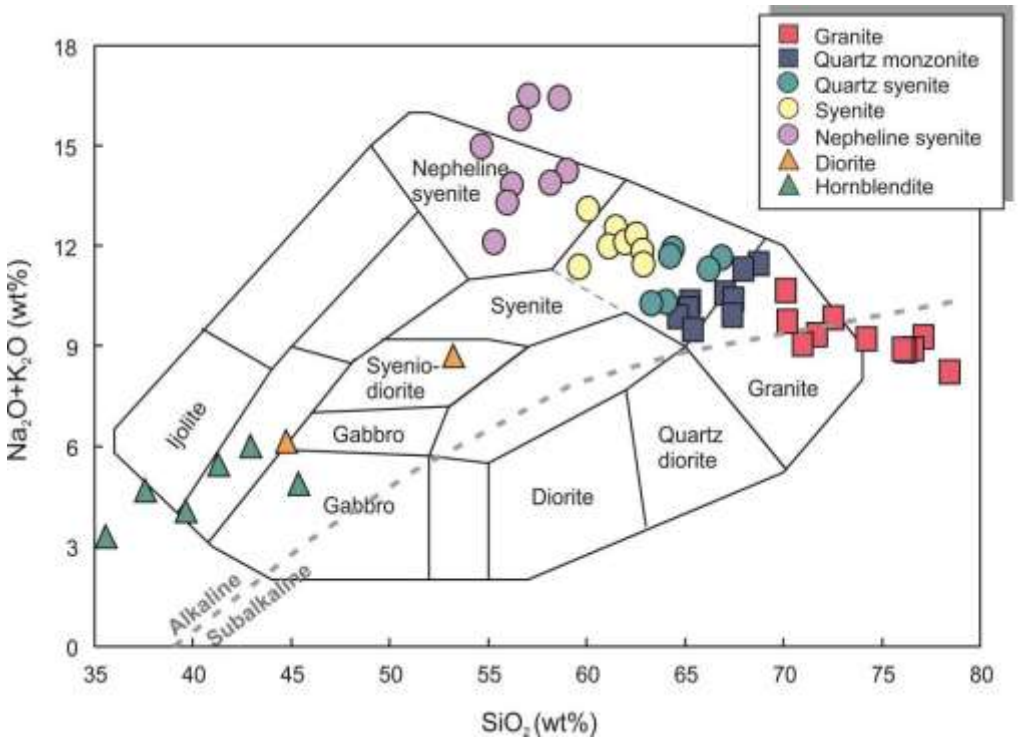

Figure 24. Classification of the examined rocks from the Ditrău Alkaline Massif on the basis of total alkali versus SiO_2 diagram by Cox et al (1979).

The presence of normative corundum does not necessarily mean that the magma was peraluminous. It also could be an artifact of variations in Fe^{3+}/Fe^{2+} ratio (unknown oxidation state), or alteration, analytical error or loss of volatiles during analysis. Slight systematic errors on Al, Si and alkali content could generate normative corundum. For example, if the assumed Fe^{3+}/Fe^{2+} ratio is too high, more Fe is allocated to magnetite, that will produce more free Al_2O_3 resulting corundum in the normative composition. To test this, ratios of Fe^{3+}/Fe^{2+} were changed between 0.1 and 0.9 in the excel spreadsheet program used for CIPW normative calculations. As the amount of normative corundum hardly changed with the variable oxidation state, it is reasonable to suppose that the normative corundum is not the result of the uncertain oxidation state. Rather the secondary Al-rich sericite, muscovite, clays, liebenerite and the loss of alkalies are account for the high amount of normative corundum in the rocks.

All he hornblendites and diorites are silica-undersaturated with the range of 3.32-11.11 wt% normative nepheline contents (Table 4). Nepheline syenites have a range of normative nepheline from 11.34 to 49.70 wt%. Some syenites have normative nepheline contents (*ne* = 0.01-2.82 wt%) with higher normative orthoclase and less plagioclase, whereas

more saturated syenite samples have orthopyroxene instead of nepheline (*Hy* = 0.04-2.29 wt%). Quartz syenites contain 6.11 to 9.27 wt% normative quartz, whereas granites have 15.73 to 40.84 wt% normative quartz.

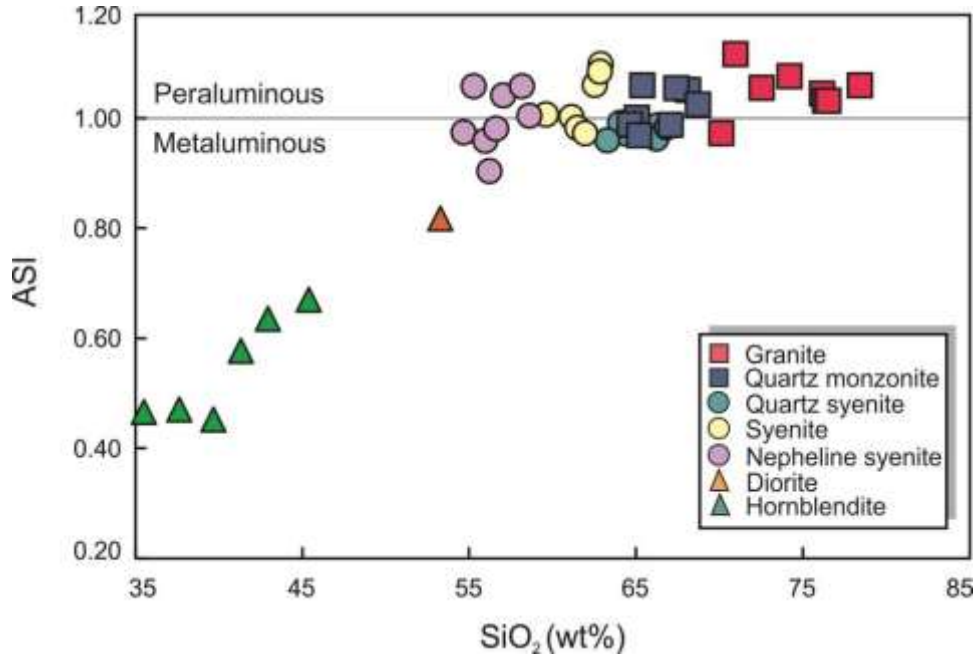

Figure 25. ASI (Aluminum Saturation Index = molar (Al/(Ca-1.67*P)+Na+K based on Frost and Frost., 2008) versus SiO_2 diagram of the examined rocks from the Ditrău Alkaline Massif.

6.3 Major element composition

The SiO_2 values of the analysed rocks have a wide variation from 35.5 to 78.4 wt% that corresponds to the range from hornblendite to granite (Fig. 26). Plots of FeO^t, CaO, MgO, P_2O_5 and TiO_2 show strong negative correlations with SiO_2 (r values are from -0.77 to - 0.87; Figs. 26A, C, D, G, H). Al_2O_3 continuously increases from the hornblendites to nepheline syenites, where it reaches its maximum (Al_2O_3 = 20.9-24.1 wt%) (Fig. 26B) whereafter it starts to decrease towards the saturated and oversaturated rocks. Roughly the same trend can be observed in the case of Na_2O as well that increases with SiO_2 from hornblendites to nepheline syenites where it attains its maximum values (Na_2O = 6-11.3 wt%) and then there is an overall decrease with increasing SiO_2 toward granites (Fig. 26E). Whereas K_2O increases with SiO_2 from the hornblendites towards the felsic rocks, the latter can be characterised by overlapping K_2O contents (Fig. 26F). The widest ranges of K_2O are demonstrated by nepheline syenites (4.42-8.34 wt%) and syenites (4.86-7.65 wt%), whereas the more evolved, quartz-bearing rocks show somewhat more restricted K_2O values. The most uniform K_2O = 5.20-5.97 wt% is presented by the quartz syenites.

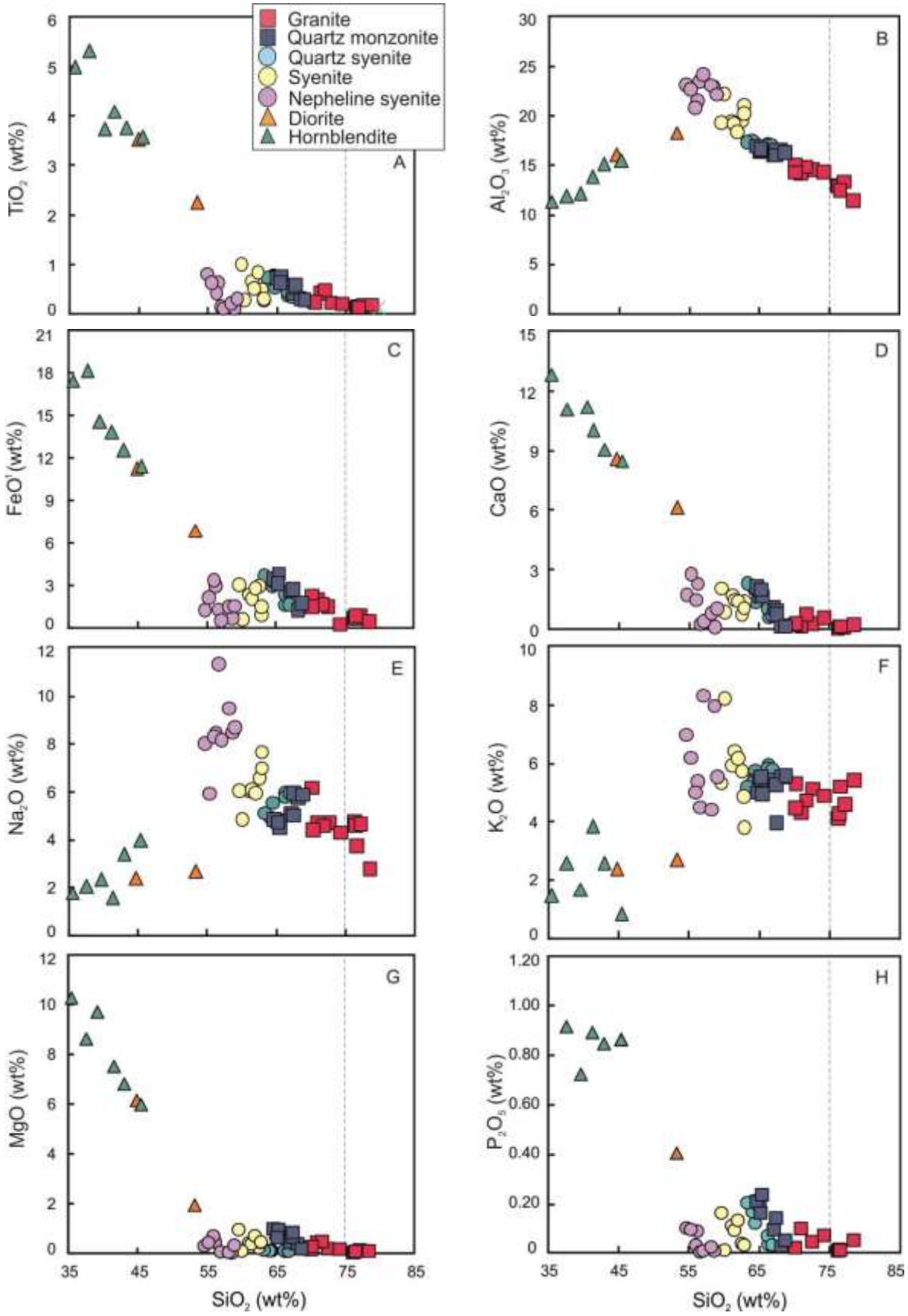

Figure 26. Major element variations in the studied rocks from the Ditrău Alkaline Massif plotted against SiO_2.

Table 4. Whole-rock major element compositions of the studied rocks from the Ditrău Alkaline Massif

Rock type	**Granite**											**Quartz monzonite**								
Sample	AOD 02	AOD 04	AOD 11	AOD 12	ÁGK 6835	ÁGK 7459	ÁGK 6847	ÁGK 6856	ÁGK 6842	ÁGK 7425/A	ÁGK 7458	AOD 03	AOD 13	AOD 24	AOD 28	AOD 32	ÁGK 6839	ÁGK 6848/A	ÁGK 7460	ÁGK 6726
Oxide (wt%)																				
SiO_2	76.2	72.5	70.9	76.3	71.7	70.1	77.1	70.2	74.2	78.4	76.5	67.1	68.1	65.1	64.6	65.4	67.4	67.4	65.2	68.7
TiO_2	0.05	0.14	0.34	0.06	0.40	0.17	0.09	0.16	0.12	0.11	0.05	0.35	0.23	0.66	0.65	0.68	0.45	0.50	0.55	0.21
Al_2O_3	12.9	14.5	14.2	12.9	14.9	15.0	13.3	14.3	14.3	11.4	12.4	16.0	16.6	16.4	16.9	16.5	16.5	16.0	16.6	16.3
FeO^t	1.07	1.85	2.40	1.04	2.00	2.59	1.24	1.84	0.61	0.80	1.20	2.96	1.61	3.72	3.80	4.18	3.06	3.10	3.48	2.12
MnO	0.02	0.05	0.05	0.02	0.06	0.14	0.02	0.08	BD	0.02	0.02	0.10	0.03	0.09	0.10	0.09	0.07	0.09	0.09	0.05
MgO	0.03	0.18	0.44	0.04	0.47	0.15	0.13	0.27	0.17	0.09	0.07	0.43	0.38	0.81	0.98	0.96	0.65	0.84	0.63	0.18
CaO	0.02	0.30	0.18	0.15	0.77	0.25	0.12	0.29	0.59	0.24	0.15	1.11	0.19	1.66	2.17	1.67	0.96	0.76	2.01	0.15
Na_2O	4.78	4.71	4.74	4.60	4.59	6.17	4.67	4.41	4.30	2.79	3.75	5.09	5.76	4.80	4.85	4.53	5.02	5.94	4.74	5.88
K_2O	4.13	5.13	4.32	4.28	4.74	4.48	4.59	5.32	4.90	5.42	5.21	5.46	5.54	5.32	5.02	4.95	5.28	3.97	5.55	5.58
P_2O_5	0.01	0.04	0.10	0.01	NA	0.02	NA	NA	0.07	0.05	0.01	0.09	0.03	0.20	0.21	0.23	NA	0.14	0.16	0.05
LOI	0.26	0.52	1.07	0.40	NA	0.80	NA	NA	0.60	0.60	0.50	0.33	0.52	0.47	0.70	0.75	NA	1.10	0.70	0.60
Total	99.5	100	98.8	99.8	99.6	99.8	101	96.8	99.9	100	99.9	98.9	99.0	99.2	100	99.9	99.4	99.9	99.7	99.8
AI	1.05	1.09	1.14	1.05	1.17	1.00	1.05	1.10	1.16	1.09	1.05	1.12	1.07	1.20	1.26	1.29	1.18	1.14	1.20	1.04
ASI	1.05	1.08	1.13	1.04	1.11	0.98	1.05	1.07	1.11	1.07	1.04	1.05	1.06	1.10	1.12	1.17	1.11	1.09	1.06	1.03
CIPW norms (wt%)																				
q	32.3	24.1	25.9	32.6	24.0	15.7	31.1	23.2	29.0	40.8	34.1	13.0	12.2	11.6	10.6	14.6	14.1	14.0	10.6	11.9
pl	40.9	41.1	41.4	40.0	42.9	52.8	39.6	40.1	39.6	24.9	32.6	48.5	50.2	48.3	50.9	45.6	47.6	54.9	48.5	51.0
or	24.6	30.5	26.2	25.5	28.2	26.8	26.8	32.5	29.2	32.3	31.0	32.7	33.3	31.9	30.0	29.6	31.4	23.8	33.3	33.3
c	0.57	0.71	1.63	0.37	0.78		0.47	0.76	0.91	0.55	0.37		0.87	0.24	0.04	1.21	0.79	0.58		0.31
di						1.08						0.23							1.96	
opx	1.00	2.00	2.91	0.98	2.46	2.18	1.32	2.30	0.79	0.82	1.23	3.33	2.13	4.54	5.06	5.31	3.83	4.30	3.05	2.14
ac						0.04														
il	0.11	0.27	0.65	0.13	0.76	0.32	0.17	0.32	0.23	0.21	0.09	0.66	0.44	1.27	1.25	1.29	0.85	0.97	1.06	0.40
mt	0.46	0.81	1.07	0.45	0.87	1.13	0.54	0.83	0.26	0.35	0.52	1.30	0.71	1.64	1.67	1.84	1.35	1.36	1.54	0.93
ap			0.23									0.21	0.07	0.46	0.49	0.56				

Fe_2O_3 = 0.3 x FeO was used Fe_2O_3 = 0.3 x FeO was used for the calculations of normative mineralogical composition of the studied rocks
Alkalinity Index (AI) = molar Al / (Na + K)
Aluminum Saturation Index (ASI) = molar Al / (Ca - 1.67 * P) + Na + K
NA - not analysed; BD - below detection limit

Table 4. (Continued)

Rock type	Quartz							Syenite								Nepheline syenite				
Sample	AOD 01	A O	AOD 10	AOD 15	AOD 22	AOD 30	AOD 31	AOD 05	AOD 26	ÁGK 7404	ÁGK 7420/2	ÁGK 7426	ÁGK 7449	ÁGK 7427	ÁGK 7446/2	AOD 06	AOD 07	AOD 20	AOD 21	AOD 25
Oxide (wt%)																				
SiO_2	66.3	64.4	66.2	66.9	64.2	64.0	63.3	61.1	62.5	59.6	61.5	62.9	62.0	62.8	60.1	56.2	54.7	56.6	58.6	57.0
TiO_2	0.30	0.46	0.37	0.27	0.70	0.66	0.66	0.59	0.41	0.92	0.44	0.19	0.76	0.23	0.20	0.55	0.73	0.06	0.03	0.03
Al_2O_3	17.1	17.2	17.1	17.0	17.1	17.5	17.3	19.4	19.5	19.3	19.2	21.1	18.4	20.3	22.2	21.5	23.2	23.5	22.9	24.2
FeO^t	1.99	3.30	2.73	2.01	3.68	3.82	4.03	2.73	3.35	3.39	2.45	1.32	3.16	1.85	0.98	3.35	1.60	1.66	1.04	0.89
MnO	0.08	0.11	0.11	0.09	0.11	0.10	0.12	0.07	0.19	0.12	0.07	0.03	0.09	0.04	0.06	0.16	0.05	0.06	0.02	0.07
MgO	0.16	0.39	0.24	0.19	0.74	0.68	0.69	0.41	0.23	0.95	0.37	0.43	0.70	0.46	0.09	0.46	0.30	BD	0.01	0.06
CaO	0.62	1.38	1.07	0.72	2.03	2.17	2.34	1.73	0.76	2.06	1.49	1.41	1.44	1.09	0.90	2.31	1.75	0.27	0.13	0.41
Na_2O	5.97	5.55	5.79	5.94	4.88	4.93	5.11	6.03	6.57	6.05	6.10	7.65	5.94	6.98	4.86	8.46	8.01	11.3	8.48	8.17
K_2O	5.97	5.75	5.85	5.79	5.42	5.36	5.20	5.96	5.76	5.33	6.44	3.80	6.18	4.87	8.24	5.39	6.98	4.50	7.97	8.34
P_2O_5	0.03	0.12	0.07	0.03	0.21	0.17	0.20	0.11	0.04	0.16	0.09	0.03	0.13	0.01	0.01	0.09	0.10	NA	0.01	0.01
LOI	0.34	0.60	0.32	0.28	0.47	0.32	0.31	0.56	0.42	1.30	1.40	0.90	0.70	0.90	2.10	NA	1.23	0.89	0.93	0.90
Total	98.9	99.3	99.8	99.2	99.6	99.8	99.3	98.8	99.7	97.9	98.1	99.7	99.5	99.5	97.7	99.5	98.6	98.9	100	100
AI	1.05	1.12	1.08	1.06	1.23	1.56	1.23	1.19	1.14	1.23	1.13	1.26	1.12	1.21	1.32	1.09	1.12	1.00	1.08	1.13
ASI	1.02	1.05	1.02	1.02	1.10	1.12	1.09	1.09	1.10	1.10	1.05	1.17	1.04	1.14	1.25	0.99	1.04	0.99	1.01	1.06
CIPW norms (wt%)																				
q	6.87	6.11	7.16	7.95	9.27	8.54	7.27													
pl	53.6	52.8	52.6	53.6	50.6	51.8	52.9	58.3	59.6	59.3	53.7	72.7	56.3	65.5	42.5	36.5	25.5	37.2	25.2	20.1
or	35.8	34.5	34.8	34.6	32.4	31.9	31.1	35.9	34.3	32.3	38.9	22.7	37.0	29.2	49.8	32.4	42.4	27.12	47.6	49.7
ne								0.95	0.01	1.73	2.82				2.25	22.4	27.1	32.9	25.9	28.0
c					0.03	0.05		0.18	1.16			1.85		1.56	3.80				0.07	0.95
di	0.48	0.88	1.37	0.62			1.20			0.37	1.16		0.86			5.20	1.13	1.16		
opx	1.64	3.03	1.98	1.71	4.27	4.30	3.97					1.04		2.29						
ac																				
ol								2.01	2.51	2.97	1.51	0.74	3.08	0.21	0.69	0.77	0.42	0.73	0.75	0.79
il	0.59	0.87	0.70	0.53	1.35	1.27	1.25	1.14	0.80	1.79	0.85	0.36	1.46	0.44	0.38	1.06	1.42	0.11	0.06	0.06
mt	0.88	1.46	1.20	0.88	1.62	1.68	1.78	1.22	1.46	1.51	1.09	0.58	0.88	0.81	0.43	1.48	0.71	0.47	0.45	0.39
ap		0.28	0.16	0.07	0.49	0.39	0.46	0.25	0.09				0.30			0.21	0.23			

Table 4. (Continued)

Rock type	Nepheline syenite				Diorite		Hornblendite						Country rock			
Sample	AOD 25d	AOD 18	ÁGK 6769	ÁGK 7446/3	AOD 08	ÁGK 6723	AOD 29	ÁGK 7434	ÁGK 7428	ÁGK 7437	ÁGK 7436	ÁGK 7451	AOD 16	AOD 17	AOD 23	AOD 27
Oxide (wt%)																
SiO_2	58.2	55.3	59.0	60.5	53.3	44.7	41.3	45.4	35.5	37.6	42.9	39.7	79.4	45.1	76.6	63.2
TiO_2	0.13	0.55	0.23	0.17	2.18	3.44	4.01	3.50	4.91	5.23	3.7	3.68	0.05	1.23	0.14	0.80
Al_2O_3	23.1	22.6	22.1	22.7	18.9	16.0	13.8	15.5	11.4	11.9	15.2	11.8	11.9	26.3	12.9	18.5
FeO^t	1.84	2.49	1.90	1.93	7.24	11.1	14.3	11.8	17.8	18.5	12.9	15.6	0.59	8.85	1.92	6.71
MnO	0.15	0.06	0.11	0.06	0.14	0.19	0.24	0.16	0.23	0.34	0.18	0.39	0.01	0.12	0.03	0.04
MgO	0.04	0.43	0.32	0.26	1.93	5.94	7.14	5.77	10.3	8.62	6.60	10.2	0.24	3.69	1.28	1.93
CaO	0.81	2.78	1.04	0.40	6.16	8.57	10.0	8.49	12.8	11.1	9.06	11.7	0.04	0.19	0.19	0.30
Na_2O	9.47	5.93	8.68	8.77	5.76	3.73	1.59	4.00	1.81	2.07	3.40	2.35	4.85	0.44	1.42	1.22
K_2O	4.42	6.20	5.56	5.17	2.70	2.40	3.86	0.86	1.47	2.60	2.60	1.69	2.38	7.99	4.22	4.43
P_2O_5	0.02	0.09	NA	NA	0.40	NA	0.89	0.86	1.95	0.91	0.85	0.72	0.01	0.16	0.02	0.11
LOI	0.65	3.24	NA	NA	0.45	NA	1.91	2.00	1.27	1.07	2.28	2.04	0.48	4.93	1.35	2.37
Total	98.8	99.7	98.9	99.9	99.1	85.1	99.2	98.3	99.4	99.9	99.7	99.7	100	98.9	100	99.7
AI	1.13	1.38	1.09	1.13	1.52	1.84	2.04	2.06	2.49	1.91	1.80	2.07	1.13	2.80	1.87	2.73
ASI	1.09	1.20	1.04	1.11	1.08	0.97	0.93	1.02	0.70	0.78	0.97	0.76	1.13	2.81	1.83	2.68
CIPW norms (wt%)																
q													41.7	3.90	49.9	34.8
pl	50.3	44.8	45.1	50.6	59.5	35.9	20.5	52.6	19.5	15.9	31.3	17.2	41.4	3.98	13.0	11.4
or	26.6	38.1	33.2	30.6	16.2	14.7	23.7	5.38		4.69	15.9	10.3	14.2	50.5	25.3	27.0
ne	19.3	11.3	18.6	13.9	4.46	9.53	7.26	3.32	8.76	9.72	9.53	11.1				
lc									7.18	8.65						
c	1.25	1.42		1.95									1.30	18.1	5.82	11.9
di			0.06		8.50	18.8	20.7	17.4	22.6	27.7	17.4	30.3				
opx													1.06	16.5	4.81	10.0
ac																
ol	1.45	1.96	1.75	1.73	2.96	8.80	11.3	8.90	18.0	12.7	10.7	15.0				
il	0.25	1.08	0.44	0.32	4.22	6.78	7.92	7.03	9.82	10.2	7.24	7.00	0.09	2.51	0.28	1.56
mt	0.81	1.13	0.84	0.87	3.20	5.47	6.48	5.42	8.16	8.24	5.81	1.74	0.26	4.12	0.84	3.02
ap		0.23			0.95		2.13			2.18	2.04			0.39	0.05	0.28

Focusing only on granites, Fig. 27 displays the major element variation digrams of these rocks. Although samples with lower silica contents (< 75 wt%) have somewhat higher average values of TiO_2 = 0.22 wt%, Al_2O_3 = 14.53 wt%, FeO^t = 1.88 wt%, CaO = 0.40 wt% and MgO = 0.28 wt% compared to the samples with higher SiO_2 contents (average TiO_2 = 0.07 wt%, Al_2O_3 = 12.6 wt%, FeO^t = 1.2 wt%, CaO = 0.14 wt% and MgO = 0.07 wt%), granites can be characterised by very similar major element compositions in general. The K_2O, Na_2O and P_2O_5 contents are fairly the same in both the SiO_2-poorer and -richer granites (Figs. 27E, F, H).

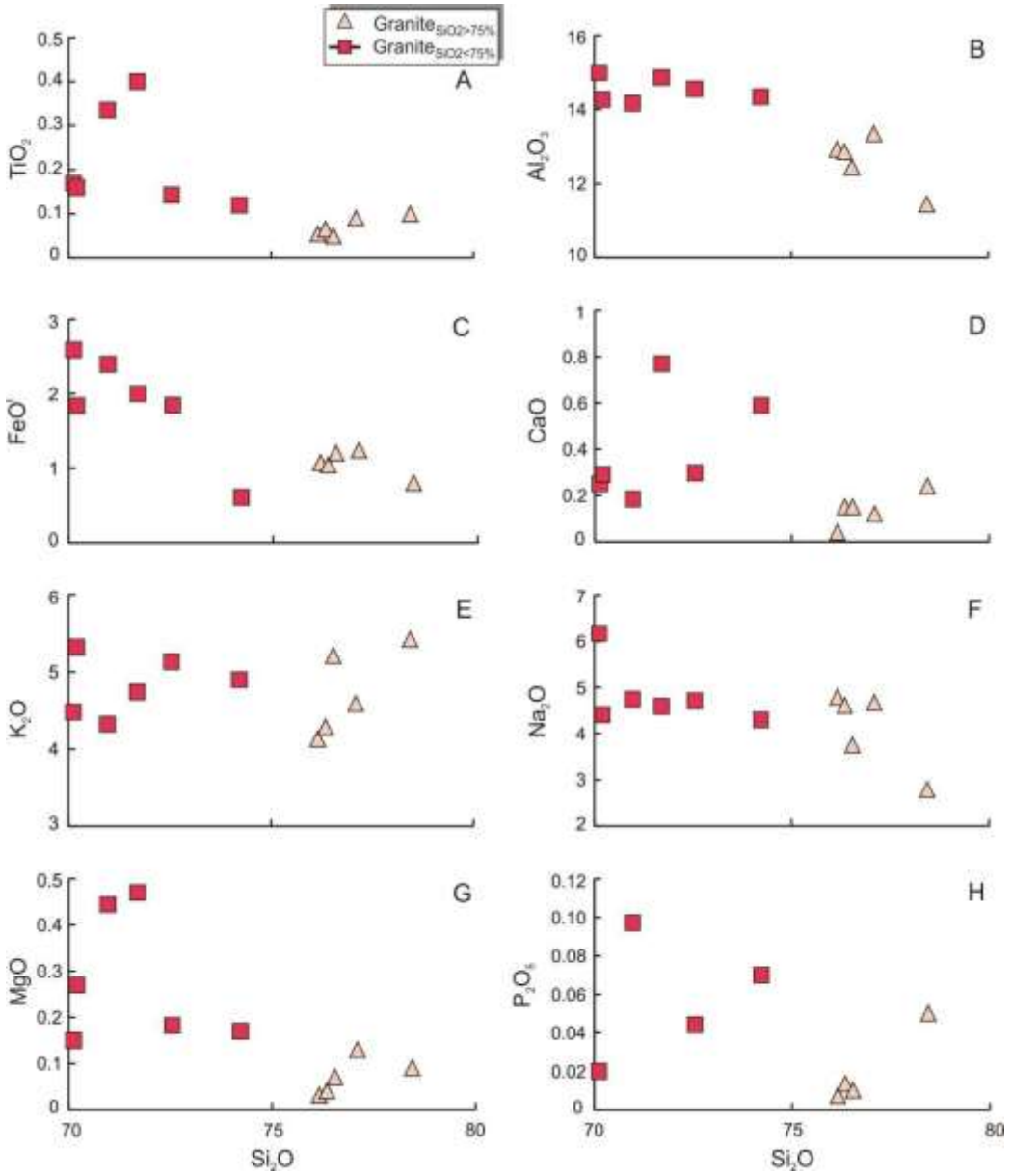

Figure 27. Major element variations in granites from the Ditrău Alkaline Massif plotted against SiO_2

6.4 Trace element composition

Trace element concentrations of the examined rocks are highly variable (Table 5). In general, correlations between the trace elements and SiO_2 are presented mainly from hornblendites to diorites as the trace element contents of felsic rocks overlaps and show wide ranges (Fig. 28). The only correlation that can clearly be observed from hornblendites to granites is demonstrated by V and SiO_2 ($r = -0.82$; Fig. 28D). The V content decreases sharply with increasing silica and granites have the lowest V values with V < 2.1 ppm.

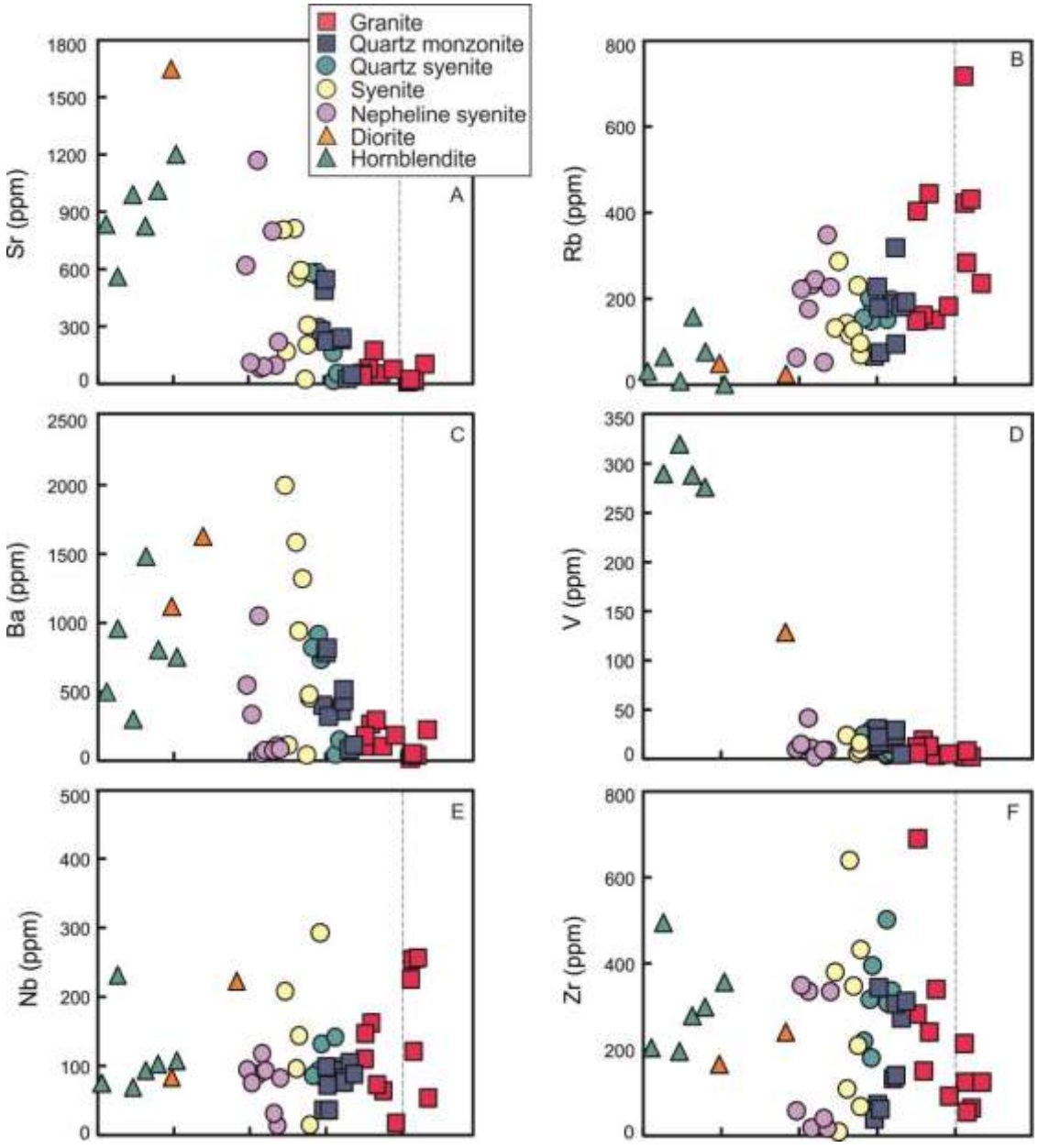

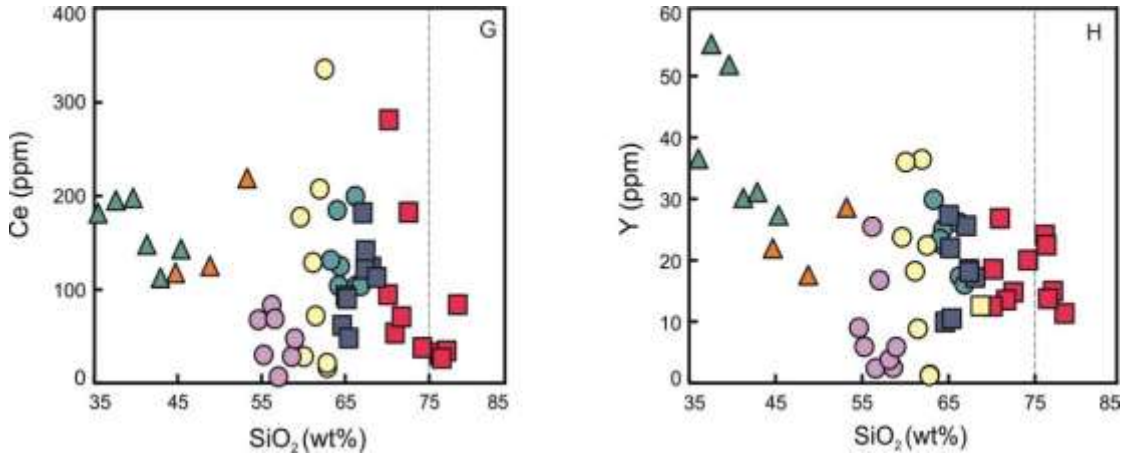

Figure 28. Trace element variations in the rocks from the Ditrău Alkaline Massif plotted against SiO_2

Sr and Ba increase with SiO_2 from hornblendites to diorites, whereas those show wide ranges in the felsic rocks, similarly to Rb (Figs. 28A, B, C). The largest range of Sr concentration (21-1051 ppm) is displayed by the nepheline syenites, whereas syenites have the widest range of Ba (40-1997 ppm). The most restricted Ba and Sr values are shown by granites (Ba = 16-293 ppm; Sr = 8-103 ppm).

Despite these low Ba and Sr contents in granites, Rb concentration show the widest range in these rocks (149-717 ppm) (Fig. 28B). The most restricted range of Rb is displayed by quartz syenites (151-201 ppm).

Considering the broad ranges of HFSEs it is difficult to make out any overall correlation similarly to the LILEs (Figs. 28E, F, G). A decrease in Y with increasing SiO_2 is distinct from hornblendite to diorite (Fig. 28H), but, apart from this, other general correlations cannot be observed. The most restricted HFSE and Y values are indicated by quartz syenites (e.g. Ce = 104-199 ppm), whereas the widest scatter is shown by syenites (Ce = 16-335 ppm).

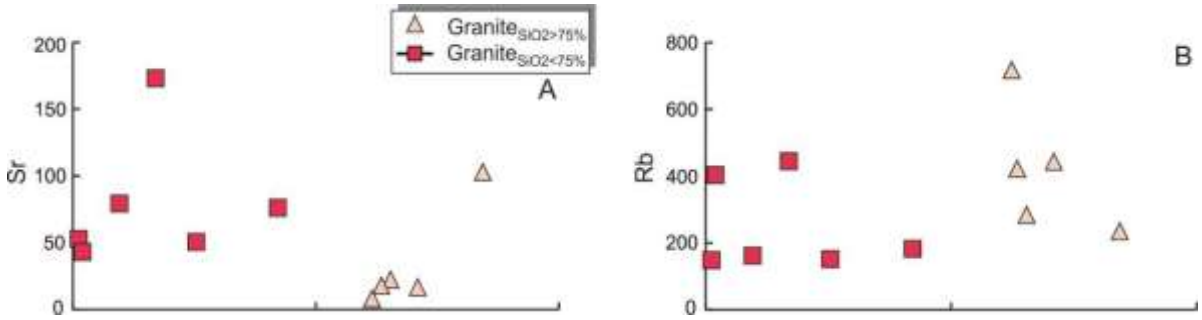

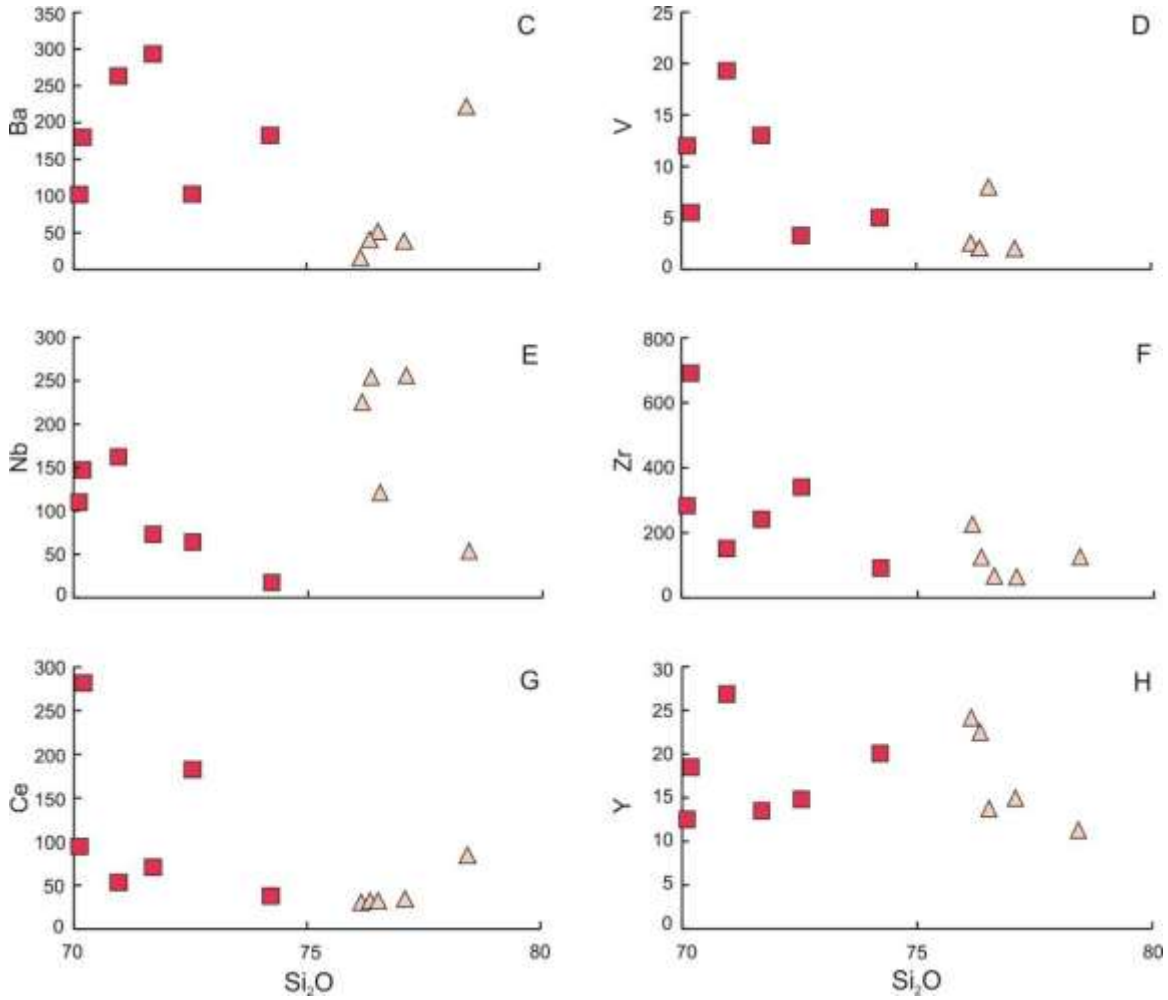

Figure 29. Trace element variations in granites from the Ditrău Alkaline Massif plotted against SiO_2

Granites with SiO_2 > 75 wt% have somewhat lower average V = 4 ppm, Zr = 116 ppm and Ce = 41 ppm (Fig. 29D, F, G) compared to the SiO_2-poorer granites ($V_{average}$ = 10 ppm, $Zr_{average}$ = 299 ppm, $Ce_{average}$ = 120 ppm), whereas they show fairly the same concentration in Sr, Rb, Ba, Nb and Y (Fig. 29A, B, C, E, H).

Table 5. Whole-rock trace element compositions of the studied rocks from the Ditrău Alkaline Massif

Rock type	**Granite**											**Quartz monzonite**								
Sample	AOD 02	AOD 04	AOD 11	AOD 12	ÁGK 6835	ÁGK 7459	ÁGK 6847	ÁGK 6856	ÁGK 6842	ÁGK 7425/A	ÁGK 7458	AOD 03	AOD 13	AOD 24	AOD 28	AOD 32	ÁGK 6839	ÁGK 6838/A	ÁGK 7460	ÁGK 6726
ppm																				
Sc	0.27	0.81	1.66	0.21	1.80	1.00	0.40	1.50	0.74	1.00	1.00	2.00	0.71	2.89	1.22	1.56	3.60	1.13	2.00	1.00
V	2.54	3.28	19.3	2.05	13.0	12.0	2.00	5.50	NA	NA	8.00	15.4	4.38	30.5	13.3	16.6	23.5	29.0	22.0	NA
Cr	5.64	5.97	5.58	5.02	4.14	NA	3.83	17.0	3.24	NA	3.41	6.57	4.85	7.34	2.91	3.88	13.0	5.53	NA	3.20
Co	0.34	0.62	2.59	0.60	4.17	1.10	0.25	7.05	0.63	0.90	0.54	2.40	0.49	4.32	2.05	2.44	5.02	2.74	3.90	0.68
Ni	3.02	2.58	BD	4.27	NA	NA	8.60	NA	85.1	NA	5.06	3.46	1.85	4.52	2.98	2.73	11.9	8.30	2.90	13.3
Cu	2.90	3.32	4.52	2.32	33.0	3.70	15.0	20.0	1.70	3.20	5.10	4.55	3.24	6.67	3.38	3.31	16.0	2.70	3.80	3.50
Pb	11.1	11.7	4.32	10.3	7.00	2.90	13.1	3.90	20.9	6.00	8.75	16.2	6.53	11.7	6.75	7.28	10.5	8.73	6.30	11.2
Zn	20.0	32.9	20.5	16.4	34.0	27.0	28.9	49.5	15.6	17.0	13.7	57.4	29.6	47.1	34.3	33.7	2.50	60.6	48.0	69.7
Ga	NA	NA	NA	NA	20.0	25.1	26.5	29.2	18.8	18.4	22.5	NA	NA	NA	NA	NA	23.1	21.1	22.2	25.3
Rb	717	151	161	422	444	148	431	403	182	235	283	188	181	226	66.1	74.9	318	93.7	178	192
Ba	15.8	102	263	39.4	293	102	38.6	180	182	222	51.8	361	81.2	781	402	319	433	515	816	113
Sr	8.04	50.4	79.1	17.8	173	52.7	15.3	43.0	76.2	103	22.4	230	25.7	487	275	223	230	240	544	48.3
Zr	214	340	151	124	241	282	64.5	690	91.6	125	54.9	132	273	72.9	38.6	62.1	306	140	344	312
Hf	9.73	7.47	4.23	5.06	NA	NA	NA	NA	NA	NA	NA	3.80	5.22	2.16	1.00	1.56	NA	NA	NA	NA
Nb	225	64.1	16	254	73.0	110	256	147	17.3	53.5	121	93.3	105	98.6	36.1	36.0	82.0	76.5	71.9	88.4
Ta	17.9	3.82	13.2	15.2	NA	NA	NA	NA	NA	NA	NA	5.79	8.48	7.58	2.20	2.30	NA	NA	NA	NA
Y	24.1	14.8	26.8	22.5	13.5	12.5	14.9	18.5	20.0	11.3	13.7	25.6	17.2	27.3	9.94	10.5	18.5	18.1	22.0	12.5
F	846	235	453	556	NA	NA	NA	NA	NA	NA	NA	472	237	932	592	787	NA	NA	NA	NA
S	261	261	273	257	90.0	NA	20.0	67.0	NA	NA	NA	261	260	261	262	259	39.0	NA	NA	NA
Cl	159	145	160	167	NA	NA	NA	NA	NA	NA	NA	252	165	459	178	203	NA	NA	NA	NA
U	6.98	5.23	9.98	15.3	NA	3.40	7.12	NA	2.42	2.60	7.78	5.95	4.49	2.52	1.08	0.87	NA	1.93	3.60	3.83
Th	74.7	32.4	35.7	67.4	NA	17.1	36.2	NA	13.6	26.4	23.9	47.1	37.1	23.1	7.56	8.43	NA	21.7	22.2	19.0

NA - not analysed
BD - below detection limit

Table 5. (Continued)

Rock type	Quartz syenite							Syenite								Nepheline syenite				
Sample	AOD 01	AOD 09	AOD 10	AOD 15	AOD 22	AOD 30	AOD 31	AOD 05	AOD 26	ÁGK 7404	ÁGK 7420/2	ÁGK 7426	ÁGK 7449	ÁGK 7427	ÁGK 7446/2	AOD 06	AOD 07	AOD 20	AOD 21	AOD 25
ppm																				
Sc	0.83	1.23	0.92	0.82	2.54	2.54	2.64	0.68	0.34	2.00	NA	NA	1.00	NA	NA	0.97	0.28	0.58	0.20	0.14
V	3.49	11.3	5.32	7.12	29.1	24.5	24.4	23.8	5.50	NA	NA	9.00	NA	16.0	NA	41.5	9.86	10.7	8.71	2.09
Cr	3.28	4.32	2.46	6.38	6.53	5.02	7.20	3.21	2.65	8.92	NA	NA	NA	3.70	NA	5.78	2.90	2.82	4.46	4.81
Co	0.42	1.96	1.14	0.84	3.65	3.63	4.22	1.73	0.60	7.06	1.50	2.10	3.70	2.72	0.70	2.77	0.97	0.26	0.26	0.29
Ni	2.16	2.41	8.41	3.44	5.10	5.19	5.04	2.94	2.81	16.4	NA	NA	NA	4.42	NA	3.38	1.72	1.66	1.93	2.17
Cu	3.39	4.16	3.09	5.28	5.14	6.25	5.45	4.98	3.12	3.90	0.80	1.00	3.30	14.0	0.70	4.51	3.20	1.12	2.54	7.63
Pb	13.0	13.5	13.1	9.86	10.5	37.5	16.9	8.57	15.1	8.04	NA	NA	NA	9.74	NA	7.39	3.76	3.57	3.10	23.0
Zn	49.0	72.4	71.8	60.3	74.1	68.0	68.0	60.6	133	126	42.0	45.0	77.0	68.3	36.0	89.3	18.6	42.8	19.5	59.1
Rb	151	180	176	197	148	201	154	142	230	132	115	69.1	126	96.7	286	175	62.8	139	232	348
Ba	44.4	733	380	149	803	915	820	1584	40.2	1997	940	454	1321	478	111	1051	547	54.3	107	73.1
Sr	16.5	295	162	54.7	565	583	580	811	23.5	805	554	306	592	203	168	1168	618	72.0	80.7	96.2
Zr	308	395	502	337	181	317	220	109	210	380	640	432	347	67.8	9.20	335	57.7	105	18.5	17.9
Hf	5.21	6.85	8.80	6.11	4.06	6.26	4.69	3.03	2.64	NA	NA	NA	NA	NA	NA	6.12	1.29	2.88	0.48	0.48
Nb	95.3	132	141	98.8	85.3	93.4	85.9	96.0	293	208	NA	NA	144	14.5	NA	88.6	94.9	469	118	13.6
Ta	5.60	7.28	6.95	5.78	4.48	5.56	6.12	6.87	13.2	NA	NA	NA	NA	NA	NA	2.13	2.50	12.3	3.02	0.28
Y	17.3	25.1	26.1	16.1	22.6	23.4	29.8	18.2	22.4	23.7	8.80	1.30	36.4	1.19	36.0	25.4	8.97	5.95	2.36	2.46
F	241	352	393	296	877	565	498	199	263	NA	NA	NA	NA	NA	NA	320	57.0	9.10	36.6	78.3
S	262	262	260	259	261	261	261	266	262	NA	NA	NA	NA	NA	NA	386	351	362	524	266
Cl	200	192	200	225	167	260	439	118	151	NA	NA	NA	NA	NA	NA	465	934	690	690	492
U	4.91	2.68	3.16	9.02	2.35	3.88	2.89	1.01	9.83	1.51	2.60	0.70	3.40	0.71	14.6	3.46	0.61	22.5	5.43	1.40
Th	26.6	21.3	31.0	24.8	16.9	23.4	16.8	5.45	32.4	8.64	9.60	2.50	18.1	2.07	6.90	11.3	3.99	51.5	12.6	5.67

Table 5. (Continued)

Rock type	Nepheline syenite				Diorite			Hornblendite						Country rock			
Sample	AOD 25d	AOD 18	ÁGK 6769	ÁGK 7446/3	AOD 08	ÁGK 7502	ÁGK 6723	AOD 29	ÁGK 7434	ÁGK 7428	ÁGK 7437	ÁGK 7436	ÁGK 7451	AOD 16	AOD 17	AOD 23	AOD 27
ppm																	
Sc	BD	0.46	NA	NA	4.60	3.75	13.0	22.7	16.53	28.0	30.8	15.4	26.9	3.17	23.2	4.13	7.30
V	8.91	14.8	NA	NA	129	NA	NA	288	NA	NA	290	276	320	1.16	175	0.97	53.8
Cr	12.4	2.30	2.70	1.85	10.0	41.2	75.4	80.0	63.0	205	53.9	NA	NA	2.88	135	1.05	38.2
Co	BD	1.15	0.48	NA	16.8	11.6	31.9	47.9	39.5	54.8	NA	54.1	NA	0.28	20.5	0.30	6.70
Ni	BD	3.10	28.8	4.82	11.9	52.5	52.0	77.0	48.8	56.1	63.9	54.1	35.9	2.97	52.3	1.83	16.8
Cu	BD	2.73	NA	NA	29.3	NA	NA	54.8	NA	NA	17.0	51.2	39.3	2.83	13.8	1.93	11.1
Pb	20.2	1.94	11.8	7.40	3.39	5.57	2.50	5.79	4.24	3.73	2.20	9.40	2.80	5.78	7.89	9.70	7.88
Zn	113	18.9	83.5	75.7	103	95.2	132	174	154	203	250	141	247	22.9	114	21.9	40.6
Rb	243	52.3	222	227	24.2	22.5	49.0	158	68.5	31.0	64.9	76.0	8.00	74.6	267	61.4	87.1
Ba	74.1	334	81.5	20.9	3999	1628	1118	1482	750	498	956	803	299	591	1277	229	284
Sr	88.9	798	109	218	3880	3024	1646	824	1200	834	560	1011	989	24.5	56.3	48.1	30.1
Zr	1093	39.9	349	335	241	181	166	278	357	204	495	299	196	62.2	197	83.9	35.2
Hf	NA	0.86	NA	NA	5.71	NA	NA	6.43	NA	NA	NA	NA	NA	2.78	4.73	2.70	1.11
Nb	93.3	31.1	75.5	82.6	222	136	83.5	93.5	107	74.9	231	103	69.0	6.00	24.2	5.41	6.26
Ta	NA	1.79	NA	NA	10.5	NA	NA	5.23	NA	NA	NA	NA	NA	0.66	1.65	0.42	0.45
Y	16.7	3.81	5.91	5.82	28.6	17.6	21.9	30.1	27.3	36.5	55.2	31.1	51.8	27.9	30.5	21.3	10.4
F	173	139	NA	NA	320	NA	NA	1086	NA	NA	NA	NA	NA	283	1014	671	639
S	263	338	NA	NA	295	NA	NA	408	NA	NA	NA	NA	NA	257	256	256	267
Cl	386	159	NA	NA	200	NA	NA	840	NA	NA	NA	NA	NA	96.4	97.4	99.1	160
U	20.0	0.29	9.05	7.00	0.82	1.14	0.70	2.15	2.36	1.24	1.50	2.30	NA	1.94	2.88	1.78	1.18
Th	30.3	1.43	23.2	23.7	6.10	4.86	3.03	7.52	8.78	3.16	10.4	8.00	3.50	10.3	21.7	8.72	6.87

6.5 Rare Earth Element variations

Bulk-rock rare earth element analyses for the examined rocks are presented in Table 6. For the sake of clarity, the chondrite-normalised REE diagrams for silica-oversaturated, saturated and undersaturated rocks are presented separately with the other rock types represented as shaded fields for comparison. All of the studied felsic rocks of the DAM show steep, sub-parallel trends with strong LREE-enrichments $(La/Sm)_N$ = 3.4-58.6 compared to the HREEs that have flat patterns for HREE ($(Gd/Yb)_N$ = 0.5-3.2) in the case of silica-oversaturated rocks (Fig. 30A). Nepheline syenites and syenites mainly show upward convex REE-patterns because of their depleted MREE contents (Fig. 30B and C).

Quartz monzonites show very similar patterns to granites. Quartz monzonite samples (AOD 28, AOD 32, ÁGK 7460) with the lowest LREE $(La/Sm)_N$ < 7.17) do not show Eu anomaly (Eu/Eu* = 0.84-0.93), whereas most of these rocks have variable LREE-enrichment ($(La/Sm)_N$ = 4.71-9.96) with different negative Eu anomalies (Eu/Eu* = 0.28-078) (Fig 30A). Quartz monzonite sample with the smallest Eu/Eu* have the highest $(La/Sm)_N$ = 9.98 content and vice versa.

All of the quartz syenites show elevated LREE concentrations with $(La/Sm)_N$ = 5.64-12.64. Samples mostly have very high Eu/Eu* values (0.47-0.99) and the increasing $(La/Sm)_N$ values associate with increasing Eu-anomalies (Fig. 30A).

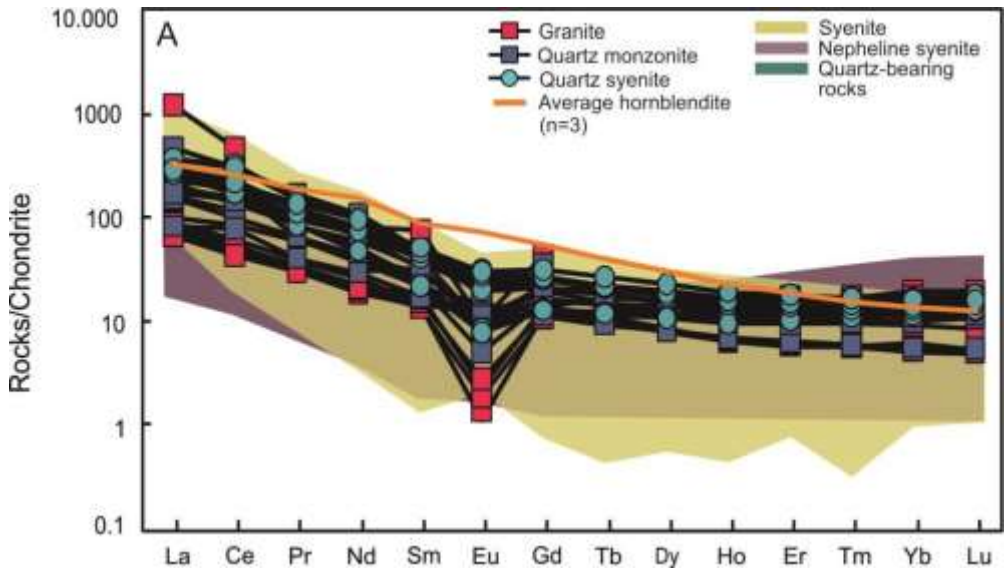

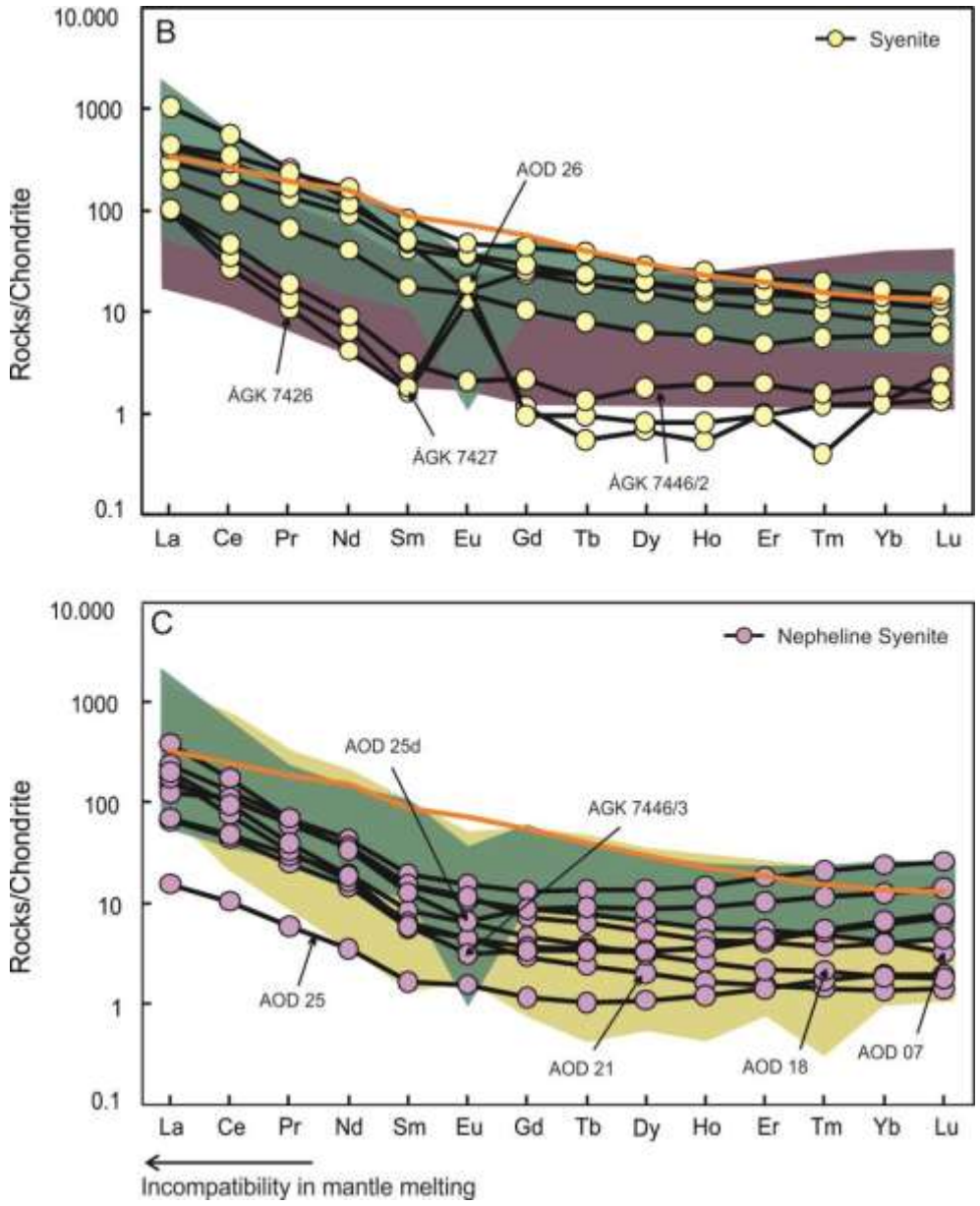

Figure 30. Chondrite-normalised REE diagrams for the (A) silica-oversaturated rocks (B) syenites and (C) nepheline syenites from the Ditrău Alkaline Massif. Normalizing values are from Sun and McDonough (1989).

The rare earth element patterns of granites are presented separately as well (Fig. 31). In Fig. 31 two different granite patterns can be distinguished. Closely uniform LREE-enrichments ($(La/Sm)_N$ = 3.93-5.68) and pronounced Eu-anomalies (Eu/Eu* = 0.1-0.2) are defined by granites with high silica contents, whereas the silica-poorer ones are mainly characterised by much higher LREE ($(La/Sm)_N$ = 4.8-15.8) with negative Eu-anomaly (Eu/Eu* = 0.2-0.5). Their increasing $(La/Sm)_N$ values associate with decreasing Eu/Eu*.

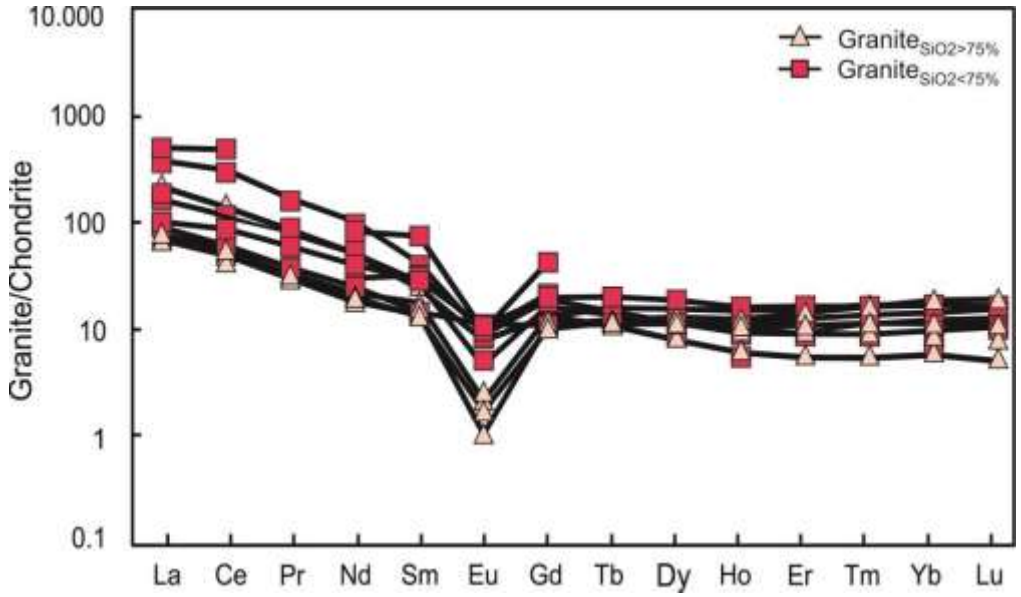

Figure 31. Chondrite-normalised REE diagrams for granites from the Ditrău Alkaline Massif. Normalizing values are from Sun and McDonough (1989). Granites with the incomplete REE data are the Hungarian samples.

The nepheline syenites and syenites show distinct patterns on the chondrite-normalised REE diagrams compared to those of the silica-oversaturated rocks (Fig. 30B, C). There are syenites (ÁGK 7426, ÁGK 7427) with low REE concentrations and pronounced positive Eu-anomaly (Eu/Eu* = 9.2-14.2) or with similarly low REE contents without any anomaly (ÁGK 7446/2) (Fig. 30B). These syenites also show strong depletion in MREEs. AOD 26 is the only sample with low Eu/Eu* = 0.5, the highest LREE concentrations together with MREE depletion. The rest of the samples are characterised by smooth patterns with moderately elevated LREE ($(La/Sm)_N$ = 5.5-11.3) and lack of any Eu-anomaly. In the case of the nepheline syenites, most of the rocks have upward convex REE patterns due to their strong depletion in the MREEs (Fig. 30C). Out of these, samples AOD 25d and ÁGK 7446/3 are the only ones with slight negative Eu-anomaly (Eu/Eu* = 0.6 and 0.70). Sample AOD 25 has a similar pattern but is distinguished because of its much lower normalised LREE and MREE concentrations and small positive Eu-anomaly (Eu/Eu* = 1.12). The only nepheline syenites that do not show upward convex patterns are AOD 18 and AOD 07. Sample AOD 21 is characterised by similar Eu-anomaly (Eu/Eu* = 1.12) but somewhat more elevated LREE concentrations.

Table 6. Whole-rock rare earth element compositions of the studied rocks from the Ditrău Alkaline Massif

Rock type	**Granite**											**Quartz monzonite**								
Sample	AOD 02	AOD 04	AOD 11	AOD 12	ÁGK 6835	ÁGK 7459	ÁGK 6847	ÁGK 6856	ÁGK 6842	ÁGK 7425/A	ÁGK 7458	AOD 03	AOD 13	AOD 24	AOD 28	AOD 32	ÁGK 6839	ÁGK 6838/A	ÁGK 7460	ÁGK 6726
ppm																				
La	16.3	86.2	23.9	17.4	37.8	30.8	18.6	112	21.4	49.5	16.0	108	53.04	45.7	36.2	19.7	60.2	68.9	41.3	55.1
Ce	30.4	182	53.2	32.3	70.6	6.00	34.2	28.0	37.7	83.9	26.5	182	124	92.8	61.6	47.9	122	141	90.2	113
Pr	2.91	15.5	5.71	3.23	NA	6.00	3.15	NA	3.66	8.04	2.88	15.9	6.03	9.18	6.28	3.87	NA	11.5	7.95	9.99
Nd	8.84	47.3	19.2	10.5	14.5	19.3	9.62	38.5	12.1	24.3	10.0	50.1	17.6	32.9	20.6	13.9	25.5	37.6	28.5	31.9
Sm	2.22	6.51	4.52	2.85	5.10	3.50	2.14	11.5	2.33	3.86	2.54	7.52	3.44	6.27	3.26	2.71	7.60	5.97	5.37	5.07
Eu	0.07	0.55	0.66	0.14	0.60	0.23	0.11	0.60	0.69	0.49	0.17	1.19	0.30	1.48	0.87	0.69	1.05	1.15	1.49	0.51
Tb	0.49	0.58	0.79	0.63	4.60	2.77	0.47	8.90	0.45	2.87	0.47	0.84	0.57	0.85	0.39	0.36	7.30	0.71	4.50	0.54
Gd	2.42	4.09	4.28	2.87	NA	0.43	2.23	NA	2.39	0.43	2.57	5.56	3.21	5.37	2.55	2.40	NA	4.51	0.70	3.52
Dy	3.49	3.08	5.00	4.16	2.30	2.49	3.08	3.40	3.08	2.17	3.02	4.92	3.55	5.10	2.08	2.11	3.50	3.96	3.91	3.03
Ho	0.75	0.56	0.96	0.89	NA	0.24	0.65	NA	0.67	0.37	0.58	0.91	0.67	0.97	0.38	0.40	NA	0.77	0.70	0.58
Er	2.51	1.61	2.87	2.72	NA	0.24	1.92	NA	2.21	0.98	1.69	2.57	1.98	2.73	1.03	1.09	0.00	2.07	1.87	1.62
Tm	0.44	0.25	0.44	0.45	NA	0.24	0.31	NA	0.37	0.15	0.25	0.39	0.30	0.41	0.15	0.16	0.00	0.32	3.91	0.26
Yb	3.34	1.77	3.02	3.06	1.30	1.75	2.05	2.10	2.58	1.07	1.58	2.58	2.06	2.62	0.89	0.98	1.70	1.95	1.94	1.71
Lu	0.51	0.29	0.44	0.43	NA	0.27	0.30	NA	0.42	0.14	0.22	0.39	0.31	0.38	0.13	0.14	NA	0.31	0.30	0.28
Eu/Eu*	0.09	0.33	0.46	0.15	0.38	0.23	0.16	0.18	0.89	0.45	0.20	0.56	0.28	0.78	0.92	0.83	0.43	0.67	0.93	0.37
$(La/Sm)_N$	4.74	8.55	3.41	3.93	4.78	5.68	5.61	6.32	5.93	8.28	4.07	9.29	9.96	4.71	7.17	4.70	5.11	7.44	4.96	7.01
$(Gd/Lu)_N$	0.59	1.77	1.20	0.82	0.00	1.27	0.92	0.00	0.71	2.53	1.46	1.76	1.27	1.73	2.45	2.06	0.00	1.79	1.85	1.58

$Eu/Eu^* = Eu_N / \sqrt{(Sm)_N * (Gd)_N}$
NA - not analysed

Table 6. (Continued)

Rock type	Quartz syenite							Syenite								Nepheline syenite				
Sample	AOD 01	AOD 09	AOD 10	AOD 15	AOD 22	AOD 30	AOD 31	AOD 05	AOD 26	ÁGK 7404	ÁGK 7420/2	ÁGK 7426	ÁGK 7449	ÁGK 7427	ÁGK 7446/2	AOD 06	AOD 07	AOD 20	AOD 21	AOD 25
ppm																				
La	65.4	63.9	82.8	62.7	62.2	88.3	69.0	69.6	244	95.4	47.1	22.7	104	23.7	23.9	56.5	37.4	30.6	16.0	3.73
Ce	104	125	199	104	104	185	131	129	335	177	71.6	16.4	207	20.9	28.2	82.9	67.4	68.6	28.1	6.51
Pr	8.04	11.7	14.1	8.00	10.4	14.2	12.9	12.7	24.2	16.2	6.23	1.01	22.1	1.29	1.79	6.83	5.90	5.95	2.43	0.56
Nd	22.5	38.8	44.4	22.5	35.7	45.2	44.2	42.3	60.3	52.1	18.8	1.90	75.9	3.04	4.20	20.1	16.9	17.2	6.90	1.67
Sm	3.34	6.65	7.23	3.40	6.46	7.06	7.90	6.32	7.20	7.70	2.68	0.25	12.2	0.27	0.47	3.02	2.28	2.36	0.87	0.26
Eu	0.51	1.49	1.18	0.47	1.88	1.65	1.78	1.99	0.93	2.11	0.87	0.74	2.74	1.06	0.12	0.91	0.63	0.68	0.26	0.09
Tb	0.47	0.80	0.85	0.45	0.80	0.83	1.01	0.70	0.85	0.87	2.13	0.24	8.92	0.04	0.44	0.51	0.29	0.24	0.09	0.04
Gd	2.78	5.27	5.43	2.70	5.26	5.50	6.53	4.80	5.12	5.94	0.29	0.02	1.43	0.19	0.05	2.77	1.82	1.52	0.61	0.24
Dy	2.97	4.79	4.94	2.77	4.51	4.81	5.87	3.90	4.80	4.99	1.57	0.17	7.05	0.20	0.45	3.53	1.70	1.35	0.52	0.28
Ho	0.62	0.92	0.97	0.56	0.83	0.90	1.09	0.69	0.90	0.95	0.33	0.03	1.40	0.05	0.11	0.85	0.33	0.24	0.09	0.07
Er	1.93	2.60	2.81	1.74	2.34	2.54	3.01	1.81	2.43	2.60	0.79	0.16	3.47	0.16	0.32	3.05	0.91	0.69	0.26	0.23
Tm	0.32	0.39	0.43	0.28	0.34	0.38	0.43	0.24	0.35	0.39	0.14	0.01	0.49	0.03	0.04	0.55	0.13	0.10	0.04	0.04
Yb	2.31	2.59	2.93	2.03	2.21	2.47	2.83	1.39	2.03	2.38	0.97	0.22	2.76	0.21	0.31	4.15	0.71	0.68	0.23	0.33
Lu	0.37	0.41	0.46	0.33	0.33	0.38	0.41	0.18	0.28	0.33	0.15	0.06	0.37	0.03	0.04	0.67	0.08	0.11	0.04	0.05
Eu/Eu*	0.52	0.77	0.58	0.47	0.99	0.81	0.76	1.10	0.47	0.95	1.11	9.24	0.80	14.2	0.81	0.97	0.94	1.09	1.11	1.12
$(La/Sm)_N$	12.6	6.20	7.39	11.9	6.21	8.07	5.64	7.11	21.8	8.00	11.3	58.6	5.49	56.1	32.8	12.1	10.6	8.36	11.9	9.45
$(Gd/Lu)_N$	0.92	1.60	1.45	1.02	1.95	1.81	1.95	3.26	2.28	2.24	1.76	0.49	2.98	0.70	1.36	0.51	2.70	1.66	2.09	0.60

Table 6. (Continued)

Rock type	Nepheline syenite				Diorite			Hornblendite						Country rock			
Sample	AOD 25d	AOD 18	ÁGK 6769	ÁGK 7446/3	AOD 08	ÁGK 7502	ÁGK 6723	AOD 29	ÁGK 7434	ÁGK 7428	ÁGK 7437	ÁGK 7436	ÁGK 7451	AOD 16	AOD 17	AOD 23	AOD 27
ppm																	
La	94.4	16.9	43.0	49.2	108	69.1	61.8	77.1	72.4	86.4	108	53.2	90.3	2.80	65.0	21.3	19.6
Ce	109	30.0	47.2	58.6	219	125	118	148	143	181	195	113	198	18.9	141	48.5	40.4
Pr	6.81	2.88	3.19	3.81	20.2	12.1	12.7	16.2	15.7	22.1	NA	NA	NA	0.86	13.9	4.99	4.50
Nd	15.9	9.08	7.89	8.72	67.5	41.5	49.5	63.5	61.5	94.8	84.4	51.5	109	3.47	50.8	18.5	16.7
Sm	1.97	1.31	0.98	0.92	10.1	6.46	8.98	11.5	11.2	17.8	NA	NA	NA	1.36	9.16	3.82	3.11
Eu	0.39	0.38	0.26	0.18	3.25	2.11	2.84	3.60	3.52	5.43	NA	NA	NA	0.14	1.67	0.34	0.58
Tb	1.82	0.14	0.13	0.13	1.15	0.73	1.03	1.30	1.27	1.90	NA	NA	NA	0.58	0.97	0.61	0.37
Gd	0.34	0.96	0.77	0.70	8.06	5.15	7.50	9.78	9.41	15.0	NA	NA	NA	2.49	6.90	3.81	2.52
Dy	2.25	0.81	0.87	0.85	6.22	3.99	5.31	7.01	6.68	9.60	NA	NA	NA	4.44	5.55	3.86	2.16
Ho	0.51	0.15	0.21	0.21	1.09	0.72	0.94	1.16	1.17	1.61	NA	NA	NA	0.97	1.03	0.77	0.39
Er	1.72	0.37	0.73	0.74	2.76	1.90	2.30	2.84	2.93	3.74	NA	NA	NA	3.05	2.88	2.27	1.13
Tm	0.30	0.06	0.13	0.14	0.36	0.26	0.29	0.36	0.38	0.44	NA	NA	NA	0.47	0.42	0.34	0.16
Yb	2.18	0.32	1.07	1.14	2.09	1.61	1.73	2.16	2.29	2.54	NA	NA	NA	3.07	2.72	2.16	1.06
Lu	0.36	0.05	0.18	0.20	0.27	0.24	0.25	0.30	0.34	0.36	NA	NA	NA	0.48	0.45	0.34	0.17
Eu/Eu*	0.63	1.03	0.91	0.70	1.10	1.12	1.06	1.04	1.05	1.02	NA	NA	NA	0.23	0.64	0.27	0.63
$(La/Sm)_N$	31.0	8.32	28.3	34.7	6.91	6.91	4.45	4.34	4.18	3.13	NA	NA	NA	1.33	4.59	3.60	4.08
$(Gd/Lu)_N$	0.62	2.58	0.52	0.43	3.64	2.66	3.68	4.04	3.44	5.16	NA	NA	NA	0.64	1.91	1.40	1.85

6.6. Multi element diagrams

The trace element distributions of the examined rocks are displayed in Fig. 32. Trace elements are normalised to the composition of primitive mantle from Sun and McDonough (1989). For the sake of clarity, the incompatible element patterns for silica-oversaturated, saturated and undersaturated rocks are presented separately. Quartz-bearing rocks show significant negative Ba-, Sr-, Ti-anomalies and strong increases in Rb, Th, U, Nb and Zr (Fig. 32A). The granites display the widest range of normalised element concentrations, whereas quartz syenites have the smallest variation. The size of negative anomalies of these elements in quartz monzonites are characteristically between that of the granites and quartz syenites (Fig 32A).

Unlike the silica-oversaturated rocks the syenites and nepheline syenites show highly variable patterns. AOD 26 is the only syenite that has both negative Ba and Sr anomalies, whereas ÁGK 7446/2 displays only low Ba_N (Fig. 32B). The latter also has unusually low Zr concentration (Zr_N = 0.8) and significantly enriched in Y_N = 7.9. Two samples (ÁGK 7427 and ÁGK 7426) differ from every other syenites because of their lower incompatible trace element contents. They are also the only syenite samples with negative Nb, Y and positive Sr, K anomalies (Nb_N = 20; Y_N < 0.3; Sr_N < 15). Apart from these ones all syenites are characterised by high normalised Nb, Zr and Y or low Ti concentrations.

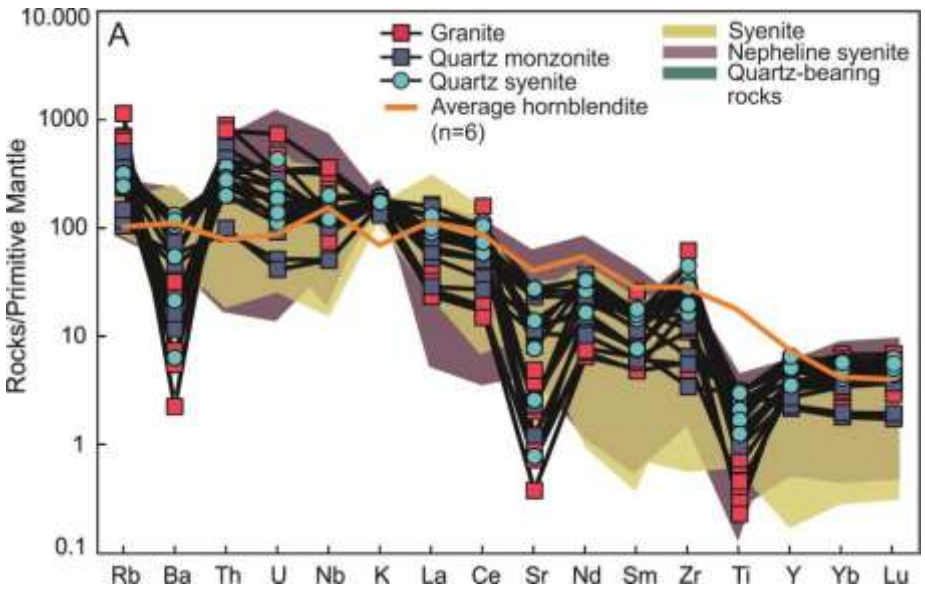

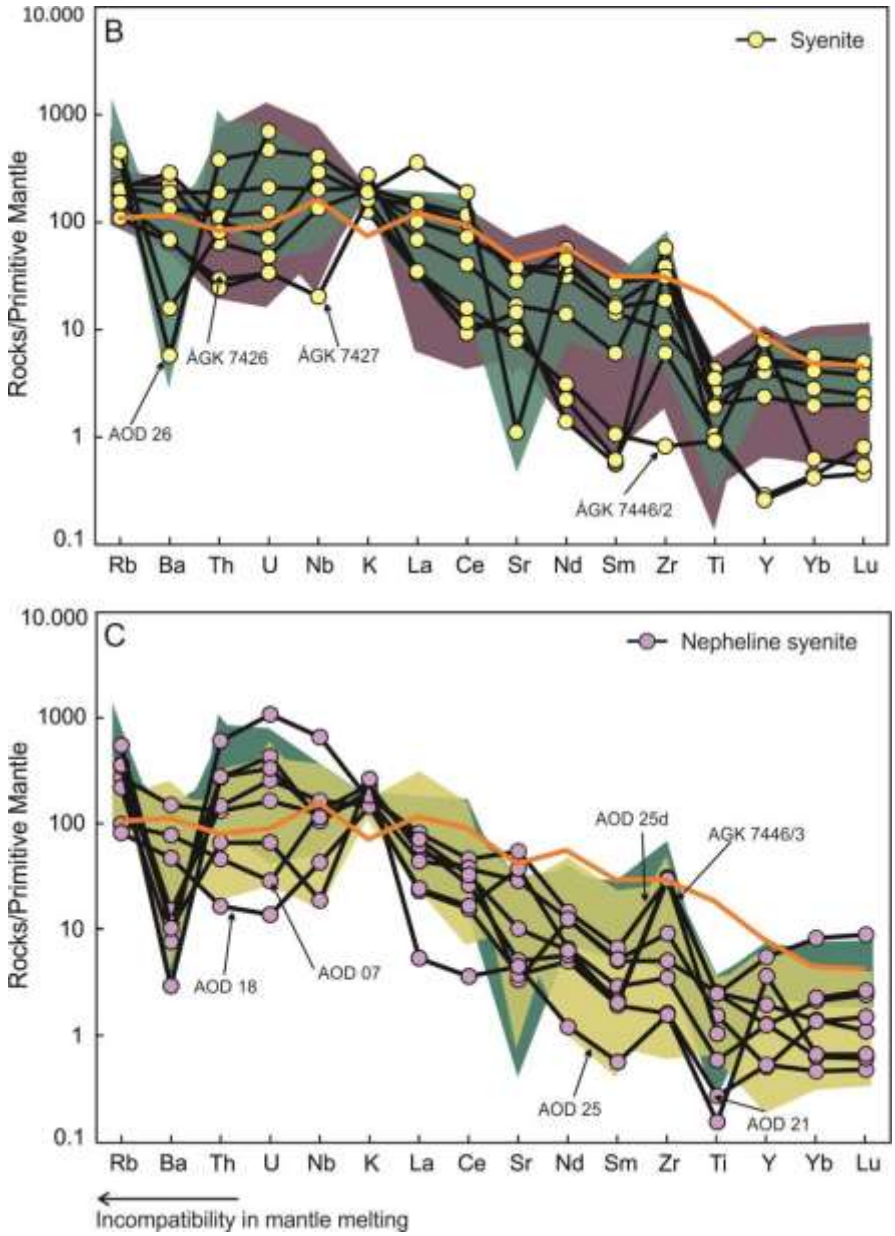

Figure 32. Primitive mantle-normalised multi-elements spider diagrams for the (A) silica-oversaturated rocks (B) syenites and (C) nepheline syenites of the Ditrău Alkaline Massif. Normalizing values are from Sun and McDonough (1989).

Nepheline syenites collectively show elevated Nb contents or strong positive Zr and negative Ti anomalies (Fig. 32C). The significant low $Ba_N < 15$ concentrations in most of the samples are associated with elevated Th, U contents and lower normalised Sr < 10.3 ppm. In contrast with these AOD 07 and AOD 18 do not show any Ba anomalies, in addition they are characterised by much lower Th and U and elevated $Sr_N > 29$. Nepheline syenite with the lowest Nb_N content of 19 is AOD 25. This sample also differs from the others due to its much lower Ti contents together with AOD 21 (Ti_N = 0.1-0.3). AOD 25d and ÁGK 7446/3 are characterised by the closely the same patterns with very high U, Th, Zr and very low Ti concentrations (Fig. 32C).

Chapter 7: Isotope results

In this chapter oxygen and radiogen isotope (Sr, Nd and Pb) data are presented. The main aim of the isotopic study is to determine the source characteristics of the studied rocks and to assess any processes that could cause changes in the magma composition (e.g. crustal assimilation or magma mixing). In addition, oxygen isotope data also will be used to ascertain the O-isotope equilibrium between the coexisting minerals in order to identify the influences of subsolidus alteration processes on the chemical and isotope compositions of the studied rocks.

7.1 Oxygen isotope geochemistry

Oxygen isotope measurements were made on mineral separates from the studied Ditrău rocks and whole rock O-isotope measurements were taken on wall-rock samples that will be used in Section 8.3.2. Quartz was analysed from every silica-oversaturated rocks and zircons from every examined rock types. O-isotope composition of titanite and monazite were measured from samples where these minerals were available. Feldspars were analysed from mostly all samples, or amphibole and pyroxene were measured from the less altered rocks in which those were presented. Quartz grains were prepared for the measurements from 24 samples, feldspars from 32, zircon from 9 samples, monazite and titanite from 11 and amphibole/pyroxene from 16 samples.

7.1.1 Oxygen isotope composition of quartz

Oxygen isotope compositions of the analysed minerals are presented in Table 7. The rock type with the narrowest $\delta^{18}O$ quartz values is the quartz monzonites (10.2-11.3‰). Quartz monzonites have the highest average value of quartz $\delta^{18}O$ as well (10.7‰; n = 7). Quartz syenites have a wider range of quartz $\delta^{18}O$ values from 9.5 to 11.6‰ than that of the quartz monzonites and slightly lower average value (10.4‰; n = 7). The Ditrău granites have the widest range of quartz $\delta^{18}O$ = 9.7-13.0‰ with an average value of 10.7‰ (n = 10; Fig. 33).

The $\delta^{18}O$ values of quartz from granites in other complexes worldwide (Bushveld complex in South Africa, Gross Spitzkoppe complex in Namibia, Podlesi Granite System in Czech Republic and Katharine pluton in Egypt) are also presented in Fig. 33 for comparison.

Granites from these igneous complexes have been singled out for comparison because of their A-type character similarly to Ditrău granites. This will be discussed in connection with the possible sources of Ditrău felsic rocks in Section 8.3.2. The average quartz $\delta^{18}O$ value for Nebo Granites in the Bushveld Complex (South Africa) is 8.0 ± 0.8‰ (Fourie and Harris, 2011), whereas in the case of granites from the Katharine pluton (area of Gebel Mussa, Egypt) it is from 8.0 to 8.5‰ (Katzir et al., 2007b). These $\delta^{18}O$ values are lower than that of the quartz in the Ditrău granites. The oxygen isotope composition of quartz from granites in the Gross Spitzkoppe complex (Damaraland complexes, Namibia) is 11.8-12.6‰ (Trumbull et al., 2004) and 9.7-11.6‰ in Podlesi Granite System (Krušnéhory Mts., Czech Republic; Žak et al., 2005). These values are very similar to the $\delta^{18}O$ values of quartz from the studied granites.

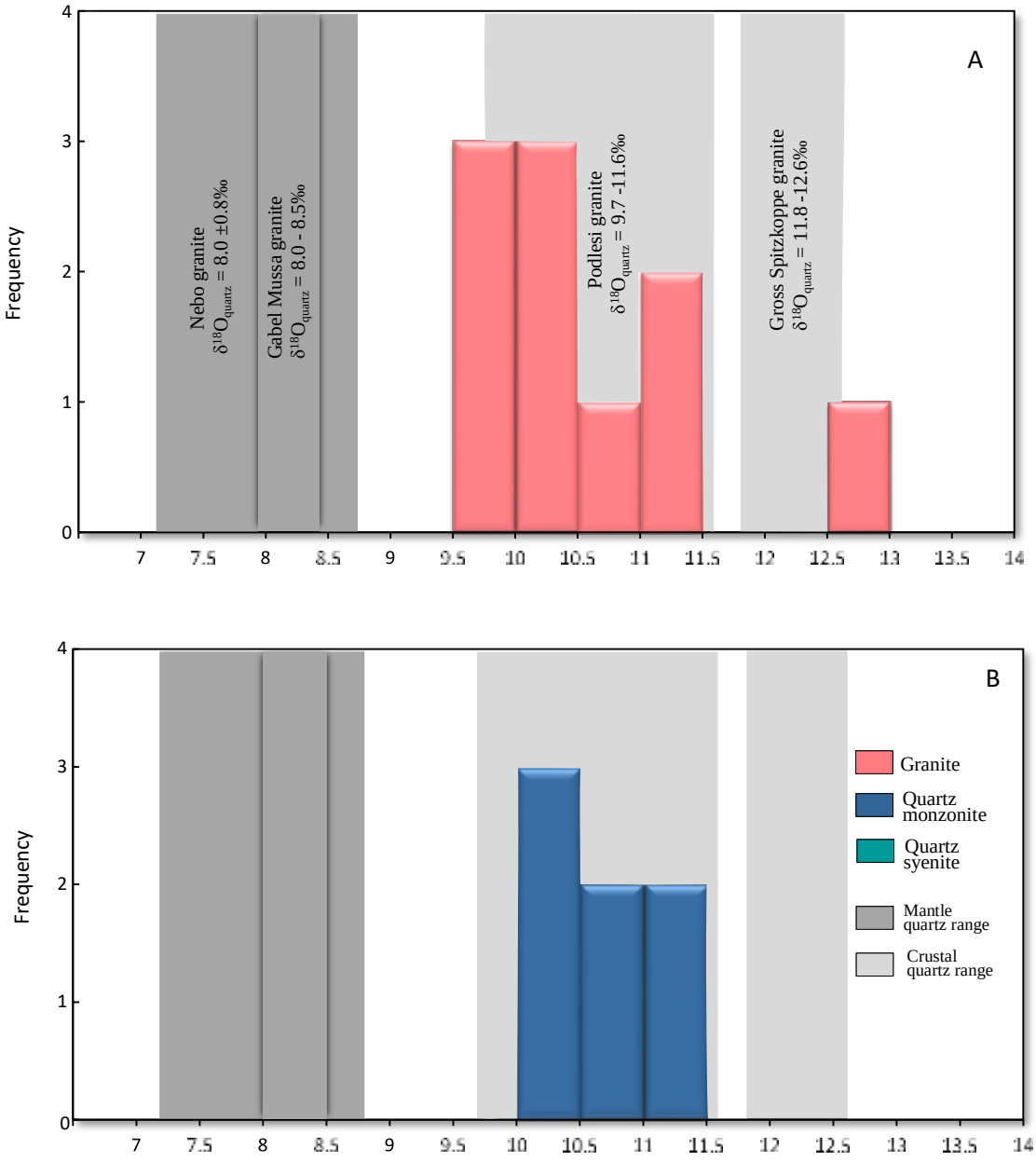

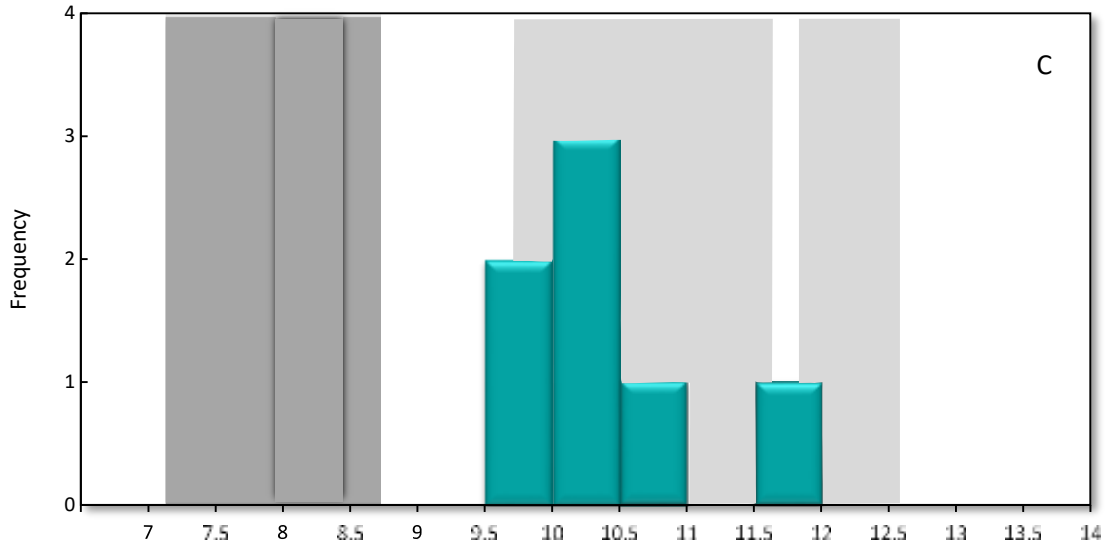

Figure 33. Histograms of quartz $\delta^{18}O$ values for (A) granites, (B) quartz monzonites and (C) quartz syenites from the Ditrău Alkaline Massif. The $\delta^{18}O$ values of granites with dominantly mantle-origin are from Fourie and Harris (2011) and Katzir et al. (2007). The O-isotope values of crustally derived granites were obtained by Trumbull et al. (2004) and Žak et al. (2005).

7.1.2 Oxygen isotope compositions of mafic minerals and feldspars

Oxygen isotope data for amphiboles from syenites, quartz syenites and quartz monzonites and pyroxene from nepheline syenites are presented in Table 7. The $\delta^{18}O$ values of amphibole in syenite range from 2.2 to 7.0‰, whereas quartz syenites and monzonites have higher values and much more restricted ranges from 5.3 to 7.2‰. Amphibole $\delta^{18}O$ values from diorites and hornblendites are characterised by nearly the same O-isotope compositions. The $\delta^{18}O$ value of diorite and hornblendite is $\delta^{18}O$ = 5.1‰.

The lowest $\delta^{18}O$ values of feldspars are found in syenites from 7.6 to 10.5‰ with an average value of 8.6‰ (n = 4). The highest average feldspar value for feldspar is shown by quartz syenites with 9.8‰ (n = 7), whereas those are from granites and quartz monzonites have similar average oxygen isotope compositions of 9.3‰ for granites (n = 9) and 9.4‰ for quartz monzonite (n = 7).

Table 7. Oxygen isotope composition of minerals from the studied rocks of Ditrău Alkaline Massif. Mineral abbreviations are after Whitney and Evans (2010): Fsp - feldspar, Qz - quartz, Zrn - zircon, Mnz - monazite, Amp - amphibol, Px - pyroxene, Ttn - titanite and WR - whole rock.

Samples	Measured $\delta^{18}O$ values (‰)						
	Fsp	Qz	Zrn	Mnz	Amp/Px	Ttn	WR
Granite							
AOD 02		9.90					
AOD 04	9.67	9.91					
AOD 11	10.06	10.14					
AOD 12	9.45	9.70					
ÁGK 6847	9.16	10.15	5.98				
ÁGK 6842	10.77	12.92					
ÁGK 6835	8.72	11.35	6.69				
ÁGK 7459	8.47	10.49					
ÁGK 7458	8.42	11.33	7.22				
ÁGK 7425/A	9.33	10.93					
Quartz-monzonite							
AOD 03	9.14	10.43			6.75		
AOD 13	9.78	10.21					
AOD 24	10.3	10.68			6.43		
AOD 28	8.86	10.81					
AOD 32	9.86	11.32					
ÁGK 6848/A	8.74	10.47	6.14				
ÁGK 6726	9.03	11.06		4.58			
ÁGK 7460			6.31				
Quartz-syenite							
AOD 01	9.41	10.00			5.26		
AOD 09	9.15	10.81			6.12		
AOD 10	9.02	10.33					
AOD 15	8.76	9.53			6.30		
AOD 22	10.01	10.25					
AOD 30	10.75	10.43			7.11		
AOD 31	11.30	11.56			7.34		
Syenite							
AOD 05	8.10				5.58	3.97	
AOD 26	7.77				7.02		
ÁGK 7404				3.68			
ÁGK 7427			6.26		2.18	7.17	
ÁGK 7426			6.01			5.50	
ÁGK 7446/2	10.47						
ÁGK 7449	7.62			4.21			
ÁGK 7420/2				4.28			
Nepheline Syenite							
AOD 06	7.91					4.59	
AOD 07						3.60	
AOD 20					3.77		
AOD 25					4.72		
ÁGK 6769			5.11		4.00		
ÁGK 7446/3			5.26		4.41	4.92	
Diorite							
AOD 08	6.93						
ÁGK 7502				4.62	5.13		
ÁGK 6723	7.80			4.75			
Hornblendite							
ÁGK 7451	8.16						
ÁGK 7437	8.72				5.14		
Country rock							
AOD 16							13.60
AOD 17							4.68
AOD 23							16.00
AOD 27							12.30

All mineral analyses were made by laser fluorination except feldspar oxygen isotope analyses that were made by conventional fluorination method.

7.1.3 Oxygen isotope composition of accessory minerals

The $\delta^{18}O$ values of analysed zircons from the granites range from 6.0 to 7.2‰ (Fig 34A). These values also represent the highest and the lowest $\delta^{18}O$ values out of the analysed zircons in silica-oversaturated and saturated rocks. Whereas zircon in quartz monzonites and syenites show very similar $\delta^{18}O$ values (Fig 34A and B), zircons in the nepheline syenites have the lowest $\delta^{18}O$ values between 5.1 and 5.3‰ (Fig 34C).

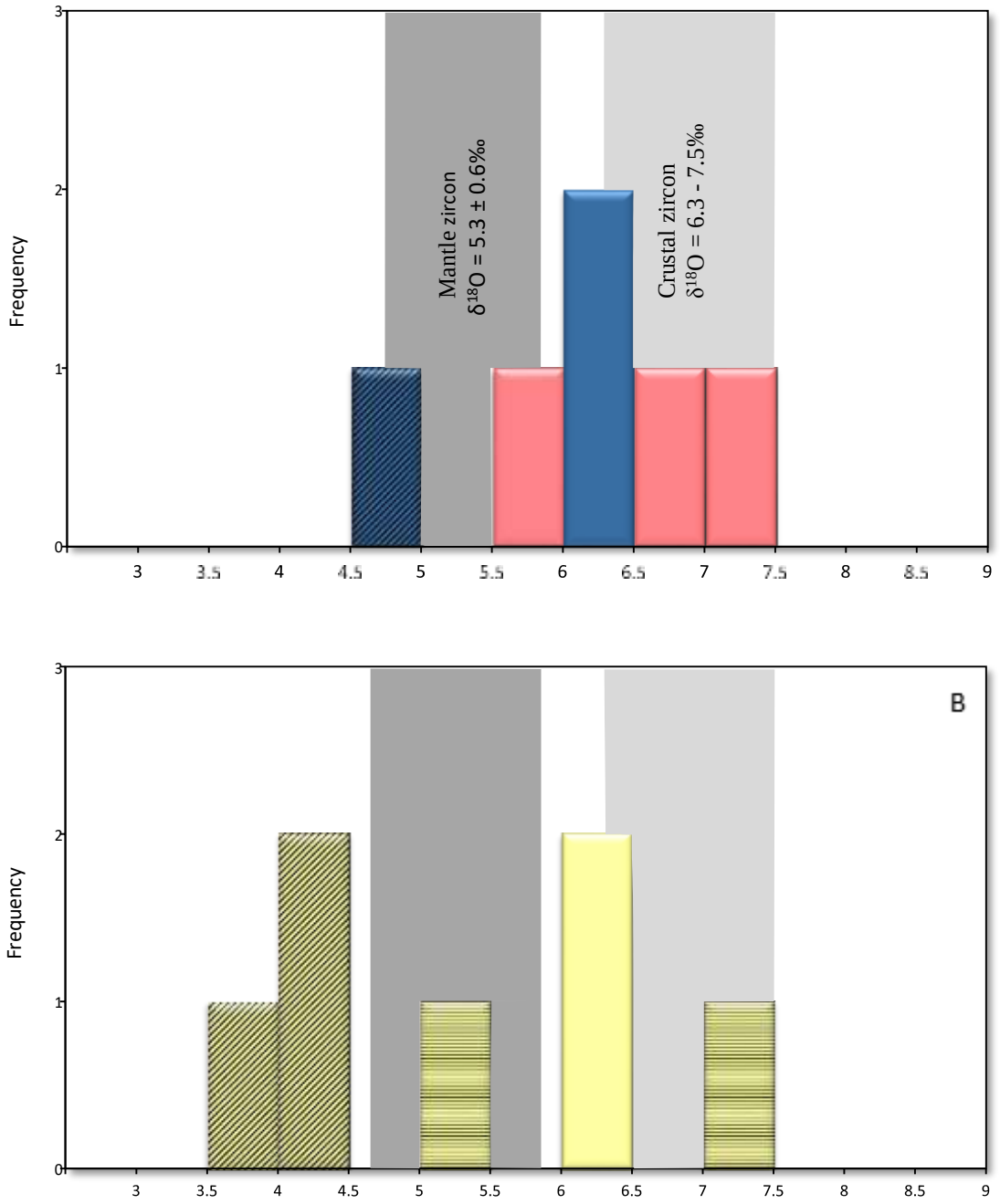

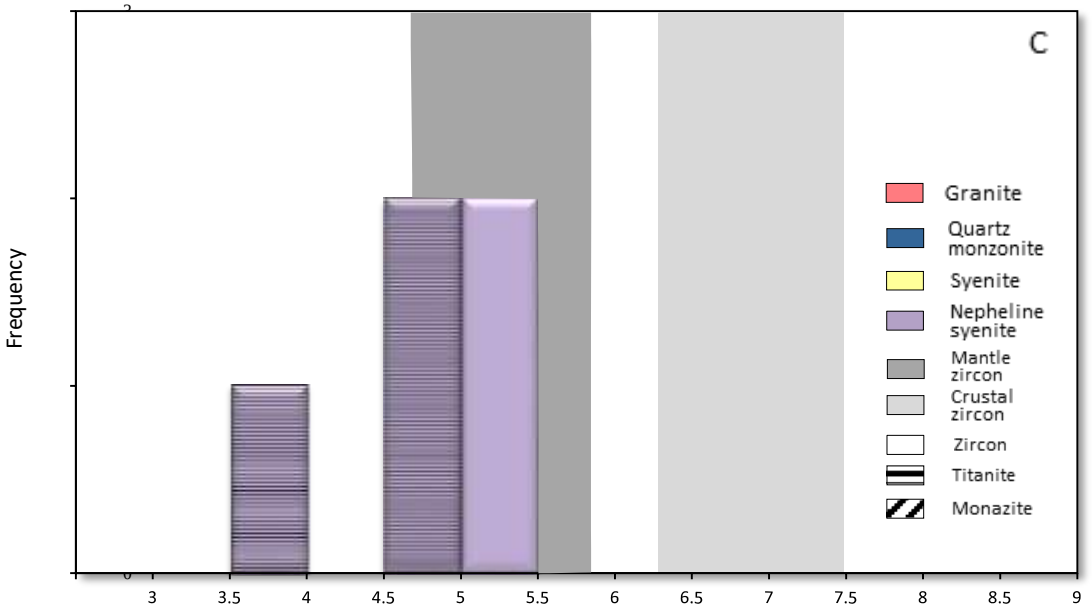

Figure 34. Histograms of $\delta^{18}O$ values of accessory minerals from (A) silica-oversaturated rocks, (B) syenites and (C) nepheline syenites from the Ditrău Alkaline Massif. The range of mantle zircons is obtained from Valley et al. (1998) and the crustal zircon range is from Valley et al. (2005). The equivalent fields for mantle monazite and titanite are not shown as these minerals are less reliable in terms of their resistance to subsolidus alterations.

According to Valley et al. (1998) igneous zircons in high temperature O-isotope equilibrium with magmas that are from the mantle have average $\delta^{18}O = 5.3\pm0.3‰$. The range of mantle-derived zircons is also presented in Fig. 34, as well as that of the zircons from felsic magmas derived by melting of sediments (Valley et al., 2005). The $\delta^{18}O$ values of monazite and titanite are also presented in Fig. 34. Monazite $\delta^{18}O$ values are quite uniform from quartz monzonites and syenites (Fig 34A and B), however titanites have much higher and more scattered $\delta^{18}O$ values in syenites (3.97-7.17‰) than in nepheline syenites with $\delta^{18}O < 4.6‰$ values (Fig. 34C).

7.2. Radiogenic isotopes

A total of 29 samples were analysed for Rb-Sr and Sm-Nd, and 16 samples for Pb isotopes. The samples were chosen for radiogenic isotope analysis to encompass the wide range of trace element contents and oxygen isotope data of the studied rocks.

Measured isotope ratios are given in Table 8 together with the element concentrations, calculated initial ratios and epsilon values for Sr and Nd. The $^{87}Rb/^{86}Sr$ and $^{147}Sm/^{144}Nd$ ratios for the age-corrections were calculated on the basis of the Equations 9 and 10:

$$\frac{^{87}\mathrm{Rb}}{^{86}\mathrm{Sr}} = \left[2.6939 + 0.2832 \text{ x} \frac{^{87}\mathrm{Sr}}{^{86}\mathrm{Sr}}\right] \text{x} \left(\frac{\mathrm{Rb}}{\mathrm{Sr}}\right)$$

Equation 9.

$$\frac{^{147}\mathrm{Sm}}{^{144}\mathrm{Nd}} = \left[0.53151 + 0.14252 \text{ x} \frac{^{143}\mathrm{Nd}}{^{144}\mathrm{Nd}}\right] \text{x} \left(\frac{\mathrm{Sm}}{\mathrm{Nd}}\right)$$

Equation 10.

where Rb, Sr, Sm, Nd are the measured concentrations (ppm) and $^{87}Sr/^{86}Sr$ and $^{143}Nd/^{144}Nd$ are the measured ratios in the studied samples. The rest are constants that were obtained from Faure (1986).

The final equations of age-correction to calculate the initial Sr and Nd isotope ratios are as follows:

$$\left(\frac{^{87}\mathrm{Sr}}{^{86}\mathrm{Sr}}\right)_{\mathrm{i}} = \left(\frac{^{87}\mathrm{Sr}}{^{86}\mathrm{Sr}}\right)_{\mathrm{m}} - \frac{^{87}\mathrm{Rb}}{^{86}\mathrm{Sr}}\left(e^{\lambda t} - 1\right)$$

Equation 11.

$$\left(\frac{^{143}\mathrm{Nd}}{^{144}\mathrm{Nd}}\right)_{\mathrm{i}} = \left(\frac{^{143}\mathrm{Nd}}{^{144}\mathrm{Nd}}\right)_{\mathrm{m}} - \frac{^{147}\mathrm{Sm}}{^{144}\mathrm{Nd}}\left(e^{\lambda t} - 1\right)$$

Equation 12.

where the subscripts i and m denote the initial and measured isotope ratios, λ is the decay contant of ^{87}Rb (1.42×10^{-11} y^{-1}) and ^{147}Sm (6.54×10^{-12} y^{-1}) or t is the estimated age of the rocks.

The initial epsilon Nd values were calculated using Equation 13:

$$\varepsilon\mathrm{Nd_i} = \left(\frac{\left(\frac{^{143}\mathrm{Nd}}{^{144}\mathrm{Nd}}\right)_{\mathrm{i}}}{\left(\frac{^{143}\mathrm{Nd}}{^{144}\mathrm{Nd}}\right)_{\mathrm{CHUR}} - \left(\frac{^{147}\mathrm{Sm}}{^{144}\mathrm{Nd}}\right)_{\mathrm{CHUR}} \text{x } (e^{\lambda t} - 1)} - 1 \right) \text{x } 1000$$

Equation 13.

where $(^{87}Sr/^{86}Sr)_{BE}$ is the $^{87}Sr/^{86}Sr$ ratio of the Bulk Earth (0.7047) at time t, $(^{87}Rb/^{86}Sr)_{BE}$ is the $^{87}Rb/^{86}Sr$ ratio of the Bulk Earth (0.0847) at time t, whereas $(^{143}Nd/^{144}Nd)_{CHUR}$ and $(^{147}Sm/^{144}Nd)_{CHUR}$ are the $^{143}Nd/^{144}Nd$ and $^{147}Sm/^{144}Nd$ ratios of the chondritic uniform reservoir (CHUR) at time t. Present day CHUR and Bulk Earth isotope values are from White (2007).

To age-correct the Pb isotope ratios the sum of the Pb isotope ratios and the percentage of each Pb isotope needs to be known:

$$\Sigma Pb = \frac{^{204}Pb}{^{204}Pb} + \left(\frac{^{206}Pb}{^{204}Pb}\right)_m + \left(\frac{^{207}Pb}{^{204}Pb}\right)_m + \left(\frac{^{208}Pb}{^{204}Pb}\right)_m$$

Equation 14.

$$\%^{204}Pb = \frac{100}{\Sigma Pb} x \frac{^{204}Pb}{^{204}Pb}$$

Equation 15.

$$\%^{206}Pb = \frac{100}{\Sigma Pb} x \left(\frac{^{206}Pb}{^{204}Pb}\right)_m$$

Equation 16.

$$\%^{207}Pb = \frac{100}{\Sigma Pb} x \left(\frac{^{207}Pb}{^{204}Pb}\right)_m$$

Equation 17.

$$\%^{208}Pb = \frac{100}{\Sigma Pb} x \left(\frac{^{208}Pb}{^{204}Pb}\right)_m$$

Equation 18.

where the subscript m denotes the measured Pb isotope ratios, ΣPb is the sum of Pb and the $\%^{204}Pb$, $\%^{206}Pb$, $\%^{207}Pb$, $\%^{208}Pb$ are the percentage of Pb isotopes.

The next stage in the Pb isotope age-correction is to calculate the atomic mass of Pb using the following equation:

$$Pb(amu) = \left(\frac{\%^{204}Pb}{100} x^{204}Pb\ (amu)\right) + \left(\frac{\%^{206}Pb}{100} x^{206}Pb\ (amu)\right) + \left(\frac{\%^{207}Pb}{100} x^{207}Pb\ (amu)\right) + \left(\frac{\%^{208}Pb}{100} x^{208}Pb\ (amu)\right)$$

Equation 19.

where the atomic mass of Pb is measured in atomic mass units (amu). The mass of the Pb isotopes are $^{204}Pb(amu) = 203.973028$, $^{206}Pb(amu) = 205.974449$, $^{207}Pb(amu) = 206.975880$, $^{208}Pb(amu) = 207.976636$ from de Laeter et al. (2003).

The next equations are used to calculate the $^{238}U/^{204}Pb$, $^{235}U/^{204}Pb$ and $^{232}Th/^{204}Pb$ ratios before the final step of the age-correction:

$$\frac{^{238}U}{^{204}Pb} = \frac{U}{Pb} x \frac{Pb(amu)}{U(amu)} x \frac{^{238}U(\%abundance)}{\%^{204}Pb}$$

Equation 20.

$$\frac{^{235}U}{^{204}Pb} = \frac{U}{Pb} x \frac{Pb(amu)}{U(amu)} x \frac{^{235}U(\%abundance)}{\%^{204}Pb}$$

Equation 21.

$$\frac{^{232}Th}{^{204}Pb} = \frac{Th}{Pb} x \frac{Pb(amu)}{Th(amu)} x \frac{^{232}Th(\%abundance)}{\%^{204}Pb}$$

Equation 22.

where U, Pb and Th are the measured concentrations of the elements in ppm, whereas the atomic mass of U(amu) and Th(amu) are 238.02891 and 232.03806 (Wieser (2006). Percentage abundances are ^{238}U = 99.2745, ^{235}U = 0.72, ^{232}Th = 100 (Rosman & Taylor (1998).

The final equations of age-correction to calculate the initial Sr and Nd isotope ratios are as follows:

$$\left(\frac{^{206}Pb}{^{204}Pb}\right)_i = \left(\frac{^{206}Pb}{^{204}Pb}\right)_m - \frac{^{238}U}{^{204}Pb}\left(e^{\lambda t} - 1\right)$$

Equation 23.

$$\left(\frac{^{207}Pb}{^{204}Pb}\right)_i = \left(\frac{^{207}Pb}{^{204}Pb}\right)_m - \frac{^{235}U}{^{204}Pb}\left(e^{\lambda t} - 1\right)$$

Equation 24.

$$\left(\frac{^{208}Pb}{^{204}Pb}\right)_i = \left(\frac{^{208}Pb}{^{204}Pb}\right)_m - \frac{^{232}Th}{^{204}Pb}\left(e^{\lambda t} - 1\right)$$

Equation 25.

where the subscripts i and m denote the initial and measured Pb isotope ratios, whereas λ are the decay constants for ^{238}U (1.55125 x 10^{-10} y^{-1}), ^{235}U (9.8485 x 10^{-10} y^{-1}), and ^{232}Th (4.9475 x $10^{-11}$$y^{-1}$) from Steiger and Jager (1977).

The Pb isotope age-correction calculations are from Ciborowski (1993).

7.2.1 Rb-Sr system

Rb and Sr concentrations in hornblendites and diorites are uniform, namely both of them have high Sr (844-3024 ppm) and low Rb (23-68 ppm) values. By contrast, the felsic rocks show high variability of Rb and Sr (Table 8). The increase of Rb in these samples is associated with a decrease in Sr contents. As a result, the felsic rocks also have a wide range of Rb/Sr. The most scattered Rb/Sr ratios are shown by granites (Rb/Sr = 2-89, n = 7) and syenites (Rb/Sr = 0.5-10, n = 4), whereas quartz monzonites and nepheline syenites demonstrate the lowest ratios with Rb/Sr = 0.2-4 (n = 4) and 0.1-2 (n = 4). The high Rb/Sr ratios in the rocks associate with high $^{87}Rb/^{86}Sr$ ratios. Granites and syenites are characterised by the highest $^{87}Rb/^{86}Sr$ = 6-277 and 0.5-29 (2σ, n = 7 and 4), whereas quartz monzonites and nepheline syenites display the lowest variation in $^{87}Rb/^{86}Sr$ with 0.7-11 and 0.2-6 (2σ, n = 4).

The Rb-Sr isochron for the studied samples based on the data presented in Table 8. Using the program Isoplot 4.1 (Ludwig, 2003) a line of best fit through the data was constructed that took the errors associated with each ratio ($^{87}Rb/^{86}Sr$, $^{87}Sr/^{86}Sr$) into account. As most of the felsic rocks have high Rb/Sr ratios and the samples had not been specifically selected for age-dating, the errors on $^{87}Rb/^{86}Sr$ ratios were calculated assuming the highest accepted analytical error for routine quadrupole ICP-MS analyses (2σ = 3%, relative) in order to improve the fit of the regression line. This means that the percent relative standard deviation (%RDS) of the measured trace element concentration data were adjusted using the highest accepted analytical error for ICP-MS analyses as final relative standard deviation FRSD = 3%. On account of the readjusted %RSD values on Rb and Sr, the fitting of the isochron was improved significantly as indicated by decreased Mean Square Weighted Deviation (MSWD) of the isochron from 2819 to 96 (not shown). The slope of this isochron yields initial $^{87}Sr/^{86}Sr$ ratio of 0.7056±0.0027 and age of 193.5±9.9 Ma in agreement with the calculated Rb-Sr isochron age of 201 Ma for the entire massif by Zincenco et al. (1994) and 200 Ma for the intrusion of ultramafic rocks by Popescu (1985). This age also matches to the lower K-Ar ages given by the mafic minerals from the Ditrău granites and nepheline syenites in Table 1 (218±8 - 196±7 Ma for granites; 216±8 - 182±7 Ma for nepheline syenites). Despite this good agreement, the high MSWD still reflects a significant scatter about the best-fit regression line that requires additional refinement. Considering only the silica- saturated and oversaturated rocks, by omitting nepheline syenites from the isochron calculations (due to the possibility of their different parental melt), further lowered the

MSWD to 42, while the initial $^{87}Sr/^{86}Sr$ ratio and the isochron age hardly changed. The whole rock Rb-Sr isotope data from all the rock types except nepheline syenites are shown on the isochron diagram (Fig. 35). The new initial $^{87}Sr/^{86}Sr$ ratio defined by the isochron of silica-saturated and oversaturated rocks from the DAM is 0.7053±0.0032 and the new estimated Rb-Sr isochron age for the Ditrău rocks is 194±10 Ma.

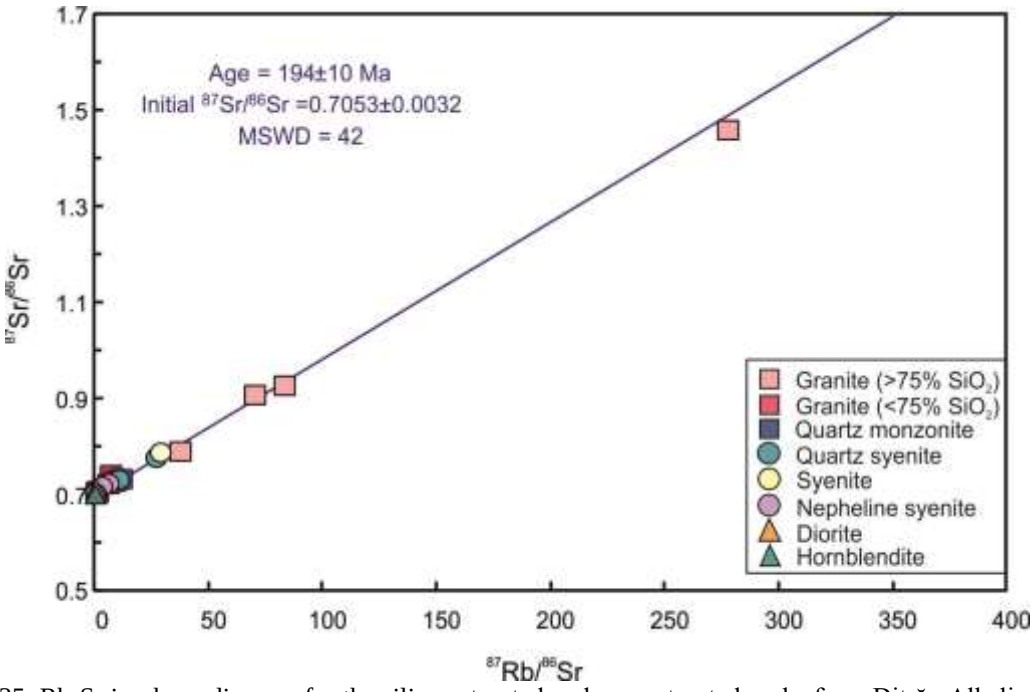

Figure 35. Rb-Sr isochron diagram for the silica-saturated and oversaturated rocks from Ditrău Alkaline Massif. Nepheline syenites are also presented on the isochron. The age, initial $^{87}Sr/^{86}Sr$ ratio and the MSWD were determined using Isoplot version 4.1 from Ludwig (2003)

However, as the latest K-Ar and Ar/Ar ages of Ditrău ultramafic-mafic rocks yield fairly congruent data (216.0±8.8 – 237.4±9.1 Ma by Pál-Molnár and Árva-Sós, 1995; 227.1±0.1 – 231.5±0.1 Ma by Dallmeyer et al., 1997), the above calculated isochron age is accepted only for silica-oversaturated and undersaturated rocks in this study. In addition, the only U-Pb age that was reported from the DAM was made on the zircon separates of syenites by Pană et al. (2000). Pană et al. (2000) obtained 230 +1.7/-1.2 Ma (MSWD = 1.7) for the Ditrău syenites that corresponds to the K-Ar and Ar/Ar ages of ultramafic-mafic rocks. For this reason, 230 Ma is preferred in the thesis for the age of hornblendites, diorites and syenites to calculate the initial radiogenic isotope compositions of their parental magma, whereas the 194±10 Ma isochron age was used during the age-correction of quartz-bearing Ditrău rocks and nepheline syenites. The calculated initial isotope ratios of the different rock types are presented in Table 8.

Based on the above ages, the $^{87}Sr/^{86}Sr_i$ ratios are the highest with the highest variation in granites (0.6888-0.7237) and nepheline syenites (0.7032-0.7109). Syenites have similar $^{87}Sr/^{86}Sr$ at 230 Ma (average of 0.7015, n = 4) to diorites and hornblendites which show range from 0.7028 to 0.7029. $^{87}Sr/^{86}Sr$ ratios for the wall rocks are 0.7214-0.7493 at 230 Ma.

7.2.2 Sm-Nd system

A similar isochron calculation was attempted for the studied rocks using the Sm-Nd isotope system (Fig. 36). Two populations can be identified on the Sm-Nd isochron diagram: a group with higher $^{143}Nd/^{144}Nd$ defined by hornblendites, diorites, syenites, and another group having lower $^{143}Nd/^{144}Nd$ ratios and composed of granites and quartz monzonites. Quartz syenites plot between the two groups. Whereas samples in the first group show positive correlation between the $^{143}Nd/^{144}Nd$ and $^{147}Sm/^{143}Nd$, granites and quartz monzonites define less clear correlation. Considering only granites with the higher Nd isotope values ($\varepsilon Nd_i > +2.8$, $^{143}Nd/^{144}Nd > 0.5126$) without the granite outlier (ÁGK 6842) and the quartz monzonite, positive correlation can be identified.

The slope of the best fit lines calculated by Isoplot give Sm-Nd isochron ages of 404±47 Ma (MSWD = 1.03) for the rocks in the first group and 271±46 Ma (MSWD = 2.2) for the granites ignoring the outlier (Fig. 36). The calculated initial $^{143}Nd/^{144}Nd$ ratios are 0.512495±0.000030 for the rocks in the first group and 0.512486±0.000039 for granites.

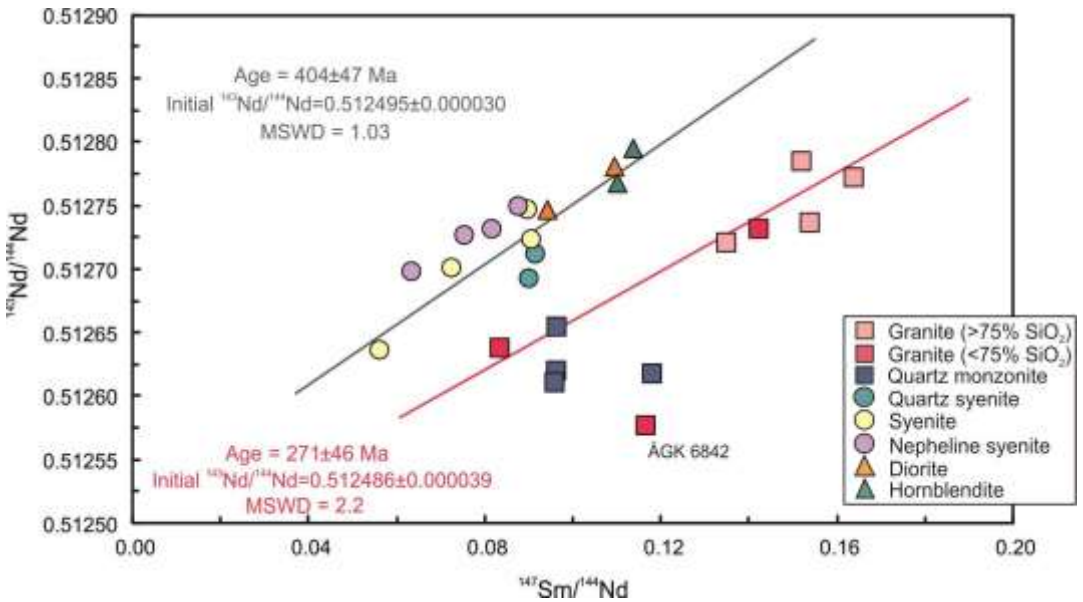

Figure 36. Sm-Nd isochron diagram for the studied rocks from Ditrău Alkaline Massif. Nepheline syenites, quartz syenites and quartz monzonites are also presented. The age, initial $^{143}Nd/^{144}Nd$ ratio and the MSWD were determined using Isoplot version 4.1 from Ludwig (2003)

Whereas in the Rb-Sr system the initial ratio is subjected to large errors because of the poor isochron, in the Sm-Nd system the error of the initial ratios is smaller as Sm/Nd does not vary significantly. But, although the calculated $^{143}Nd/^{144}Nd_i$ ratios of the original magma are closely the same, the Sm-Nd isochron ages cannot be accepted as those are significantly higher than the ages suggested by the Rb-Sr isochron and Ar-Ar and K-Ar ages as mentioned in the Rb-Sr system section. The significant age differences can originate from the Sm-Nd method as due to the young age of the rocks (~ 200-230 Ma) the precision of the method is not adequate because of the long half life of ^{147}Sm ($t_{1/2} = 1.06x10^{11}$ y).

In spite of the wide $^{87}Sr/^{86}Sr_i$ values of the Ditrău rocks due to the wide variation in Rb/Sr, the calculated initial $^{143}Nd/^{144}Nd$ ratios are very restricted ($^{143}Nd/^{144}Nd_i$ = 0.51264-0.51243), but still show significant variations correlating with different rock types (Fig. 37, Table 8). As differences in $^{143}Nd/^{144}Nd$ between the magmatic suites are strictly comparable if the studied rocks have the same age, DePaolo and Wasserburg (1976) introduced the epsilon notation (Equation 13.) that allows the comparison of samples with different ages by measuring the deviation of the isotope ratio of a sample relative to a reference sample which is the CHUR in the case of the Sm-Nd system.

According to this, the calculated εNd_i values ranging from +3.9 to +0.8 in granites (194 Ma; n = 7) (Fig. 37). Mostly, granites have εNd = +3.9-2.8, the only outlier with less primitive value is the sample ÁGK 6842 (εNd = +0.8). Quartz syenites and quartz monzonites have $\varepsilon Nd_{(194\ Ma)}$ values overlap with granites (average +3.8 for quartz syenites, n=2; average +2.1 for quartz monzonites, n = 4).

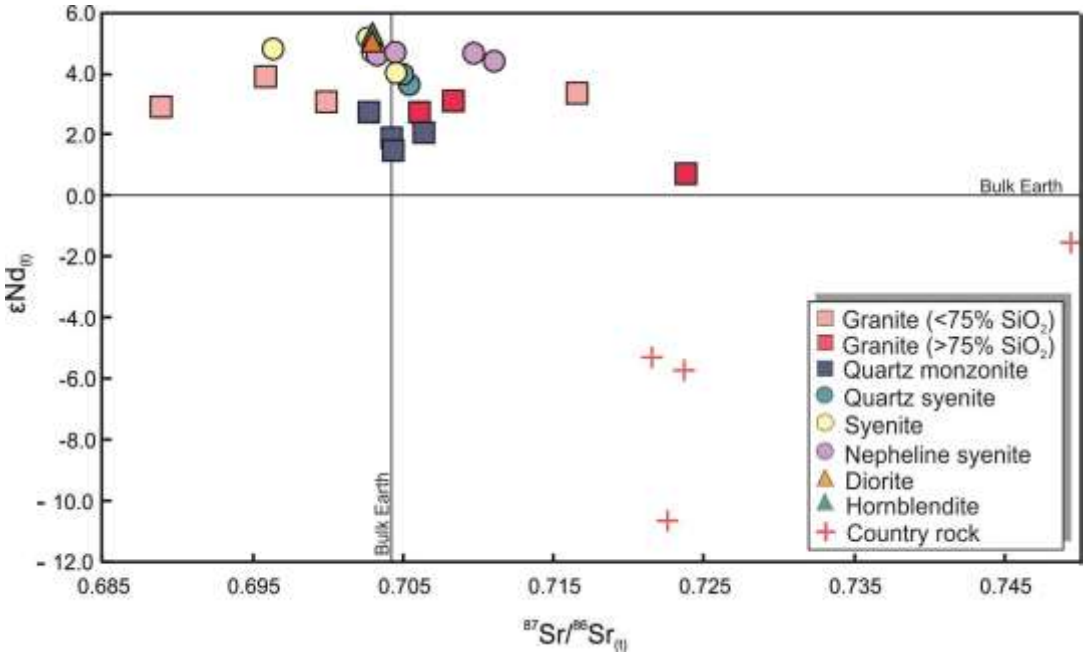

Figure 37. Initial $^{87}Sr/^{86}Sr$ ratios versus εNd_i variation diagram for the studied rocks from the DAM.

The calculated εNd for hornblendites and diorites are more radiogenic with the values of +5.5-5.0 (230 Ma; n = 2), whereas syenites have εNd values of +5.2-4.1 (230 Ma; n = 4). Surrounding country rock εNd values at 230 Ma are from -1.5 to -10.6. The errors associated with most of the calculated εNd values were very low (±2σ = 0.52-0.19; Table 8).

The $^{87}Sr/^{86}Sr_{(230\ Ma)}$ ratios range from 0.70279 to 0.70287 in two hornblendite and diorite samples on the initial $^{87}Sr/^{86}Sr$ vs εNd diagram (Fig. 37). Two syenites show similar $^{87}Sr/^{86}Sr_{(230\ Ma)}$ = 0.70255-0.70285, whereas the AOD 26 has an anomalously low value of 0.69625. Fig. 37 shows that the syenite ÁGK 7427 displays similarities to the more evolved felsic rocks with its $^{87}Sr/^{86}Sr_{(230\ Ma)}$ = 0.70444.

Whereas the $^{87}Sr/^{86}Sr_{(194\ Ma)}$ ratios in quartz syenites and monzonites range from 0.70263 to 0.70629 (n = 2 and 4), granites and nepheline syenites show wide range of initial Sr isotope compositions (n = 7 and 4) with the highest value of 0.72372 in the ÁGK 6842 outlier granite sample. The low $^{87}Rb/^{86}Sr$ ratio of 6.9 of this granite coupled with low 2σ = 0.588 suggesting its plausable calculated initial ratio in contrast to the ÁGK 6847, ÁGK 7458, AOD 02 and AOD 12 granites. These samples are characterised by the highest calculated $^{87}Rb/^{86}Sr$ ratios (37.3-277.3) and the widest range of $^{87}Sr/^{86}Sr_{(194\ Ma)}$ (Fig. 37). The age-corrected Sr isotope data of these samples still show significant scatter. Due to their impossibly low $^{87}Sr/^{86}Sr_{(194\ Ma)}$ values, Sr isotope data of these samples will not be considered during the interpretation. Despite the wide rage of $^{87}Sr/^{86}Sr_{(194\ Ma)}$ of nepheline syenites, their calculated $^{87}Rb/^{86}Sr$ ratios are significantly lower than that of the granites with much smaller analytical errors (2σ = 0.016-0.501). The calculated $^{87}Sr/^{86}Sr$ of the metamorphic wall rocks range from 0.72146 to 0.74932 using the age of 230 Ma (Fig. 37, Table 8).

7.2.3 Pb isotope compositions

The measured Pb isotope ratios show broad ranges, especially in the case of the granites (Table 8). The granites have the widest range in measured $^{206}Pb/^{204}Pb$ and $^{208}Pb/^{204}Pb$ ratios are from 40.29 to 44.63 and from 19.97 to 25.40 (n = 4). The syenites have somewhat lower and narrower ranges of $^{206}Pb/^{204}Pb$ = 39.36-40.62 and $^{208}Pb/^{204}Pb$ = 19.56-21.15 (n = 2), whereas the rest of the studied rocks show similar ratios. The granites also have the widest range and highest $^{207}Pb/^{204}Pb$ ratios with 15.71-15.98 (Table 8). The granite samples with the highest Pb isotope ratios are those granites that show significant scatter in the Sr isotope data (see the previous section).

The measured Pb isotope compositions were combined with U, Th, Pb concentrations and the crystallisation ages (230 Ma for syenites and 194 Ma for nepheline syenites, quartz syenites, quartz monzonites and granites) to calculate the initial Pb isotope values. The age-correction of Pb isotopes, however, is not always as straightforward as in the case of Nd or even of Sr isotopes. Because alteration processes can affect the U/Pb and Th/Pb ratios, the parent-daughter ratios might change during the subsolidus exchange reactions, which leads to over or under age-correction. Table 8 contains both the age-corrected and measured Pb isotope ratios. The differences between the measured and age-corrected data are well demonstrated in Fig. 38. The significantly more restricted age-corrected data suggest that in the case of most of the rocks alteration did not overwrite the Pb, U and Th compositions, so the age-correction applied is not too large. The only exceptions are granite samples AOD 02, AOD 11 and AOD 12, which have the highest Th/Pb and U/Pb ratios (> 6.55 and > 0.63) as well as the widest range of age-corrected Pb isotope values (Fig. 38, Table 8).

The age-corrected $^{207}Pb/^{204}Pb$ ratios are the lowest in the nepheline syenites and syenite with 15.634 and 15.633 (Fig. 38A, Table 8). Syenite sample AOD 26 are more radiogenic (15.675) compared to AOD 05 similarly to quartz syenites and monzonites ranging from 15.680-15.685 and 15.670-15.675. Granites can be characterised by the widest range of initial $^{207}Pb/^{204}Pb$ from 15.667 to 15.816. Wall rocks show $^{207}Pb/^{204}Pb$ ratios (age-corrected to 194 Ma) overlap with most of the samples (15.656-15.769). In terms of $^{208}Pb/^{204}Pb_{(194\ Ma)}$ nepheline syenites are the most radiogenic (39.082-39.083) followed by the granite AOD 12 (Fig. 38B). At the same time granites AOD 02 and AOD 11 show the lowest $^{208}Pb/^{204}Pb_i$ ratios (37.393 and 38.432) together with quartz monzonites (38.733-38.774). In the syenites and quartz syenites, the range is from 38.867 to 38.898 and from 38.924 to 39.018. Metamorphic country rocks are characterised by low 38.296-39.194 age-corrected $^{208}Pb/^{204}Pb$ ratios. Fig. 38B indicates that the most primitive initial $^{206}Pb/^{204}Pb$ ratio of 18.973 is shown by the quartz monzonite AOD 28 followed by granite AOD 04. Compared to the other rocks, granites display much wider scatter with the highest $^{206}Pb/^{204}Pb_{(194\ Ma)}$ value of 21.528. The nepheline syenites have somewhat higher $^{206}Pb/^{204}Pb_i$ = 19.478-19.527 than that of syenites (Fig. 38), whereas most of the wall rocks are less radiogenic with initial $^{206}Pb/^{204}Pb$ = 18.566-19.526 apart from AOD 17 that overlaps with syenites and nepheline syenites.

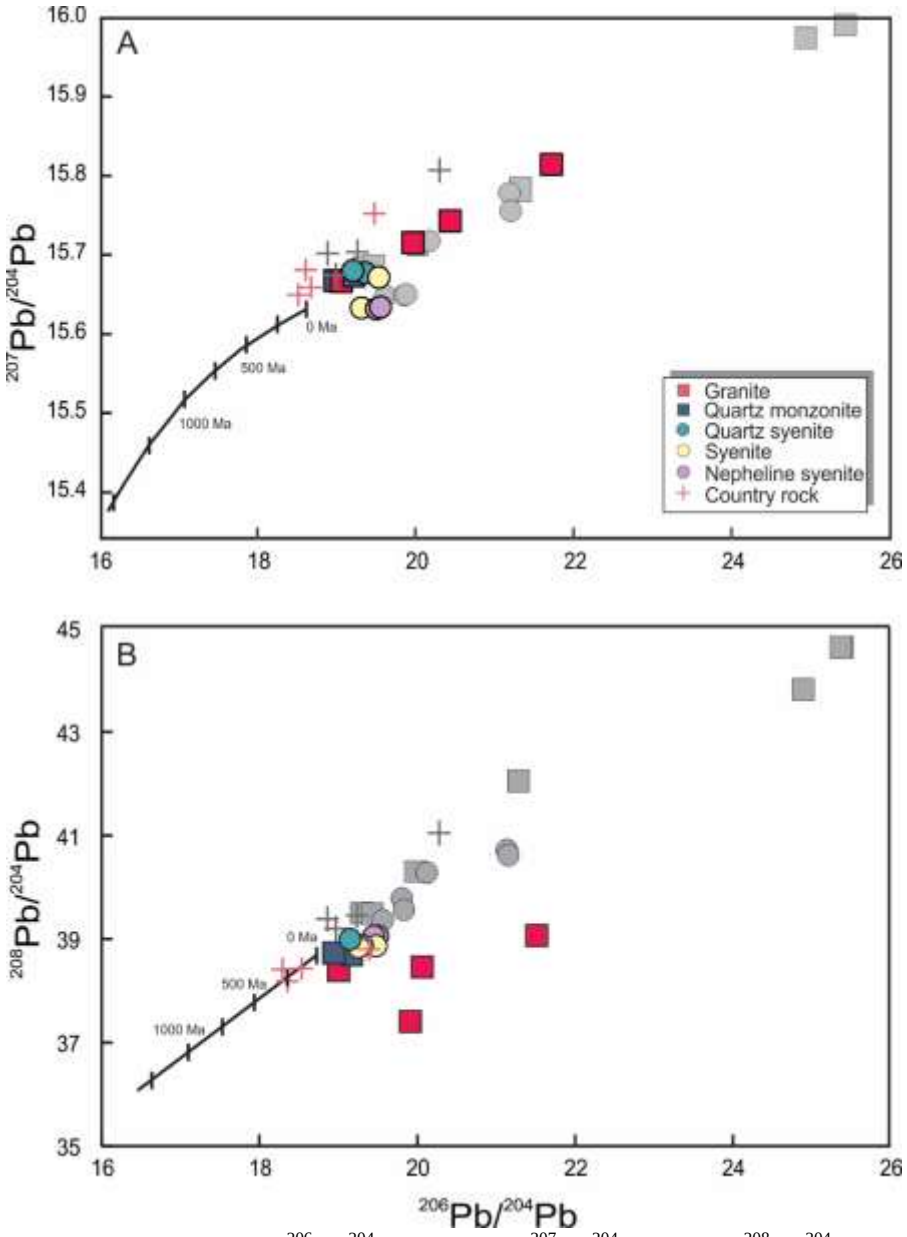

Figure 38. Age-corrected and measured $^{206}Pb/^{204}Pb$ versus (A) $^{207}Pb/^{204}Pb$ and (B**)** $^{208}Pb/^{204}Pb$ isotope variations in the studied felsic rocks from the Ditrău Alkaline Massif. Grey symbols represent the plot of measured Pb isotope ratios, coloured symbols are the age-corrected data. The black curves represent terrestrial Pb evolution model according to Stacey and Kramers (1975) for reference. Ticks along the μ-curve are drawn in 250 myr intervals.

Most of the samples in Fig. 38 extend to significantly higher Pb isotope compositions than found in modern lead (present-day lead indicated by the average crustal growth curve; Stacey and Kramers, 1975) due to their high radiogenic Pb isotope contents. Those granites that are characterised by the highest measured and age-corrected $^{206}Pb/^{204}Pb$ and $^{207}Pb/^{204}Pb$ or one of the lowest $^{208}Pb/^{204}Pb$ ratios, are the same samples that display the highest and lowest $^{87}Sr/^{86}Sr_i$ ratios as mentioned above. Despite their much narrower range of age-corrected Pb isotopes, these granite samples still show wide scatter that has to be take into consideration during the interpretations.

Table 8. Radiogenic isotope data for the studied rocks from the Ditrău Alkaline Massif

Samples	Rb	%RSD	Sr	%RSD	Rb/Sr	$^{87}Sr/^{86}Sr_m$	±2σ	$^{87}Rb/^{86}Sr$	±2σ	$^{87}Sr/^{86}Sr_i$
Granite										
ÁGK 6847	431	0.36	15.3	0.50	28.1	0.9289	0.000017	83.02	7.044	0.6998
ÁGK 6842	182	0.34	76.2	1.51	2.39	0.7428	0.000012	6.925	0.588	0.7237
ÁGK 7458	286	0.34	22.4	0.46	12.8	0.7918	0.000014	37.33	3.168	0.6888
AOD 02	717	0.70	8.04	0.23	89.2	1.4608	0.000057	277.2	23.52	0.6958
AOD 04	151	0.34	50.4	0.33	2.99	0.7298	0.000023	8.676	0.736	0.7059
AOD 11	161	0.07	79.1	0.10	2.04	0.7246	0.000012	5.908	0.501	0.7082
AOD 12	422	0.14	17.8	0.21	23.7	0.9095	0.000036	69.95	5.935	0.7165
Quartz monzonite										
ÁGK 6848/A	93.7	0.06	240	0.31	0.39	0.7094	0.000010	1.128	0.096	0.7063
ÁGK 6726	192	0.08	48.3	0.48	3.97	0.7344	0.000011	11.52	0.978	0.7026
AOD 28	66.1	0.74	275	0.20	0.24	0.7061	0.000009	0.694	0.059	0.7041
AOD 32	74.9	0.17	223	0.66	0.34	0.7069	0.000014	0.970	0.082	0.7042
Quartz syenite										
AOD 01	151	0.46	16.5	0.74	9.17	0.7789	0.000015	26.71	2.267	0.7052
AOD 15	197	0.54	54.7	0.50	3.61	0.7339	0.000015	10.47	0.888	0.7050
Syenite										
ÁGK 7404	132	0.29	805	0.64	0.16	0.7041	0.000013	0.473	0.040	0.7026
ÁGK 7427	96.7	0.56	203	0.58	0.48	0.7090	0.000014	1.379	0.117	0.7044
AOD 05	142	0.23	811	0.25	0.18	0.7045	0.000013	0.507	0.043	0.7029
AOD 26	230	0.31	23.5	0.59	9.82	0.7900	0.000012	28.64	2.430	0.6963
Nepheline syenite										
ÁGK 6769	222	0.22	109	0.30	2.04	0.7259	0.000015	5.902	0.501	0.7096
ÁGK 7446/3	227	0.44	218	0.60	1.04	0.7193	0.000012	3.018	0.256	0.7110
AOD 07	62.8	0.70	618	0.12	0.10	0.7040	0.000012	0.294	0.025	0.7032
AOD 18	52.3	0.77	798	0.32	0.07	0.7049	0.000011	0.189	0.016	0.7044
Diorite										
ÁGK 7502	22.5	0.35	3024	0.18	0.01	0.7029	0.000010	0.021	0.002	0.7028
ÁGK 6723	49.0	0.31	1646	0.27	0.03	0.7031	0.000009	0.086	0.007	0.7028
Hornblendite										
ÁGK 7428	31.0	0.22	834	0.50	0.04	0.7031	0.000010	0.107	0.009	0.7028
ÁGK 7434	68.5	0.29	1202	0.20	0.06	0.7034	0.000011	0.165	0.014	0.7029
Country rock										
AOD 16	74.6	0.73	24.5	0.43	3.05	0.7504	0.000012	8.850	0.751	0.7215
AOD 17	267	0.49	56.3	0.71	4.74	0.7946	0.000025	13.83	1.173	0.7493
AOD 23	61.4	0.22	21.5	0.72	2.86	0.7508	0.000014	8.295	0.704	0.7236
AOD 27	87.1	0.83	30.1	1.00	2.89	0.7500	0.000011	8.408	0.713	0.7225

Table 8. (Continued)

Samples	Nd	%RSD	Sm	%RSD	$^{143}Nd/^{144}Nd_m$	±2σ	$^{147}Sm/^{144}Nd$	±2σ	$^{143}Nd/^{144}Nd_i$	εNd_i
Granite										
ÁGK 6847	9.61	0.47	2.14	0.18	0.51272	0.000008	0.135	0.011	0.51255	+3.1
ÁGK 6842	12.1	0.70	2.33	0.86	0.51258	0.000010	0.116	0.010	0.51243	+0.8
ÁGK 7458	10.0	0.87	2.54	0.88	0.51274	0.000012	0.153	0.013	0.51254	+3.0
AOD 02	8.84	0.46	2.22	0.85	0.51279	0.000013	0.152	0.013	0.51259	+3.9
AOD 04	47.3	0.50	6.51	0.66	0.51264	0.000011	0.083	0.007	0.51253	+2.8
AOD 11	19.3	0.72	4.52	0.95	0.51273	0.000011	0.142	0.012	0.51255	+3.2
AOD 12	10.6	0.37	2.85	0.66	0.51277	0.000010	0.163	0.014	0.51256	+3.4
Quartz monzonite										
ÁGK 6848/A	37.6	0.41	5.97	1.92	0.51262	0.000009	0.096	0.008	0.51250	+2.1
ÁGK 6726	31.9	0.26	5.07	1.15	0.51265	0.000008	0.096	0.008	0.51253	+2.8
AOD 28	20.6	0.78	3.26	0.90	0.51261	0.000011	0.096	0.008	0.51249	+1.9
AOD 32	13.9	0.45	2.71	0.64	0.51262	0.000014	0.118	0.010	0.51247	+1.5
Quartz syenite										
AOD 01	22.5	0.30	3.34	0.91	0.51269	0.000012	0.089	0.008	0.51258	+3.7
AOD 15	22.5	0.52	3.40	1.03	0.51271	0.000014	0.091	0.008	0.51260	+4.0
Syenite										
ÁGK 7404	52.1	0.33	7.70	1.36	0.51275	0.000011	0.089	0.008	0.51261	+5.2
ÁGK 7427	3.03	1.36	0.28	0.98	0.51264	0.000012	0.056	0.005	0.51255	+4.1
AOD 05	42.3	0.40	6.32	0.69	0.51272	0.000007	0.090	0.008	0.51259	+4.8
AOD 26	60.3	0.67	7.20	1.02	0.51270	0.000014	0.072	0.006	0.51259	+4.9
Nepheline syenite										
ÁGK 6769	7.89	0.09	0.98	1.54	0.51273	0.000011	0.075	0.006	0.51263	+4.7
ÁGK 7446/3	8.72	0.56	0.91	1.29	0.51270	0.000014	0.063	0.005	0.51262	+4.5
AOD 07	16.9	1.29	2.28	0.69	0.51273	0.000012	0.081	0.007	0.51263	+4.7
AOD 18	9.08	0.31	1.31	0.88	0.51275	0.000011	0.087	0.000	0.51264	+4.9
Diorite										
ÁGK 7502	41.5	0.17	6.46	0.76	0.51275	0.000009	0.094	0.001	0.51261	+5.1
ÁGK 6723	49.5	0.65	8.95	0.41	0.51278	0.000012	0.109	0.002	0.51262	+5.3
Hornblendite										
ÁGK 7428	94.8	0.62	17.8	0.69	0.51280	0.000010	0.113	0.002	0.51262	+5.5
ÁGK 7434	61.5	0.61	11.2	1.53	0.51277	0.000008	0.109	0.004	0.51260	+5.0
Country rock										
AOD 16	3.47	0.13	1.36	0.54	0.51243	0.000010	0.237	0.003	0.51208	-5.2
AOD 17	50.8	0.24	9.16	0.06	0.51243	0.000009	0.109	0.001	0.51227	-1.5
AOD 23	18.5	1.54	3.82	0.75	0.51224	0.000013	0.124	0.004	0.51205	-5.7
AOD 27	16.8	0.69	3.11	0.52	0.51197	0.000017	0.112	0.002	0.51180	-10.6

Samples	$^{208}Pb/^{204}Pb_m$	$^{207}Pb/^{204}Pb_m$	$^{206}Pb/^{204}Pb_m$	Pb	Th	U	$^{238}U/^{204}Pb$	$^{235}U/^{204}Pb$	$^{232}Th/^{204}Pb$	$^{208}Pb/^{204}Pb_i$	$^{207}Pb/^{204}Pb_i$	$^{06}Pb/^{204}Pb_i$
Granite												
AOD 02	42.054	15.784	21.282	11.1	74.7	6.98	43.68	0.317	483.3	37.393	15.718	19.947
AOD 04	40.295	15.715	19.975	11.7	32.4	5.23	29.72	0.215	190.4	38.459	15.669	19.067
AOD 11	44.633	15.994	25.397	4.32	35.7	9.98	173.8	1.261	642.9	38.432	15.729	20.086
AOD 12	43.822	15.977	24.895	10.3	67.4	15.3	110.2	0.799	501.5	38.986	15.809	21.528
Quartz monzonite												
AOD 28	39.502	15.685	19.292	6.75	7.56	1.08	10.45	0.076	75.49	38.774	15.669	18.973
AOD 32	39.487	15.687	19.425	7.28	8.43	0.87	7.796	0.056	78.18	38.733	15.675	19.186
Quartz syenite												
AOD 01	40.281	15.719	20.122	13.0	26.6	4.91	25.07	0.182	140.7	38.924	15.680	19.356
AOD 15	40.724	15.780	21.137	9.86	24.8	9.02	62.20	0.451	176.8	39.018	15.685	19.237
Syenite												
AOD 05	39.358	15.648	19.563	8.57	5.45	1.01	7.664	0.056	42.93	38.867	15.634	19.285
AOD 26	40.617	15.757	21.155	15.1	32.4	9.83	44.06	0.319	150.2	38.898	15.675	19.554
Nepheline syenites												
AOD 07	39.779	15.649	19.804	3.76	3.99	0.61	10.69	0.078	72.18	39.083	15.633	19.478
AOD 18	39.565	15.650	19.831	1.94	1.43	0.29	9.938	0.072	49.98	39.082	15.635	19.527
Country rock												
AOD 16	39.454	15.703	19.240	5.78	10.3	1.94	21.90	0.159	120.0	38.296	15.669	18.571
AOD 17	41.046	15.807	20.279	7.89	21.7	2.88	24.64	0.179	191.9	39.194	15.769	19.526
AOD 23	39.198	15.674	18.972	9.70	8.72	1.78	11.85	0.086	60.11	38.618	15.656	18.609
AOD 27	39.387	15.701	18.863	7.88	6.87	1.18	9.711	0.070	58.36	38.824	15.686	18.566

%RSD - percent relative standard deviation. Analytical uncertainty of the measured Rb, Sr, Sm and Nd concentrations (ppm)

±2σ - 2 sigma standard deviation from the mean was calculated for the Rb-Sr and Sm

-Nd isochrons subscript i - age-corrected radiogenic isotope ratios

subscript m - measured radiogenic isotope ratios

Chapter 8: Discussion

The main aim of this chapter is to assess the role of the mantle and crustal components in the generation of the Ditrău Alkaline Massif and determine the relationship between the silica-oversaturated and undersaturated rocks by this. To achieve these aims consideration of the influence of hydrothermal and low-temperature alterations on the isotope composition of the rocks is required in order to eliminate the secondary postmagmatic effects. Then determination of the nature of the source of the studied rocks, and finally the possibility of crustal assimilation is considered.

8.1 Oxygen isotope equilibrium between the coexisting minerals

The degree of internal oxygen isotope equilibrium can be evaluated by using δ-δ diagrams (Fig. 39; e.g. Gregory and Criss, 1986). The $\delta^{18}O$ value of the mineral with lowest rate of exchange between oxygen and the fluid is usually represented on the X-axis on these plots, whereas that of the coexisting mineral with higher susceptibility to O-isotope exchanges is on the Y-axis. Isotherms are plotted on the diagram, which are defined by the ideal, constant per mil differences (Δ) between the two coexisting phases at a particular temperature in closed system. The constant per mil differences for the mineral pairs were calculated on the basis of Equation 4 (Section 1.3). The three isotherms are shown for temperatures 1000°C, 700°C and 550°C. In the case of closed-system fractionation the examined mineral pairs should form arrays defined by constant Δ values showing oxygen isotope equilibrium at magmatic temperature. However, the final O-isotope compositions do not depend only on the $\delta^{18}O$ value of the source region, and the 1‰ increase during the closed-system fractional crystallisation (Fig. 2). As described in Section 1.3, subsolidus water-rock interactions can induce significant disturbance by generating O-isotope disequilibrium in the rocks. Where there is no evidence for post-magmatic alterations and the system remained closed, differences in cooling rate, modal proportions, grain size and closure temperatures of minerals can control the mineral $\delta^{18}O$ values and cause small deviations from the ideal $\Delta^{18}O$ of mineral pairs (Jenkin et al., 1994). However, in the case of open-system processes, patterns defined by the O-isotope composition of the mineral pairs probably will not follow the arrays of constant per mil differences due to the post-magmatic alterations.

Figs. 39A, B and D show the $\delta^{18}O$ values of feldspar, amphibole and zircon vs the coexisting quartz and Fig. 39C that of the titanite vs the coexisting zircon. Minerals are characterised by distinct $\delta^{18}O$ variations. O-isotope compositions of feldspar, titanite and quartz from the silica-oversaturated rocks and syenites show large $\delta^{18}O$ variations, whereas amphibole and zircons have more restricted O-isotope compositions in every rock types. Because of its highest diffusion rate to oxygen out of the silicate minerals, feldspar has high susceptibility to subsolidus exchanges (Giletti et al, 1978). Therefore, the magnitude of $\Delta_{quartz\text{-}feldspar}$ is a very effective monitor of hydrothermal alterations. It can be seen in Fig. 39A that the majority of data plot either below or above the O-isotope equilibrium range ($\Delta_{quartz\text{-}feldspar}$ = 0.66-1.11) and there is only one quartz syenite sample (AOD 15) with equilibrium $\Delta_{quartz\text{-}feldspar}$ = 0.77.

The $\Delta_{quartz\text{-}feldspar}$ value of 0.77 of the quartz syenite AOD 15 yields apparent O-isotope temperature of 866°C, which is in accordance with the crystallisation temperature of Ditrău quartz monzonite sample ÁGK-6839 (zircon saturation temperature = 770 - 860°C and 880 - 930°C; Kovács and Pál-Molnár, 2005), although it is important to emphasise that it is not intended that 866°C is taken as a precise single temperature of crystallisation. Quartz occurs as unaltered grains in the thin sections, has a much lower diffusion rate for oxygen at <500°C (Giletti and Yund, 1984) and is generally resistant to low-temperature alterations <300°C (Taylor, 1977). It is, therefore, reasonable to assume that $\delta^{18}O$ values of quartz were not significantly affected by any hydrothermal fluids. Thus, the per mil difference of this mineral pair below or above the O-isotope equilibrium range are likely to be due to the change of $\delta^{18}O$ values of feldspars. Higher $\Delta_{quartz\text{-}feldspar}$ values can be produced by the depletion of ^{18}O in feldspar, and the increase of feldspar $\delta^{18}O$ values induces lower per mil differences.

The average apparent temperature suggested by the higher $\Delta_{quartz\text{-}feldspar}$ values is 460°C (n = 11) that is close to closure temperature of these minerals (550°C; Giletti, 1986). As in slow cooling systems such as the Ditrău complex as well, the oxygen diffusion and thus the re-equilibration of oxygen isotopes between the coexisting phases can take place for a longer period of a time, it is reasonable to suggest that the feldspar $\delta^{18}O$ values were shifted towards the lower values due to the interaction with high-temperature deuteric fluids, whereas quartz continued the oxygen exchange with the coexisting minerals until its closure temperature and its $\delta^{18}O$ values became increased because of the O-isotope re-equilibration during the slow cooling.

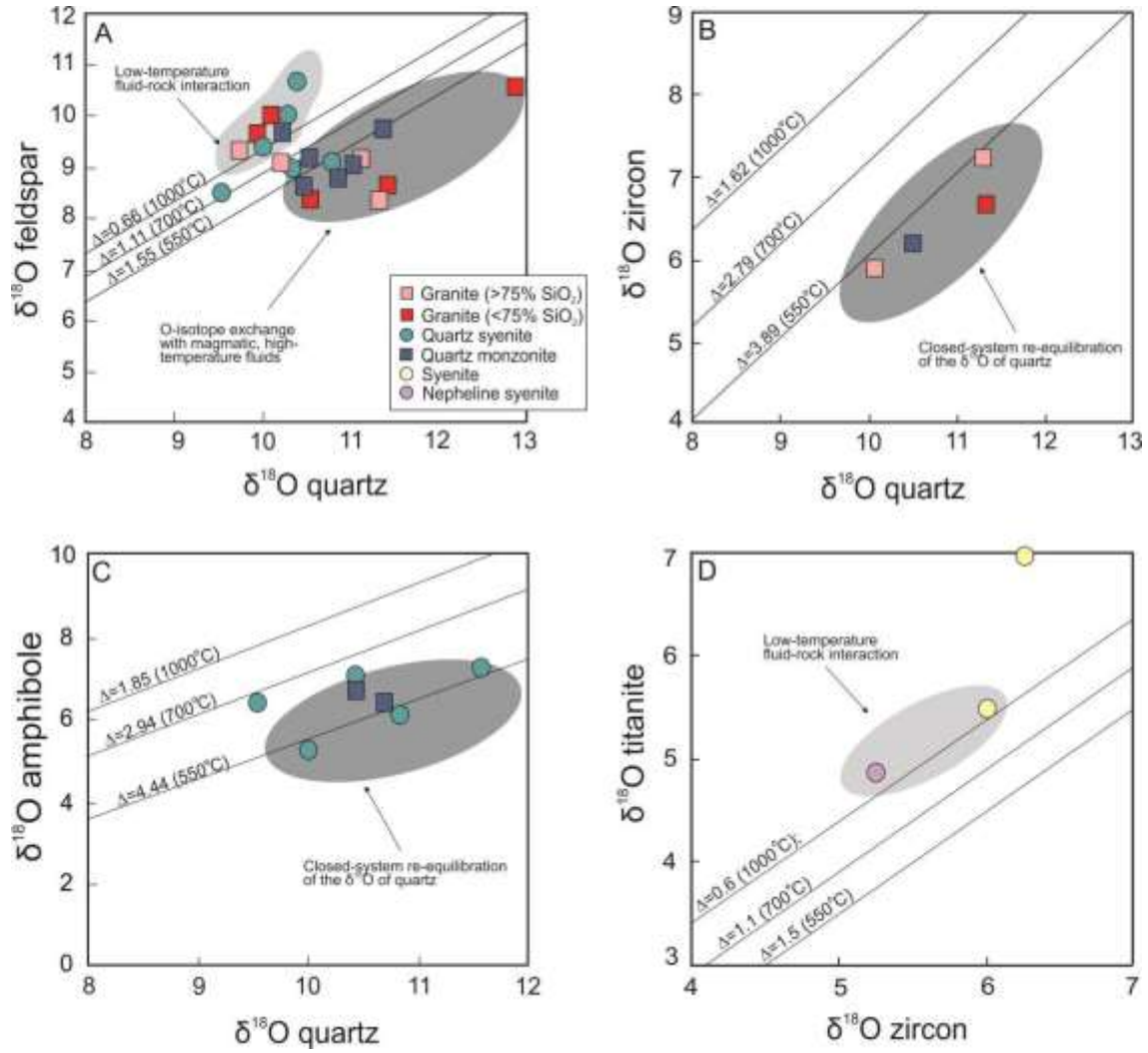

Figure 39. Plot of $\delta^{18}O$ values of quartz vs feldspar, amphibole, zircon and zircon vs titanite $\delta^{18}O$ values from the felsic rocks of Ditrău Alkaline Massif. Fractionation factors for quartz-feldspar pairs are from Clayton et al., (1989); quartz-amphibole pairs are from Lackey et al. (2008); quartz-zircon pairs are from Valley (2003) and zircon-titanite pairs are from Valley (1994).

Clustering of most of the samples around the 550°C isotherm on the plot of amphibole vs quartz (Fig. 39B) is consistent with the reset of oxygen isotope composition of amphiboles by magmatic fluids and the subsolidus re-equilibration of quartz during the slow cooling. There are also amphiboles in quartz syenites with $\delta^{18}O$ values which show lower $\Delta_{quartz\text{-}amphibole}$ = 3.23-3.32 that are very close to the equilibrium range corresponding to apparent temperatures 693 and 680°C.

It is important to emphasise that the interpretations of zircon-titanite pair are based on only two data points. The plot of titanite vs zircon demonstrates apparent O-isotope disequilibrium as the $\Delta_{zircon\text{-}titanite}$ values are too low compared to $\Delta_{zircon\text{-}titanite}$ values that define the magmatic temperature (Fig. 39C). As in the case of zircon, titanite also have high closure temperatures (T_{ttn} = 650 °C) that would make them ideal minerals to preserve the magma

$\delta^{18}O$ values, however, they cannot retain their original oxygen isotope signatures under hydrothermal conditions as effectively as zircons (Zhang et al, 2006; Cherniak et al., 2004) and this is represented in Fig. 39C. One syenite samples (ÁGK 7427) has unusually low titanite $\delta^{18}O$ value with $\Delta_{zircon\text{-}titanite} = -0.9$, which raises the possibility of analytical problems during the analyses or indicates impurities in the analysed titanite. The overall small per mil differences between zircon and titanite would imply oxygen isotope exchanges caused by low-temperature external fluids. However, because of the resistant nature of these minerals to O-isotope exchanges, the uncertainty in the fractionation factor used in the calculations is a more probable explanation.

As illustrated in Fig. 39B, quartz-zircon pairs also show apparent temperatures close to 550°C. Because of its very strong resistant nature to alteration and very high closure temperature to oxygen (>900°C, Watson and Cherniak, 1997), zircon effectively retains the magma $\delta^{18}O$ values and are more resistant to changes than that of quartz (Valley, 2003; Lackey et al., 2006). Therefore, unchanged zircon $\delta^{18}O$ values are expected to be uniform and reflect the original magma oxygen isotope compositions even after intensive subsolidus alterations. However, zircons in Ditrău granites show $\delta^{18}O$ variability. The possible explanations for this variation could be:

1. Some of the zircons in granite are xenocrysts that were not related to the magmatic process produced the Ditrău granites.
2. Variations in zircon $\delta^{18}O$ values equal with variable magma $\delta^{18}O$ value that is because of:

    2a. Zircons are derived from different magma batches that fed the Ditrău massif. These different magma intrusions originated from mantle source with different O- isotope compositions.

    2b. The higher zircon $\delta^{18}O$ values are the consequences of the crustal contamination of the mantle magma by higher $\delta^{18}O$ material during its crystallisation.

Both the unzoned zircon grains and the positive correlation between $\delta^{18}O$ values of zircon and quartz (Fig. 39B) suggest that the analysed zircons cannot be xenocrysts. The oxygen isotope correlation of quartz and zircon rather indicates either that their host magma was subjected to progressive contamination by higher $\delta^{18}O$ crustal material or different magma batches are from different mantle sources. As the mantle source is unlikely to vary

very much, the variable zircon $\delta^{18}O$ values are possibly the result of crustal contamination.

In summary, oxygen isotope re-equilibration of the quartz took place down to its closure temperature (550°C; Giletti, 1986) during slow cooling stage as indicated by the high $\Delta_{quartz\text{-}mineral}$ values (e.g. $\Delta_{quartz\text{-}feldspar}$ = 1.60-2.9). Less resistant minerals like feldspars recorded interactions with both magmatic (~ 400-550 °C; Chacko et al. 2001) and low-temperature, external fluids at the post-magmatic stage of the evolution, which overwrote the O-isotope compositions of feldspar grains. High temperature alteration is suggested by the $\Delta_{quartz\text{-}feldspar}$ = 0.99-2.91, whereas $\Delta_{quartz\text{-}feldspar}$ = -0.32-0.59 values suggest low temperature exchanges. However, the influence of the crustal fluids was not significant as there are no steep disequilibrium arrays on delta-delta diagrams, which is a characteristic feature of the intensive hydrothermal alteration (Criss and Taylor, 1986).

8.1.1 Influence of the subsolidus hydrothermal fluids on the radiogenic systems

As described in Section 7.2, the granites have the widest range of radiogenic isotope compositions. It was also suggested on the basis of the degree of oxygen isotope equilibrium between the coexisting phases in the samples that subsolidus exchange occurred at both high and low temperatures in the Ditrău magmatic complex. Assessment of the relationship between the radiogenic isotope values and the different hydrothermal fluids affected the studied rocks was necessary to identify the modified radiogenic isotope compositions and avoid incorrect interpretations.

Whereas the Nd isotope ratios of the studied rocks have a restricted range, certain granite samples (ÁGK 6847, ÁGK 7458, AOD 02) and syenite AOD 26 have impossibly low $^{87}Sr/^{86}Sr_i$ ratios (< 0.7; Fig. 37), which means that Rb-Sr system was disturbed. Granite AOD 11 and 12 show the highest $^{87}Sr/^{86}Sr_i$ ratios with > 0.70825 ignoring the granite outlier ÁGK 6842. These granites and the syenite are also characterised by the highest Rb/Sr ratios from 10 to 90 that makes their $^{87}Sr/^{86}Sr_i$ ratios uncertain. The highest $^{87}Sr/^{86}Sr_i$ ratio is displayed by the granite outlier ÁGK 6842 (0.72372). Unlike the above-mentioned granite and syenite samples, the high $^{87}Sr/^{86}Sr_i$ ratio of ÁGK 6842 has the lowest Rb/Sr = 2. Furthermore, the high initial Sr isotope ratio is coupled with the lowest εNd_i value of +0.8 out of the studied rocks, which is consistent with crustal contamination. Therefore, the Sr isotope composition of the ÁGK 6842 is not considered to have been significantly modified by post-magmatic fluids.

The highest $^{206}Pb/^{204}Pb$ and $^{207}Pb/^{204}Pb$ ratios are shown by granite AOD 02, AOD 11 and AOD 12 (> 19.947 and >15.718 age-corrected data; Fig. 38). These samples also have the highest ratios of Th/Pb = 6.55-8.28, U/Pb = 0.63-2.31 (Table 8) and initial $^{87}Sr/^{86}Sr$.

The oxygen isotope per mil difference between quartz and feldspar ($\Delta_{quartz\text{-}feldspar}$) from granite samples AOD 04, 11, 12, ÁGK 6847, 7458, from quartz syenite samples AOD 01, 15 and form quartz monzonite samples AOD 28, 32, ÁGK 6848/A, 6726 was plotted against $^{87}Sr/^{86}Sr_i$ and $^{206}Pb/^{204}Pb_i$ in order to assess the relationship between the influence of post- magmatic fluids and radiogenic isotope compositions of the silica-oversaturated rocks (Fig. 40). The isotherms plotted are for temperatures of 800°C ($\Delta_{quartz\text{-}feldspar}$ = 0.87) and 1000°C ($\Delta_{quartz\text{-}feldspar}$ = 0.66) that corresponds to the crystallisation temperature of granites (880- 930°C; Kovács and Pál-Molnár, 2005). Fig. 40A demonstrates well that the granites AOD 11 and 12, which have the highest initial Sr isotope ratios, were affected by low temperature crustal fluids as suggested by their low $\Delta_{quatrz\text{-}feldspar}$ values (< 0.66; Figs. 39A and 40A). The $\Delta_{quartz\text{-}feldspar}$ > 0.87 values of the ÁGK 6847 and ÁGK 7458 granites are consistent with interactions with high temperature magmatic fluids that probably lowered the $^{87}Sr/^{86}Sr_i$ ratios of these rocks (Fig. 39A and 40A). Quartz monzonites were also subjected to high temperature subsolidus isotope modifications. However, because of the high Sr concentrations of AOD 28, 32, ÁGK 6848/A and 6726 (48-275 ppm), deuteric fluids could not decrease the $^{87}Sr/^{86}Sr_i$ ratios of these rocks to the same degree as granites with much lower Sr contents (15-22 ppm).

Granite AOD 4, quartz monzonite ÁGK 6848/A and quartz syenite AOD 01 have similar $^{87}Sr/^{86}Sr_i$ ratio to that of the quartz syenite AOD 15 (Fig. 40A). The latter is the only sample that has $\Delta_{quartz\text{-}feldspar}$ consistent with O-isotope equilibrium between its coexisting minerals ($\Delta_{quartz\text{-}feldspar}$ = 0.77). It is, therefore, suggested that the Sr isotope range, enclosed by the dashed lines in Fig. 40A, represents samples that experienced the least secondary isotope exchanges. Syenite AOD 26 belongs to the group of samples with low $^{87}Sr/^{86}Sr_i$ ratios and has one of the lowest feldspar $\delta^{18}O$ values of 7.7‰. Due to the lack of quartz, the degree of O-isotope equilibrium can only be assessed by the combination of the fractionation factors of the quartz-amphibole and quartz-feldspar pairs (see the Section 8.1). Assuming 2.01 fractionation factor for the quartz-amphibole, the measured amphibole $\delta^{18}O$ values of 7.02 and feldspar $\delta^{18}O$ values of 7.7‰ yield $\Delta_{amphibole\text{-}feldspar}$ = 0.75 that corresponds to an apparent temperature of 1364°C. The low $\Delta_{amphibole\text{-}feldspar}$ value is consistent with interaction with high temperature fluids that is in accordance with the unusually low Sr isotope (0.69625).

Due to the lack of Pb isotope data from the granites interacted with magmatic fluids, only the effect of crustal fluids on the Pb isotope compositions can be investigated. Similarly to Sr isotopes, low temperature crustal fluids appear to had influence on the elevated $^{206}Pb/^{204}Pb_i$ ratios of the same granite samples characterised by the highest Sr isotope compositions (Fig. 40B). As these granite samples show the same patterns for $^{207}Pb/^{204}Pb_i$ and $^{208}Pb/^{204}Pb_i$ ratios against $\Delta_{quartz\text{-}feldspar}$ values, those are not shown in the thesis.

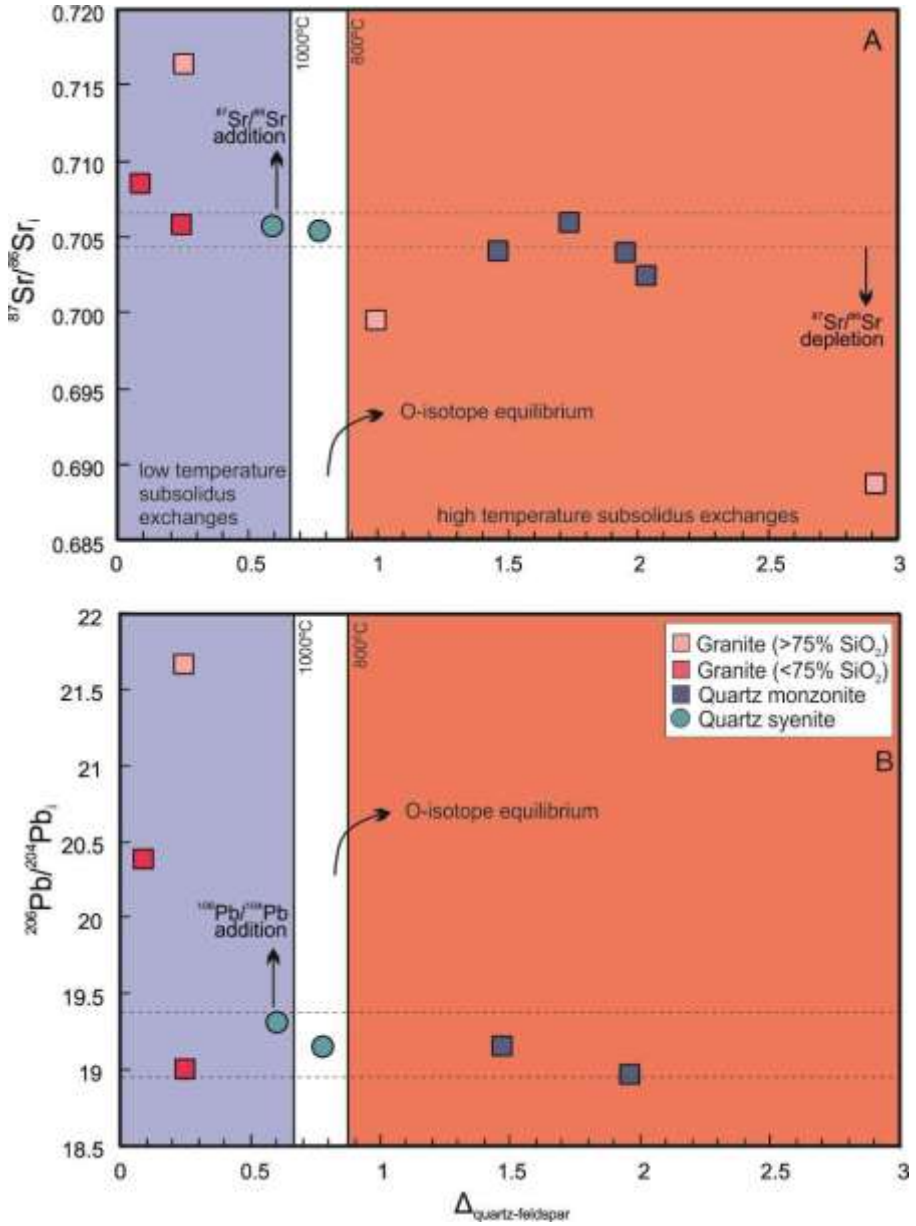

Figure 40. Plots of (A) $^{87}Sr/^{86}Sr_i$ and (B) $^{206}Pb/^{204}Pb_i$ vs $\Delta_{quartz\text{-}feldspar}$ of the silica-oversaturated rocks from the Ditrău Alkaline Massif. Range of $^{87}Sr/^{86}Sr_i$ and $^{206}Pb/^{204}Pb_i$ values defined by the dashed lines indicate the samples with isotope compositions that were not experienced significant secondary exchange reactions as it is suggested by their similar Sr and Pb isotope ratios to that of the AOD 15 quartz syenite. The white field represents the O-isotope equilibrium range at the temperature of crystallisation assuming no errors in measurements of $\delta^{18}O$ values.

Representing the location of the studied rocks together with the nature of the hydrothermal fluids that interacted with them on the sampling area, two different zones can be identified (Fig. 41). The blue zone is the field for low temperature alteration based on $\Delta_{quartz\text{-}feldspar} < 0.66$, whereas the red one shows the samples most likely affected by deuteric fluids on the basis of their $\Delta_{quartz\text{-}feldspar} > 0.87$. The main red zone is situated right next to the main nepheline syenite body of the central part of the DAM (its location is marked by purple colour on the Fig. 41; detailed geological map of the DAM is presented in Fig. 15). As nepheline syenites formed later than the silica-saturated, oversaturated rocks and intruded into approximately the same depth than the granites (~ 15 km; Fall et al., 2007; Pál-Molnár et al., 2015a), it is consistent with the high temperature magmatic fluids from the nepheline syenites being responsible for the lowering of $^{87}Sr/^{86}Sr$ in some of the studied rocks. This is also confirmed by the existence of a smaller red zone in the north part of the massif that is defined by the $\Delta_{quartz\text{-}feldspar}$ value of 1.95 of the quartz monzonite AOD 28 (Fig. 41). Even though the sample AOD 28 was taken far from the main nepheline syenite body of the central part of the DAM, it has high $\Delta_{quartz\text{-}feldspar}$ value that probably relates to the adjacent minor nepheline syenite intrusion (purple area in the north part of the map; Fig. 41).

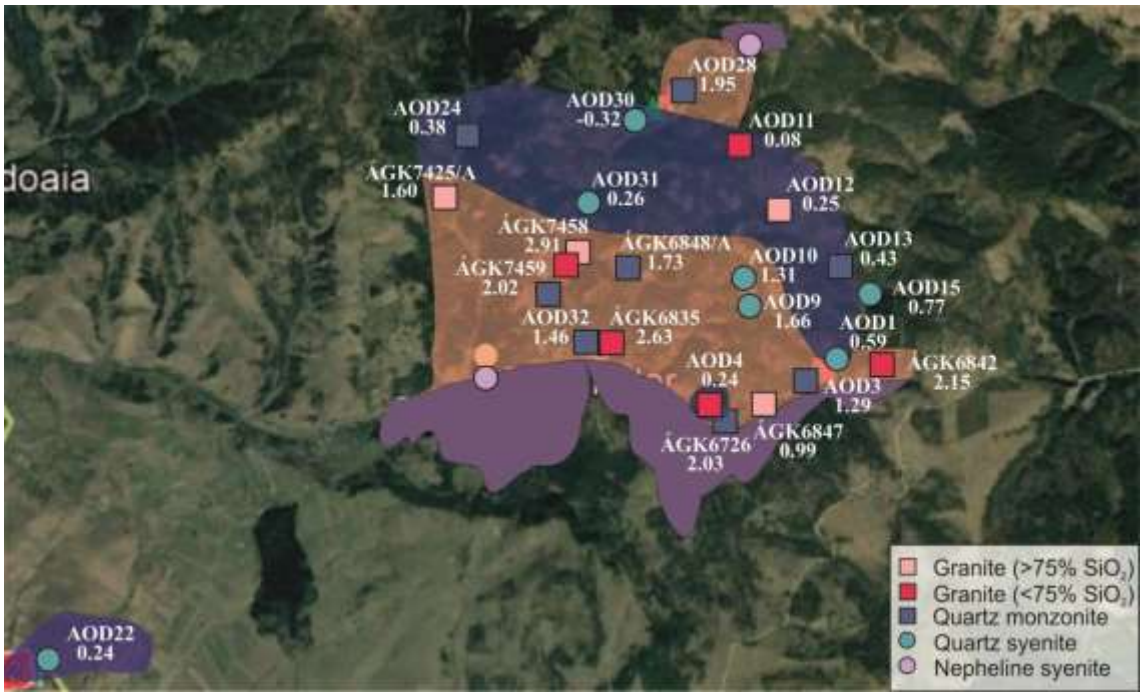

Figure 41. Spatial variation of $\Delta_{quartz\text{-}feldspar}$ values of the silica-oversaturated rocks. Red zones indicate the influence of low $\Delta_{quartz\text{-}feldspar}$ values. Blue zones represent the spread of high $\Delta_{quartz\text{-}feldspar}$. The values under the sample codes are the $\Delta_{quartz\text{-}feldspar}$ values of samples. Outcrop of nepheline syenites are demonstrated by the purple areas. Note that the latter does not represent the entire nepheline syenite body.

Unlike the influence of magmatic fluids, low temperature alteration took place at the internal parts of the granitoid sampling area represented by the $\Delta_{quartz\text{-}feldspar} < 0.66$ values of some studied rocks in Fig. 41. $\Delta_{quartz\text{-}feldspar}$ value of quartz syenite AOD 22, located at the southwestern corner of the map, also shows low temperature alteration processes, which is consistent with the lack of nepheline syenite in the close proximity of this quartz syenite outcrop (Fig. 41). The $\Delta_{quartz\text{-}feldspar}$ value of 0.24 of the granite sample AOD 04 yields interactions with crustal fluids in spite of the fact that AOD 04 was collected from the main red zone. As AOD 04 is a loose granite that was not connected to an outcrop, it might originate from a different part of the massif e.g. from the main blue zone that has higher elevation compared to the valley, where the AOD 04 was collected from.

In contrast with the Sr and Pb isotope systems, Nd isotope system does not appear to have been modified by hydrothermal fluids. The lack of significant variations of $^{143}Nd/^{144}Nd_i$ in the different rock types suggest that those were unrelated to the type and the degree of hydrothermal alterations probably by virtue of the immobile nature of Nd (McCulloch et al., 1981; Stewart and DePaolo, 1992) and low and constant Sm/Nd ratios. Besides the influence of post magmatic fluids on isotope composition, fluids might also be responsible for the peraluminous nature of the studied rocks coupled with the normative corundum contents. The presence of additional secondary, Al-rich phases like sericite, clay in silica-saturated and silica-oversaturated rocks, or liebnerite, clay in nepheline syenites can account for the corundum as a normative phase.

In summary, the Sr and Pb isotope compositions of mainly the Ditrău granites and syenites were disturbed by different alterations caused by magmatic and crustal fluids. As a result of this, these samples do not have Sr and Pb isotope ratios that reflect crystallisation values even after the age-corrections. As a consequence of this, Sr and Pb isotopes from only the freshest samples (based on $\Delta_{quartz\text{-}feldspar}$ values) will be used in the subsequent interpretations of magmatic processes especially for Ditrău magma types.

8.2 Role of crystal fractionation in the formation of the Ditrău massif

Looking at the entire data set, two main data arrays are present on the total alkalis-SiO_2 diagram (Fig. 42E): A weakly alkaline series from basanite-alkali basaltic towards silica-saturated (highlighted by the light gray band in Fig. 42) and a strongly alkaline, undersaturated series from basanite-alkali basaltic compositions to nepheline syenite. The

small number of ultramafic-mafic rocks does not allow a more precise linking between the various felsic rock types and the two different basic end-members on the basis of Na_2O+K_2O vs silica. Whereas the weakly alkaline series from alkali basalt towards rhyolite are well defined by the Na_2O+K_2O and Si_2O contents of most of the studied rocks, the intermediate tephritic composition of the characteristic series from basanite to phonolite (Wilson, 1989) is missing in the case of the Ditrău massif.

8.2.1 Interpretation of major and trace element trends

Almási, (2015) calculated the trace element composition of the melt that was in equilibrium with the clinopyroxene and amphibole from Ditrău hornblendites. According this model the composition of the calculated melt corresponds to the composition of alkali lamprophyres (camptonites) in the Ditrău massif, suggesting that a melt similar to camptonites can be the potential parental magma of the hornblendites. The major element composition of the studied rocks, the representative compositions of their minerals and the average composition of the alkali lamprophyres (Batki, 2009) as the parental melt of hornblendites are demonstrated in Fig. 42.

The mineralogical compositions of the hornblendites, gabbros and diorites are closely similar (amphibole, clinopyroxene, biotite, plagioclase, accessory minerals; Pál-Molnár, 2015). Silica-saturated and oversaturated felsic rocks of the DAM consist of amphibole, biotite, plagioclase, K-feldspars, accessory minerals, ±quartz. Given their similar mineralogical compositions, the scatter in the major element compositions of different rock types must arise from the different proportion of minerals. This is consistent with a cumulative nature for Ditrău felsic rocks as well as the Ditrău hornblendites as described by earlier studies (Morogan et al., 2000; Pál-Molnár, 2000; Almási, (2016). To interpret the major element compositions of the studied rocks in the light of their main constituents, representative composition of the major minerals should take into account (Fig. 42).

It can be seen in Fig. 42 that the high TiO_2, CaO, FeO^t and MgO content of hornblendites is controlled mainly by the presumed accumulation of amphibole, clinopyroxene and titanite at the early stage of the evolving basic melt. The low values of Na_2O+K_2O and Al_2O_3 in hornblendites are in accordance with their abundant alkali- and Al_2O_3-poor mafic minerals and their low amount of plagioclase (5-8 wt% modal plagioclase) (Figs. 42B, E). Probably the accumulation of amphibole, clinopyroxene and titanite exert the major control on the variation of TiO_2, CaO, FeO^t and MgO contents of diorites as well,

however, their importance decreased because of the increased plagioclase content of these rocks. The increasing proportion of plagioclase at the expense of mafic minerals is well illustrated by the decreasing TiO_2, CaO, FeO^t and MgO and increasing Al_2O_3 contents from hornblendites to diorites with increasing SiO_2 (Figs. 42).

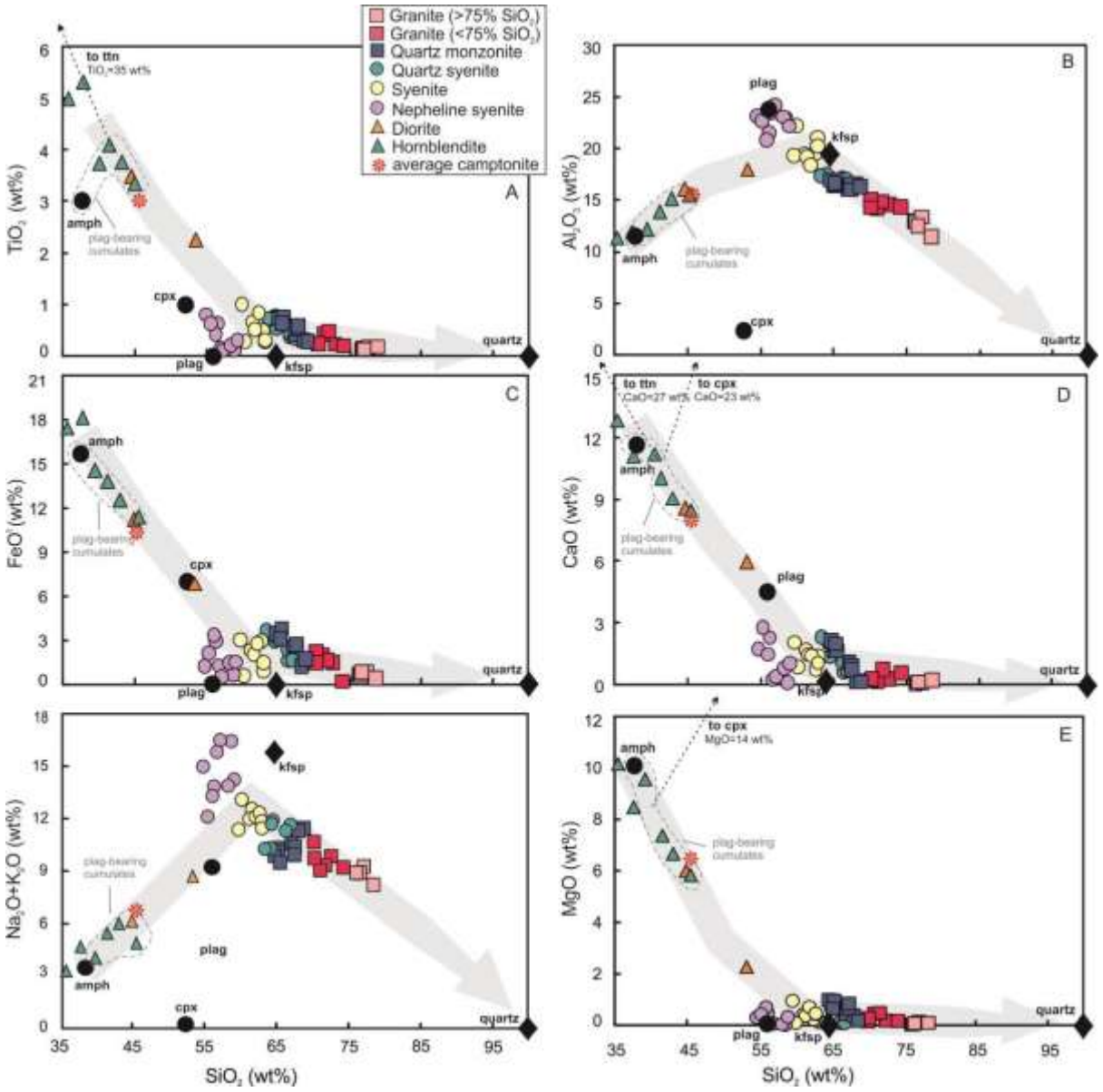

Figure 42. Major element variations of the studied rocks against SiO_2. Representative compositions of plagioclase feldspar, clinopyroxene, amphibole, titanite from hornblendite (sample ÁGK 6547; Almasi, E., 2015), K-feldspar from syenite (sample ÁGK 7404; Sogrik, E., 2010), the composition of quartz and the average composition of Ditrău camptonites (Batki, 2009) are also shown. Black circles indicate amphibole, plagioclase feldspar and clinopyroxene from plagioclase-bearing hornblendite cumulates; black diamonds show K-feldspar from syenite and the average composition of quartz; red asterisk represents the composition of average camptonite. The grey field shows the path of the evolving magma as a function of the accumulation of amphibole, clinopyroxene, titanite, plagioclase, K-feldspar and quartz.

The variation in composition in the weakly alkaline felsic rocks can be adequately explained by the different proportion of their main constituents like albite, K-feldspars and quartz. Accumulation of K-feldspar as the second alkali- and Al_2O_3-rich phase next to albite provided the opportunity for the generation of syenites. The syenites consist mainly of alkali feldspar (85-90 wt% modal alkali feldspar) that is responsible for their highest alkali and Al_2O_3 contents out of the rocks in the weakly alkaline series (Figs. 42B, E). The negative correlation between the Na_2O+K_2O, Al_2O_3 and SiO_2 (r = -0.78 to -0.93) from syenites to the silica-oversaturated rocks shows the increasing importance of quartz relative to alkali feldspar (with a minor amphibole and biotite as the ferromagnesian phases) (Figs. 42B, E). The lowest values of TiO_2, CaO, FeO^t and MgO in granites is caused by their lowest amount of mafic mineral and titanite contents that is consistent with the petrographic observations.

Besides the high alkali feldspar content of nepheline syenites, their abundant nepheline with high alkali- and Al_2O_3 contents also contributed to the highest values of Na_2O+K_2O and Al_2O_3 in the studied nepheline syenites (Figs. 42B, E). The low proportion of mafic mineral in the nepheline syenites is indicated by the low CaO, FeO^t and MgO contents of these rocks (Figs. 42C, D and F).

On the basis of the above, the early crystallisation of the Na_2O+K_2O, Al_2O_3 and SiO_2 - poor mafic minerals drove the camptonite melt, from which the hornblendites crystallised, to evolve through the diorites towards the trachyte composition. The fact that the syenite samples plot on the presumed path of the evolving magma between K-feldspar and the diorites (Fig. 42B and E) is consistent with a genetic relationship between ultramafic-mafic and the more evolved weakly alkaline felsic rocks. The major element compositional variation between the different rock types of weakly alkaline series can be explained by the accumulation of their presented minerals in a varying proportion. In all probability, the wide range of major element concentrations in the nepheline syenites can be explained in the same way. However, unlike the hornblendites, the felsic cumulate rocks of the DAM (syenites, quartz monzonites and quartz syenites) do not show the distinct textures of cumulates probably owing to the higher viscositiy of their more evolved magma that prevented the crystal settling (Chappell and Wyborn, 2004).

Further evidence for the cumulate nature of most of the studied rocks is also provided by the variations of their trace elements (Fig. 28, Table 4). The increase of Sr, Ba and Rb from hornblendites to the felsic rocks is in accordance with the increasing proportion of feldspars in the cumulate succession (Figs. 28A, B and C). The negative correlation of V vs SiO_2 corresponds to the high amount of Ti-phases (mainly titanite) in hornblendites and

diorites (Fig. 28D) and their lower ratio in the felsic rocks. The wide range of Ce (from 6.51 to 33 ppm) in felsic rocks could be caused by disproportional accumulation of monazite and allanite (Fig. 28G). Crystallisation of Ti-bearing accessory phases like titanite and ilmenite probably had influence on the Nb contents of the studied rocks (Fig. 28E) as it is demonstrated by the high Nb concentrations of titanites from the hornblendites (Almási, 2015). Variation in proportion of zircon is responsible for the wide scatter of the rocks on the Zr vs SiO_2 variation diagram (Fig. 28E) during both the early and the later stages of the crystal accumulation.

To confirm the important role of the mineral accumulation in the evolution of Ditrău Alkaline Massif, studied rocks were plotted on the Nb versus Zr diagram (Fig. 43). When the rocks represent liquid compositions and are related by fractional crystallisation, both Nb and Zr remain incompatible throughout the entire fractionation in the case of closed system, and the rocks should plot along the same constant Zr/Nb line that indicates the main fractionation trend (Wilson et al., 1995). Thus, plot of incompatible elements provides a useful tool to test the fractional crystallisation-controlled origin of the genetically related rock series. On the basis of these, any deviation from the constant incompatible element ratios can be generated by either crustal assimilation or the accumulation of accessory minerals in varying proportions.

Variations of these elements in Ditrău rocks clearly do not define consistent Zr/Nb ratios as it is expected from rocks with cumulative nature (Fig. 43). Despite the wide scatter of the data, two different groups can be identified: (a) wide range of Nb coupled with low Zr contents (< 200 ppm) is mainly represented by the silica-richer granites, AOD 11 out of the granites with SiO_2 < 75 wt%, diorites and syenite AOD 26 (indicated by grey dashed line); (b) samples with higher Zr (> 200 ppm) and more restricted Nb contents plot around the constant line of Zr/Nb = 3, defined by the best fit of these samples. As the first group is defined mainly by samples with disturbed Sr and Pb radiogenic isotope compositions that had been interpreted above as being related to subsolidus alterations (based on their $\Delta_{quartz\text{-}feldspar}$ values; see Fig. 40) and without any obvious petrographic differences compared to the rocks of the other group (i.e. higher ilmenite or titanite contents), it would be reasonable to suppose that the elevated Nb contents could be the consequences of the interaction with hydrothermal fluids. However, as Nb is considered immobile during hydrothermal alterations (Brenan et al., 1995b; Elliot et al., 1997), this cannot be the reason of elevated Nb contetns. A more probable explanation would be the slight differences in accessory mineral assemblages of the rocks. Sogrik (2010) reported cheralite and baddeleyite inclusions from

syenites samples from Ditrău that could be identified only via SEM. In addition, Ditrău granites also contain small charalite and thorite inclusions that could be identified only in course of the chemical analyses of the minerals. The occurrence or the lack of these HFSE-rich inclusions in the rocks can be responsible for the elevated or reduced concentrations of these elements, however this clearly requires additional research. Considering the other group of rocks in Fig. 43, the significant scatter of Zr and Nb around the Zr/Nb = 3 line is consistent with the irregular accumulation of accessory phases in the studied rocks. The lowest contents of Zr and Nb occur in the quartz monzonite (AOD 32 and 28), syenite (ÁGK 6727) and granite (ÁGK 6842) samples that are also characterised by the lowest εNd_i and the highest magma $\delta^{18}O$ values (Fig. 43, Table 8). Furthermore, AOD 32 and 28, ÁGK 6727 and ÁGK 6842 also plot together with the wall rock samples (grey field in Fig. 43), which suggests that probably other processes then closed system crystallisation and crystal accumulation played an important role in the petrogenesis of the studied rocks because their incompatible element contents could be lowered by crustal contamination with the low HFSE-bearing country rocks as contaminants.

As for the nepheline syenites, the lowest Zr and Nb concentrations are not presented by the samples with the lowest εNd_i values. A possible explanation for the wide scatter of Nb and Zr contents of the nepheline syenites is the varying proportion of accessory minerals like zircon and titanite in these rocks.

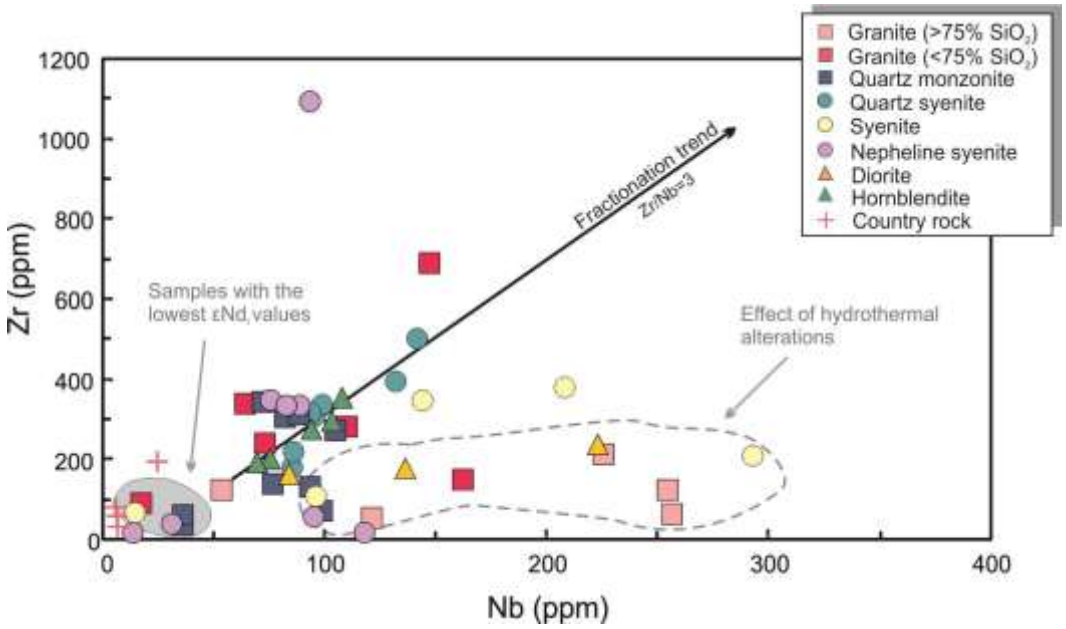

Figure 43. Variation of Nb vs Zr for the studied rocks from the Ditrău Alkaline Massif. Black arrow, defined by the best fit of the samples with higher Zr content, would indicate the expected fractionation trend from ultramafic towards the most evolved rocks if the dominant differentiation process was the fractional crystallisation. Grey field shows the samples characterised by the lowest εNd_i values, whereas grey dashed line highlights the samples with the disturbed Sr and Pb isotope characteristics based their $\Delta_{quartz\text{-}feldspar}$ values.

8.2.2 Interpretation of rare earth element patterns

Whereas chondrite-normalised REE diagrams of the syenites and nepheline syenites show similarities, the silica-oversaturated rocks are characterised by different REE patterns. In the case of syenites and nepheline syenites 3 patterns have been defined (Section 6.5; Fig. 37): (a) samples with positive Eu-anomalies and MREE-depletion (ÁGK 7426, 7427 syenites and AOD 25 nepheline syenites); (b) samples with negative Eu-anomalies, high LREE, and minor MREE depletion (AOD 26 syenite and AOD 25d, ÁGK 7446/3 nepheline syenites); (c) samples with no Eu-anomaly and moderate LREE enrichment.

The partition coefficients for middle rare earth elements in titanite are well known as it is shown by the experimental data of Green (1994): $Kd_{ttn}^{La} = \sim 2$, $Kd_{ttn}^{Sm} = \sim 9$, $Kd_{ttn}^{Ho} = \sim 8.5$, $Kd_{ttn}^{Lu} = \sim 5$ calculated for basalt-andesite melt at 1000°C and 0.75 GPa conditions. However, considering the chondrite-normalised REE pattern of titanite from Ditrău hornblendites (Almási, 2015) (not shown in the thesis), it can be concluded that the decreasing amount of titanite from hornblendites towards the felsic rocks cannot alone be responsible for the MREE-depletion of syenites (e.g. ÁGK 7426 and 7427) and nepheline syenites (e.g. AOD 25) as Ditrău titanites do not show MREE-enrichment compared to their LREE and HREE element contents (Almási, 2015). Apart from titanite, crystallisation of amphibole also can cause strong depletion in MREEs (Bernth et al., 2002, Wilson et al., 1995). The chondrite-normalised REE pattern of both intercumulus and cumulus amphibole, separated from Ditrău hornblendites by Almási (2015) (not shown in the thesis), demonstrates the elevated MREE content of this mineral. On the basis of the REE contents of amphibole and titanite of Ditrău hornblendites, these minerals together are adequate candidates to explain the broad range of LREE- and MREE-compositions of Ditrău syenites and nepheline syenites. This is also supported by the variable amount of titanite and amphibole in these rocks.

The closely identical REE patterns of nepheline syenites and syenites (see the Section 6.5 for the description) despite their highest variability of rare earth element contents out of the studied rocks would suggest that both silica-undersaturated and silica-oversaturated magmas experienced similar magmatic processes until this level of their evolution. As the REE patterns of both Ditrău nepheline syenites and syenites correspond to that of cumulates whose basaltic parental melt was contaminated by metapelitic upper crust from Kumar and Singh (2014) (see the explanation below), these consistent processes could be the crystal settling and crustal assimilation. According tos the theoretical model calculations made by Kumar and Singh (2014), cumulate piles from a basaltic parental melt experienced upper

crustal assimilation show continuous increase of REE concentrations with the progressive crystal fractionation and assimilation. This is well illustrated by the enriched REE contents of cumulates at the 'advanced stage' (F = below 20%) of the crystal accumulation in Fig. 44. Furthermore, the model calculation shows that the 'early cumulates' (F = up to 40%) are characterised by positive Eu-anomalies, whereas cumulates that formed later at the more evolved stage of crystal fractionation (F = below 20%) show no, or negative Eu-anomaly even if they still contain a lot of plagioclase.

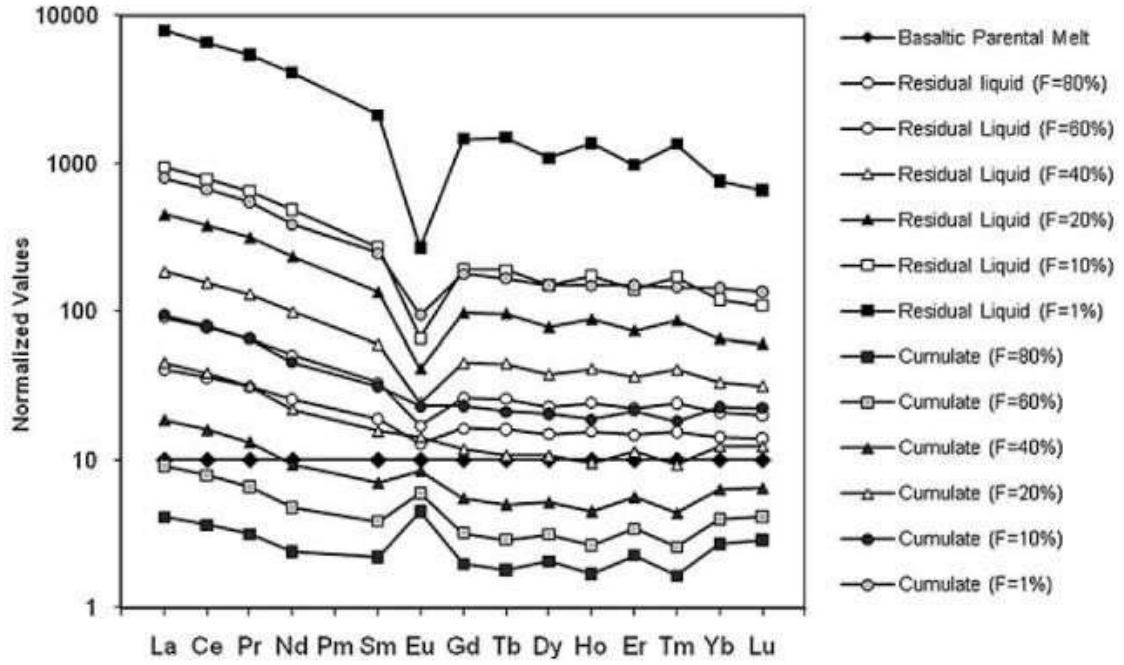

Figure 44. Increase of the REE contents of cumulates during the progressive crystal accumulation and upper crustal assimilation in the hypothetical model of Kumar and Singh (2014). F - fraction of magma remaining. REE concentrations are normalised to parent magma.

In this regard REE patterns of syenites ÁGK 7426, 7427 and nepheline syenites AOD 25 are in accordance with the early stages of crystal accumulation (Fig. 45), whereas samples with higher REE contents with no or negative Eu-anomalies represent 'advanced cumulates' that formed at the later stages of the crystal settling and experienced higher degree of crustal contamination (similarly to the cumulates F = below 20% in Fig. 44). Quartz-bearing rocks also should be considered as 'late stage', more evolved cumulates, as suggested by their overlap with the 'advanced cumulate' phase of syenites (Fig. 45A).

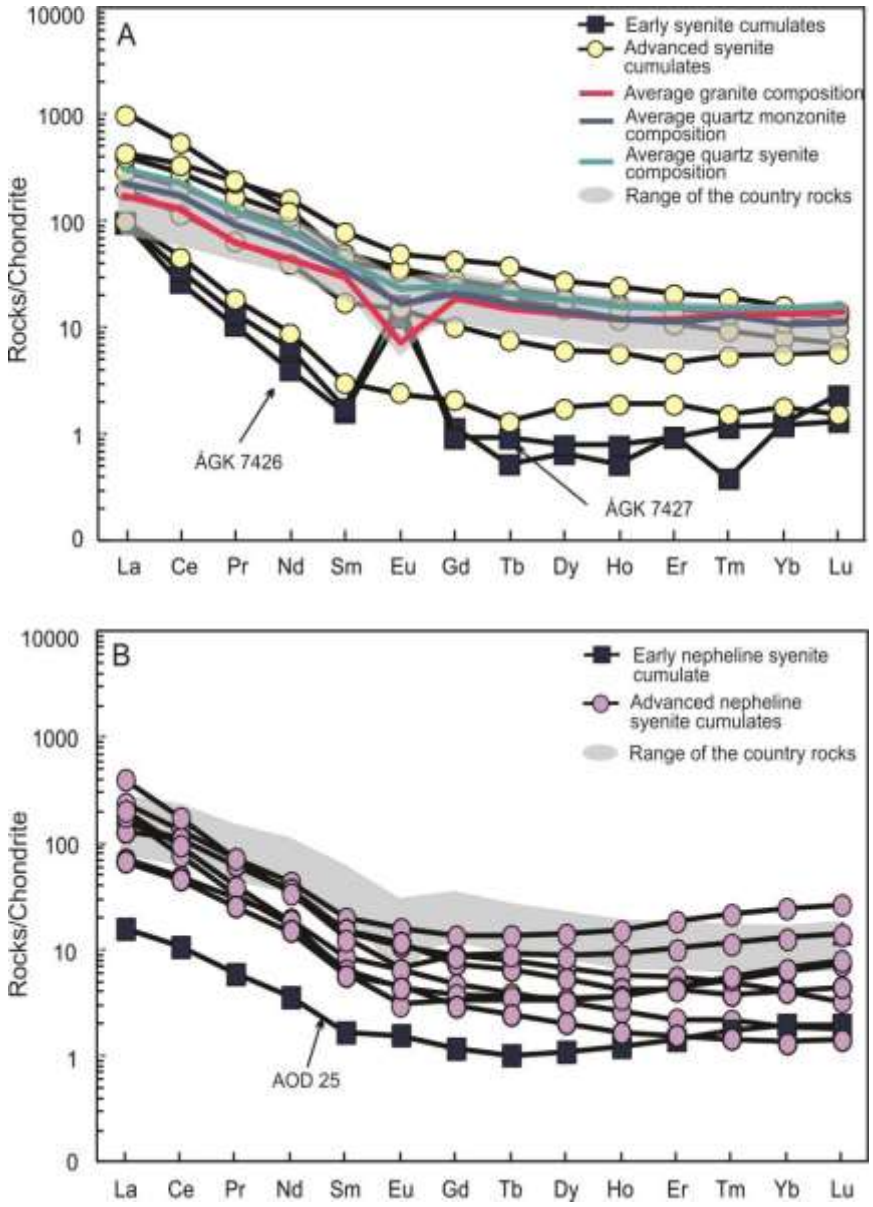

Figure 45. Chondrite-normalised REE diagrams for the (A) syenites and (B) nepheline syenites from the Ditrău Alkaline Massif. The REE spread of profile of the country rocks and average REE profiles of granites, quartz monzonites and quartz syenites are also presented. Normalizing values are from Sun and McDonough (1989).

However, instead of showing continuous increase in their REE contents, suggested by the model calculations of Kumar and Singh (2014), the REE-enrichment is not shown during the development of the cumulate succession from syenites to granites (Fig. 45A). Considering the REE-profiles of the basement rocks analysed this study, it can be seen in Fig. 45A that country rocks have somewhat lower REE contents than that of the 'advanced' Ditrău syenites. In this regard, besides the disproportional crystal accumulation (e.g. lack or varying amount of titanite, amphibole or certain accessory minerals), a supposed crustal involvement in the generation of Ditrău quartz-bearing rocks would be an adequate explanation for the decrease of REEs from syenites to granites.

In spite of their uniform REE-patterns, the silica-oversaturated rocks show variability in regards of the size of negative Eu-anomaly (0.15-0.99) and normalised LREE concentrations. The decrease of Eu/Eu* from the average quartz syenites towards the average granites coupled with the continuous decrease of normalised LREE contents is consistent with the progressive removal of LREE-enriched titanite and probably other LREE-rich accessory phases (e.g. allanite). This is also supported by the presence of both titanite and allanite in quartz syenites, whereas granites contain only minor allanite. However, taking a closer look at the relationship between the LREEs (represented by Ce) and the degree of negative Eu-anomlies (measure of the plagioclase fractionation), it can be seen in Fig. 45 that the correlation between the Eu/Eu* and LREE contents is not as straightforward as there is no correlation between the Ce contents and Eu/Eu*. This further supports the hypothesis of variable accumulation of accessory phases on the trace element contents.

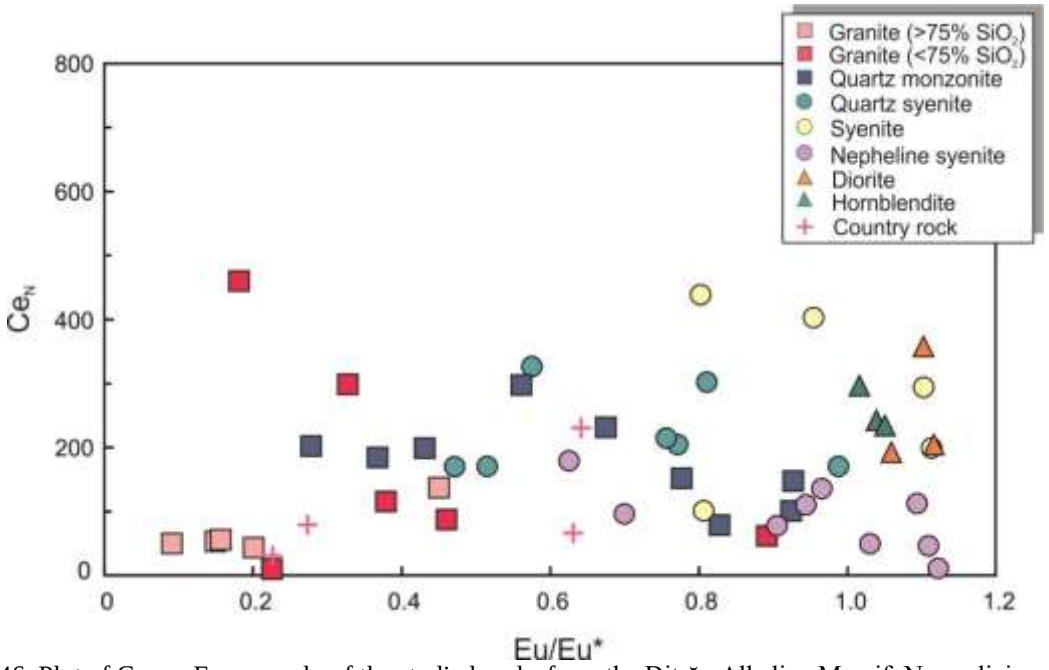

Figure 46. Plot of Ce_N vs Eu-anomaly of the studied rocks from the Ditrău Alkaline Massif. Normalizing values are from Sun and McDonough (1989).

In spite of the indication that crustal contamination may also contributed to the chemical compositions of the felsic rocks based on the overlapping REE-profiles of quartz syenite, quartz monzonite, granite and country rocks, the question is whether the nepheline syenites and granites were produced from different sources or whether crustal contamination was involved in generating the silica-oversaturated rocks from undersaturated magmas. Before assessing the role of contamination, findings on the nature of the source of the magmas are necessary.

8.3 Constraints on the source of the rocks in Ditrău Alkaline Massif

8.3.1 Estimation of the $\delta^{18}O$ values of the original magmas

The $\delta^{18}O$ value of the original rock can be calculated on the basis of the $\delta^{18}O$ values of the minerals and their modal proportions (see discussion in Harris et al., 2005) in the case of fresh rocks (e.g. Gregory and Criss. 1986; Harris et al., 1997). As the studied rocks are composed mainly of feldspar, which may have experienced some post-magmatic alteration, the result of this method would be potentially misleading. Therefore, quartz was used to determine the oxygen composition of the melt, or when data were available zircon or amphibole (Table 8). In theory, the $\delta^{18}O$ values of the minerals differ from the $\delta^{18}O$ value of their host magma by their individual mineral-melt fractionation factor ($\Delta_{mineral\text{-}melt}$). However, the calculated equilibrium $\Delta_{mineral\text{-}melt}$ at magmatic temperature (e.g. Zhao and Zheng, 2003) is not directly applicable here as the prolonged oxygen diffusion between quartz and coexisting phases would result in the quartz $\delta^{18}O$ shifting to the higher values. Thus, individual $\Delta_{quartz\text{-}melt}$ values were calculated for the Ditrău silica-oversaturated rocks by using the Equation 4. (Section 1.3) and the same A factors for quartz-feldspar, quartz-amphibole pairs that were used to calculate the internal O-isotope equilibrium between the coexisting phases in Section 8.1.

Assuming that the rocks consist of quartz, feldspars and amphibole, the modal proportions used for the calculations were: 25:67:8 for granites, 12:75:13 for quartz syenites and 16:74:10 for quartz monzonites. After the closure temperature of amphibole (800°C; Fourie and Harris, 2011) the oxygen is partitioned only between quartz and feldspars down to their closure temperature, $\Delta_{quartz\text{-}feldspar}$ was calculated at 550°C and $\Delta_{quartz\text{-}amphibole}$ at 800°C. Using the obtained per mil differences and the modal proportions of the minerals, the estimated $\Delta_{quartz\text{-}melt}$ values were 1.2 for granites, 1.3 for the quartz monzonites and 1.4 for quartz syenites. The calculated oxygen isotope compositions of the original magmas are represented in Table 9.

Zircons are an alternative proxy for magma $\delta^{18}O$ value and their O-isotope composition is easier to relate to the magma $\delta^{18}O$ than quartz. This is because of the slow diffusion rate of oxygen isotopes in zircon, their resistant nature to alteration and high closure temperature to oxygen (> 900°C) relative to most other minerals (Watson and Cherniak, 1997; Valley, 2003). Additionally, as zircon starts to crystallise early in the granitic magma (King et al., 2004), those are more likely present the initial $\delta^{18}O$ value of the host melt than

minerals that crystallise later and have lower closure temperature like quartz. The $\delta^{18}O$ value of crystallizing zircon can only change if material with different oxygen isotope composition affects its magma in the early stage of crystallisation via open-system processes. According to Valley et al. (1994), the $\delta^{18}O$ value of the crystallizing magma increases with the SiO_2 content because fractional crystallisation removes ^{18}O-depleted minerals, whereas the $\delta^{18}O$ value of zircon is nearly constant with SiO_2 of melt. This means that if the zircon is in isotope equilibrium with its host magma there is a positive correlation between the $\Delta^{18}O_{\text{whole rock-zircon}}$ and the SiO_2. Using this linear function, Lackey et al. (2008) determined the empirical relationship (Equation 21) that enables the calculation of magma oxygen isotope composition on the basis of $\delta^{18}O$ values of zircon and the related whole rock SiO_2:

$$\Delta^{18}O_{(\text{whole rock-zircon})} \approx 0.0612 * (SiO_2 \text{ wt\% whole rock}) - 2.50‰$$

Equation 21.

In the case of diorite, hornblendite and one syenite sample, only amphiboles were available for the estimation of their magma $\delta^{18}O$ values. Using -0.6 for the $\Delta_{\text{amphibole-melt}}$ as it was suggested by Harris et al. (2000), the magma $\delta^{18}O$ value of the syenite is 7.6‰, whereas that of the diorite and hornblendite is 5.7‰ (Table 9).

The estimated $\delta^{18}O_{\text{magma}}$ values on the basis of zircon data are consistently lower than those estimated on the basis of quartz $\delta^{18}O$ values (Table 9). The differences are less pronounced in granites than in the case of quartz monzonites. Using $\delta^{18}O$ values of zircon, the average $\delta^{18}O$ value for granitic magma is 6.6‰, whereas quartz suggests 9.0‰ (excluding the extreme quartz $\delta^{18}O$ = 12.9‰ of the sample ÁGK 6842). On the other hand, zircons from quartz monzonites yield 7.7‰ for the average magma $\delta^{18}O$ values, whereas on the basis of the O-isotope contents of quartz it is 9.5‰. Magma O-isotope composition calculations based on amphibole in syenites produced the same $\delta^{18}O$ values as zircons. The differences in the estimation of the $\delta^{18}O$ values of the original magmas could originate from the uncertainties of the fractionation factor, cooling rate, grain size or the model that was used to estimate the $\Delta^{18}O_{\text{quartz-magma}}$ (Fourie and Harris, 2011).

Table 9. Estimated magma O-isotope compositions on the basis of the mineral $\delta^{18}O$ values

Samples	Measured $\delta^{18}O$ values (‰)			Calculated $\delta^{18}O$ values (‰)
	Qz	Zrn	Amp	Magma
Granite				
AOD 02	9.90			8.7
AOD 04	9.91			8.7
AOD 11	10.14			9.0
AOD 12	9.70			8.5
ÁGK 6847		5.98		8.2
ÁGK 6842	12.92			11.7
ÁGK 6835		6.69		8.6
ÁGK 7459	10.49			9.3
ÁGK 7458		7.22		9.4
ÁGK 7425/A	10.93			9.7
Quartz-monzonite				
AOD 03	10.43			9.1
AOD 13	10.21			8.9
AOD 24	10.68			9.3
AOD 28	10.81			9.5
AOD 32	11.32			10
ÁGK 6848/A		6.14		7.7
ÁGK 6726	11.06			9.7
ÁGK 7460		6.31		7.8
Quartz-syenite				
AOD 01	10.00			8.6
AOD 09	10.81			9.4
AOD 10	10.33			8.9
AOD 15	9.53			8.1
AOD 22	10.25			8.8
AOD 30	10.43			9.0
AOD 31	11.56			10
Syenite				
AOD 26			7.02	7.6
ÁGK 7427		6.26		7.6
ÁGK 7426		6.01		7.4
Nepheline Syenite				
ÁGK 6769		5.11		6.2
ÁGK 7446/3		5.26		6.4
Diorite				
ÁGK 7502			5.13	5.7
Hornblendite				
ÁGK 7437			5.14	5.7

8.3.2 Nature of the possible source components

The lowest initial $^{87}Sr/^{86}Sr$ ratios (< 0.70287) and the highest εNd_i values (+5.5 - +5.0) of Ditrău rocks belong to the hornblendites, diorites and syenite ÁGK 7404 (Table 8). These isotope characteristics are consistent with a generation from a mantle source. According to the most recent studies, the parental melt of Ditrău complex was similar to OIB-like magmas (Morogan et al., 2000; Batki et al., 2014). This theory can be confirmed by the positive εNd_i values of the studied rocks as OIB magmas have predominantly positive εNd values (e.g. White, 2010). The high LILE and HFSE contents (e.g. Rb, Zr, Nd, Nb; Table 5) of Ditrău hornblendites, diorites and syenite ÁGK 7404 also support the enriched-mantle source, furthermore the lack of negative Nb and positive Ba, K anomalies in these rocks show that the enrichment of the mantle in LILE and HFSE was not via the interaction with subducting oceanic slab (Pearce and Peat, 1995; Fazlnia and Alizade, 2013).

Besides the similarities with OIB mantle source, Sr and Nd isotope compositions of Ditrău hornblendites, diorites, syenite ÁGK 7404 and certain nepheline syenites (AOD 07 and 18) overlap with that of the LREE-depleted lower crustal mafic granulite xenoliths from the western part of Pannonian Basin as well (Fig. 47C; Kempton at al., 1997). Fig 47C also shows the Sr and Nd isotope compositions of the LREE-enriched granulite xenoliths from the western part of Pannonian Basin (Kempton et al., 1997), the ultramafic mainly spinel lherzolith xenoliths from the local lithospheric upper mantle (Vaselli et al., 1995) and the local upper crustal rocks from Mason et al. (1996). Local spinel peridotites are variable. There are peridotites that are cut by metasomatic amphibole veins and have lower Nd and higher Sr isotope compositions compared to the non-metasomatised peridotites (Vaselli et al., 1995). Spinel peridotites with the metasomatic amphiboles are marked separately in Fig. 47C. Whereas hornblendites, diorites, syenites and nepheline syenites overlap with both the local mantle field and LREE-depleted lower crust, quartz-bearing rocks show similar Nd and Sr isotope ratios to the LREE-enriched lower crust. The highest $^{87}Sr/^{86}Sr_i$ ratio is found in granite ÁGK 6842 that is consistent with upper crustal input (Fig. 47C).

Fields of the local mantle and basement rocks together with the lower crustal xenoliths from the western Pannonian Basin are also represented on the $^{207}Pb/^{204}Pb_i$ and $^{208}Pb/^{204}Pb_i$ versus $^{206}Pb/^{204}Pb_i$ diagrams (Figs. 47A and B). However, because of the limited data set and the high degree overlap of the crustal components their role in the genesis of Ditrău complex remains unclear on the basis of Pb isotope comopositions.

Whereas Sr and Nd ratios of hornblendite, diorite, syenite and certain nepheline syenite AOD 07 and 18 can be explained on the basis of either the involvement of local mantle or LREE-depleted lower crust in their genesis, quartz-bearing rocks overlap with the LREE-enriched lower crust and the local upper crust (Fig. 47C). Based on the above, the contribution of the local mantle and crustal components to the formation of DAM cannot be resolved, therefore O-isotopes are considered as additional constraint.

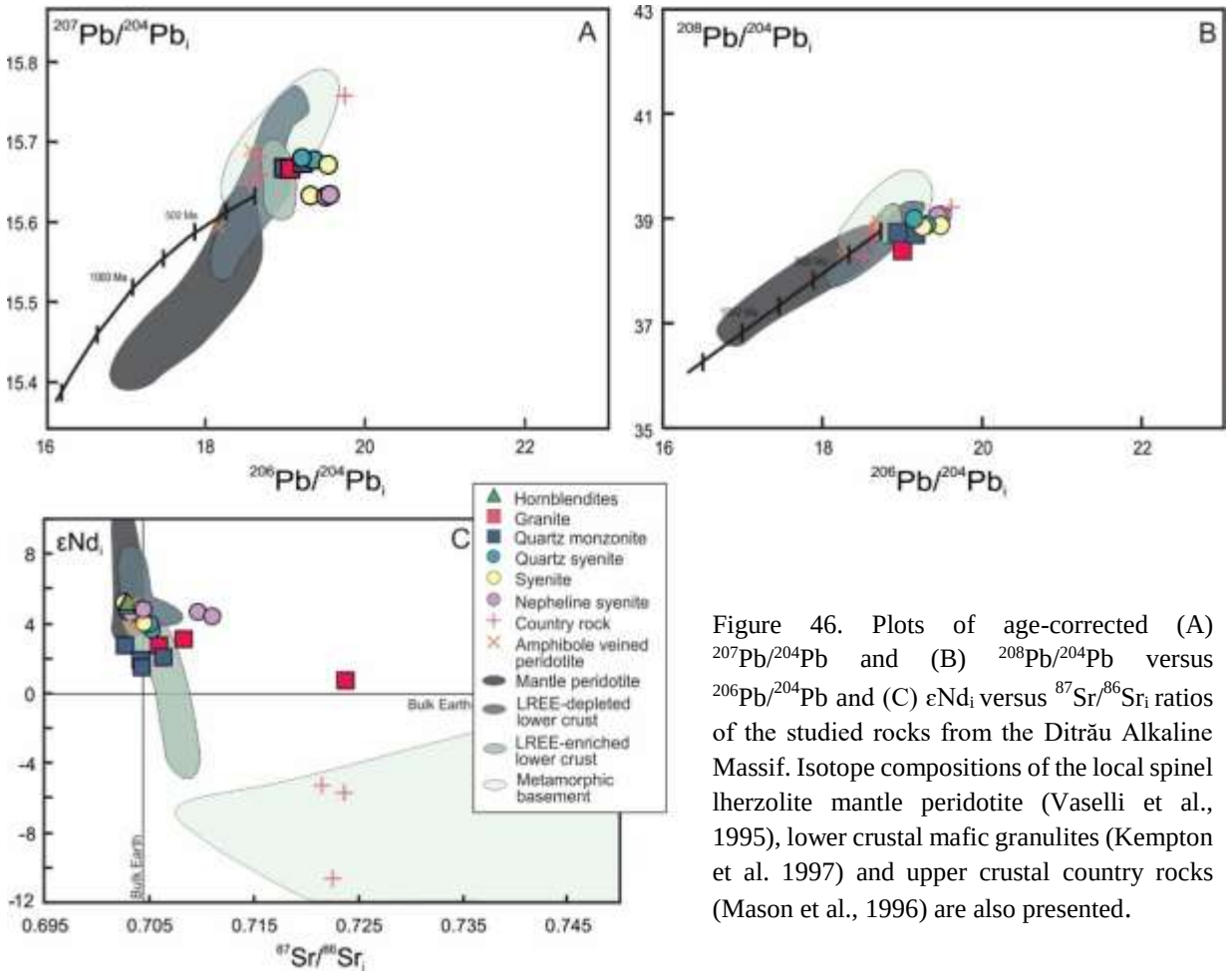

Figure 46. Plots of age-corrected (A) $^{207}Pb/^{204}Pb$ and (B) $^{208}Pb/^{204}Pb$ versus $^{206}Pb/^{204}Pb$ and (C) εNd_i versus $^{87}Sr/^{86}Sr_i$ ratios of the studied rocks from the Ditrău Alkaline Massif. Isotope compositions of the local spinel lherzolite mantle peridotite (Vaselli et al., 1995), lower crustal mafic granulites (Kempton et al. 1997) and upper crustal country rocks (Mason et al., 1996) are also presented.

Mantle-derived magmas have a narrow range of $\delta^{18}O$ values (from +5.5 to +6‰; Taylor, 1986; Eiler, 2001) compared to crustal rocks ($\delta^{18}O$ generally > 6‰; James, 1981). Therefore, because of the relatively limited O-isotope variation in the mantle and the higher and more variable crustal O-isotope ratios, oxygen isotopes are effective means of tracing any interaction between the mantle and continental crust.

The O-isotope compositions of quartz from Damaraland (Namibia) and Bushveld complexes (South Africa), Katharine Pluton (Egypt) and Podlesi Granite System (Czech Republic) were presented on Fig. 33 in Section 7.1.1 in order to compare them to $\delta^{18}O$ values of quartz from the DAM. The common feature of Nebo and Katharine granites is the dominant mantle involvement in their origin, whereas the isotope compositions of Gross Spitzkoppe complex and Podlesi Granite System require a dominantly crustal source. Although, most of the previous studies assumes a mantle origin (± minor crustal assimilation) for the source of Ditrău granites (Morogan et al., 2000; Pál-Molnár, 2000, 2015a), their similar $\delta^{18}O$ quartz values to the granites from Podlesi and Gross Spitzkoppe complexes suggests that the crustal involvement was much more significant in the formation of Ditrău granites than previously assumed. The overlapping O-isotope ratios from the quartz syenites and quartz monzonites with that of the granites support the importance of crustal component in the petrogenesis of all silica-oversaturated rocks.

The average $\delta^{18}O$ value of zircons from the studied granites is 6.5‰, which is over 1‰ higher than the mantle average (Fig. 33; Section 7.1.3). Also, as there is not known zircon above 6‰ from mantle source (Muehlenbachs and Byerly, 1982; Valley et al., 2005), the zircon $\delta^{18}O$ values of Ditrău granites require a high $\delta^{18}O$ component input to the mantle. The somewhat lower, but still above 6‰, average oxygen isotope ratios of zircons from the quartz syenites and quartz monzonites (6.22‰ and 6.13‰) are in good agreement with the involvement of crustal material in their formation as well. Only zircons from the nepheline syenites have $\delta^{18}O$ values consistent with a mantle origin.

The calculated magma oxygen isotope ratios are also higher than it would be expected for a mantle-derived magma that has undergone closed-system fractionation. This is illustrated in Fig. 48 where the average quartz and whole-rock $\delta^{18}O$ values of the uncontaminated mantle-derived peralkaline granites from Ascension Island are compared with Ditrău granites. Oxygen isotope compositions of Ascension granites (quartz $\delta^{18}O$ = 7.2‰, whole-rock $\delta^{18}O$ = 6.5‰) are after Sheppard and Harris (1985). Sheppard and Harris (1985) suggest 0.75-1‰ oxygen isotope enrichment of basaltic magma experienced fractional crystallisation up to 80% to produce rhyolitic melt. This means that $\delta^{18}O$ values outside of the range of 5.5-7‰ for alkali magmas require addition of high $\delta^{18}O$ component (i.e. crust) in addition to fractional crystallisation of basaltic magmas.

The average calculated magma O-isotope composition of the Ditrău granites (9.18‰) is 2.7‰ higher than it would be expected from mantle-derived granites (Fig. 48). Magma

$\delta^{18}O$ values of quartz syenites and quartz monzonites show 2.5‰ or 2.47‰ higher values than that of the Ascension granites (not shown). Thus, the most likely explanation for the high O-isotope ratios of silica-oversaturated Ditrău rocks is the crustal contamination that is also responsible for the variable $\delta^{18}O$ values of the studied rocks (Harris et al., 2018).

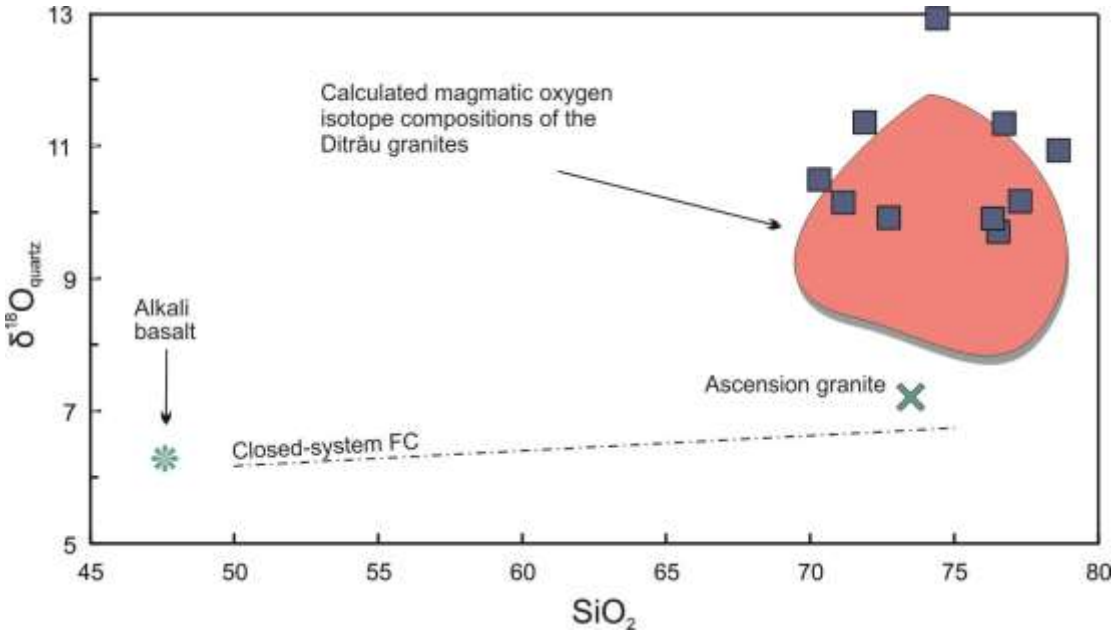

Figure 48. Plot of quartz $\delta^{18}O$ vs SiO_2 for the Ditrău granites. Calculated $\delta^{18}O_{magma}$ values of Ditrău granites and the path of the O-isotope enrichment from alkali basalt to the peralkali Ascension granites are also presented. The green cross represents the average quartz $\delta^{18}O$ value of Ascension granites. Figure is modified from Sheppard and Harris (1985) and Harris et al. (2018).

Estimated magma $\delta^{18}O$ values of hornblendite, diorite and nepheline syenites are the lowest with 5.7-6.4‰. According to the latest study, phonolitic magmas from which the Ditrău nepheline syenites crystallised were produced as fractionation residues of the basanitic parent magma (Morogan et al., 2000). Harris et al. (2000) calculated the variation of the silica-undersaturated lavas from the Tristan da Cunha and Gough Islands in $\delta^{18}O$ values with the increasing SiO_2. Assimung that the $\delta^{18}O$ value of the parental magma of the Tristan and Gough undersaturated rocks was 5.7‰ at SiO_2 = 45 wt%, Harris et al. (2000) calculations show the much smaller $\delta^{18}O$ enrichment (0.3-0.7‰) in the course of the closed-system fractionation of silica-undersaturated melts than it was suggested for Ascension magmas. Based on this, magma $\delta^{18}O$ = 6.2-6.4‰ of Ditrău nepheline syenites are consistent with their proposed mantle origin by Morogan et al. (2000) with little or no crustal contamination.

Variation of the calculated values of magma $\delta^{18}O$ versus the selected major element oxides and trace element concentrations of the studied rocks are shown in Fig. 49. The lack

of the correlations (except the weak correlation of SiO_2 vs magma $\delta^{18}O$; r = 0.65) are due to the small variation of oxygen isotope ratios of the rocks compared to the wide range of their major and trace element contents. This may be because the chemical composition of the studied rocks is primarily controlled by the proportion of minerals and the crustal contamination had significant influence on SiO_2.

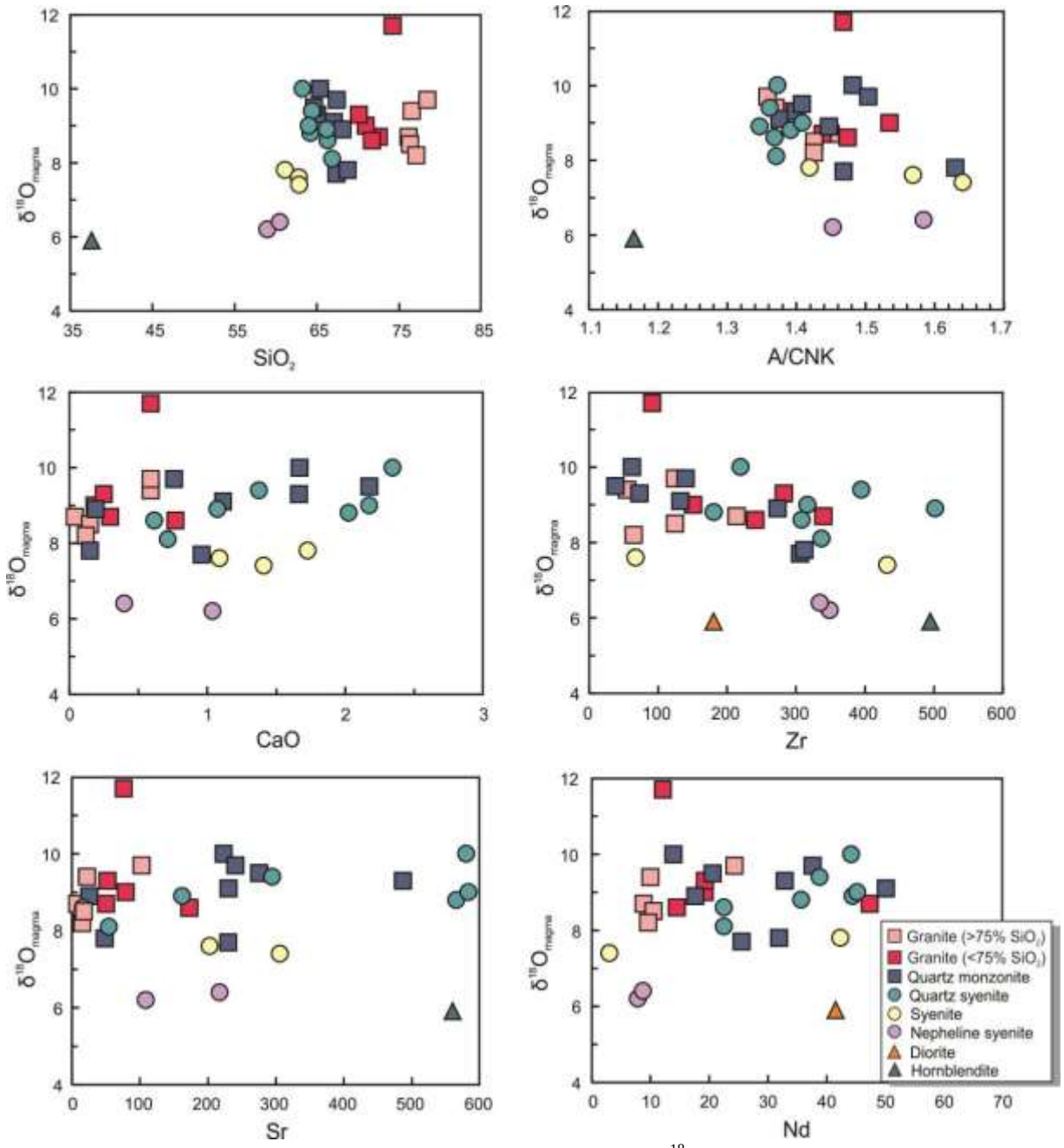

Figure 49. Selected major oxides and trace element contents versus $\delta^{18}O_{magma}$ values of the studied rocks from the Ditrău Alkaline Massif. $Al_2O_3/CaO+Na_2O+K_2O$ (A/CNK) values were calculated using oxide wt% of the major elements.

The weak relationship between the element concentration and the magma $\delta^{18}O$ values also can be the result of the incoroporation of different crustal components with variable compositions in the formation of the studied rocks. To test this assumption, magma $\delta^{18}O$ values were plotted against the εNd_i. Despite the highly variable O-isotope compositions of the Ditrău rocks (magma $\delta^{18}O$ = 5.7-11.7‰ from horblendites to granites) there is a strong negative correlation between magma $\delta^{18}O$ values and εNd_i in Fig. 50 (r = -0.86), which clearly demonstrates compositionally uniform mantle and invariable crustal components for most of the rock types. The only exceptions are the quartz monzonites.

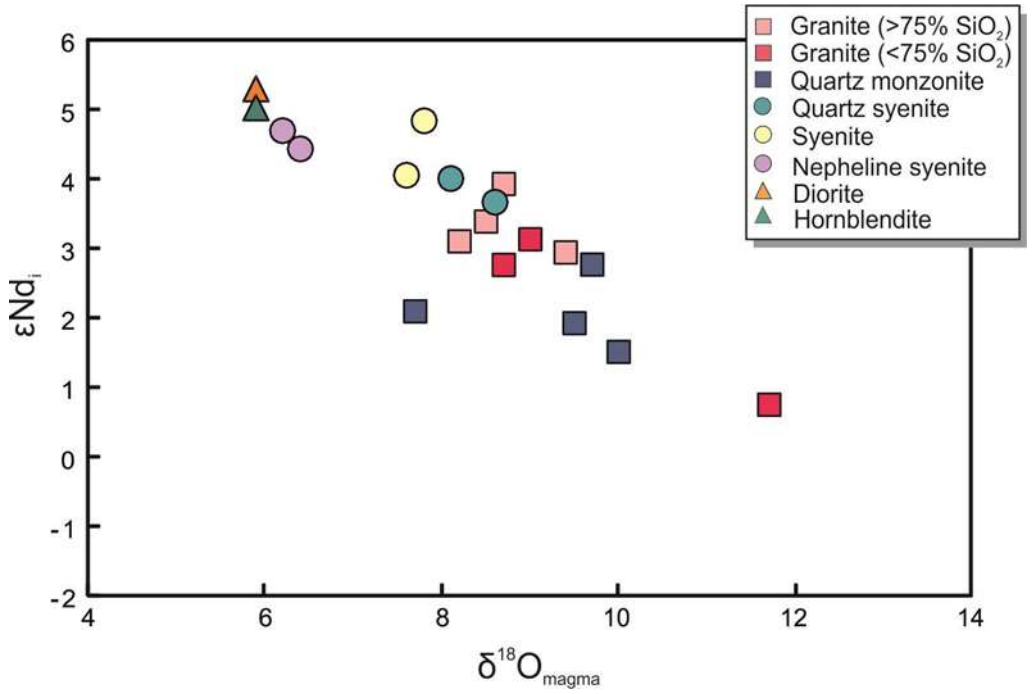

Figure 50. Plot of the magma $\delta^{18}O$ value versus εNd_i of the Ditrău rocks

Quartz monzonite sample ÁGK 6848/A has magma $\delta^{18}O$ = 7.7‰, whereas the rest of the quartz monzonites show significantly higher magma $\delta^{18}O$ > 9.5‰. Possible explanations for the differences in magma $\delta^{18}O$ values of quartz monzonites are:

1. If it is supposed that the minerals are co-magmatic, $\delta^{18}O$ values of quartz had to be shifted towards the higher values because of the highly resistant nature of zircon. Elevated oxygen isotope ratios of quartz can be caused by either interaction with low temperature fluids or O-isotope re-equilibration that took place during slow cooling.

2. The magma $\delta^{18}O$ value of the sample ÁGK 6848/A was calculated using O-isotope composition of zircons, whereas for the other quartz monzonite samples the value of quartz $\delta^{18}O$ was used. The difference in magma $\delta^{18}O$ values can be the consequence of inherited zircons from a co-genetic melt with somewhat lower $\delta^{18}O$ values or from the country rock.

As inherited zircon cores or zoning were not identified in the quartz monzonite thin sections in the course of the petrographic investigations, it is not likely that certain zircons would be antecrysts or xenocrysts. The $\delta^{18}O$ value of sample ÁGK 6848/A experienced high-temperature fluid interaction on the basis of its $\Delta_{quartz\text{-}feldspar}$ (Fig. 40) as opposed to low-temperature alteration. The differences in the calculation of the $\delta^{18}O$ values of the original magmas can originate from cooling rate, grain size or the model that was used to estimate the $\Delta^{18}O_{quartz\text{-}magma}$ (Fourie and Harris, 2011). Granites and quartz monzonites have similar texture with the same size of minerals. On the basis of their close spatial proximity these rocks must have experienced similar cooling rates. Considering the similar geological processes in the formation and cooling period of these rocks and the uniform magma $\delta^{18}O$ values of granites, the magma $\delta^{18}O$ calculations are accurate in the case of quartz monzonites as well. Therefore, a third explanation is required for the different $^{18}O_{magma}$ values of quartz monzonites:

3. Assuming the magma oxygen isotope values are correct, the most viable interpretation for the variable $\delta^{18}O_{magma}$ values of quartz monzonites is that their mantle-derived melt experienced interactions with the local crustal characterised by variable $\delta^{18}O$ values.

8.4 Modelling of crustal contamination between the mantle-derived magma and variable crustal-materials in the generation of the DAM

Radiogenic and oxygen isotope variations in the studied rocks were modelled as simple mixing mainly because of its simplicity. In any case the high temperature rift-related environment of the Ditrău massif (as discussed in Chapter 3) would favour the high assimilation/crystallisation rates (r factor) in the case of AFC processes. If the r factor is high enough, the AFC and simple mixing curves approach each other (Martinez et al., 1996, Trumbull et al., 2004), which allows the interpretation of the isotope variations in Ditrău

rocks in terms of binary mixing. On the basis of the high proportion of OH-bearing minerals in Ditrău hornblendites and their high concentration of LIL and HFS element contents, Almási (2015) supposed that sub-lithospheric amphibole-rich veins played a very important role in the formation of the parent magmas in the DAM. Besides, Batki also reported 4% melting of the enriched garnet–amphibole lherzolite mantle source at approximately 80 km depth for the generation of Ditrău camptonites that corresponds to a sub-lithospheric metasomatic zone.

During the first binary mixing model calculations (not discussed in the thesis) the average radiogenic isotope compositions of the local lithospheric mantle peridotites (Vaselli et al., 1995) were used as the mantle end-member. However, the model calculations did not reproduce the data array for Nd and O isotopes of Ditrău rocks. Therefore, mixing calculations were made using only isotope compositions of the metasomatised amphibole veins from Vaselli et al. (1995), which crosscut the local mantle peridotites as it was described in Section 8.3.2. Sample BC-10 from Vaselli et al. (1995) was chosen to represent the mantle end-member of the model to avoid the extreme isotopic ratios that characterises the other two amphibole vein samples. Isotope compositions of BC-10 sample is marked by M in Figs. 51 and 52. Bacause of the lack of oxygen isotope data from the local mantle, the average mantle value of 5.5‰ (Mattey et al., 1994; Eiler, 2001; Zhao et al., 2016) was taken into consideration. LREE-depleted mafic granulites from the eastern part of the Pannonian Basin formed from tholeiitic mantle melt and the LREE-enriched granulite shows mixing between the depleted tholeiitic mafic melt and the local upper crust (Dobosi et al., 2003) were used to represent lower crustal compositions in the model. LREE-depleted granulite sample Bo3024 (Kempton et al., 1997) was chosen for the model calculations because of its most primitive radiogenic isotope compositions and lowest O-isotope value. It is marked by LCd in Fig. 51B. The most contaminated granulite sample (Szg3004; Kempton et al., 1997) was used to represent the LREE-enriched lower crust (LCe) as the other lower crustal component (Figs. 51 and 52). The composition of upper crust (marked by UC in Figs. 51 and 52) is indicated by the samples collected from the country rock (AOD 16, AOD 17, AOD 23 and AOD 27).

Table 10. Trace element contents and isotope compositions of the end-members that were used during the binary mixing calculations.

End-members	$\delta^{18}O$ (‰)	Sr (ppm)	$^{87}Sr/^{86}Sr_i$	Nd (ppm)	εNd_i	Pb (ppm)	$^{207}Pb/^{204}Pb_i$
Mantle (BC 10)	5.5	523	0.70336	33	+5.7	663	15.55
LREE-enriched low crust (Szg3004)	10.4	103	0.70862	18	-4.4		
LREE-depleted low crust (Bo3024)	3.9			11	+7.5		
Upper Crust (AOD 16)	16.0	22	0.72786	3	-5.1	6	15.67
Upper Crust (AOD 17)				51	-1.9	8	15.77
Upper Crust (AOD 23)				19	-6.0	10	15.65
Upper Crust (AOD 27)				17	-11.0	8	15.69

Mixing curves were calculated between the mantle end-member and the four collected wall rock samples (Fig. 51A). The coupled Pb and Nd isotope modelling for the DAM is insufficient because of the lack of any clear trend (Fig. 51A). This can be the consequence of both the small number of analysed sample for Pb isotopes and the influence of hydrothermal alteration as discussed above in Section 8.1.1. By contrast the model curve approximates the Nd and O isotope data array defined by Ditrău rocks (Fig. 51B). The best-fitting curves are demonstrated in Fig. 51B. Comparison of the data array defined by the studied rocks with the calculated mixing lines indicated that the upper crust the most likely crustal component (wall rock sample AOD 23) in the formation of syenites and quartz syenites and granites. A mixture of mantle and LREE-enriched lower crust provides a good fit for the quartz monzonite sample ÁGK 6848/A that is characterised by the lowest magma $\delta^{18}O$ value out of the quartz monzonites. Quartz monzonites with higher $\delta^{18}O$ values plot off the mantle-LREE- enriched lower crust curve (Fig. 51B).

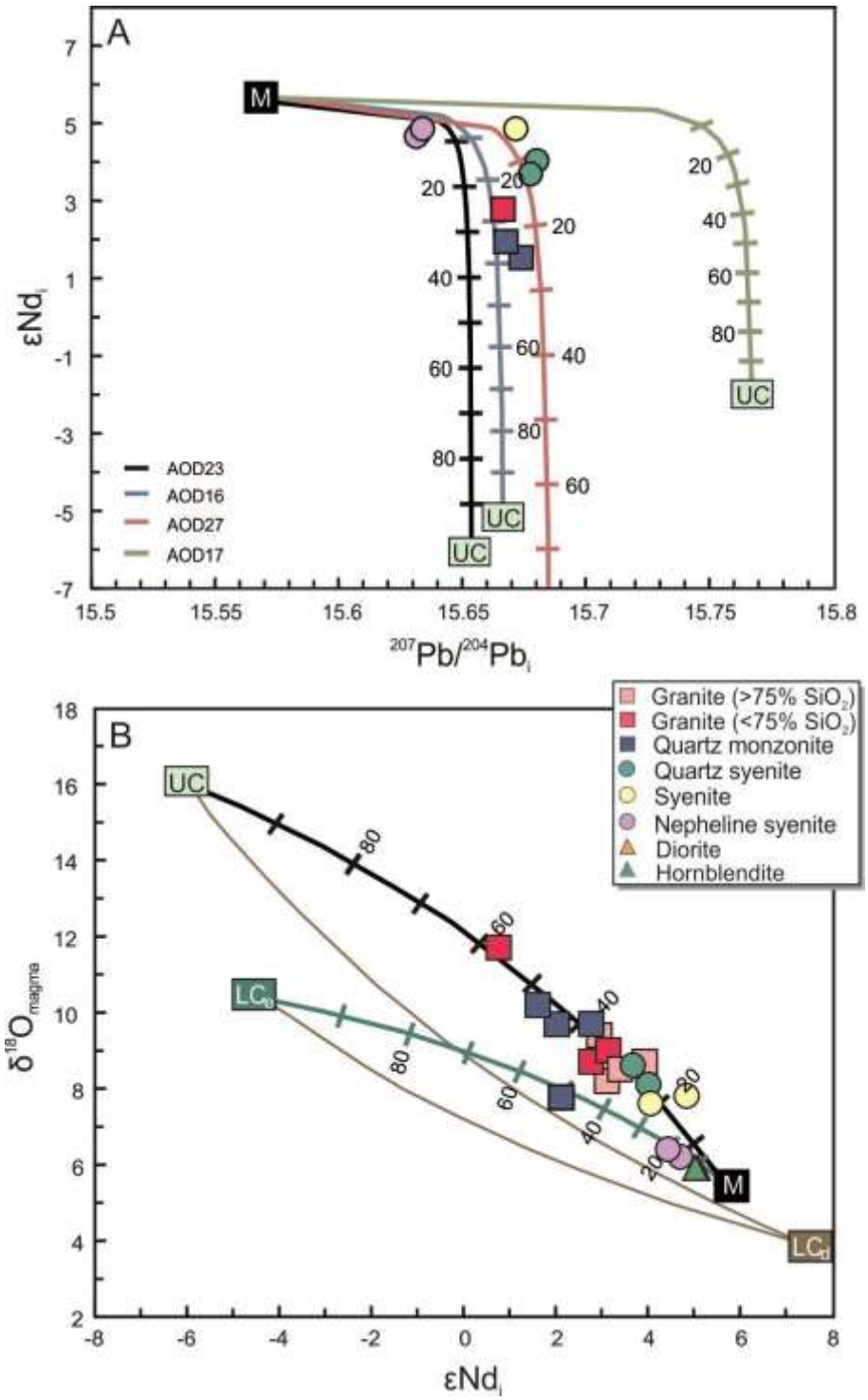

Figure 51. Plots of εNd_i versus (A) age-corrected Pb isotope and (B) magma O-isotope compositions of the studied rocks from the Ditrău Alkaline Massif. Calculated mixing curves propose contamination of mantle-derived magma by partial melts of both LREE-enriched lower crustal granulites and upper crustal acidic metavolcanics. M indicates the metasomatised amphibole veins cutting the local lithospheric mantle peridotite (sample BC 10; Vaselli et al, 1995). LCd as LREE-depleted lower crustal granulite has thought to represent a possible lower crustal protolith (sample Bo3024; Kempton et al., 1997), whereas LREE-enriched granulites (LCe; sample Szg3004) of Kempton et al. (1997) and the collected country rocks (UC) are the other lower crustal and upper crustal end-members. UC indicates sample AOD 23.

The higher $\delta^{18}O$ values of these quartz monzonites require the input of another crustal material in their genesis, which has higher $\delta^{18}O$ values than that of the LREE-enriched lower crust. The local upper crust would be a good candidate, which increased the $\delta^{18}O$ values of the quartz monzonites, because of its high $\delta^{18}O$ value of 16‰ (Table 10). The suggested variable crustal components in the formation of quartz monzonites supports the argument made in the previous section that proposes the contribution of different crustal components in the generation of the quartz monzonites and also rules out the role of LREE-depleted lower crust as the source of Ditrău rocks, as proposed on the basis of the overlap of LREE-depleted lower crust with the hornblendites, diorites and certain syenites in Fig. 47C.

The calculated binary mixing model is consistent with a small involvement of the LREE-enriched lower crust in the formation of the hornblendite, diorite and nepheline syenites (Fig. 51B). An alternative interpretation is supposing that the mantle is variable and in the case of somewhat lower εNd isotope mantle values, hornblendite, diorite and nepheline syenites would show entirely mantle origin. As the formation of hornblendite, diorite and nepheline syenites generally does not require crustal involvement, moreover the Nd and O isotope values of these rocks are consistent with that of the mantle (Tables 8 and 9), the Ditrău hornblendites, diorites and nepheline syenites are considered being 100% mantle-derived.

Despite of the good fit of Nd and O isotopes, variations of Sr vs O and Nd isotopes cannot be modeled by simple mixing (Figs 52A and B) as none of the calculated mixing curves fit the variation of hornblendite-diorite-quartz monzonite ÁGK 6848/A with nepheline syenites and syenites-quartz syenites-granites with quartz monzonites. Figs. 52A and B show only the mixing between the mantle and the preferred crustal end-members of LREE-enriched lower crust and AOD 23 as upper crust. Comparison of the mixing lines with the variations of the isotope ratios of the rocks confirms the upper crust as the most likely crustal component in the formation of quartz monzonites with high magma $\delta^{18}O$ values.

Sr content of the crustal end-members, however, is too low to show a good fit with the main trends. Calculation of the best-fitting mixing curves (marked by the dashed lines in Figs. 52A and B) for the syenites-quartz syenites-granites trend requires Sr contents in the AOD 23 upper crustal component that is 3.5 times higher than that of the mantle end-member and 7 times higher than the original Sr content of AOD 23. Small degree partial melting can concentrate the incompatible trace elements in the newly formed melt compared to the source rock.

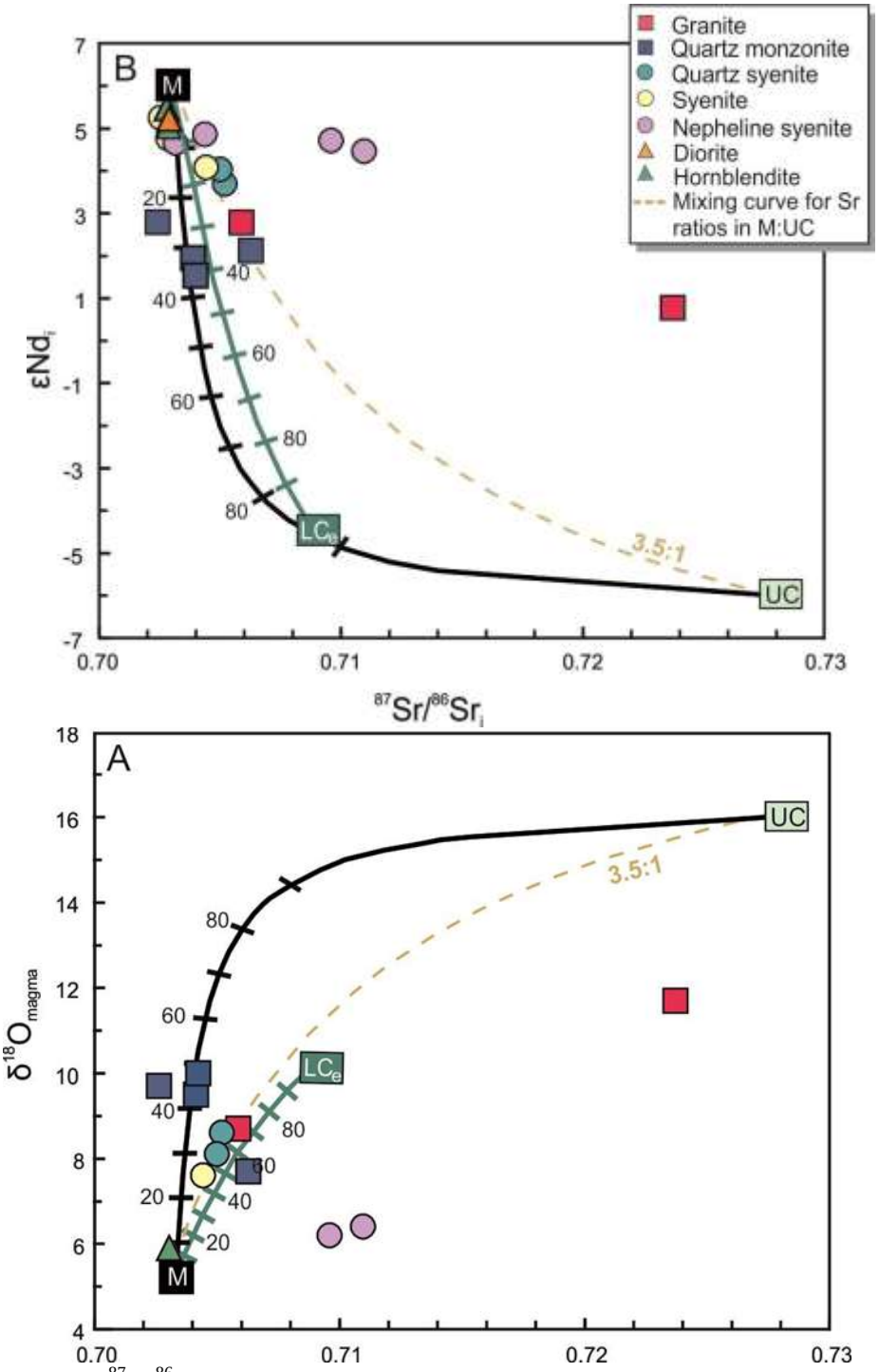

Figure 52. Variations of $^{87}Sr/^{86}Sr_i$ with the (A) magma O-isotope and (B) εNd_i in the studied rocks of the Ditrău Alkaline Massif. Calculated mixing curves with solid lines demonstrate the contamination of mantle-derived magma by partial melts of both LREE-enriched lower crustal granulites and upper crustal acidic metavolcanics. Dashed line mixing curve represents the mixing path in the case of Sr content of mantle vs crustal components are 3.5:1. UC indicates country rock sample AOD 23, whereas LCe represents LREE-enriched granulites (sample Szg3004; Kempton et al., 1997). M shows the metasomatised amphibole veins cutting the local lithospheric mantle peridotite (sample BC 10; Vaselli et al, 1995).

If it is assumed that the upper crustal component originally had 7 times higher Sr content than the measured Sr concentration, the partial melting before the mixing event would be a plausibe mechanism for the loss of upper crustal Sr. However, because of the

compatibility of Sr with plagioclase feldspar, it would have been partitioned largely into partial melting residue during crustal anatexis (e.g. Giraud et al., 1986; Rudnick, 2003) that does not support the above decribed speculation. Considering the high Sr contents of quartz monzonites (> 223 ppm) and their fit to the mantle-upper crust mixing curve, possibly the low concentration of Sr in quartz syenites and granites (< 76 ppm) places the syenite-quartz syenite-granite trend away from the preferred mixing curves by making their Sr isotope compositions sensitive to addition of radiogenic ^{87}Sr during alteration. Therefore, because of the ambiguity of initial Sr and Pb isotope ratios those are less useful than the Nd and O isotopes in characterizing the contribution of different source components in the petrogenesis of the DAM.

On the basis of the above, the Nd and O isotope variation is consistent with the increase of the upper crust (from 35 to 65%) in the source composition of granites (Fig. 51B, Table 11). Quartz syenites agrees with the incorporation of 25-35% upper crustal material into the mantle-derived melt, whereas the same it is between 20 and 25% in the case of syenites. Nd and O isotope compositions of quartz monzonite ÁGK 6848/A require 50% LREE- enriched lower crust and 50% mantle contribution in their source composition, whereas the formation of the high $\delta^{18}O$ value quartz monzonites is probably in accordance with the involvement of the $\delta^{18}O$ value local upper crust into the already contaminated mantle melt by the LREE-enriched lower crust. The calculated mixing curve for the mantle and LREE- enriched lower crust implies the entirely mantle origin of nepheline syenites and hornblendites-diorites, or alternatively a minimal crustal involvement (20 and 10% crust) also could be in the source of of Ditrău nepheline syenites and hornblendites-diorites (Table 11).

Table 11. Involvement of the mantle, lower crust and upper crust in the generation of Ditrău rocks on the basis of binary mixing calculations.

Rock type	Mantle (%)	Lower crust (%)	Upper crust (%)
Granite	35-65		35-65
Quartz monzonite ($\delta^{18}O = 7.7‰$)	50	50	
Quartz monzonite ($\delta^{18}O > 9.5‰$)	50	50	involvement in the mantle and lower crustal hybrid magma (50:50) to produce the high $\delta^{18}O$ quartz monzonites
Quartz syenite	70-75		25-30
Syenite	80-85		20-25
Nepheline syenite	100	or 15-20	
Diorite	100	or 10	
Hornblendite	100	or 10	

Chapter 9: Petrogenetic model for the Ditrău Alkaline Massif

Before proposing a petrogenetic model for the Ditrău Alkaline Massif it is important to briefly discuss its tectonic enviroment. According to the major and trace element geochemistry of Ditrău silica-saturated and oversaturated rocks, those can be classified as ferroan A-type (Fig. 53A and E).

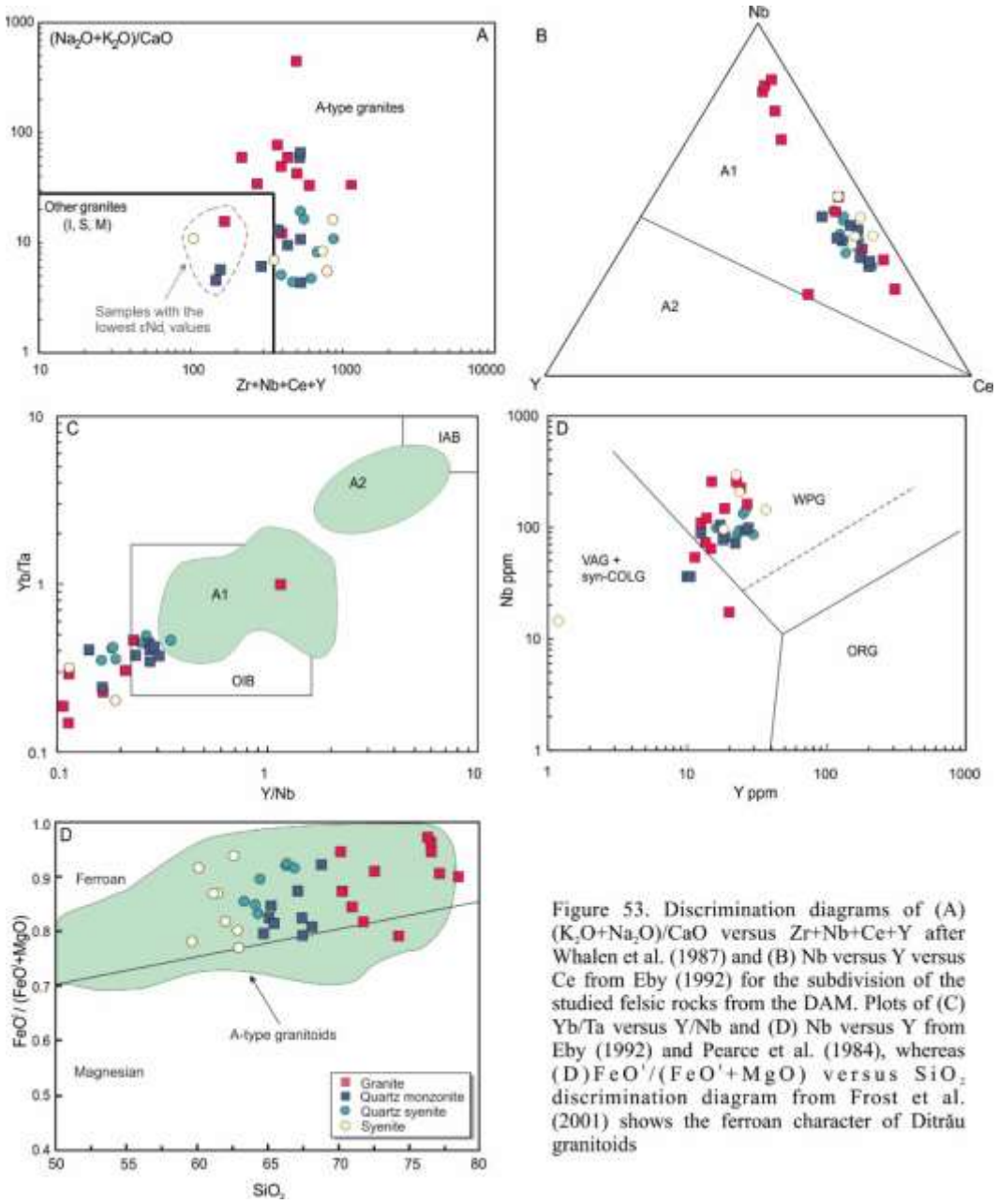

Figure 53. Discrimination diagrams of (A) $(K_2O+Na_2O)/CaO$ versus Zr+Nb+Ce+Y after Whalen et al. (1987) and (B) Nb versus Y versus Ce from Eby (1992) for the subdivision of the studied felsic rocks from the DAM. Plots of (C) Yb/Ta versus Y/Nb and (D) Nb versus Y from Eby (1992) and Pearce et al. (1984), whereas (D) $FeO'/(FeO'+MgO)$ versus SiO_2 discrimination diagram from Frost et al. (2001) shows the ferroan character of Ditrău granitoids

As mentioned in Section 2.3, A-type granites crystallise under low H_2O conditions either from the differentiation of alkali basalt parental magma (with or without crustal contamination or by partial melting of lower crustal granulitic residue in non-orogenic settings

(Loiselle and Wones, 1979; White, 1979; Collins, 1982). The studied rocks belong to the A1 group of Eby (1992) that represents mantle-derived granitoids occured in continental rift systems or intraplate environments (Fig. 53B).

The low Y/Nb ratios of the rocks (Fig. 53C) suggest an OIB affinity for the mantle component in their source composition that is in accordance with the findings of previous authors (Morogan et al., 2000; Batki et al., 2014; Pál-Molnár et al., 2015b) and also corresponds well with the fields on Fig. 53D where the studied rocks plot and the ferroan nature of the studied rocks indicate the reduced character of their mantle source (Fig. 53E).

The discussion of tectonic settings is important mainly in terms of the heat supply that is necessary to melt the continental crust. The lithospheric thinning in the rift-related tectonic environment can provide the sufficient heat flow via asthenospheric upwelling and subsequent mantle magmatism to induce partial melting of the crust.

The petrogenetic model of the Ditrău Alkaline Massif has been principally based on explaining the variable Nd and O-isotope compositions of the different rock types in order to reveal their relationships and the process of their generation.

The results of the present study are only partly in agreement with the conclusions of previous studies (Morogan et al., 2000; Pál-Molnár 2000; Batki et al., 2014, Almási, 2015), which suggest mainly fractional crystallisation of a mantle-derived magma as a differentiation process in the DAM. Whereas the earliest studies (e.g. Streckeisen and Hunziker, 1974; Jakab, 1981, 1982; Kräutner and Bindea, 1998) considered the different rock associations (e.g. hornblendites + gabbro + diorites, syenites ± quartz-bearing rocks and nepheline syenites) as the fractionation (± assimilation) products of different types of magma intrusions (with mafic, trachytic and phonolitic compositions) originating from the same mantle source, the most recent papers conclude that the origin of hornblendites and diorites was from a camptonite magma that was evolved from a basanitic parental melt (Pál-Molnár et al., 2015b). The suggested lamprophyre melt originates from a basanite parental magma by Pál-Molnár et al. (2015b) is preferred and adopted in the description of the petrogenetic history of the DAM in the present thesis. According to Batki et al. (2018) Ditrău ijolites and nepheline syenites are derived from a Na-rich melt without specifying the composition of this magma. Batki et al. (2018) also emphasise the importance of the recharging mantle melts and mixing between these mantle-derived alkali magmas in the evolution of the DAM based the occurence of clinopyroxene antecrysts in most of the Ditrău rocks. The Nd and oxygen isotope data of the Ditrău Alkaline Massif agree with these latest studies in terms of the importance of the complex open-system processes both at the time of its generation and

during postmagmatic stages. To explain the Nd and O isotope values of the studied rocks of the DAM also require multiple replenishment events of the mantle melts (see discussion below) as well as various degree of mixing between compositionally diverse magmas to produce the hybrid cumulate rocks of the DAM. Although, the focus is mainly on the generation of silica-oversaturated and undersaturated felsic rocks in the present study, the result of the mixing calculations also reveal new indications in connection with the formation of early cumulates like hornblendite and diorite. Hereinafter, the various events leading to the formation of the complex is going to be discussed in 6 stages:

Stage 1. Mantle melting
Stage 2. Formation of hornblendite – diorite cumulate
Stage 3. Formation of quartz monzonites
Stage 4. Formation of syenite – quartz syenite – granite succession
Stage 5. Intrusion of lamprophyre dykes
Stage 6. Formation of nepheline syenites

Stage 1. The magmatic activity that generated the Ditrău Alkaline Massif took place in a rift-related environment. With progressive rifting, the lithosphere would have become thinner and the upwelling asthenospheric mantle induced the melting of the local depleted shallow lithospheric spinel peridotite that was cut by LILE and HFSE enriched metasomatic amphibole veins (Vaselli et al, 1995). The contribution of the metasomatic amphibole veins to the emerging partial mantle melt that is consistent with the production of alkaline mafic magma have been emphasised by previos authors (Fitton et al., 1988; Foley, 1992; Médard et al., 2006; Pilet et al., 2008) as well as the role of the high pressure partial melting conditions in the formation of the silica-undersaturated melts (Falloon et al., 1988; Hirose and Kushiro, 1993; Kushiro, 1996). The significant contribution of the major and trace element enriched, more radiogenic amphibole veins (compared to the surrounding mantle) for the formation of the Ditrău complex is well supported by the good fit of Nd-O isotope model calculations, the enriched LILE and HFSE characteristics and the hydrous nature of mainly the early cumulates like hornblendite and diorite. The suggested amphibole-bearing lithospheric mantle source for the Ditrău hornblendites, diorites, syenites and nepheline syenites on the basis of the mixing model is in agreement with the required conditions of depth and mantle characteristics to produce the alkaline, silica-undersaturated basanitic parental melt of the DAM.

Stage 2. The ascending initial basanitic magma evolved to camptonite compositions by fractionation and hornblendites, gabbros and diorites formed from the lamprophyric magma (Pál-Molnár et al., 2015b). Gabbros occur in the massif, but those are not detailed in the present study due to the lack of gabbro samples collected. Hornblendites, gabbros and diorites consist of the same minerals in different modal proportion (Pál-Molnár, 2000) that suggests the existence of a cumulate pile at the bottom of the magma reservoir in which the abundance of plagioclase feldspar was increasing towards the top of the crystal mush. The common mantle origin of the Ditrău hornblendite and diorite suggests that the chemical differences between these rocks are rather attributed mostly to the disproportional accumulation of their minerals than differencies in their source composition.

Stage 3. The intrusion of the camptonite magma into the upper part of the lower crust probably heated up the surrounding LREE-enriched granulite (based on the Nd-O model calculations; Fig 51B) and caused its partial melting. Quartz-free monzonites occur in the massif (Pál-Molnár, 2000), however, these monzonites are not detailed in the thesis because of the absent of monzonite samples collected. The quartz-free variety of Ditrău monzonites were probably generated before the quartz-bearing monzonites based on their quartz-free mineral compositions (additional isotopic investigations are needed to confirm this specuation). The subequal involvement of the lower crustal and mantle-derived melts in the progressive mixing at the roof part of the magma reservoir probably gave rise the generation of quartz monzonites with the lower O-isotope ratios ($\delta^{18}O$ = 7.7‰; ÁGK 6848/A). The growing and expanding partial melting of the local lower crust probably affected the upper crust as the formation of high $\delta^{18}O$ quartz monzonites ($\delta^{18}O$ > 9.5‰; samples ÁGK 6726; AOD 28 and 32) requires the input of a material with higher $\delta^{18}O$ values than that of the lower crust (see the discussion in the previous section). Because of the similar Nd isotope composition of the two crustal end-members (εNd_i = -4.4 for LREE lower crust and -6.0 for upper crust) and the significant difference in their oxygen isotope values (10.4‰ and 16.0‰), the incorporation of the upper crust in the generation of the high $\delta^{18}O$ quartz monzonites would provide a proper explanation for the similar εNd_i (+2.1 of the ÁGK 6848/A and +2.8 - +1.5 of the high $\delta^{18}O$ quartz monzonites), but different $\delta^{18}O$ values of the Ditrău quartz monzonites (Fig. 51B).

The illustration of the petrogenetic model of the Ditrău Alkaline Massif starts from this stage of its evolution (Fig. 54). Fig. 54 proposes that the bottom of the magma chamber is mainly occupied by the hornblendite-diorite cumulate pile overlied by the crystal mush

with monzonitic composition. The uppermost part of the magma reservoir is occupied by the quartz monzonites.

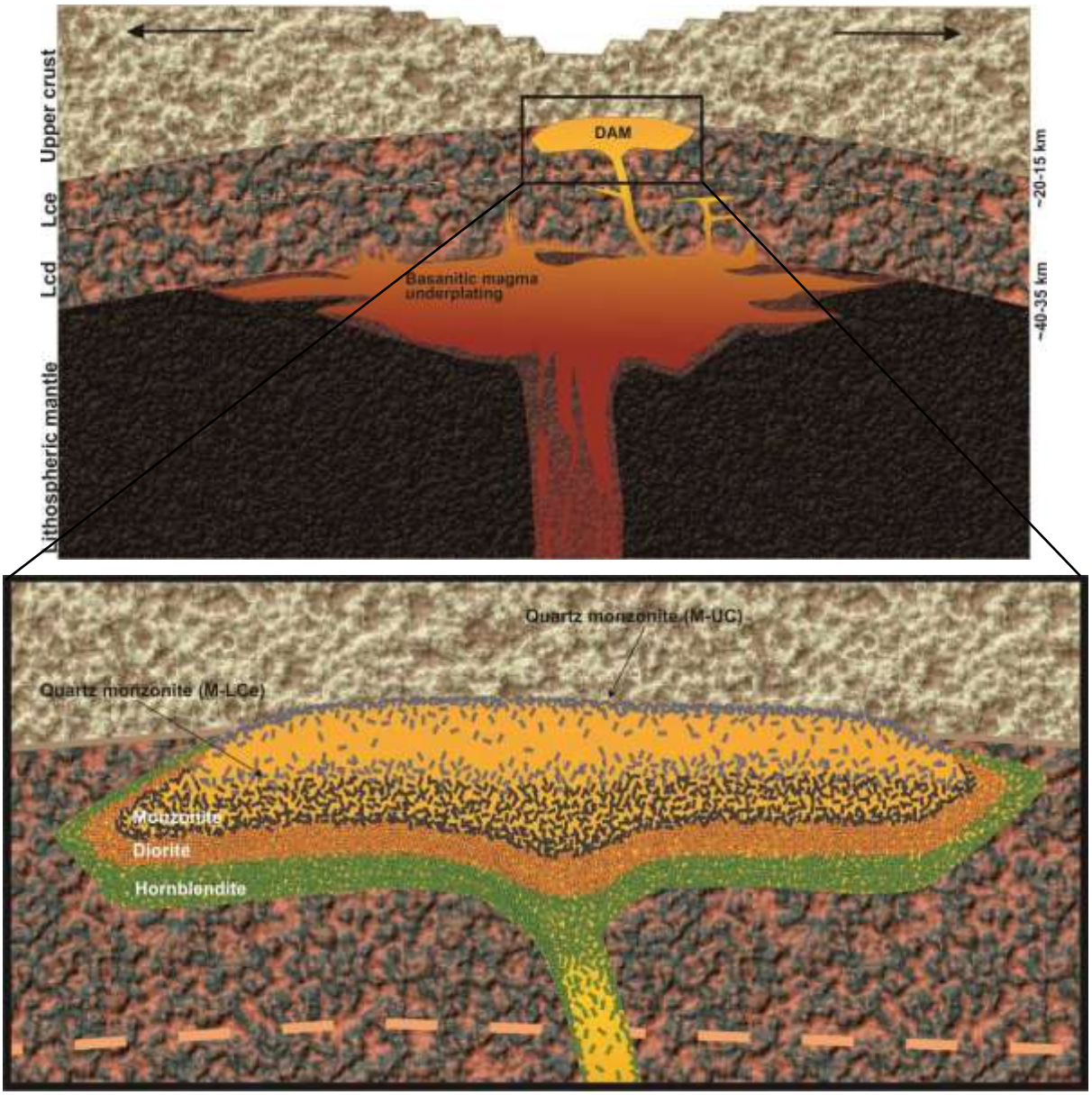

Figure 54. Schematic represantation of the evolution of hornblendites, diorites, monzonites and the two varieties of quartz monzonites of the Ditrău Alkaline Massif at the boundary of the lower and upper crust. Depth of the lithospheric mantle - lower crust and lower crust - upper crust boundaries are from Horváth, 1993, Tašárová et al., 2009. LCd - LREE-depleted lower crustal granulite; LCe – LREE-enriched lower crustal granulite.

Stage 4. Further partial melting of the upper crust to produce the proportion of crustal melt that was involved in the generation of Ditrău syenites, quartz syenites and granites (from 20 to 65% crustal component) presumably required additional heat flux. A repeated injection of camptonite melt into magma chamber is a plausible candidate to provide the needed extra heat. This successive replenishment of the mantle magma was likely able to increase the

degree of the upper crustal anatexis continuously giving rise to the formation of syenites followed by quartz syenites and eventually granites when the hybrid melt reached ~35% upper crustal compositions (Fig. 51B).

The pre-existing hornblendite-quartz monzonite crystal mush along the bottom and the wall-side of the conduits and the magma reservoir could prevent the contamination of the recharging mantle melt from the lower crustal granulites (Fig. 55). At the same time this replenishment could be responsible for the disturbance (and probably the certain degree of remelting) of the initially horizontal, somewhat compacted hornblendite-diorite cumulate layers giving an adequate explanation for the present occurence of hornbledites as lenticular and block shaped bodies in gabbros and diorites (Pál-Molnár, 2000).

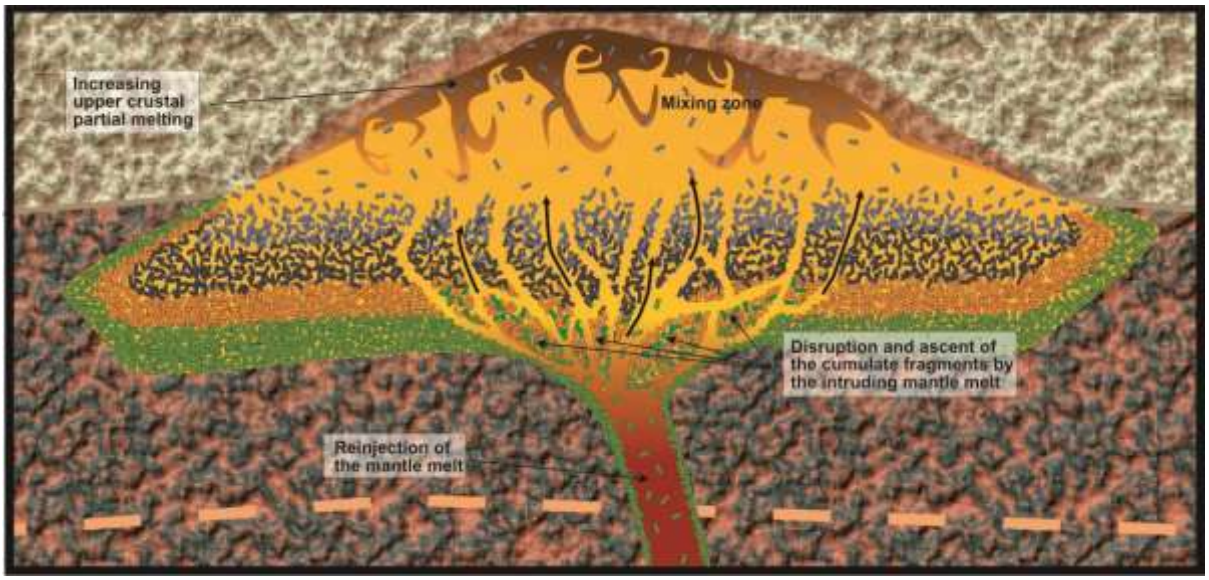

Figure 55. Recharge of the mantle-derived melt into the magma reservoir causing the disturbance and disruption of the cumulate pile of hornblendite, diorite, monzonite and quartz monzonites. The re-injected mantle melt also provided the heat flux for further crustal anatexis.

The trace element contents of the syenites, quartz syenites and granites were probably affected by the increasing proportion of the trace element-poor upper crustal partial melts or aasimilant in their source, as it is suggested by the close relation between the lowest HFSE and LILE concentrations and the lowest εNd_i, highest $\delta^{18}O$ values of these rocks (Tables 5, 8 and 9). The ~80% involvement of the LILE- and HFSE-enriched local mantle in the generation of syenites is reflected by the high trace element concentrations of syenite ÁGK 7404 with the highest $\varepsilon Nd_i = +5.1$. Furthermore, the assumed low amount of primary upper crustal partial melt, which was presumably enriched in incompatible elements on the basis of the behaviour of incompatible trace elements during the partial melting (Shaw, 1977; Allégre

and Minster, 1978), in the genesis of syenites also maintined the higher LIL and HFS element concentrations of the less contaminated syenites. The continuous melt extraction presumably lowered the incompatible element contents of the upper crustal melt. This is demonstrated by the lower LILE

and HFSE concentrations of the syenites with the highest proportion of upper crust in their source (Fig. 51B, Tables 5 and 8). The most contaminated quartz syenites (AOD 01 has εNd_i = +3.7 and $\delta^{18}O$ = 8.6) and granites (ÁGK 6848 has εNd_i = +0.8 and $\delta^{18}O$ = 11.7) are also characterised by the lowest LIL and HFS element concentrations (Tables 5 and 8) most likely as the result of greater proportion of crustal melt in their source and the continuous dilution of this anatectic melt in terms of trace element concentrations with the increasing melt volume.

Ditrău granites with different SiO_2 contents (from 70.12 to 74.22 and from 76.16 to wt%) are possibly also the result of the slight distinct proportion of mantle and upper crust end-members in their genesis. Granite samples with the higher SiO_2 contents (> 75 wt%) have lower average εNd_i and higher $\delta^{18}O$ values (+2.3 and 9.8‰; n = 3) than that of the SiO_2 - poorer granite samples with < 75 wt% (3.4 and 8.7‰; n = 4). Besides the small differences in the proportion of the trace element - enriched mantle and the trace element - poorer upper crust in the source of Ditrău granite, disproportional mineral accumulation was probably also contributed to the chemical diversity of these rocks.

Stage 5. Later on, as one of the last stages of the evolution of the Ditrău massif, mantle-derived camptonite melt was injected into the magma chamber as it is represented by the lamprophyre dykes occur in the massif. This camptonite melt was probably isolated from the crustal wall rock by the pre-existing ultramafic-felsic cumulates of the Ditrău complex, which prevented this lamprophyre melt from the crustal contamination. The lamprophyre dykes crosscut all of the Ditrău rocks.

The involvement of lower and upper crust in the evolution of the DAM suggested by the petrogenetic model described above, agrees with the results of amphibole thermobarometry calculations of Ditrău hornblendites and granites (0.7 GPa by Pál-Molnár et al., 2015b and 0.3 GPa by Pál-Molnár et al., 2015a). Amphiboles from the hornblendites yield ~25 km crystallisation depth, whereas crystallisation pressure of amphiboles from granites indicates ~14 km (Pál-Molnár et al., 2015a). The former is lower crust, the latter is upper crust. The formation of hornblendites at lower crustal depth raises the question about the presence of the

ultramafic-intermediate rocks in the upper crust embedded within the syenites at the northern part of the complex (Fig. 57). One of the possible reasons is that the mantle-derived magma replenishments not only re-melted and mixed the hornblendite-quartz monzonite cumulate piles but also disrupted them (Fig. 55). The mixed hornblendite-diorite and the overlying monzonitic fragments were slowly transferred upwards by the successive recharges and the ascent of the mantle melts and become embedded into the syenitic mush at the upper part of the magma chamber. If this is the case, the hornblendite, diorite and monzonitic bodies can be considered as autoliths in the syenite pile. Ultramafic-diorite fragments probably sank towards the bottom levels of the syenite mush because of their higher density, whereas monzonites and quartz monzonites got stucked at the upper regions because of their similar mineralogical compositions to syenites (Fig. 56).

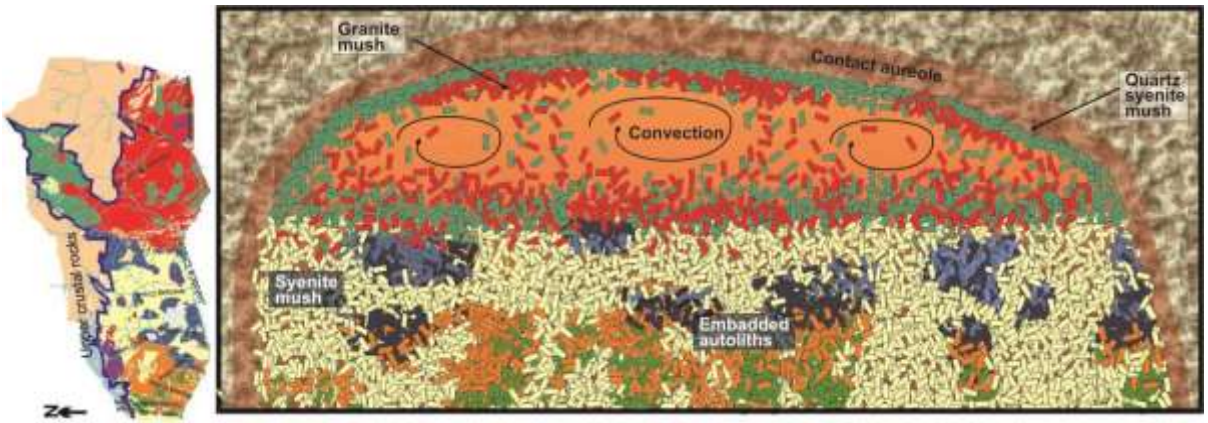

Figure 56. Schematic illustration of the disrupted and transferred hornblendite, diorite and monzonitic fragments into the upper crustal syenitic crystal mush (see the discussion in text). The north part of the geological map of the Ditrău Alkaline Massif (left-hand side) is oriented in its original vertical position, before it become tilted during the Alpine nappe formation, in order to demonstrate the correlations between the layered cumulate succession on the field and in the upper part of the magma chamber.

As it is noted in Section 3.3 there is a continuous gradation between the Tarniţa Complex (consists of hornblendite, gabbro, diorite) and monzonites, quartz monzonites, syenites, quartz syenites and granites from the north-west towards the north-east part of the DAM considered as a tilted magmatic sequence (Pál-Molnár et al., 2015b). The horizontal position of the magmatic succession is interpreted as a crystallised magmatic body that was uprooted from its source and tectonically tilted by the nappe movements during the Alpine orogeny (Pál-Molnár et al., 2015b). Fig. 56 shows the upper part of the magma reservoir of the Ditrău massif that was illustrated in accordance with the field relations of the north part of the DAM and the results of the amphibole thermobarometry from Ditrău granites (14 km upper crustal depth by Pál-Molnár et al., 2015a).

Stage 6. The last magmatic event of the Ditrău Alkaline Massif was the intrusion of phonolitic magma into the crust that formed the nepheline syenites. εNd_i vs $\delta^{18}O$ plot suggests a mantle origin of the melt of Ditrău nepheline syenites (Figs. 51B). The phonolite magma intruded into the upper crust that is suggested by both the upper crustal wall rocks around the entire massif (see the geological map of the DAM in Fig. 57) and the ~15 km cooling depth of the nepheline syenites suggested by Fall et al. (2007). The dominance of the mantle component in the genesis of nepheline syenites is evidenced by their O and Nd isotope compositions ($\delta^{18}O < 6.4‰$ and $\varepsilon Nd_i = +4.9$ to $+4.5$; Fig. 51B). Based on the uniform source composition of the nepheline syenites, the chemical variations of Ditrău nepheline syenites is probably the result of the disproportional crystal accumulation.

As the mantle end-member used in the mixing model of the studied rocks (Fig. 51B) shows good agreement with the generation of both nepheline syenites and hornblendites granite series, it raises the question how the same mantle source could produce mineralogically and chemically such a different rock types like feldspathoid-free hornblendites - granites and the nepheline syenites. The most likely explanation for the coexistence of Ditrău nepheline syenites and the silica-saturated and oversaturated series is the formation of parental melts of different compositions that were produced by the same mantle source. As described in Section 1.4, high pressure melting conditions promote the formation of silica-undersaturated rock series (e.g. Holm et al., 2006). However, the magmatic activity of the Ditrău massif relates to a continental rifting system, which requires reduced melting pressures with time. Consequently, if it is supposed that the pressure was changed between the formation of hornblendite-granite and the ijolite-nepheline-syenite-tinguaite series, partial melting of the mantle would have favoured the genetration of more silica-oversaturated rocks as the last magmatic event. Thus, the most probable explanation for the formation of silica- undersaturated series as the latest magmatic stage of the evolution of the DAM is that other parts of the local mantle source probably got involved into the increasing degree of the mantle melting next to the HFSE- and LREE-enriched amphibole veins. In spite of the fact that this seems a viable explanation, the speculation requires additional investigations.

Interaction of the ascending parental melt of nepheline syenites and the pre-existing hornblendite-granite succession is suggested on the basis of the diorite, syenite, quartz syenite and granite enclaves occur in the nepheline syenite body (Fig. 57). The diorite fragments occur in the northern part of the nepheline syenite body, the appearance of syenites

in the central and the quartz syenite and granite inclusions in the south-western part of the nepheline syenite demonstrate the layered occurence of the diorite, syenite, quartz syenite and granite enclaves in the enclosing nepheline syenites. This does not only suggest that the nepheline syenite succession was tectonically tilted together with the hornblendite-granite body during the Alpine orogeny, but also proposes the rotation of the nepheline syenite body away from the hornblendite-granite series. The northern part of the nepheline syenite with the diorite fragments is proposed to be originally the bottom of the nepheline syenite succession, whereas the south-western part of the nepheline syenite complex associated with the quartz syenite and granite enclaves represent the upper levels of the nepheline syenite cumulate pile that was in contact with the quartz-bearing rocks of Ditrău massif.

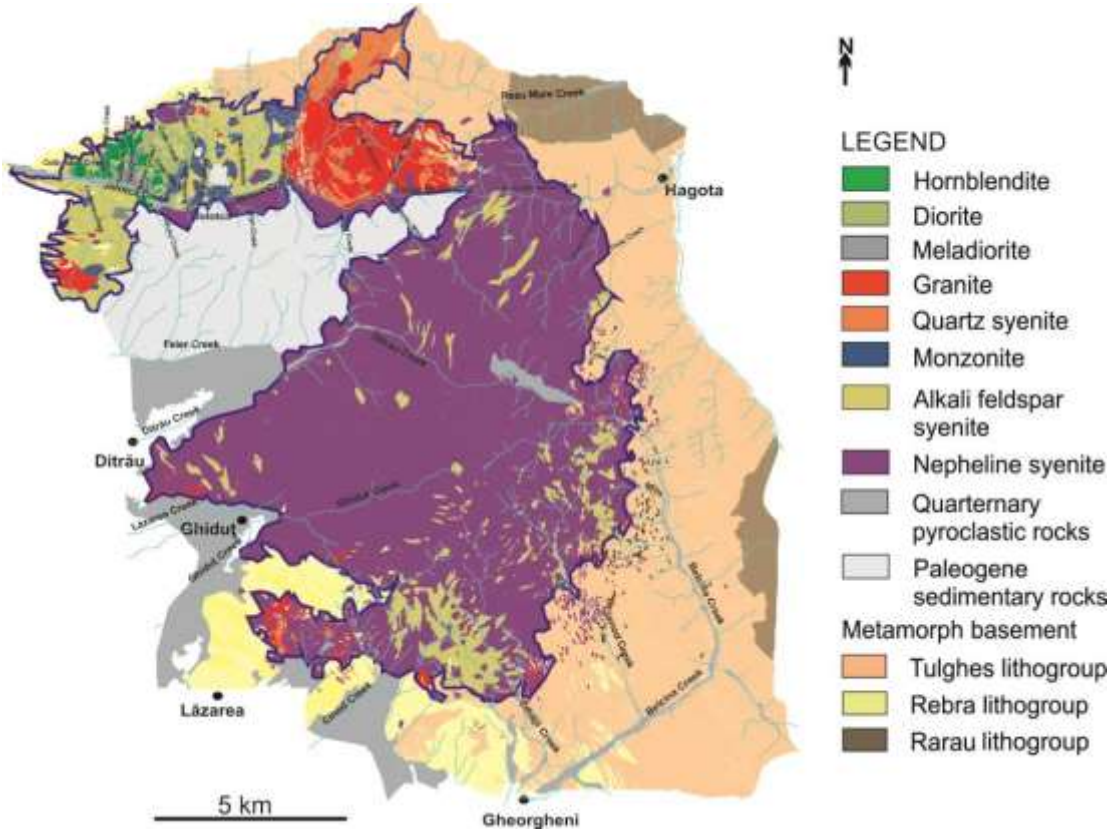

Figure 57. Geological map of the Ditrău Alkaline Massif (adapted from Pál-Molnár et al., 2015b)

Chapter 10: Concluding remarks

The present study is the first to attempt to explain the origin and the relationship of the Ditrău rocks on the basis of their isotopic composition. In particular, the project had the aim of understanding the coexistance of the silica-undersaturated and oversaturated felsic rocks mainly on the basis of isotope data. Following are the main conclusions of this research:

1. The whole-rock analyses of the studied rocks confirm the identification of the following major rock types made by previous authors: hornblendite, diorite, syenite, quartz syenite, quartz monzonite, granite and nepheline syenite were identified during the complex isotope study of the Ditrău Alkaline Massif. The re- investigation of major and trace element compositions of the Ditrău rocks suggests that most of the Ditrău rocks have formed by the accumulation of crystals (except granites) and not only hornblendites as proposed by the earlier studies (Morogan et al., 2000; Pál-Molnár et al., 2015b; Almási, 2015). This interpretation highlights that the bulk compositions of the studied plutonic rocks defined primarily on the proportion of their mineral composition, therefore the whole-rock data are not always the appropriate way to identify the composition of the melts from which they crystallised. Besides, subsolidus alterations can also have on influence on the bulk rock major and trace element data as it is represented well by for example the slightly peraluminous nature of the alkaline nepheline syenites possibly because of their abundant Al-rich secondary minerals (e.g liebenerite, sericite and clay minerals).

2. The $\delta^{18}O$ values of the analysed quartz in silica-oversaturated rocks range from 9.5 to 12.9‰ (average $\delta^{18}O = 10.6$‰; n = 24) which is consistent with the quartz $\delta^{18}O$ values of the dominantly crustal-derived granites from the Gross Spitzkoppe complex (Namibia) and Podlesi Granite System (Czech Republic). The $\delta^{18}O$ values of feldspar from the Ditrău rocks are from 7.0 to 10.8‰ (average $\delta^{18}O = 9.1$‰; n = 32), whereas that of the amphibole/pyroxene from hornblendites, diorites, nepheline syenites, syenites, quartz syenites and quartz monzonites are between 2.1 and 7.3‰ (average $\delta^{18}O = 5.4$‰; n = 16). The most consistent $\delta^{18}O$ values are shown by monazites from hornblendite, diorite, syenite and quartz monzonites ranging from 3.7 to 4.7‰ (average 4.35‰; n = 6), whereas titanite from syenites and nepheline syenites have

the widest $\delta^{18}O$ values out of the accessory minerals range from 3.6 to 7.2‰ (average 5.0‰; n = 6). Zircon have $\delta^{18}O$ values between 5.1 and 7.2‰ (average 6.1‰; n = 9) that is somewhat below the $\delta^{18}O$ values of crustal zircons ($\delta^{18}O$ > 7.5‰; Valley et al., 2005) and in accordance with the $\delta^{18}O$ values of mantle zircon (5.3‰; Valley et al., 1998).

3. Quartz and the coexisting minerals of the silica-oversaturated felsic rocks demonstrate varying degrees of O-isotope disequilibrium that is consistent with post-magmatic exchange reactions caused by both low temperature crustal and high temperature magmatic fluids. This emphasises the interpretation of the mobile major and trace element contents as well as the related radiogenic Sr and Pb isotope ratios with caution. The influence of secondary alteration on isotope compositions is well demonstrated e.g. by the extremely low $^{87}Sr/^{86}Sr$ ratios of certain granite and syenite samples that interacted with high temperature hydrothermal fluids.

4. The studied rocks have $^{208}Pb/^{204}Pb_i$ ratios from 37.393 to 39.083 (average 38.720; n =12), $^{207}Pb/^{204}Pb_i$ ratios from 15.633 to 15.809 (average 15.684; n = 12), whereas $^{206}Pb/^{204}Pb_i$ ratios range from 19.067 to 21.528 (average 19.602; n = 12). The initial $^{87}Sr/^{86}Sr$ ratios of the studied rocks are between 0.70255 and 0.72372 (average 0.70624; n = 21) excluding the extremely low disturbed $^{87}Sr/^{86}Sr$ ratios of < 0.69981 in granite and syenite samples, whereas εNd_i values range from +5.5 to +0.8 (average +3.9; n = 25). The radiogenic isotope characteristics of Ditrău hornblendites, diorites, syenites and nepheline syenites agree with that of the enriched mantle source (Zindler and Hart, 1986; White, 2010, Jackson and Dasgupta, 2008).

5. Quartz, zircon and amphibole were used as a proxy for the magma $\delta^{18}O$ values (assuming $\Delta_{quartz\text{-}magma}$ = 1.2-1.4‰; $\Delta_{zircon\text{-}magma}$ = -1.35 to - 2.22‰ and $\Delta_{amphibole\text{-}magma}$ -0.6‰). The estimated magma $\delta^{18}O$ values for Ditrău rocks are from 5.7 to 11.7‰. The calculated magma $\delta^{18}O$ values are consistent with significant crustal involvement in the origin of silica-oversaturated rocks that is essentially for their formation in an anorogenic continental rift zone (e.g. Harris, 1995), whereas hornblendites, diorites and nepheline syenites have mantle-like magma $\delta^{18}O$ values. The Nd isotope ratios of the mantle magma did not change in the course of the interaction with crustal melts on account of the juvenile Nd isotope compositions of the local crust.

6. Correlation between the $\delta^{18}O$ and εNd_i reflects the very complex origin of the Ditrău rocks. Model calculations demonstrate the variation of crustal involvement in the generation of Ditrău rocks for the first time and also emphasise that the positive εNd_i values do not necessarily reflect the dominance of mantle derivation. The two different data arrays defined by O and initial Nd isotope values of the rocks indicate the interaction between both of the lower and upper crustal partial melts and the amphibole veined shallow lithospheric mantle-derived magma. The present study was the first to consider the local mantle and crustal compositions and integrated them into the petrogenetic history of the DAM. Furthermore, the modelling suggests the existence of the western Pannonian Basin mafic granulites below the eastern region as well, which is important because of the absence of lower crustal xenoliths on the eastern area.

7. The close relationship between the highest $\delta^{18}O$ and lowest εNd_i values and the lowest HFSE and LILE element concentrations in the silica-oversaturated rocks and syenites reflects the impact of the trace element-poor crustal proportion on the chemical composition of the studied rocks besides the disproportional accumulation of their minerals.

8. The subequal mantle and crustal end-members, involved in the genesis of both the hornblendite-granite series and nepheline syenites (based on the mixing calculations), proposes the generation of slightly distinct parental melt for the silica-undersaturated series from the local mantle source to explain the different mineralogical and chemical compositions of nepheline syenites compared to the rocks of the hornblendite-granite association.

9. The silica-saturated and oversaturated felsic rocks of the DAM with variable Nd and O isotope values all have A-type characteristics on the basis of their major and HFS element compositions. The only exceptions are the syenite ÁGK 7427, quartz monzonites AOD 28, 32 and granite ÁGK 6842 with the highest crustal input in their source composition based on their highest $\delta^{18}O$ and lowest εNd_i. One of the main factors controlling the trace element contents of the Ditrău rocks is the proportion of the trace element-enrinched mantle and trace element-poor crustal end-members in their source compositions next to the modal compositions of the rocks. This means that practically the A-type character of the studied rocks relates to the HFSE-enriched

metasomatic amphiboles in the local mantle peridotite. This implies that the A-type character in the Ditrău complex does not relate strongly to the tectonic environment as metasomatic mantle amphiboles are reported not solely from rift-related tectonical settings (e.g. Dawson and Smith, 1982; Bodinier et al., 1990; Li et al., 2016).

10. This comprehensive isotopic investigation of the Ditrău massif shows well the complex evolution of the coexisted silica-oversaturated and undersaturated rocks in the DAM. The results of the present study suggest the combination of the three different proposed models to explain the coexistence of these associations in the Ditrău massif. The models were:

1. the co-spatial silica-oversaturated and undersaturated rocks are co-magmatic and the oversaturated rocks were produced by AFC processes (Foland et al., 1993)

2. the associated silica-oversaturated and undersaturated rocks are from the same mantle source, but not from the same parental melt and the generation of different magmas require distinct depths of melting (Giret and Lameyre, 1985)

3. if the magmas are derived from heterogenous sources, the silica-oversaturated magmas are the products of crustal anatexis (Harris, 1995).

The initially undersaturated parental melt of the hornblendite-granite series required extensive interactions with anatectic crustal melts to produce the quartz-bearing rocks, which partly supports the theory of Foland et al. (1993) and in full agreement with the findings of Harris (1995). The crustal anatexis associated with the intruding mantle melts in the genesis of the DAM is a well known characteristic feature of bimodal suites (Huppert and Sparks, 1988). In addition, the return of the pure mantle melt at the end of the evolution of hornblendite-granite series, as represented by the lamprophyre dykes, also agrees with the main characteristic process that causes the bimodality of bimodal associations. However, the occurence of the abundant intermediate rocks is against the bimodal nature of the Ditrău magmatism. The most plausible explanation for the coexistence of silica-oversaturated and undersaturated rocks is probably the generation of two distinct parental melt from the local mantle of the Ditrău massif, which would support the theory of Giret and Lameyre (1985). However, the variable depth in the generation of the silica-oversaturated and undersaturated melts suggested by Giret and Lameyre (1985) is not supported by the

results of the thesis. The uniform mantle source of both the Ditrău silica-saturated, oversaturated and the silica-undersaturated rocks rather suggests a small-scale extent of the mantle melting involving the more depleted, not metasomatised regions of the local mantle as well to produce the parental melt of the silica-understaurated rocks series of the DAM. To follow the viability of this speculation, further extended investigations are necessary.

REFERENCES

Allégre, C. J. and Minster, J. F. (1978). Quantitative models of trace element behaviour in magmatic processes. *Earth and Planetary Science Letters*, 66, pp. 191-213.

Allégre, C. J. (2008). *Isotope Geology*. Cambridge University Press.

Almási, E. (2015). A Ditrói Alkáli Masszívum ultramafikus kumulátum kőzeteinek petrogenetikája. Szegedi Tudományegyetem - PHD értekezés, Szeged.

Amri, I., Benoit, M. and Ceuleneer, G. (1996). Tectonic setting for the genesis of oceanic plagiogranites: evidence from a palaeo-spreading structure in the Oman ophiolite. *Earth and Planetary Science Letters*, 139, pp.177-194.

Anastasiu, N. and Constantinescu, E. (1980). Structure du massif alcalin de Ditrău. *An. Univ. Buc. Seria Geol.*, 29, pp. 3-22.

Anderson J. L. (1983). Proterozoic anorogenic granite plutonism of North America, *Geological Society of America Memoir*, 161, pp. 133-154.

Annen, C., Blundy, J. D. and Sparks, R. S. J. (2006). The genesis of intermediate and silicic magmas in deep crustal hot zones. *Journal of Petrology*, 47, pp. 505-539.

Baertschi, P. (1976). Absolute ^{18}O content of standard mean ocean water. *Earth and Planetary Science Letters*, 31, pp. 341-344.

Bagdasarien, G. P. (1972). Despre vârsta absolută a unor roci eruptive şi metamorfice din masivul Ditrău şi Munţii Banatului din românia. *Stud. Cerc. Geol. Geofiz. Geogr. Ser. Geol.*, 17 (1), pp. 13-21.

Bailey, D. K. (1978). Continental Rifting and Mantle Degassing. In: E. R., Neumann, I. B., Ramberg I.B., eds., *Petrology and Geochemistry of Continental Rifts*. NATO Advanced Study Institutes Series (Series C - Mathematical and Physical Sciences), Dordrecht: Springer, pp. 36.

Balintoni, I., Balica, C., Ducea, M., Chen, F., Hann, H. P. and Sabliovschi, V. (2009). Late Cambrian-Early Ordovician Gondwanan terranes in the Romanian Carpathians: a zircon U/Pb provenance study. *Gondwana Research*, 16, pp. 119-133.

Balintoni, I., Gheucă, I. and Vodă, A. (1983). Alpine and Hercynian overthrust Napps from Central and Southern Areas of the East Carpathians Crystalline Mesozoic Zone. *Anuarul Instutului de Geologie şi Geofizică*, LX, pp. 15-22.

Barker, F., Wones, D. R., Sharp, W. N. and Desborough, G. A. (1975). The Pikes Peak batholith, Colorado Front Range, and a model for the origin of the gabbro–anorthosite–syenite–potassic granite suite. *Precambrian Research*, 2, pp. 97-160.

Batki, A. (2009). A Ditrói Alkáli Masszívum lamprofírjainak petrogenezise. Szegedi Tudományegyetem - PHD értekezés, Szeged.

Batki, A., Pál-Molnár, E., Dobosi, G. and Skelton, A. (2014). Petrogenetic significance of ocellar camptonite dykes in the Ditrău Alkaline Massif, Romania, *Lithos*, 200-201, pp. 181-196.

Batki, A., Pál-Molnár, E., Jankovics, M. É., Kerr, A. C., Kiss, B., Markl, G., Heincz, A. and Harangi, SZ. (2018). Insights into the evolution of an alkaline magmatic system: An in situ trace element study of clinopyroxenes from the Ditrău Alkaline Massif, Romania. *Lithos*, 300-301, pp. 51-71.

Bernth, U., Brousse, R., Frei, R. and Sørensen, H. (2002). The origin of phonolites and trachytes from the Col de Guéry area, le Mont-Dore, Massif Central, France. Matematisk-Fysiske Meddelelser 50, The Royal Danish Academy of Sciences and Letters.

Bindeman, I. (2008). Oxygen isotopes in mantle and crustal magmas as revealed by single crystal analysis. *Reviews in Mineralogy and Geochemistry,* 69, pp. 445-478.

Bodinier, J. L., Vasseur, G., Vernieres, J., Dupuy, C. and Fabriès, J. (1990). Mechanisms of mantle metasomatism: geochemical evidence from the Lherz orogenic peridotite. *Journal of Petrology,* 31, pp. 597-628.

Bonin, B. (2007). A-type granites and related rocks: evolution of a concept, problems and prospects. *Lithos,* 97, pp. 1-29.

Bonin, B. and Giret, A. (1984). The plutonic alkaline series the problem of their origin and differentiation, the role of their mineralogical assemblages. *Physics of the Earth and Planetary Interiors,* 35, pp. 212-221.

Bowen, N. L. (1937). Recent high-temperature research on silicates and its significance in igneous geology. *American Journal of Science,* 33, pp. 1-21.

Brenan, J. M., Shaw, H. F., Ryerson, F. J. and Phinney, D. L. (1995b). Mineral-aqueous fluid partitioning of trace elements at 900°C and 200 GPa: constraints on the trace element chemistry of mantle and deep crustal fluids. *Geochimica et Cosmochimica Acta,* 59, pp. 3331-3350.

Chacko, T., Cole. D. R. and Horita, J. (2001). Equilibrium oxygen, hydrogen and carbon isotope fractionation factors applicable to geologic systems. *Reviews in Mineralogy and Geochemistry,* 43, pp. 1-81.

Chappell, B. W. and White, A. J. R. (1974). Two contrasting granite types. *Pacific Geology,* 8, pp. 173-174.

Chappell, B. W. and Wyborn, D. (2004). Cumulate and cumulative granites and associated rocks. *Resource Geology,* 54, pp. 227-40.

Chappell, B. W. and White, A. J. R. (2001). Two contrasting granite types: 25 years later. *Australian Journal of Earth Sciences* 48, pp. 827-831.

Cherniak, D. J., Zhang, X. Y., Nakamura, M., Watson, E. B. (2004). Oxygen diffusion in monazite. *Earth and Planetary Science Letters,* 226, pp. 161-174.

Ciborowsky, T. (2013). The geochemistry and petrogenesis of the early Proterozoic Matachewan Large Igneous Province. PhD Thesis. University of Cardiff, Wales.

Clark, I. and Fritz, P. (1999). Environmental Isotopes in Hydrogeology, 327, Lewis Publishers, Saarbrucken, Germany.

Clarke, D. B. (1992). Granitoids Rocks. Topics in the Earth Sciences. Chapman and Hall, 7, pp. 283. Clayton, R. N., Goldsmith, J. R. and Mayeda, T. K. (1989). Oxygen isotope fractionation in quartz, albite, anorthite and calcite. *Geochimica et Cosmochimica Acta,* 53, pp. 725-733.

Clemens, J. D., Holloway, J. R., White, A. J. R. (1986). Origin of an A-type granite: experimental constraints. *American Mineralogist,* 71, pp. 317-324.

Codarcea, A. Codarcea, D. M. and Ianovici, V. (1957). Structura geologică a masivului de roci alkaline de la Ditrău. *Bul. St. R.P.R. Geol. Geofz.,* II (3-4), pp. 385-446.

Collins, W. J., Beams, S. D., White, A. J. R. and Chappell, B. W. (1982). Nature and origin of A- type granites with particular reference to southeastern Australia. *Contributions to Mineralogy and Petrology,* 80, pp. 189-200.

Constantinescu, E. and Anastasiu, N. (1979). Nepheline from the alkaline massif of Ditrău. *Analele Univ Buc, Geol,* XVIII, pp. 15-27.

Coplen, T. B., Kendall, C. and Hopple, J. (1983). Comparison of stable isotope reference samples. *Nature,* 302, pp. 236-238.

Cox, K. G., Bell, G. D., Pankhurst, R. J. (1979). The interpretation of igneous rocks. George Allen and Unwin, London, pp. 450.

Creaser, R. A., Price, R. C., Wormald, R. J. (1991). A-type granites revisited: assessment of a residual-source model. *Geology*, 19, pp. 163-166.

Criss, R. E. and Taylor, H.P. Jr. (1986). Meteoric-hydrothermal systems. In: J. W. Valley, H. P. Jr. Taylor and J. R. O'Neill, Eds., *Stable Isotopes in High Temperature Geological Processes*, *Mineralogical Society of America Reviews in Mineralogy*, 16, pp. 373-424.

Currie, K. L., Eby, G. N. and Gittins, J. (1986). Petrology of the Mont Saint Hilaire complex, southern Quebec: an alkaline gabbro-peralkaline syenite association. *Lithos*, 19, pp. 65-81.

Elliot, T., Plank, T., Zindler, A., White, W. and Bourdon, B. (1997). Element transport from slab to volcanic front at the Mariana arc. *Journal of Geophysical Research*, 102, pp. 14991-15019.

Elsenheimer D. and Valley J.W. (1992). In situ oxygen isotope analysis of feldspar and quartz by Nd:YAG laser microprobe. *Chemical Geology*, 101, pp. 21-42.

Dallmeyer, D. R., Kräutner, H-G. and Neubauer, F. (1997). Middle-late Triassic $^{40}Ar/^{39}Ar$ hornblende ages for early intrusions within the Ditrau alkaline massif, Rumania: Implications for Alpine rifting in the Carpathian orogen. *Geologica Carpathica*, 48, pp. 347-352.

Dansgaard, W. (1964). Stable isotopes in precipitation. *Tellus*, 16, pp. 436-463.

Dasgupta, R. and Hirschmann, M. M. (2007). Partial melting experiments of peridotite + CO_2 at 3 GPa and genesis of alkalic ocean island basalts. *Journal of Petrology*, 48, pp. 2093-2124.

Davies, G. R. and Macdonald, R. (1987). Crustal influences in the petrogenesis of the Naivasha basalt–comendite complex: combined trace element and Sr–Nd–Pb isotope constraints. *Journal of Petrology* 28, pp. 1009-1031.

Dawson, J. B. and Smith, J. V. (1982). Upper-mantle amphiboles: a review. *Mineralogical Magazine*, 45, pp. 35-46.

de La Roche, H., Leterrier, J., Grandclaude, P. and Marchal, M. (1980). A classification of volcanic and plutonic rocks using R1–R2 diagram and major element analyses. Its relationships with current nomenclature. *Chemical Geology*, 29, pp. 183-210.

DePaolo, D. J. and Wasserburg, G. J. (1976). Nd isotopic variations and petrogenetic models. *Geophysical Research Letters*, 3, pp. 249-252.

Didier, J. and Lameyre, J. (1969). Les granites du Massif Central Francais. Etude comparée des leucogranites et granodiorites. *Contributions to Mineralogy and Petrology*, 24, pp. 219-238.

Dobosi, G., Kempton, P. D., Downes, H., Embey-Isztin, A., Thirlwall, M., Greenwood, P. (2003). Lower crustal granulite xenoliths from the Pannonian basin, Hungary, part 2: Sr-Nd-Pb-Hf and O isotope evidence for formation of continental lower crust by tectonic emplacement of oceanic crust. *Contributions to Mineralogy and Petrology*, 144, pp. 671-683.

Downes, H. (1984). Sr and Nd isotope geochemistry of coexisting alkaline magma series, Cantal, Massif Central, France. *Earth and Planetary Science Letters*, 69, pp. 321-34.

Dunworth, E. A. and Bell, K. (2001). The Turiy massif, Kola peninsula, Russia: isotopic and geochemical evidence for multi-source evolution. *Journal of Petrology* 42, pp. 377-405.

Eby, G. N. (1990). The A-type granitoids: a review of their occurrence and chemical characteristics and speculations on their petrogenesis. *Lithos*, 26, pp. 115-134.

Eby, G. N. (1992). Chemical subdivision of the A-type granitoids: petrogenetic and tectonic implications. *Geology*, 20, pp. 641-644.

Eggler, D. H. (1974). Effect of CO_2 on the melting of peridotite. Yb Carnegie Instn Wash,73, pp. 215-224.

Eiler, J. M. (2001). Oxygen isotope variations of basaltic lavas and upper mantle rocks. *Reviews in Mineralogy and Geochemistry*, 43(1), pp. 319-364.

Fall, A., Bodnar, R. J., Szabó, Cs. and Pál-Molnár, E. (2007). Fluid evolution in the nepheline syenites of the Ditrău Alkaline Massif, Transylvania, Romania. *Lithos*, 95, pp. 331-345.

Falloon, T. J., Green, D. H., Hatton, C. J. and Harris, K. L. (1988). Anhydrous partial melting of a fertile and depleted peridotite from 2 to 30 kb and application to basalt petrogenesis. *Journal of Petrology*, 29, pp. 257-1282.

Faure, G. (1986). Principles of isotope geology. 2nd ed. New York, Wiley.

Fazlnia, A. and Alizade, A. (2013). Petrology and geochemistry of the Mamakan gabbroic intrusions, Urumich (Urmia), Iran: Magmatic development of an intra-oceanic arc. *Periodico di Mineralogia*, 82 (2), pp. 263-290.

Fitton, J. G. (1987). The Cameroon line, West Africa: a comparison between oceanic and continental alkaline volcanism. In: J. G., Fitton, and B. G. J., Upton, eds., *Alkaline Igneous Rocks*. Oxford: Blackwell, pp. 273-291.

Fitton, J. G., James, D., Kempton, P. D., Ormerod, D. S. and Leeman, W. P. (1988). The role of lithospheric mantle in the generation of Late Cenozoic basic magmas in the western United States. *Journal of Petrology*, 1, pp. 331-349 (Special Volume).

Floyd, P. A., Yaliniz, M. K. and Göncüoğlu, M. C. (1998). Geochemistry and petrogenesis of intrusive and extrusive ophiolitic plagiogranites, Central Anatolian Crystalline Complex, Turkey. *Lithos*, 42, pp. 225-241.

Foland, K. A., Landoll, J. D., Henderson, C. M. B. and Chen, J. F. (1993). Formation of cogenetic quartz and nepheline syenites. *Geochimica et Cosmochimica Acta*, 57, pp. 697-704.

Foley, S. (1992). Vein-plus-wall-rock melting mechanisms in the lithosphere and the origin of potassic alkaline magmas. *Lithos*, 28, pp. 435-453.

Fourie, D. S. and Harris, C. (2011). O-isotope study of the Bushveld Complex granites and granophyres: constraints on source composition, and assimilation. *Journal of Petrology*, 52 (11), pp. 2221-2242.

Frost, C. D. and Frost, B. R. (2011). On ferroan (A-type) granites: their compositional variability and modes of origin. *Journal of Petrology*, 52, pp. 39-53.

Frost, B. R. and Lindsley, D. H. (1992). Equilibria among Fe-Ti oxides, pyroxenes, olivine, and quartz: Part II. Application. *American Mineralogist*, 77, pp. 1004-1020.

Frost, B. R. and Frost, C. D. (2008). A geochemical classification for feldspathic igneous rocks. *Journal of Petrology*, 49, pp. 1955-1969.

Frost, B. R., Arculus, R. J., Barnes, C. G., Collins, W. J., Ellis, D. J. and Frost, C. D. (2001). A geochemical classification of granitic rocks. *Journal of Petrology*, 42, pp. 2033-2048.

Frost, C. D. and Frost, B. R. (1997). Reduced rapakivi-type granites: the tholeiite connection. *Geology*, 25, pp. 647-650.

Galer, S. J. and Abouchami, W. (1998). Practical application of lead triple spiking for correction of instrumental mass discrimination. *Mineralogical Magazine*, 62 (A), pp. 491-492

Giletti, B. J. and Yund, B. A. (1984). Oxygen diffusion in quartz. *Journal of Geophysical Research Solid Earth*, 89, pp. 4039-4046.

Giletti, B. J., Semet, M. P. and Yund, R. A. (1978). Studies in diffusion-III. Oxygen in feldspars, an

ion microprobe determination. *Geochimica and Cosmochimica Acta,* 42, pp. 45-57.

Giletti, B. J. (1986). Diffusion effects on oxygen isotope temperatures of slowly cooled igneous and metamorphic rocks. *Earth and Planetary Science Letters*, 77, pp. 218-229.

Giraud, A., Dupuy, C., Dostal, J. (1986). Behaviour of trace elements during magmatic processes in the crust: application to silicic volcanic rocks of Tuscany. *Chemical Geology*, 57, pp. 269-288.

Giret, A. and Lameyre, J. (1985). Inverted alkaline-tholeiitic sequences related to lithospheric thickness in the evolution of continental rifts and oceanic islands. *Journal of African Earth Sciences,* 3, pp. 261-268.

Giret, A., 1990. Typology, evolution, and origin of the Kerguelen plutonic series, Indian Ocean: a review. *Geological Journal*, 25, pp. 239-247 (W.S. Pitcher Special Issue).

Giret, A., Bonin, B. and Léger, J. M. (1980). Amphibole compositional trends in oversaturated and undersaturated alkaline plutonic ring complexes. *Canadian Mineralogist,* 18, pp. 481-495.

Green, T. H. (1994). Experimental studies of trace-element partitioning applicable to igneous petrogenesis - Sedona 16 years later. *Chemical Geology*, 117 (1-4), pp. 1-36.

Green, T. H. and Pearson, N. J. (1983). Effect of pressure on rare earth element partition coefficients in common magmas. *Nature*, 305, pp. 414-416.

Gregory, R. T. and Criss, R. E. (1986). Isotopic exchange in open and closed systems. In: J. W., Valley, H. P. Jr. Taylor and J. R., O'Neil, eds., *Stable Isotopes in High-Temperature Geological Processes*. Mineralogical Society of America, Reviews in Mineralogy, 16, pp. 91- 127.

Grove, T. L., Elkins-Tanton, L. T., Parman, S. W., Chatterjee, N., Müntener, O. and Gaetani, G. A. (2003). Fractional crystallisation and mantle-melting controls on calc-alkaline differentiation trends. *Contributions to Mineralogy and Petrology*, 145, pp. 515-533.

Hamilton, D. L. and MacKenzie, W. S. (1965). Phase-equilibrium studies in the system $NaAlSiO_4$ (nepheline)-$KAlSiO_4$ (kalsilite)-SiO_2-H_2O. *Mineralogical Magazine,* 34, pp. 214-231.

Heaman, L. M. and Machado, N. (1992). Timing and origin of midcontinent rift alkaline magmatism, North America: evidence from the Coldwell Complex. *Contributions to Mineralogy and Petrology* 110, 289-303.

Harris, C. (1995). Oxygen isotope geochemistry of the Mesozoic anorogenic complexes of Damaraland, northwest Namibia: evidence for crustal contamination and its effect on silica saturation, *Contributions to Mineralogy and Petrology*, 122, pp. 308-321.

Harris, C. and Ashwal, L. D. (2002). The origin of low $\delta^{18}O$ granites and related rocks from the Seychelles. *Contributions to Mineralogy and Petrology*, 143, pp. 366-376.

Harris, C. and Vogeli, J. (2010). Oxygen isotope composition of garnet in the Peninsula Granite, Cape Granite Suite, South Africa: Constraints on melting and emplacement mechanisms. *South African Journal of Geology*, 113, pp. 401-412.

Harris, C., Dreyer, T. and le Roux, P. (2018). Petrogenesis of peralkaline granite dykes of the Straumsvola complex, western Dronning Maud Land, Antarctica. *Contributions to Mineralogy and Petrology*, 173 (8).

Harris, C., Faure, K., Diamond, R.E. and Scheepers, R. (1997). Oxygen and hydrogen isotope geochemistry of S- and I-type granitoids: the Cape Granite suite, South Africa. *Chemical Geology*, 143, pp. 95-114.

Harris, C., Pronost, J. J. M., Ashwal, L. D. and Cawthorn, R. G. (2005). Oxygen and hydrogen isotope stratigraphy of the Rustenburg Layered Suite, Bushveld Complex: constraints on crustal

contamination. *Journal of Petrology,* 46, pp. 579-601.

Harris, C., Smith, H. S. and le Roex, A. P. (2000). Oxygen isotope composition of phenocrysts from Tristan da Cunha and Gough Island lavas: variation with fractional crystallization and evidence for assimilation. *Contributions to Mineralogy and Petrology*, 138, pp. 164-175.

Hart, W. K. (1985). Chemical and isotopic evidence for mixing between depleted and enriched mantle, northwestern U.S.A. *Geochimica et Cosmochimica Acta,* 49, pp. 131-144.

Hauser, N., Matteini, M., Omarini, R. H. and Pimentel, M. M. (2010). Constraints on metasomatized mantle under Central South America: evidence from Jurassic alkaline lamprophyre dykes from the Eastern Cordillera, *NM Argentina Mineralogy and Petrology,* 100, pp. 153-184.

Hawkesworth, C. J. and van Calsteren, P. W. C. (1984). Radiogenic isotopes - some geological applications. In: P., Henderson, ed., *Rare earth element geochemistry*. Amsterdam: Elsevier, pp. 375-421.

Hirose, K. and Kushiro, I. (1993). Partial melting of dry peridotites at high pressures: Determination of compositions of melts segregated from peridotite using aggregates of diamond. *Earth and Planetary Science Letters,* 114, pp. 477-489.

Hoefs, J. (1987). *Stable Isotope Geochemistry*, 3rd edition. Berlin: Springer-Verlag. Hoefs, J. (2005). *Stable Isotope Geochemistry*, 5th edition. Berlin: Springer-Verlag

Holm, P. M., Wilson, J. R., Christensen, B. P., Hansen, L., Hansen, S. L., Hein, K. M., Mortensen, A. K., Pedersen, R., Plesner, S. and Runge, M. K. (2006). Sampling the Cape Verde mantle plume: evolution of melt compositions on Santo Antão, Cape Verde Islands. *Journal of Petrology,* 47, pp. 145-189.

Holocher, K. (2005). Planilha Excel® livre acesso no site: http//www.union. edu/public/geodept/ courses/petrology/norms.htm.

Huppert, H. E. and Sparks, R. S. J. (1988). The generation of granitic magmas by intrusion of basalt into continental crust. *Journal of Petrology,* 29, pp. 599-624.

Ianovici, V. (1938). Considérations sur la consolidation du massif syénitique de Ditrău, en relation avec la tectonique de la région. *C. R. Acad. Sci. Roum*, II (6), pp. 689-694.

Ishihara, S. (1977). The magnetite-series and ilmenite-series granitic rocks. *Mining Geology*, 27, pp. 293-305.

Jackson, M. G. and Dasgupta, R. (2008). Compositions of HIMU, EM1, and EM2 from global trends between radiogenic isotopes and major elements in ocean island basalts. *Earth and Planetary Science Letters*, 276, pp. 175-186.

Jakab, Gy. (1981). O nouă concepţie privind succesiunea cronologică a fazelor de intruziune în masivul alcalin de la Ditrău. *Acta Hargitensia,* 2, An. Muz. Harghita, M.-Ciuc.

Jakab, Gy. (1982). Studiul mineralogic şi geochimic al mineralizaţiilor metalifere dintre Voşlobeni şi Corbu. PhD thesis, Universitate Alexandru. Ioan Cuza, Iaşi, Manuscript.

Jakab, Gy. (1998). Geologia Masivului alcalin de la Ditrău. Pallas-Akad., M.-Ciuc., pp. 298.

James, D. E. (1981). The combined use of oxygen and radiogenic isotopes as indicators of crustal contamination. *Annual Reviews of Earth and Planetary Sciences,* 9, pp. 311-344.

Jenkin, G. R. T., Farrow, C. M., Fallick, A. E. and Higgins, D. (1994). Oxygen isotope exchange and closure temperatures in cooling rocks. *Journal of Metamorphic Geology* 12, pp. 221-235.

Muehlenbachs, K. and Byerly, G. (1982). ^{18}O-enrichment of silicic magmas caused by crystal

fractionation at the Galapagos spreading center. *Contributions to Mineralogy and Petrology*, 79, pp. 76-79.

Katzir, Y., Litvinovsky, B. A., Jahn, B. M., Eyal, M., Zanvilevich, A. N., Valley, J. W., YeVapnik, Beeri, Y., Spicuzza, M. J. (2007b). Interrelations between coeval mafic and A-type silicic magmas from composite dykes in a bimodal suite of southern Israel, northernmost Arabian-Nubian Shield: geochemical and isotope constraints. *Lithos*, 97, pp. 336-364.

Kemp, A. I. S., Wormald, R. J., Whitehouse, M. J., Price, R. C. (2005b). Hf isotopes in zircon reveal contrasting sources and crystallization histories for alkaline and peralkaline granites of Temora, southeastern Australia. *Geology*, 33, pp. 797-800.

Kempton P. D. and Casey, J. F. (1997). Petrology and geochemistry of cross-cutting diabase dikes, Sites 920 and 921. In: J. A., Karson, M., Cannat, D. J., Miller and D., Elthon, eds., *Proceedings ODP Science Results* 153. Ocean Drilling Program, College Station, TX, pp. 363-377.

Kilinc, I. A. and Burnham, C.W. (1972). Partitioning of chloride between a silicate melt and coexisting aqueous phase from 2 to 8 kilobars. *Economic Geology*, 67, pp. 231-235.

Koch, A. (1879). A ditrói syenittömzs kőzettani és hegyszerkezeti viszonyairól. *Magyar TudományosAkadémiai Értekezések*, IX (2).

Kovács, G. and Pál-Molnár, E. (2005). A Ditrói alkáli masszívum granitoid kőzeteinek petrogenezise [Petrogenesis of granitoid rocks from the Ditrău Alkaline Massif – in Hungarian]. *Földtani Közlöny*, 135 (1), pp. 121-143.

Kramm, U. and Kogarko, L. N. (1994). Nd and Sr isotope signatures of the Khibina and Lovozero agpaitic centres, Kola Province, Russia. *Lithos* 32, pp. 225-242.

Kräutner, H. G. and Bindea, G. (1995). The Ditrău alkaline intrusive complex and its geological environment. *Romanian Journal of Mineralogy*, 77 (3), pp. 1-44.

Kräutner, H. G. and Bindea, G. (1998). Timing of the Ditrau alkaline intrusive complex (Eastern Carpathians, Romania). *Slovak Geological Magazine*, 4, pp. 213-221.

Kumar, S. and Singh, R. N. (2014). Modelling of magmatic and allied processes; Edited by Santhosh Kumar and Ram Narain Singh, Springer.

Kumar, V. K., Frost, C. D., Frost, B. R. and Chamberlain, K. R. (2007). The Chimakurti, Errakonda, and Uppalapadu plutons, Eastern Ghats Belt, India: an unusual association of tholeiitic and alkaline magmatism. *Lithos*, 97, pp. 30-57.

Kushiro, I. (1968). Compositions of magmas formed by partial zone melting of Earth upper mantle. *Journal of Geophysical Research*, 73, pp. 619-634.

Kushiro, I., (1996). Partial melting of a fertile mantle peridotite at high pressures: an experimental study using aggregates of diamond. In: A., Basu and S. R., Hart, eds., *Earth processes: reading the isotopic code*. AGU *Geophysical Monograph*, 95, pp. 109-122.

Kyser, T. K. (1987). Equilibrium fractionation factors for stable isotopes. In: T. K., Kyser, ed., *Stable Isotope Geochemistry of Low Temperature Fluids*. Short course handbook 13. *Mineralogical Association of Canada*, pp. 1-84.

Lackey, J. S, Valley, J. W., Hinke, H. J. (2006). Deciphering the source and contamination history of peraluminous magmas using delta ^{18}O of accessory minerals: examples from garnet-bearing plutons of the Sierra Nevada batholith. *Contributions to Mineralogy and Petrology*, 151, pp. 20-44.

Lackey, J. S., Valley, J. W., Chen, J. H. and Stockli, D. F. (2008). Dynamic magma systems, crustal recycling, and alteration in the central Sierra Nevada Batholith: the oxygen isotope record.

Journal of Petrology, 49, pp. 1397-1426.

Lameyre, J. and Bowden, P. (1982). Plutonic rock types series: discrimination of various granitoid series and related rocks. *Journal of Volcanology and Geothermal Research*, 14, pp. 169-186.

Le Maitre, R. W. (Ed.). (1989). A classification of igneous rocks and glossary of terms. Blackwell Scientific Publ., Oxford, pp. 193.

le Roex, A. P., Bell, D. R. and Davis, P. (2003). Petrogenesis of Group I kimberlites from Kimberley, South Africa: evidence from bulk-rock geochemistry. *Journal of Petrology*, 44, pp. 2261-2286.

le Roex, A., Späth, A. and Zartman, R. (2001). Lithospheric thickness beneath the southern Kenya Rift: implications from basalt geochemistry. *Contributions to Mineralogy and Petrology*, 142, 1, pp. 89-106.

Leake, B. E., Brown, G. C. and Halliday, A. N. (1980). The origin of granite magmas: a discussion. *Journal of the Geological Society of London*, 137, pp. 93-97.

Li, H. Y., Chen, R. X., Zheng Y. F. and Hu, Z. (2016). The crust-mantle interaction in continental subduction channels: Zircon evidence from orogenic peridotite in the Sulu orogeny. *Journal of Geophysical Research Solid Earth*, 121, pp. 687-712.

Lilienbach, L. (1833). Journal d' un voyage géologique fait en travers toute la chaíne des Carpathes, en Bucovine, en Transylvanie et dans le Marmarosch. *Mémoires de la Société géologique de France*, 1, pp. 237-316.

Loiselle, M. C. and Wones, D. R. (1979). Characteristics and origin of anorogenic granites. Abstracts of papers to be presented at the Annual Meetings of the Geological Society of America and Associated Societies, San Diego, California, November 5-8, 11, pp. 468.

Ludwig, K. R. (2003). Isoplot 3.00: a geochronological toolkit for Microsoft Excel. Berkeley Geochronology. Center Special Publication, pp. 71.

Maniar, P. D. and Piccoli, P. M. (1989). Tectonic discrimination of granitoids. *Geological Society of America Bulletin*, 101, pp. 635–643.

Marks, M., Vennemann, T., Siebel, W. and Markl, G. (2003). Quantification of Magmatic and Hydrothermal Processes in a Peralkaline Syenite–Alkali Granite Complex Based on Textures, Phase Equilibria, and Stable and Radiogenic Isotopes. *Journal of Petrology* 44 (7), pp. 1247-1280.

Martinez, I. A., Harris, C., Le Roex, A. P. and Milner, S.C. (1996). Oxygen isotope evidene for extensive crustal contamination in the Okenyenya complex, Namibia. *Geochimica et Cosmochimica Acta*, pp. 4497-4508.

Mason, P. R. D., Downes, H., Thirwall, M. F., Seghedi, I., Szakacs, A., Mattey, D. P., Lowry, D. (1996). Crustal contamination as a major petrogenetic process in the East Carpathian Neogene and Quaternary continental margin arc, Romania. *Journal of Petrology*, 37, pp. 927-960.

Mattey, D., Lowry, D. and Macpherson, C. (1994). Oxygen isotope composition of mantle peridotite, *Earth and Planetary Science Letters*, 128, pp. 231-241.

Mauritz, B. (1909). Das Syenitmassiv von Ditró. *Földtani Közlöny*, 39, p. 522.

Mauritz, B. (1912). A ditrói kankrinit. *Mat. term. tud. Értesítő,* XXX, pp. 673-687.

Mauritz, B., Vendl. M. and Harwood, H. F. (1923). Adatok a ditró szienitmaszívum abisszikus kőzeteinek ismeretéhez. *Mat. term. tud. Értesítő*, XL, pp. 271-313.

Mauritz, B., Vendl. M. and Harwood, H. F. (1925). A ditrói szienit további petrokémiai vizsgálata. M*at. term. tud. Értesítő*, XLI, pp. 61-73.

McCulloch, M. T., Gregory, R. T., Wasserburg, G. J. and Taylor, H. P. Jr. (1981). Sm-Nd, Rb-Sr, and $^{18}O/^{16}O$ isotopic systematics in an oceanic crustal section: evidence from the Samail Ophiolite. *Journal of Geophysical Research Solid Earth,* 86, pp. 2721-2735.

McDonough, W. F. and Sun, S. S. (1995). Composition of the Earth. *Chemical Geology,* 120, pp. 223-253.

Meade, F. C., Troll, V. R., Ellam, R. M., Freda, C., Font, L., Donaldson, C. H. and Klonowska, I. (2014). Bimodal magmatism produced by progressively inhibited crustal assimilation. *Nature Communications* 5, pp. 4199.

Médard, E., Schmidt, M. W., Schiano, P. and Ottolini, L. (2006). Melting of amphibole-bearing wehrlites: an experimental study on the origin of ultra-calcic nepheline-normative melts. *Journal of Petrology,* 47. pp. 481-504.

Middlemost, E.A.K., 1989. Iron oxidation ratios, norms andthe classification of volcanic rocks. *Chemical Geology*, 77(1), pp. 19-26.

Mikova, J. and Denkova, P. (2007). Modified chromatographic separation scheme for Sr and Nd isotope analysis in geological silicate samples. *Journal of Geosciences,* 52, pp. 221-226.

Miller, C. F., Wooden, J. F., Bennett, V. C., Wright, J. E., Solomon, G. C. and Hurst, R. W. (1990). Petrogenesis of the composite peraluminous–metaluminous Old Woman-Piute Range batholith, southeastern California; isotopic constraints. In: J. L., Anderson, ed., *The Nature and Origin of Cordilleran Magmatism*. *Geological Society of America, Memoir*, 174, pp. 99-109.

Mingram, B., Trumbull, R. B., Littman, S. and Gerstenberger, H. (2000). A petrogenetic study of anorogenic felsic magmatism in the Cretaceous Paresis ring complex, Namibia: evidence for mixing of crust and mantle-derived components. *Lithos* 54, 1–22.

Misra, S., Reinhardt, J. and Wilson, A. H. (2017). Petrochemical evolution of the White Mfolozi granite pluton: Evidence for a late Palaeoarchaean A-type granite from the SE Kaapvaal craton, South Africa. *Lithos*, 286, pp. 480-501.

Moldoveanu S. (2012). Geochemical characteristics of rare earth elements and selected trace elements from the Mănăila ore deposit (Eastern Carpathians). *Carpathian Journal of Earth and Environmental Science*, 7 (3), pp. 193-198.

Morogan, V., Upton, B. G. J. and Fitton, J. G. (2000). The petrology of the Ditrau alkaline complex, Eastern Carpathians. *Mineralogy and Petrology*. 69, pp. 227-265.

Murphy, J. B., Shellnutt, J. G. and Collins, W. J. (2018). Late Neoproterozoic to Carboniferous genesis of A-type magmas in Avalonia of northern Nova Scotia: repeated partial melting of anhydrous lower crust in contrasting tectonic environments. *International Journal of Earth Sciences*, 107 (2), pp. 587-599.

Musselwhite, D. S., De Paolo, D. J. and McCurry, M. (1989). The evolution of a silicic magma system-isotopic and chemical evidence from the Woods Mountain Volcanic Center, Eastern California. *Contributions to Mineralogy and Petrology*, 101, pp. 19-29.

Neumann, E. R., Sørensen, V. B., Simonsen, S. L. and Johnsen, K. (2000). Gabbroic xenoliths from La Palma, Tenerife and Lanzarote, Canary Islands: evidence for reactions between mafic alkaline Canary Islands melts and old oceanic crust. *Journal of Volcanology and Geothermal Research*, 103, pp. 313-342.

Nier, A. O. (1939). The isotopic constitution of radiogenic leads and the measurement of geological time. II. *Physical Review,* 55, pp. 53-163.

Pál-Molnár, E. (1992). Petrographical characteristics of Ditró (Orotva) hornblendites, Eastern Charpatians, Transylvania (Romania): a preliminary description. *Acta Mineralogica-Pertrographica,* 33, pp. 67-80.

Pál-Molnár, E. (1998). A Ditrói szienitmasszívum földtani felépítése és petrológiája, különös tekintettel a hornblenditek és dioritok kialakulására. I-II. Ph. D. értekezés, JATE, Szeged, pp. 219.

Pál-Molnár, E. (2000). Hornblendites and diorites of the Ditrău Syenite Massif. Ed. Dept. Of Mineralogy, Geochemistry and Petrology, University of Szeged, Szeged, pp. 172.

Pál-Molnár, E. and Árva-Sós, E. (1995). K/Ar radiometric dating on rocks from the northern part of the Ditrău Syenite Massif and its petrogenetic implications. *Acta Mineralogica-Pertrographica*, Szeged, 36, pp. 101-116.

Pál-Molnár, E., Batki, A., Almási, E., Kiss, B., Upton, B. G. J., Markl, G., Odling, N. and Harangi, S. (2015b). Origin of mafic and ultramafic cumulates from the Ditrău Alkaline Massif, Romania. *Lithos*, 239, pp. 1-18.

Pál-Molnár, E., Batki, A., Ódri, Á., Kiss, B. and Almási, E. (2015a) Geochemical implications of the magmatic origin of granitic rocks from the Ditrău Alkaline Massif (Eastern Carpathians, Romania). *Geologia Croatica*, 68 (1), pp. 51-66.

Pană, D., Balintoni, I. and Heaman, L. (2000). Precise U-Pb zircon dating of the syenite phase from Ditrău Alkaline Igneous Complex. Studia Universitatis Babeş-Bolyai. *Geologia*, 45 (1), pp. 79-89.

Patiño Douce, A. E. (1997). Generation of metaluminous A-type granitoids by low-pressure melting of calc-alkaline granitoids. *Geology*, 25, pp. 743-746.

Pearce, J. A. (1996). A user's guide to basalt discrimination diagrams. In: D. Wyman, ed., *Trace element geochemistry of volcanic rocks: appliction for massive sulphide exploration,* Winnipeg: Geological Association of Canada, Mineral Deposits Division, pp. 79-113.

Pearce, J. A. and Peate, D. W. (1995). Tectonic implications of the composition of volcanic arc magmas. *Annual Reviews of Earth and Planetary Sciences* 23, pp. 251-285.

Pearce, J. A., Harris, N. B. W. and Tindle, A. G. (1984). Trace element discrimination diagrams for the tectonic interpretation of granitic rocks. *Journal of Petrology*, 25, pp. 956-983.

Petford, N. and Atherton, M. (1996). Na-rich partial melts from newly underplated basaltic crust: the Cordillera Blanca Batholith, Peru. *Journal of Petrology*, 37, pp. 1491-1521.

Pilet, S., Baker, M.B. and Stolper, E.M. (2008). Metasomatize lithosphere and the origin of alkaline lavas. *Science*, 320, pp. 916-919.

Pin, C., Briot, D., Bassin, C. and Poitrasson, F. (1994). Concominant separation of strontium and samarium–neodymium for isotopic analysis in silicate samples, based on specific extraction chromatography. *Analytica Chimica Acta*, 298, pp. 209-217.

Pitcher, W. S. (1983). Granite Type and Tectonic Environment. In: K., Hsu, Ed., *Mountain Building Processes*, London: Academic Press, pp. 19-40.

Pitcher, W. S. (1987). Granites and yet more granites forty years on. *Geologische Rundschau*, 76, pp. 51-79.

Poitrasson, F., Duthou, J. L. and Pin, C. (1995). The relationship between petrology and Nd isotopes as evidence for contrasting anorogenic granite genesis: example of the Corsican Province (SE France). *Journal of Petrology*, 36, 1251-1274.

Popescu, G., (1985). Rb-Sr geochronological data on rocks of the Ditrau Massif (in romanian, manuscript). Arch. GEOLEX Harghita (Miercurea Ciuc).

Pupin, J. P. (1980). Zircon and granite petrology. *Contributions to Mineralogy and Petrology*, 73, pp. 207-220.

Rosmana, K. J. R. and Taylor, P. D. P. (1998). Isotopie compositions of the elements 1997. *Pure and Applied Chemistry*, 70, pp. 217.

Rousseau, R., Willis, J. and Duncan, A. (1996). Practical XRF calibration proecedures for major and trace elements. *X-ray Spectometry*, 25 (4), pp. 179-189.

Rudnick, R. L. (2003). The Crust. In: H.D., Holland and K. K., Turekian, eds., *Treatise on Geochemistry*, Volume 3, Oxford: Elsevier-Pergamon.

Rutherford, E. and Soddy, F. (1903). Radioactive change. *Philosophical Magazine*, 6, pp. 576-591.

Săndulescu, M. (1984). Geotectonica României. Editura Technică, pp. 336.

Săndulescu, M., Kräutner, H. G., Balintoni, I., Russo-Săndulescu, M. and Micu, M. (1981). The Structure of the East Carpathians (Moldavia - Maramures Area) Guide Exc. B1, Carp.-Balk. Geol. Assoc., XII Congr. Inst. Geol. Geophys., pp. 92, Bucuresti.

Schairer, J. F. (1950). The alkali-feldspar join in the system $NaAlSiO_4$-$KAlSiO_4$-SiO_2. *Journal of Geology*, 58, pp. 512-517.

Schmitt, A. K., Emmermann, R., Trumbull, R. B., Bühn, B. and Henjes-Kunst, F. (2000). Petrogenesis and $^{40}Ar/^{39}Ar$ geochronology of the Brandberg Complex, Namibia: evidence for a major mantle contribution in metaluminous and peralkaline granites. *Journal of Petrology* 41, 1207–1239.

Sharp, Z. (2006). Principles of Stable Isotope Geochemistry. Prentice Hall

Shaw, D. M. (1977). Trace element behavior during anatexis, in Magma Genesis. Edited by Dick H.J.B. Oregon Department of Geology and Mineral Industries Bulletin. 96, pp. 189-213.

Sheppard, S. M. F. and Harris, C. (1985). Hydrogen and oxygen isotope geochemistry of Ascension Island lavas and granites: variation with crystal fractionation and interaction with sea water. C*ontributions to Mineralogy and Petrology*, 91, pp.74-81.

Skjerlie K. P. and Johnston A. D. (1992). Vapor-absent melting at 10 kbar of a biotite- and amphibole-bearing tonalitic gneiss: implications for the generation of A-type granites. *Geology*, 20, pp. 263-266.

Sogrik, E. (2010). A Ditrói Alkáli Massyivum syienitjeinek kőzettana. Szegedi Tudományegyetem - Diplomamunka, Szeged.

Stacey, J.S., and Kramers, J.D., 1975, Approximation of terrestrial lead isotope evolution by a two-stage model. *Earth and Planetary Science Letters*, 26, pp. 207–221.

Steiger, R. H. and Jäger, E. (1977). Subcommission on geochronology: convention on the use of decay constants in geochronology and cosmochronology. *Earth and Planetary Science Letters*, 36, pp. 359-362.

Stewart, B. W. and DePaolo, D. J. (1992). Diffusive isotopic contamination of mafic magma by coexisting silicic liquid in the Muskox intrusion. *Science*, 255, pp. 708-711.

Streckeisen, A. (1931). Sur la tectonique des Carpates méridionales. *An. Inst. Geol. Roum*., 16, 328-417, besonders pp. 408-413.

Streckeisen, A. (1938). Das Nephelinsyenit-Massiv von Ditro in Rumänien als Beispiel einer kombinierten Differentiation und Assimilation. *Verhandlungen der Schweizerischen Naturforschenden Gesellschaft*, pp. 159-161.

Streckeisen, A. (1952). Das Nephelinsyenit-Massiv von Ditro (Siebenbürgen), I. *Teil. chweizeriche Mineralogische und Petrographische Mitteilungen*, 32, pp. 251-309.

Streckeisen, A. (1954): Das Nephelinsyenit-Massiv von Ditro (Siebenbürgen), II. *Teil. Schweizeriche Mineralogische und Petrographische Mitteilungen*, 34, pp. 336-409.

Streckeisen, A. (1960). On the structure and origin of the Nephelinsyenite Complex of Ditro (Transylvania, Roumania). Rep. 21th IGC, 13, pp. 228-238.

Streckeisen, A. (1973). Plutonic Rocks. Classification and nomenclature recommended by the IUGS Subcommission on the Systematics of Igneous Rocks. *Geotimes,* 18 (10), pp. 26-30.

Streckeisen, A. and Hunziker, I. C. (1974). On the origin of the Nephelinesyenite Massif of Ditró (Transylvania, Romania). Schweiz. *Min. Petr. Mitt*. 54, pp. 59-77.

Sun, S. and McDonough, W. F. (1989). Chemical and isotopic systematics of oceanic basalts: implications for mantle composition and processes. Geological Society, London, Special Publications 42, pp. 313-345.

Sylvester P. J. (1989). Post-collisional alkaline granites, *Journal of Geology,* 97, pp. 261-280.

Szádeczki, Gy. (1899): A kolozsvári egyetem ásvány-földtani intézetének és az erdélyi Múzeum ásványtárának kiállítása Párizsban az 1900. évben. *Orvos-természettudományi Értesítő*. XXI. p. 209.

Tanaka, T., Togashi, S., Kamioka, H., Amakawa, H., Kagami, H., Hamamoto, T., Yuhara, M., Orihashi, Y., Yoneda, S., Shimizu, H., Kunimaru, T., Takahashi, K., Yanagi, T., Nakano, T., Fujimaki, H., Shinjo, R., Asahara, Y., Tanimizu, M. and Dragusanu, C. (2000). JNdi-1: a neodymium isotopic reference in consistency with LaJolla neodymium. *Chemical Geology,* 168, pp. 279-281.

Taylor, H. P. Jr. (1986). Igneous rocks: II. Isotopic case studies of circumpacific magmatism. *Reviews in Mineralogy,* 16, pp. 273-316.

Taylor, H. P. Jr. (1977). Water/rock interactions and the origin of H_2O in granitic batholiths. *Journal of the Geological Society, London,* 133, pp. 509-558.

Taylor, R. P., Strong, D. F. iand Kean, B. F. (1980). The Topsails igneous complex: Silurian-Devonian peralkaline magmatism in western Newfoundland. *Canadian Journal of Earth Sciences*, 17, pp. 427-439.

Taylor, S. R. and McLennan, S. M. (1985). The continental crust: its composition and evolution. Blackwell Scientific Publication, Carlton, pp. 312.

Tepper, J. H., Nelson, B. K., Bergantz, G. W. and Irving, A. J. (1993). Petrology of the Chililwack batholith, North Cascades, Washington. Generation of calc-alkaline granitoids by melting of mafic lower crust with variable water fugacity. *Contributions to Mineralogy and Petrology,* 113, pp. 333-351.

Tindle, A. G. and Pearce, J. A. (1983). Assimilation and partial melting of continental crust: Evidence from the mineralogy and geochemistry of autoliths and xenoliths. *Lithos*, 16, pp. 185-202.

Trumbull, R., Harris, C., Frindt, S. and Wigand, M. (2004). Oxygen and neodymium isotope evidence for source diversity in Cretaceous anorgenic granites from Namibia and implications for A-type granite genesis. *Lithos,* 73 (1-2), pp. 21-40.

Turner, S. P., Foden, J. D. and Morrison, R. S. (1992). Derivation of some A-type magmas by fractionation of basaltic magma: an example from the Pathaway Ridge, South Australia. *Lithos*, 28, pp. 151-179.

Urey, H. (1947). The thermodynamic properties of isotopic substances, J. Chem. Soc. (London), pp. 562-581.

Valley, J. W., Chiarenzelli, J. R. and McLelland, J. M. (1994). Oxygen isotope geochemistry of zircon. *Earth and Planetary Science Letters*, 126, pp. 187-206.

Valley, J. W. (2001). Stable isotope thermometry at high temperatures. *Reviews in Mineralogy and Geochemistry*, 4, pp. 365-413.

Valley, J. W., Kinny, P. D., Schulze, D. J., Spicuzza, M. J. (1998). Zircon megacrysts from kimberlite: oxygen isotope variability among mantle melts. *Contributions to Mineralogy and Petrology*, 133, pp. 1-11.

Valley, J. W., Kitchen, N., Kohn, M. J., Niendorf, C. R., Spicuzza, M. J. (1995). UWG-2, a garnet standard for oxygen isotope ratio: strategies for high precision and accuracy with laser heating. *Geochimica et Cosmochimica Acta.* 59, pp. 5223-5231.

Valley, J. W., Lackey, J. S., Cavosie, A. J., Clechenko, C., Spicuzza, M. J., Basei, M. A. S., Bindeman, I. N., Ferreira, V. P., Sial, A. N., King, E. M., Peck, W. H., Sinha, A. K. and Wei, C. S. (2005). 4.4 billion years of crustal maturation: oxygen isotope ratios of magmatic zircon. *Contributions to Mineralogy and Petrology*, 150, pp. 561-580.

Valley, J. W. (2003). Oxygen isotopes in zircon. In: J. M., Hanchar and P. W. O., Hoskin, eds., *Zircon.* Mineralogical Society of America and Geochemical Society, *Reviews in Mineralogy and Geochemistry*, 53, pp. 343-385.

Vaselli, O., Downes, H., Thirlwall, M., Dobosi, G., Coradossi, N., Seghedi, I., Szakacs, A. and Vannucci, R. (1995). Ultramafic xenoliths in Plio-Pleistocene alkali basalts from the Eastern Transylvanian Basin: depleted mantle enriched by vein metasomatism. *Journal of Petrology*, 36, pp. 23-53.

Voda, A. and Balintoni, I. (1994). Corelari lithostratigrafice în cristalinul Carpaţilor Orientali. Studia Universitates Babeş-Bolyai, *Geologia*, XXXIX, pp. 61-66.

Watson, E. B. and Cherniak, D. J. (1997). Oxygen diffusion in zircon [J]. E *Earth and Planetary Science Letters*, 148, pp. 527-544.

Weaver, B. L. (1991). The origin of ocean island basalt end-member compositions: Trace-element and isotopic constraints: *Earth and Planetary Science Letters*, 104, pp. 381-397.

Wedepohl, K. H. (1991). Chemical composition and fractionation of the continental crust. *Geologische Rundschau*, 80, pp. 207-223.

Weis, D., Kieffer, B., Maerschalk, C., Barling, J., Jeroen, de Jong, J., Williams, G. A., Hanano, D., Pretorius, W., Mattielli, N., Scoates, J. S., Goolaerts, A., Friedman, R. M. and Mahoney, J. B. (2006). High-precision isotopic characterization of USGS reference materials by TIMS and MC-ICP-MS. *Geochemistry Geophysics Geosystems*, 7, Q08006.

Weis, D., (1983). Pb isotopes in Ascension Island rocks: oceanic origin for the gabbroic to granitic plutonic xenoliths. *Earth and Planetary Science Letters*, 62, pp. 273-282.

Whalen, J. B., Currie, K. L. and Chappell, B. W. (1987). A-type granites: geochemical characteristics, discrimination and petrogenesis. *Contributions to Mineralogy and Petrology*, 95, pp. 407-419.

White, A. J. R. (1979). Sources of Granitic Magma. Abstracts of Papers to be Presented at the Annual Meetings of the Geological Society of America and Associated Societies, San Diego, California, November 5–8, 1979, 11, pp. 539.

White, A. J. R. and Chappell, B. W. (1983). Granitoid types and their distribution in the Lachlan Fold Belt, south-eastern Australia. *Geological Society of America, Memoir*, 159, pp. 21-34.

White, W. (2010). Oceanic island basalts and mantle plumes: the geochemical perspective. *Annual Reviews of Earth and Planetary Sciences*, 38, pp. 133-160.

White, W. M. (2007). Chapter 6 - Geochronology in the online book *Geochemistry*. Available at: http: //www.geo.cornell.edu/geology/classes/geo455/Chapters.HTML.

Whitney, D. L. and Evans, B. W. (2010). Abbreviations for names of rock-forming minerals. *American Mineralogist*, 95 (1), pp. 185-187.

Willis, J. P. and Duncan, A. R. (2008). Understanding XRF Spectrometry, Volume 2: Quantitative analysis and special sample preparation and presentation methods. Almelo: PANalytical B.V.

13-11 to 13-16.

Wilson, M. and Downes, H. (1991). Tertiary-Quaternary extension-related alkaline magmatism in Western and Central Europe. *Journal of Petrology,* 32 (4), pp. 811-849.

Wilson, M., Downes, H. and Cebria, J. M. (1995). Contrasting fractionation trends in coexisting continental alkaline magma series; Cantal, Massif Central, France, *Journal of Petrology,* 36, pp. 1729-1753.

Wilson, M. (1989). Igneous petrogenesis - a global approach. London: Unwin-Hyman.

Yoder, H. S. and Tilley, C. E. (1962). Origin of basalt magmas: An experimental study of natural and synthetic rock systems. *Journal of Petrology,* 3, pp. 342-352.

Žak, K., Pudılová, M. and Breıter, K. (2005). Oxygen isotope study of the highly fractionated Podlesí granite system, Krušné hory Mts., Czech Republic. *Bulletin of Geosciences,* 80, pp. 139-143.

Zhang, X. Y., Cherniak, D. J. and Watson, E. B. (2006). Oxygen diffusion in titanite: Lattice diffusion and fast-path diffusion in single crystals [J]. *Chemical Geology.* 235, pp. 105-123.

Zhao, Z. and Zheng, Y. F. (2003). Calculation of oxygen isotope fractionation in magmatic rocks. *Chemical Geology,* 193, pp. 59-80.

Zhao, Z., Di-Cheng, Z., Dong, L. and Xuanxue, M. (2016). In situ SIMS oxygen isotope analysis of olivine in the Tibetan mantle xenoliths. EGU General Assembly 2016 held 17-22 April, 2016 in Vienna Austria, id. EPSC2016-10960

Zheng, Y. F. (1993a). Calculation of oxygen isotope fractionation in anhydrou silicate minerals. *Geochimica et Cosmochimica Acta,* 57, pp. 1079-1091.

Zheng, Y. F. (1993b). Calculation of oxygen-isotope fractionation in hydroxyl-bearing silicates. *Earth and Planetary Science Letters,* 120, pp. 247-263.

Zincenco, D. and Vlad, C. (1978). Studiul geochimic-metalogenetic al masivului Ditrău şi al formaţiunilor adiacente cu privire specială asupra mineralizaţiilor associate. Partea I. Structura, petrografia şi petrologia masivului. Archiva IPEG „Harghita", Manuscript.

Zindler, A. and Hart, S. R. (1986). Chemical geodynamics. *Annual Reviews of Earth and Planetary Sciences,* 14, pp. 493-571.

Zirkel, F. (1866). Lehrbuch der Petrographie, Bonn, 595.